Dynamic Performance of a PEM Fuel Cell System

Rabbani, Raja Abid

Publication date:
2013

Document Version
Publisher's PDF, also known as Version of record

Dynamic Performance of a PEM Fuel Cell System

Abid Rabbani

PhD Dissertation

Department of Mechanical Engineering

Technical University of Denmark

Kongens Lyngby 2013

Dynamic Performance of a PEM Fuel Cell system

PhD Thesis

DTU Mechanical Engineering
Thermal Energy Section
Technical University of Denmark

Nils Koppels Allé, Bldg. 403,
DK–2800 Kongens Lyngby,
Denmark.
Phone: (+45) 4525 4107
Fax: (+45) 4588 4325
www.mek.dtu.dk
ISBN: 978–87–7475–359–9
DCAMM Special Report: S154

Preface

This thesis is submitted in partial fulfilment of the requirements for the Ph.D. degree at the Technical University of Denmark (DTU). The research was conducted under the supervision of Assoc. Prof. Masoud Rokni at the Thermal Energy Section, Department of Mechanical Engineering and represents a culmination of work and learning that has taken place from April 2010 to March 2013. The project was realized within the framework of LINK2009 which is mainly financed by the Danish Energy Agency EUDP program. Presented work was carried out in direct collaboration with H2Logic A/S, a company involved in design and development of automotive fuel cell systems.

This thesis mainly covers dynamic aspects of a PEM fuel cell system and is presented as a monograph, but it also contains a number of papers based on the work in this research.

Abid Rabbani
Lyngby, March 2013

Acknowledgements

A PhD dissertation is apparently a work of one, but only with the support of many helping hands behind the curtain. Fortunately for my case, I was accompanied by an extended team of professionals who contributed in their different ways to help me through the completion of this thesis. For this, I would like to extend my appreciation to them.

First and foremost, I offer my sincerest gratitude to my supervisor and mentor, Assoc. Prof. Masoud Rokni, whose patience and kindness, as well as academic experience have been invaluable to me. I appreciate his vast knowledge and expertise in many areas, his assistance in writing scientific papers, and allowing me the freedom and opportunity to select the course of my research. I must also acknowledge Henrik Mortensen from H2Logic Company, for his suggestions and collaboration throughout this period. Special thanks to my colleague Elham Hosseinzadeh for engaging in many productive discussions and her valuable suggestions.

The support and encouragement of my colleagues at TES section has been indispensable, and I would like to extend my deepest gratitude to all of them. During my stay at DTU, I got to share my office with fellow PhD students who truly broadened the value of work: Tuong–Van Nguyen, Jorrit Wronski and Leonardo Pierobon. I very much enjoyed exchange of ideas and thoughts, and all the fun moments together. Furthermore, I am grateful to the Head of Section Assoc. Prof. Brian Elmegaard, for always taking time to discuss problems and his encouragement. Special thanks go to Arne Egelund for his valuable comments and assistance in translation of thesis abstract. I owe heartfelt appreciation to the section secretary, Eva Stitz Larsen, for her motherly love and exceptional care during the course of my studies.

I would take this opportunity to express due indebtedness to my beloved parents, who have been a constant source of emotional, moral and financial support throughout my life. I must not forget to thank my brothers, each of them with unique traits: Amjad's integrity, Majid's foresight, Sajid's perseverance and Atif's wisdom, all of which I admire and seek for my personal and professional development. Undoubtedly, my wife Saima deserves a special word of gratitude for her understanding, moral support, patience and love through the duration of my research.

Abstract

Concerns about climate change and projections of fossil fuel depletion within the next century have prompted our interest towards energy efficient and therefore more sustainable alternatives. Transport sector is one of the major consumers of oil and predictions imply a further surge with an increasing trend of more vehicles. This necessitates focus for alternative fuel which is not only sustainable but also environmentally benign well into the future. Hydrogen is expected to play a major role in future energy economy in this context and fuel cells have shown a significant potential as an efficient solution for harnessing energy of hydrogen. The polymer electrolyte membrane fuel cells (PEMFCs) currently appear to be the preferred fuel cell for the automotive industry due to their inherent virtue of being compact with quick start–up and higher efficiencies with very low emissions. Nonetheless, there are many issues related to the fuel cell durability, cost and performance which hinder their commercialization and competence with present automotive engines.

The overall aim of this research is to investigate the dynamic behaviour of a PEMFC system in order to improve the efficiency of the system. Such systems when employed in automobiles are subjected to continuous changes in load and external operating conditions, making it important to investigate the dynamic performance of the system. Current research was focused towards addressing key problems related to fuel and air supply, species transportation within the fuel cell, water and thermal management of the system. These objectives were achieved by firstly developing a PEMFC stack and a humidifier model in a component based simulation tool (Aspen Dynamics) and then simulations of the entire system with integrated controls were carried to emulate an actual fuel cell system operating under varying operating conditions with the influence of external parameters.

Effects of these controls and other components on overall performance of the system were also investigated in this work.

System analyses were conducted for start–up sequence and transitory load changes. Issues related to thermal and water management were addressed with considerable focus on species crossover mechanisms across the fuel cell. Finally, study on nitrogen crossover was conducted and associated purging strategies are discussed. Different purging techniques were simulated to further gain insight into hydrogen dilution issues caused by nitrogen accumulation in the fuel cell anode. The research conducted here could be helpful in understanding intricate transient processes within the fuel cell and system model could be used as a thorough tool for predicting PEMFC dynamics and to contribute as a basis for the design and optimization of system controls and purging strategies.

Resumé

Bekymringer om klimaændringer og forudsigelser om udtømning af de fossile brændstofressourcer inden for det næste århundrede har resulteret i et ønske om energieffektive og dermed mere bæredygtige alternativer. Transportsektoren er en af de største forbrugere af olie og med den forventede stigning i antal køretøjer vil dette forbrug yderligere stige. Dette nødvendiggør at der sættes fokus på alternative brændstoffer, som ikke kun er ressourcemæssigt bæredygtige, men også miljøvenlige langt ind i fremtiden. Brint forventes at spille en stor rolle i fremtidens energiøkonomi og i denne sammenhæng har brændselsceller vist et betydeligt potentiale som en effektiv måde at udnytte energien i brint. Polymerelektrolytmembran brændselsceller (PEMFCs) synes i øjeblikket at være den foretrukne brændselscelle til bilindustrien i kraft af at være kompakt med hurtig opstart, højere effektivitet og meget lave emissioner. Ikke desto mindre er der mange forhold i forbindelse med brændselscellers holdbarhed, deres omkostninger og ydeevne, som vanskeliggør deres anvendelse i eksisterende bilmotorer– og dermed deres kommercialisering.

Det overordnede formål med denne forskning er at undersøge den dynamiske opførsel af et PEMFC system med henblik på at forbedre effektiviteten af systemet. Sådanne systemer er, når de anvendes i biler, udsat for stadige ændringer i belastning og eksterne driftsbetingelser, hvilket gør det vigtigt at undersøge systemets dynamiske ydeevne. Den udførte forskning var fokuseret på at løse centrale problemer i forbindelse med brændstof–og lufttilførsel, stoftransport inden for brændselscellen samt styring af vand–og varmestrømme i systemet. Disse mål blev opnået ved først at udvikle modeller af en PEMFC stak og en luftfbefugter i et komponentbaseret simuleringsværktøj (Aspen Dynamics) og derefter simulere hele systemet med integreret styring med det formål at efterligne

en virkelig brændselscelle, der arbejder under forskellige driftsbetingelser og under indflydelse af ydre parametre. Virkningen af styringesenheder og andre komponenter på den samlede ydelse af systemet blev også undersøgt i dette arbejde.

Systemanalyser blev udført for opstartsekvenser og forbigående belastningsændringer. Spørgsmål vedrørende styring af vand– og varmestrømme blev behandlet med særligt fokus på stofovergang på tværs af brændselscellen. Endelig blev undersøgelse af kvælstofovergang gennemført og relevante rensningsstrategier diskuteret. Forskellige rensningsteknikker blev simuleret for yderligere at få indsigt i problemet med brintfortynding som følge af nitrogenakkumulering i brændselscellens anode. Den forskning, som er udført her, vil kunne være en hjælp til at forstå indviklede forbigående processer i brændselscellen, og systemmodellen vil kunne anvendes som et nyttigt redskab til at forudsige dynamikken af en PEMEC og danne grundlag for design og optimering af styrings– og rensningsstrategier for systemet.

List of Publications

The main body of this thesis is based on the following papers:

Rabbani, A & Rokni, M. "Dynamic Simulation of a Proton Exchange Membrane Fuel Cell System for Automotive Applications", Proceedings of Sustainable Energy & Environmental Protection (SEEP) Conference, Dublin, 2012; 311–316.

Rabbani A, Rokni M, Hosseinzadeh E, Mortensen H. "Start–up Analysis of a PEM Fuel Cell System in Vehicles", International Journal of Green Energy, 2013; 11: 1–21.

Rabbani, A & Rokni, M. "Dynamic characteristics of an automotive fuel cell system for transitory load changes", Journal of Sustainable Energy Technologies & Assessments, 2013; 1: 34–43.

Rabbani, A & Rokni, M. "Effect of nitrogen crossover on purging strategy in PEM fuel cell systems", accepted for Journal of Applied Energy, 2013.

Other related publications

Hosseinzadeh E, Rokni M, Rabbani A, Mortensen H. "Thermal and water management of low temperature PEM fuel cell in forklift truck power system", Journal of Applied Energy, 2013; 104: 434–444.

Contents

List of Figures

List of Tables

Nomenclature

Roman symbols

A	area (cm^2)
a	activity (–)
a_w	water activity (–)
C	constant (–)
C_t	stack thermal capacitance (kW)
c^*	concentration (mol cm^{-3})
D_w	water diffusion (cm^2s^{-1})
D_λ	water diffusion coefficient (–)
E	theoretical voltage (V)
e	error (%)
E_{N_2}	activation energy (kJ mol^{-1})
$\dot{E}$	exergy rate (kW)
$\dot{E}x$	energy rate (kW)
$\dot{E}x_D$	rate of exergy destruction (kW)
F	Faraday's constant (C $mol^{-1}K^{-1}$)
f_v	volumetric ratio of water in membrane (–)
$\overline{g}_f^0$	Gibbs free energy (J mol^{-1})
$\overline{H}$	enthalpy (J mol^{-1})
I	current (A)
i	current density (A cm^{-2})
i_0	exchange current density (A cm^{-2})
$i_{\lim}$	limiting current density (A cm^{-2})
i_{loss}	internal current density (A cm^{-2})

$i_{\max}$	maximum current density (A cm^{-2})
J_{H_2O}	water molar flux (mol $s^{-1}cm^{-2}$)
J_{N_2}	molar flux of nitrogen (mol $s^{-1}cm^{-2}$)
k	reaction speed constant (mol $s^{-1}cm^{-2}$)
K_P	proportional gain (–)
K_{N_2}	nitrogen permeance (kmol $s^{-1}cm^{-1}bar^{-1}$)
M_m	molecular weight of membrane (Kg mol^{-1})
$\dot{n}$	molar flow rate (mol s^{-1})
N_{cell}	number of cells (–)
n_e	electrons transferred (mol_e mol_{fuel}^{-1})
n_{el}	number of electrons in rate step reaction (–)
n_{drag}	electro osmotic drag (–)
OP	controller output (–)
P	pressure (bar)
$\overline{P}$	average pressure (bar)
P_{H_2}	hydrogen partial pressure (–)
P_{O_2}	oxygen partial pressure (–)
$\dot{P}_{net}$	stack power (kW)
P_{stack}	power produced by stack (kW)
$\dot{Q}$	heat transfer rate (kW)
r	resistance (Ω cm^2)
R	universal gas constant (J $mol^{-1}K^{-1}$)
RH	relative humidity (–)
S	stoichiometric ratio (–)
$\overline{S}$	entropy (J $mol^{-1}K^{-1}$)
T	temperature (K)
t	instantaneous time (s)
τ	integration variable (s)
t_m	membrane thickness (cm)
V	voltage (V)
$\dot{W}$	rate of work delivered (kW)
y_i	molar fraction of species (–)

Greek symbols

α	transfer coefficient (–)
α_{N_2}	perm scale factor (–)

β	symmetry factor (–)
η	efficiency (–)
λ	water content (–)
ρ_{dry}	membrane density (g cm^{-3})
σ_m	membrane activity (S cm^{-1})
ξ	constant (–)

Subscripts

a	anode
act	activation
air	air
Ar	argon
c	cathode
cell	single fuel cell
conc	concentration
d	derivative
diffusion	back diffusion
drag	electro–osmotic drag
dry	dry membrane
el	electrical
exh	fuel cell cathode exhaust
f	hydrogen
FC	fuel cell
i	integral
in	inlet
inv	inverter
int rev	internally reversible
ion	ionic
loss	loss to the ambient
mass	mass flow
max	maximum
mem	membrane
ohmic	ohmic
out	outlet
ref	reference state
sat	saturated
st	stored
stack	fuel cell stack
sys	system

Superscripts

0	standard conditions
a	anode
c	cathode
ch	chemical
ph	physical
sat	saturation
t	total

Abbreviations

BEV	Battery Electric Vehicle
BoP	Balance of Plant
DOE	Department of Energy, USA
DTU	Technical University of Denmark
EMF	Electro–Motive Force
FCV	Fuel Cell Vehicle
FCEV	Fuel Cell Electric Vehicle
FCHEV	Fuel Cell Hybrid Electric Vehicle
GDL	Gas Diffusion Layer
GHG	Greenhouse Gas
HHV	Higher Heating Value
ICE	Internal Combustion Engine
LHV	Lower Heating Value
MEA	Membrane Electrode Assembly
OCV	Open Circuit Voltage
PEMFC	Polymer Electrolyte Membrane Fuel Cell
PFSA	Per–Fluoro Sulfonic Acid
PID	Proportional Integral Derivative
SOFC	Solid Oxide Fuel Cell

Chapter 1

Introduction

1.1 Motivation

For decades, fossil fuels have dominated the energy market of the world. However, it is becoming increasingly obvious that they ought to diminish sooner or later. Regardless of it, our growing reliance on these fuels is another concern. It is reported that fossil fuels provided 85% of the total primary energy demand in 2008, which raises a number of concerns. Combustion of these fossil fuels leads to local and global emissions of pollutants such as NOx, SOx and greenhouse gases (GHG). It is believed that GHG emissions associated with the provision of energy services is a major cause of climate change. Increase in global average temperature since the mid of 20^{th} century is undoubtedly attributed to the increase in GHG levels. Furthermore, the combustion of fossil fuels accounted for 56.6% of all anthropogenic GHG emissions and these concentrations have continued to grow 39% above pre–industrial levels by the end of 2010. In the last two centuries, global use of fossil fuels (coal, oil and gas) has substantially increased to lead the energy supply market, resulting in rapid surge of CO_2 emissions. The amount of carbon in fossil fuel reserves and resources not yet burned has the potential to add more quantities of CO_2 to the atmosphere and the overwhelming majority of the projections show even higher emissions in 2100 compared with those in 2000. Rise in GHG concentrations imply an increase in global mean temperatures with potentially irreversible climate changes, contributing to adverse impacts on water resources, ecosystems, human health, food security and aquatic life near coasts. In order to be confident of deterring the temperature, atmospheric GHG concentrations would need to be stabilized; i.e. that global emissions of CO_2 have to decrease by 50 to 85% below the levels of year 2000 by 2050. At the moment, CO_2 concentrations are continuing to increase, necessitating an immediate goal of inverting this trend towards a decline till 2015 [1].

Transport sector's utilization of world primary energy consumption of oil has increased from 45.4 % (1973) to 61.5 % (2010), which is predicted to surge with an increasing trend of more vehicles [2]. Also, world mobility is bound to escalate with growing population in developing countries like China and India. Consequently, individual mobility in the future is directly associated with the availability of fuel for transportation. Though oil production is expected to peak in the near future, oil reserves are finite and will deplete soon. Scarcities of energy sources are another reason for price fluctuations and speculations in the energy market, which raise the issue of energy security for many countries which have a strong dependence on imported oil.

All these factors necessitate focus for alternative fuels which are not only sustainable but also environmental friendly. Hydrogen is suggested to be one of the options and is argued to be an attractive substitute for petroleum as the main fuel for transportation in the future. Fuel cell systems, being the most capable utilizers of hydrogen, have received substantial attention in recent years and research on these systems has drastically increased mainly due to their characteristic advantages of clean and efficient energy conversion. Existing fuel cell systems are categorized based on the type of electrolyte and preferred operating conditions. Among various types of fuel cells, the Proton Exchange Membrane Fuel Cells (PEMFC) is currently the best choice for portable power generation due to its relatively low operating temperature, quick start–up, high power density and efficiency, system robustness and low degradation due to corrosion. This thesis focuses on PEMFC system for automotive applications such as forklifts.

1.2 Scope of the research project

The work presented here is a part of a larger project (LINK–2009), which is a consortium of academia and industrial partners. This project encompasses different aspects of hydrogen based infrastructure with specific focus on implementation of fuel cell technologies including a demonstration of a new PEM Fuel Cell Vehicle. The project consists of ten work packages and DTU–Mechanical Engineering is leading WP7 (as well as WP8), which deals with the design and development of the fuel cell system. The current PhD project is aimed at investigation of fuel cell transients and the research is directly collaborated with *H2Logic* A/S, which is one of the industrial partners involved in integration of fuel cell systems in material handling vehicles.

Other project collaborators include:

- Vestforsyning A/S
- Rotrex A/S
- Dana–Tank A/S
- Hytor A/S
- Teknologisk Institute
- Parker Hannifin Danmark A/S
- Hydrogen Link Association
- Holstebro Kommune

1.3 Objectives of the thesis

The aim of this dissertation is to investigate the dynamic behaviour of a PEMFC system in order to improve system efficiency when it is operating at different loads and operating conditions. One of the objectives was to identify components that are not responding properly at different operating conditions, and finally, recommending new operational strategies for different operating scenarios.

The abovementioned objectives were achieved by indulging in the following aspects of the current research work:

i. Development of a dynamic PEMFC stack model.
ii. Implementation of controls for the fuel cell system.
iii. Exergy analysis of the fuel cell stack.
iv. Start–up and transitory load change analysis.
v. Water and thermal management of the fuel cell stack.
vi. Investigation of species crossover across the fuel cell membrane.
vii. Analysis of anode–purge strategies at different operating conditions.

1.4 Methodology

The main portion of the work is based on computer simulations. The characteristics of the PEMFC system described above are implemented in Aspen Plus Dynamics ™ [3] which is a simulation tool for process modelling and energy system analysis. It is a component based simulation tool with a built–in unit operation modules library. The component library includes models of heat exchangers, reactors, turbo machinery, decanters and separators, pressure relief valves, controllers along with utility components and manipulators. These components are built upon by a standard set of equations representing their

physical properties, such as isentropic and mechanical efficiencies in blowers and turbines. Also, user–based custom models can be imported into the program.

In Aspen plus Dynamics, the physical model of the complete system is devised by connecting the relevant component models through work, heat or material streams and by defining operating conditions for the system. The numerical solvers then convert these inputs into set of dynamic mathematical equations which are either solved by sequential modulation or simultaneously with equation oriented methods. These equations include mass and energy conservation for all units and connecting streams, as well as relations for the states and thermodynamic properties of the working fluids. In addition, the program has the ability to run steady–state, initialization and dynamic simulations for the same model by changing model or module specifications. Occurrences of disturbances and operation constraints can be enforced by adding control modules to the constructed system. An implicit integrator ensures stable solution of the dynamic simulation and varies the integration step to ensure simulation accuracy.

Model for PEMFC stack and humidifier is built using Aspen Custom Modeller. The fuel cell stack model constitutes equations for fuel cell electrochemistry, mass and energy balances, water crossover in membrane and fuel cell thermodynamics. The model is implemented into ASPEN Dynamics and system controls are implemented in order to emulate real system behaviour characterizing the transient nature of operations.

1.5 Limitations and Validation

This project is only focused on dynamics of the PEMFC system and only a few potential issues related to fuel cell performance were addressed to keep the focus well within the scope of research. Though steady–state models of the fuel cell stack were developed for validation purposes, most of the emphasis has been set on dynamic operations of the system. Moreover, only a specific fuel cell stack of 21.2 kW nominal power is selected for modelling and power conditioning modules such as inverters and batteries have been neglected.

Veracity of the developed models is validated by previous studies and design data provided by the fuel cell manufacturers. Assumptions relating to component models and operating conditions are based on open literature and personal communications. Simulation results and associated analysis should therefore be considered in view of all the assumptions presented in the dissertation and appended papers.

1.6 Overview of Thesis

The thesis is based on appended papers and is divided into 10 chapters and 2 appendices:

Chapter 1 presents the statement of purpose for this research project. The objectives of the study are outlined with a brief description of the primary methodologies used, and limitations curtailing the work are outlined.

Chapter 2 provides the background of fuel cells with the challenges faced, key constituents of the fuel cell system and literature review of the underlying studies.

Chapter 3 presents the layout of the studied system with breakdown of PEM fuel cell and description of ancillary components.

Chapter 4 elaborates on system control design and associated strategies for fuel cell stack management.

Chapter 5 elucidates on the detailed modelling of the PEM fuel cell stack.

Chapter 6 covers the exergy analysis of the fuel cell stack.

Chapter 7 encompasses the simulation of start–up sequence of the fuel cell system and discusses on its preliminary findings.

Chapter 8 presents the system response and stack behaviour during transitory load changes.

Chapter 9 describes the effect of nitrogen crossover in the fuel cell and its impact on purging strategies of anode recirculation.

Chapter 10 summarizes the work with concluding remarks and suggestions for improvements in proceeding studies.

Appendix A contains the programming codes of modelled components in Aspen dynamics.

Appendices B–E comprise of journals and conference papers published during this research.

Chapter 2

Background

2.1 Hydrogen economy

Hydrogen economy refers to the vision of using hydrogen as a clean energy source and is anticipated to compete with coal, natural gas and gasoline as a fuel for power generation and transportation applications in the future. Nonetheless, hydrogen is an energy carrier and not an energy source i.e. it is not found in pure form and it must be produced from other means of energy sources; such as natural gas, biomass, alcohols and water. Currently, most of the hydrogen is produced in the chemical industry by steam reforming of natural gas. As we are gradually becoming dependent on natural gas and its extensive use will progressively make it more expensive, reserves for natural gas will eventually deplete in the long run. Additionally, production of hydrogen from fossil fuel reformation still generates CO_2, which would further require its capture and sequestration.

Due to the reasons above, the climate change impact of using hydrogen depends on the carbon footprint of the energy used to produce it. Other alternatives of producing hydrogen with very low CO_2 formation or no CO_2 at all need be explored. Electrolysis of water by electricity produces no CO_2, though electric power used has to be supplied from the grid raising questions on carbon dioxide emissions associated to the electrical power used. However, if electricity generated through renewable resources such as wind power, hydropower and solar photovoltaic cells is used in water electrolysis, hydrogen produced in this process is accounted to be virtually carbon–free. Biomass feed stocks such as wood can be chemically or thermally reformed to produce hydrogen as well. This method releases relatively less carbon dioxide and argued to be almost neutral since all of the produced CO_2 is recycled by the growth cycle of biomass. The biological reformation of biomass using micro–organisms is yet another mode of hydrogen production with a relatively lower carbon footprint.

Future prospects of hydrogen advocate it to be an important energy carrier and deliver energy in a usable form to end consumers. Hydrogen may be able to store useful energy from intermittent renewable sources, such as solar and wind power plants when there is low demand for electricity or during part load conditions. Electricity from these sources could be used to electrolyze water and produce hydrogen, which can be easily stored onsite. Figure 2.1 depicts the amount of energy required per kg of H_2 produced and associated GHG emissions for three main processes. Production of H_2 by using Photovoltaic (PV) could be considered the best choice in terms of both energy requirements and emissions. Hydrogen is already used extensively in the process industry so issues related to its storage, handling and large–scale distribution can be addressed quite easily. Hydrogen is therefore considered by many a key proponent for the future energy systems with low carbon footprints and potential cost benefits as well.

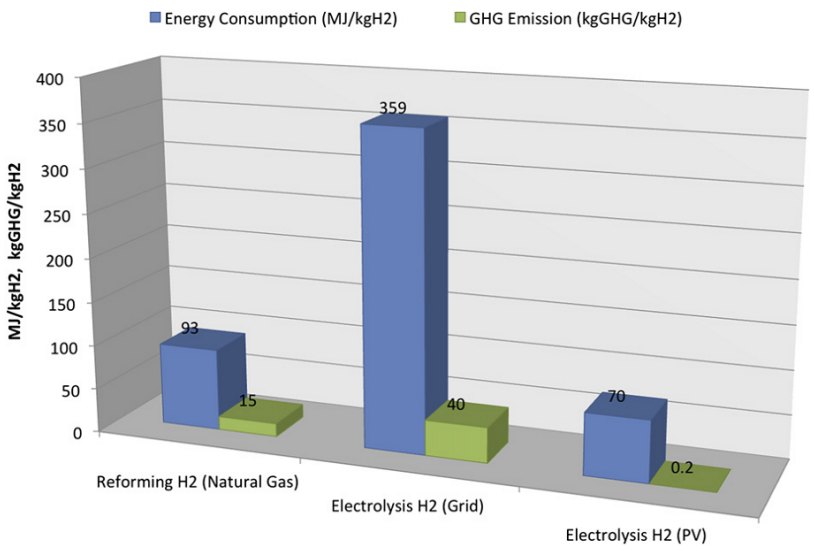

Figure 2.1: Energy consumption and corresponding GHG emissions for different types of hydrogen production processes [4].

One of the most promising ways of utilizing hydrogen is its use as a fuel for automotive applications. Hydrogen when used in conjunction with a fuel cell directly generates electricity which transfers the power to vehicle through electric motor. Fuel cells are a promising technology and are deemed attractive because they are far more efficient than the internal combustion engines and hold several other advantages. Hydrogen is ubiquitous to fuel cells which operate best on pure hydrogen. PEM fuel cells use hydrogen and oxygen to produce electricity, heat and

water as the only by-product. In comparison to batteries, fuel cells do not discharge and provide power as long as fuel is supplied.

2.2 PEM fuel cells for automobiles

PEM fuel cells have shown the greatest potential for automotive applications. The PEM system allows compact design and achieves a high energy to weight ratio. The principal advantage of the PEMFC is its ability to operate at moderate temperatures of 80°C and a relatively quick start-up when hydrogen is used as the fuel. System efficiencies for PEMFCs falls above 50% in comparison to internal combustion engines (ICE), which are around 30% (gasoline)-40% (Diesel) efficient[5]. Also, the fuel cell technology enables low noise and vibration operation, even during rapid accelerations and in some cases is found to be 50% lower than the corresponding ICEs [6]. In respect, fuel cells also contribute the least to the environmental emissions; direct hydrogen fuel cell vehicles emit only water vapour. Figure 2.2 displays the projected GHG pollutions for different types of light duty vehicles in the coming years.

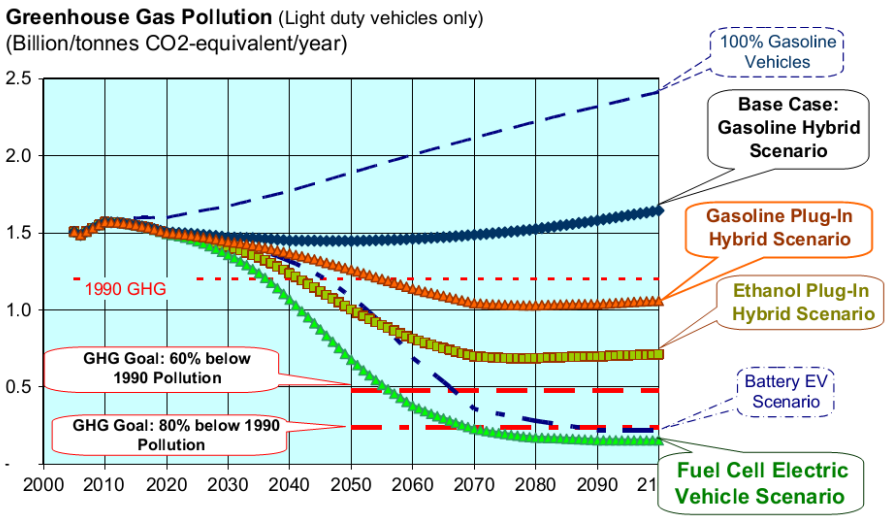

Figure 2.2: Predictions for GHG pollution for different vehicles [7].

Major limitations in commercialization of the PEM fuel cell systems are high manufacturing costs and complex water management systems. Varying seasonal ambient temperatures are a further challenge. During winter, the fuel cell stack is more susceptible to damage caused by ice formation within the stack. Heating of

the stack for cold start-ups is therefore usually recommended by the manufacturers to prevent freeze damage. Furthermore at colder ambient conditions, the fuel cell takes more time to reach the operating temperatures and the stack performs inefficiently during this period.

Thermal management is another issue which affects the stack life. Lower temperatures hinder the performance of the fuel cell whereas on the other hand, excessive heat could cause damage to the stack. Effective management requires control of operating temperatures through cooling mechanisms, as well as adequate supply of reactants require blowers and pumps that consume around 15% of the power produced by the fuel cell. Another challenge is the cost of these fuel cells. At present, the estimated service life of PEMFCs operating in a vehicle is in the range of 2000–4000 hours. The DOE has set the target 5,000 hours of service life for 2015. Reaching such goals would require advanced manufacturing techniques for more durable stacks, which further increase production costs. There are also plans to reduce this cost to half of that at present by 2015 [8]. Currently, the fuel cells cost significantly higher than internal combustion engines and until mass-produced, they will not be competing with the engines used currently.

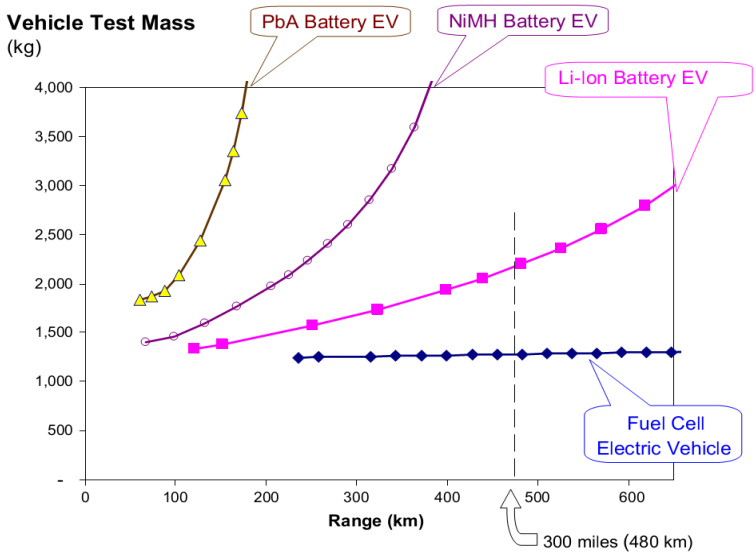

Figure 2.3: Vehicle mass for different types of battery electric vehicles in comparison with fuel cell vehicles [7].

Partly for these reasons, and partly due to uncertainties of practical and commercial advent of fuel cell vehicles (FCVs), market attention has been diverted

towards battery electrical vehicles (BEVs). Even with these limitations, the fuel cells have quite a many advantages over batteries. A practical concern for BEVs is the weight and volume occupied by the on–board battery in the vehicle. On the other hand, FCV would only require storage for the fuel. Fig. 2.3 exemplifies the travel distance for vehicles with different energy storages and corresponding weight of the vehicles. It can be observed that in order to have larger driving range, the mass of the vehicle with batteries increases substantially. In this respect, the FCV can afford to conquer longer distances and can be regarded similar to IC engine cars.

Hydrogen is a high energy content fuel. Still, its low density presents many technical challenges in on–board storage design. One approach of avoiding such a problem is on–board reforming of hydrogen–rich fuels. In case of PEMFC systems, pure hydrogen is the preferable fuel of choice as other fuels can cause decomposition of the polymer membrane. PEM fuel cells being very sensitive to carbon monoxide require additional purification making it an expensive option [9], [10]. Out of all prospective options, on–board compressed hydrogen storage in cylinders seems to be a feasible storage option. At the moment, the price of hydrogen is about twice to that of gasoline and there is also a need to develop the hydrogen infrastructure for availability and supply of fuel to dispensing outlets. Refuelling stations for hydrogen to support the increasing number of vehicles are very expensive to build presently.

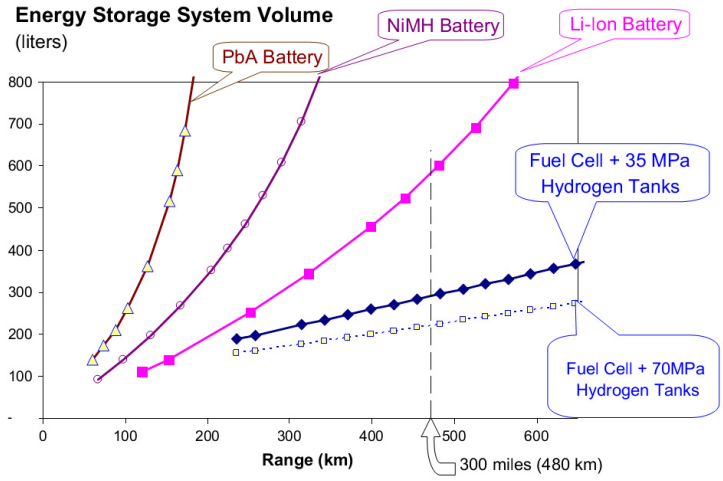

Figure 2.4: Comparison of storage volumes for battery operated vehicles and fuel cell electric vehicles [7].

In comparison to FCVs, the charging unit for the plugin BEVs is cheaper at the moment; however the charging times are very high compared to the refilling of hydrogen for fuel cells. Moreover, storage volume occupied by the batteries is many folds more than required for the PEMFCs. The logarithmical curves of storage volumes for batteries place limitations in terms of size of the vehicle. In comparison, the hydrogen tank pressurized at 700 bar takes the least of the volume (see Fig. 2.4), and is more appropriate for light duty vehicles where size of the automobile is one of the main concerns.

In spite of analogous outcomes of the fuel cells and IC engines in automotive applications, FCVs require an on–board battery coupled to the fuel cell, mainly due to the poor response time and narrow power ranges of the PEM fuel cells. A hybrid FCEV would be a better choice for near future, mainly due to reduction in fuel cell stack costs by employing smaller FC modules and a corresponding plugin battery to supplement the fuel cell at start–ups and during high load operations. It is also likely that tougher environmental regulations are implemented by some governments in the future, which would mandate the use of FCEVs/FCHEVs or BEVs. Also, fossil fuels will eventually get depleted and fuel cells could become the power source in the future. Meanwhile, research and development of the fuel cell could continue to make it economically and practically viable for providing alternative options against the IC engines.

2.3 PEM Fuel cell system

2.3.1 Fuel cell theory

A fuel cell is a device that electrochemically converts fuel into electricity through a chemical reaction, with energy loss in the form of heat. A single PEMFC consists of a polymer electrolyte membrane between two electrodes and two gas diffusion layers that facilitate oxygen and hydrogen reactions at cathode and anode respectively. These cells are connected in series to construct a fuel cell stack capable of developing large voltage potentials and consequently generate high powers. Figure 2.4 shows the basic operations of a single PEMFC. Hydrogen gas is supplied at the anode and oxygen or air is fed at the cathode. Hydrogen molecules are dissociated into ions and electrons at the cell anode. The negative electrode provides a path for the electrons to flow out into the external load and reach the positive electrode. H^+ ions, at the same time cross through the membrane and combine with the electrons and oxygen in the cathode to produce water, which is

expelled out of the fuel cell. If air is used instead of pure oxygen, then cathode exhaust also constitutes unreacted air along with the produced water.

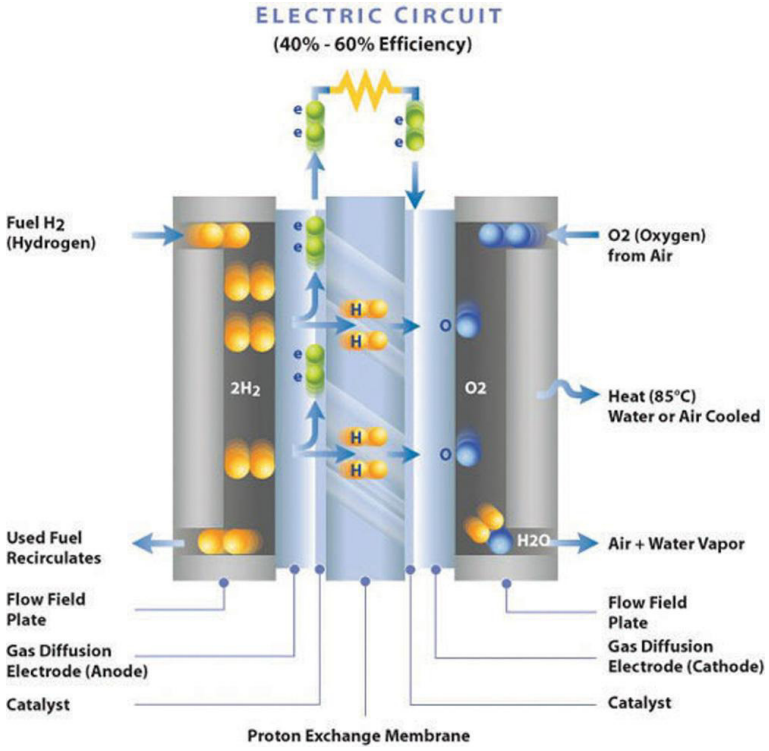

Figure 2.5: Working principle of a single PEM fuel cell [11].

The two chemical reactions occurring at the anode and the cathode are described as:

$$H_2 \leftrightarrow 2H^+ + 2e^-$$

$$½O_2 + 2H^+ + 2e^- \leftrightarrow H_2O$$

$$H_2 + ½O_2 \leftrightarrow H_2O + heat$$

For hydrogen fuelled PEMFC, the reactions at cathode and anode only produce water and heat in addition to the electrical power. Such a power system seems quite simple; nonetheless it requires well–suited conditions to operate successfully. These conditions are controlled by ancillary components which define the overall system performance and effect the lifetime of the fuel cell stack. A complete fuel cell system would comprise the following components:

- Fuel cell stack
- Fuel and oxidant supply system
- Water management
- Heat management
- Electrical power conditioning subsystem
- Controls

2.3.2 Reactant supply system

PEMFC systems are comparatively compact due to allowance of higher operating pressures. Air entering the stack is pressurized by a compressor or blower depending on the anode pressure of the fuel. Although this increases the power density of the stack, it comes at the expense of additional cost of compressor and power consumed by it which leads to a reduction in overall system efficiency. Moreover, the fuel cell stack usually operates at higher fuel and air stoichiometry in order to avoid catalyst degradation and related operational problems [12],[13]. Removal of generated water is also attributed to the higher stoichiometry in the fuel cell cathode. Similarly for the anode side, hydrogen is fed by a control valve at low utilization factors. Hydrogen starvations within cell sites are another issue to be handled to have a stable operation and prolonged stack life. It is therefore imperative to have an efficient and reliable feed system for the PEMFC stack.

2.3.3 Water Management

The proton conductivity of the fuel cell depends heavily on the water content of the membrane. To ensure sufficient conductivity and prevent damage to the membrane, it must be sufficiently humidified. On the other hand, a lot of effort has to be put into expelling the generated water to avoid the flooding, or blockage at the reaction sites on the electrode. For systems with recirculation loops, additional equipment is required to condense, trap and reuse the water collected at the exhausts of the stack

2.3.4 Heat Management

Most of the reactions occurring in the fuel cell are exothermic in nature and produce heat in addition to electrical power. In case of PEMFCs, the electrical efficiency can reach up to 60% and rest is converted to heat energy. For physical stability of the stack, a constant operating temperature needs to be maintained by effective rejection of the produced heat. A cooling circuit comprising of heat

exchangers and air radiators is responsible for thermal management of the system with liquid coolant as the medium. Proper sizing of heat exchangers and radiators is critical in system design as they would occupy a larger volume which is undesirable in light duty vehicles.

2.3.5 Control system

Fuel cell operating requirements in vehicles are more inflexible than stationary applications. These systems have to operate at varying conditions related to temperatures, pressures, power load and humidity. All the auxiliary components, such as air and fuel supply system which include air blower (compressor) and control valves, and the thermal control system which comprises of heat exchangers, coolant pumps and air radiators need to control the input for fuel cell stack. Therefore, system level control of key parameters becomes useful in stable and efficient operation of the PEMFC system.

2.4 Literature review

Many PEM fuel cell models have been developed in recent years. Whereas, steady–state models of these systems are present in abundance. A few others have studied these system components individually, where most of the research focuses on the fuel cell or the stack itself. Ceraolo et al. [14] developed a simplistic dynamic model based on cathode kinetics. Amphlett et al. [15] extended their previous steady–state model and presented a generalized transient model. Another bulk dynamic model catering to inverter load effects is presented by Yerramalla et al. [16]. Pathapati et al. [17] developed a fuel cell model that included effects of double charge layers at cell sites along with flow dynamics and pressure gradient in flow channels. Jia et al. [18] also followed suit and developed a dynamic model in MATLAB/Simulink to investigate fuel cell transient electrical responses under various operating conditions.

Multi–dimensional models on the other hand, disseminate complex characteristics of reactant flows and charge transportation within fuel cells. Hu et al. [19] represented a three–dimensional computational PEMFC model with conventional and inter–digitized flow fields. Another three–dimensional mixed–domain PEM fuel cell model of Kim et al. [20], which integrates intrinsic transport mechanisms, has been applied to investigate effects of the fully coupled transport phenomena. These models might be useful in predicting cell or stack performance, however due

to high computational times and limitations to integrate with BoP components, these models are not suitable for system–level modelling.

Start–up behaviour of PEMFC stacks at sub–zero temperatures has been studied and reported by few researchers. Li et al. [21] conducted experiments and validated their model based on the results. Yan et al. [22] investigated effects of sub–freezing temperatures on fuel cell performance and start–up. A model for freeze start is also developed by Mangold et al. [23] and compared to experimental data. Meng [24] and Sundaresan and Moore [25] both proposed thermal models for cold start of PEMFC. However, start–up behaviour of a stack above the freezing temperatures which accounts for multiple varying operating conditions and changing auxiliary components outputs has not been reported to a greater extent.

Heat management in PEMFCs being a critical factor in its operations and performance is accounted for in open literature as well. Issues related to temperature dynamics are dealt and studied by Vasu and Tangirala [26], which could predict the effects of temperature and feed flows on system transient behaviour. Khan and Iqbal [27] proposed a transient model to predict voltage output and cell efficiency, and a thermal model including heat transfer coefficients and energy balance for the stack. Shan and Choe [28] analysed the temperature distribution on fuel cells by developing a two–dimensional model. Another control–oriented thermodynamic model is also proposed by del Real et al. [29].Coolant control strategies were suggested by Ahn and Choe [30] after investigation of temperature effects on the system. Jung and Ahmed [31] developed a stack model based on real–time simulator in MATLAB/ Simulink environment and validated it with experimental setup of *Ballard* Nexa fuel cell. A thermal management system for a PEMFC was designed by Asghari et al. [32]. Influence of temperature on fuel cell's characteristics is also reported by Beicha [33]. While some researchers such as Park and Choe [34] presented a transient stack model and analysed the temperature distribution on fuel cells, management of stack temperature by coolant flow controls becomes vital in efficient operations and reliable performance of the fuel cell system.

A very few studies have been conducted on exergy analysis of dynamic fuel cell systems, although most of studies are carried out on individual fuel cells or stacks at steady–state. Blomen [35] was one of the first to introduce the concept of exergy analysis in fuel cells. Study on the energy and exergy analysis of a PEMFC–assisted combined heat and power system is published by Saidi et al. [36]. Barbir and Gomez [37] investigated the efficiency and economics of PEM fuel cells. Kazim [38] reported an exergy analysis of a PEM fuel cell with respect to operating parameters, and performed exergo–economic (thermo–economic) analysis of a PEM fuel cell at

various operating conditions [39]. A similar study was conducted by Mert et al. [40]. Recently Miansari et al. [41], reported a performance analysis of PEMFC based on exergetic parameters. Leo et al. [42] and Uyanga et al. [43] studied exergies for PEM fuel cells in marine applications and experimental work on Nexa module, respectively.

Literature available on water and gas crossover through PEMFC membranes is not uncommon. Kocha et al. [44] characterized gas crossovers by applying an in–situ electrochemical technique to determine hydrogen crossover rates and devised a model to predict the amount of nitrogen accumulation in the anode channels. Ahluwalia and Wang [45] modelled and analysed the buildup of N_2 in the anode recirculation loop and the impact of this buildup on the performance of 90 kW PEMFC stack. Catalano et al. [46] reported the effects of relative humidity on gas permeability and swelling in Nafion membranes used in fuel cells. Baik and Kim [47] calculated nitrogen permeability coefficients (NPC) by employing a mass spectrometer and analyzed N_2 crossover under open circuit voltage and power generation conditions. Weber [48] reported the effects of membrane pinholes and increase in gas–permeation on PEMFC's performance. It was also shown that water and thermal management is also affected where there are large pinholes in the membrane.

From a control perspective, it is important to develop a complete model that emulates the real behaviour of PEMFC stack when subject to varying operating conditions. Therefore, a need to develop a system–level model is identified that responds to dynamic effects of all the necessary BoP components which is lacking in the aforementioned studies. Of all publications in open literature, relatively limited studies account for control–oriented PEMFC models. Pukrushpan et al. [49] presented a transient study on PEM fuel cell, which included compressor flow controls and incorporated inertia dynamics, membrane humidification and pressure effects into the model. A control–oriented thermal dynamic model is also proposed by Del Real et al. [29]. Ahn and Choe [30] investigated temperature effects on the overall system performance and suggested strategies for coolant controls.

There are a few published papers investigating the purge process modelling in general or specifically pertaining to individual aspects of the process. Zhu et al. [50] experimentally determined the critical flow rate in anode exhaust stream by manual purging of Nexa Power module. Tang et al. [51] also investigated the transient response of the aforementioned module and identified factors influencing its performance. Zhai et al. [52] also presented their study on anode water flooding and simulated the gas purge effect for medium current densities.

Gou et al. [53] presented a one–dimensional computational model to study the dynamic behaviour of pressure in anode flow field during the purge process. It was shown that different current densities had minimal influence on the pressure drop and the pressure swing during this transient process. A dynamic three–phase transport model was developed by Wang et al. [54], which lead in identification of the optimum water uptake parameters for purge cycles during startup from subfreezing temperatures and subsequent shutdowns. Karimaki et al. [55] setup a test bench to study inert gas buildup effects on fuel cell stack and introduced the use of online hydrogen sensor to measure gas crossover across the cell. Promislow et al. [56] built a simple analytical model to describe the steady state profile of anode N_2 concentration in PEMFCs with straight gas channels and identified an optimum bleed rate for the specified stack. Some others have published papers addressing the anodic dead–end mode of operations in the fuel cell anode. Hou et al. [57] developed a dynamic voltage model for a 'dead–ended' FC to simulate hydrogen purging in order to prevent water accumulation in the anode. Muller et al. [58] also correlated nitrogen accumulation with a 20–cell temporal fuel cell performance operating in anodic 'dead–end' mode by estimating permeability characteristics of typical Nafion membranes. Siegel et al. [59] modelled a PEM fuel cell operating with a 'dead–end' mode and experimentally verified the evolution of liquid water and nitrogen fronts along the length of anode channels. They further developed the 1D model with periodically–purged anode channels and incorporate simple resistance model for predicting nitrogen permeance and water transportation through the membrane and presented their findings in Yesilyurt et al. [60]. Another experimental study was conducted by Choi et al. [61] in which purge characteristics of a cathodic dead–end mode PEMFC for a submarine were analysed.

Chapter 3

System Configuration

The fuel cell stack is basically sustained by supporting equipment and together constitute a fuel cell system. Figure 3.1 shows the schematics of fuel cell system analysed in this study. The PEM fuel cell stack [62], has a nominal power output of 21.2 kW and constitutes 110 cells with the cell area of 285.8 cm^2. Auxiliary equipment, also referred to as balance of plant (BOP) includes components such as air blower and humidifier, pumps, heat exchangers and radiator for the cooling circuit, flow valves and controllers. Compressed air is cooled and humidified before entering the cathode side of the stack. On the other side, pressurized hydrogen from storage tank is fed to the anode of fuel cell.

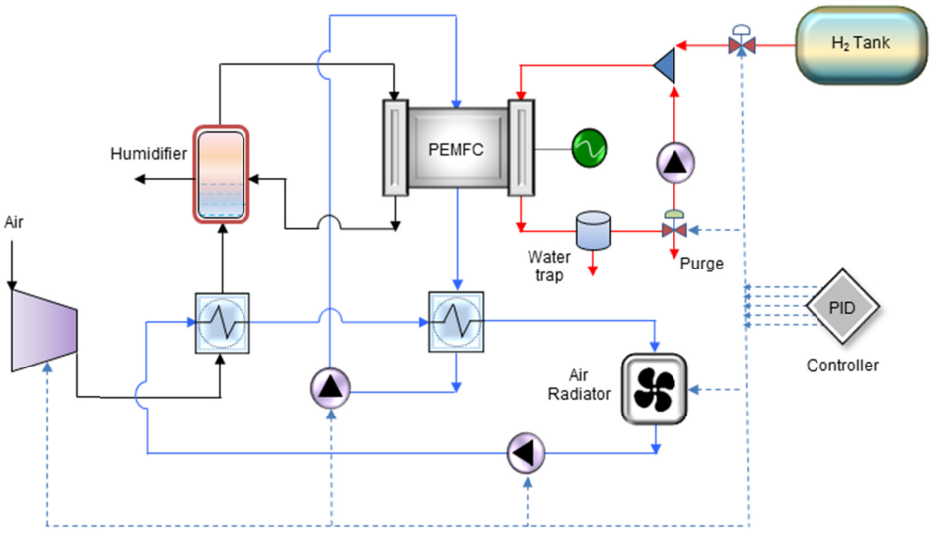

Figure 3.1: Schematic of a PEM fuel cell system with auxiliary components and control layout.

Since a higher fuel stoichiometry is maintained, anode exhaust is recirculated back to the feed stream via a recirculation pump. Liquid water present in the anode exhaust is collected in a water trap, whereas the remaining water present in the stream is purged with the other gases by a solenoid valve before mixing with the inlet stream.

Heat produced in the stack is absorbed by the coolant which circulates in a circuit associated with the stack and a heat exchanger. An external cooling loop, connected to the interior heat exchanger, in turn cools the water in the internal circuit. This circuit also comprises of a heat exchanger to precool the blown air and an air radiator for heat rejection from the system. Flow of water is regulated by pumps in the respective circuits. This system layout is implemented in Aspen Dynamics simulation tool [3] along with the developed models of Fuel cell stack and the humidifier.

Table 3.1: Nominal operating conditions for PEMFC stack

Reactant Parameter		**Current (A)**					
		15	30	60	120	240	300
Fuel (Pure Hydrogen)							
Inlet stoichiometry Min.		6.3	3.4	2.2	1.9	1.6	1.6
Nominal Inlet Pressure	(kPa)	115	116	131	155	200	220
Pressure Drop	(kPa)	9	13	13	14	16	18
Oxidant (Ambient Air)							
Inlet stoichiometry Min.		5.1	2.4	1.8	1.8	1.8	1.8
Nominal Inlet Pressure	(kPa)	108	110	117	138	180	200
Pressure Drop	(kPa)	8	13	12	16	40	53
Relative Humidity	(%)	95	95	95	95	95	95
Coolant							
Inlet Temperature Max.	(°C)	60	60	60	60	60	60
Outlet Temperature Max.	(°C)	61	63	66	67	68	70
Minimum Coolant flow	(lpm/cell)	0.05					

In order to ensure a stable operation of the system, a control system is needed to regulate flows, temperatures and pressures in the feed streams, cooling circuits and plant components. Here, PID controllers are deployed to emulate the system in real time and thereby analyse response characteristics under varying operating conditions. Aspen Dynamics comprises of built–in PID controllers and manipulators. Combinations of these components are used to devise controls for

entire system. These controllers collect data from various component inlet and outlets which are regarded as pressure, temperature and flow transmitters, and manipulate the corresponding components to reach the desired state. Due to this fact, current system responses and its behaviour are attributed to the formulated control strategy which is based on fuel cell stack limitations and recommendations by the manufacturer. Component properties related to these limitations are discussed in the following subsections whereas intricate details of system controls are dealt in the relevant section later.

3.1 PEM Fuel Cell stack

In a PEMFC, the electrolyte membrane is pressed between two catalyst layers followed by gas diffusion layers. These layers form the electrochemical part of the cell and are often merged to the term MEA (membrane electrode assembly). Bipolar plates on each side of MEA complete a single cell formation. The main components used in a single cell are briefly described in terms of their functionality and structure.

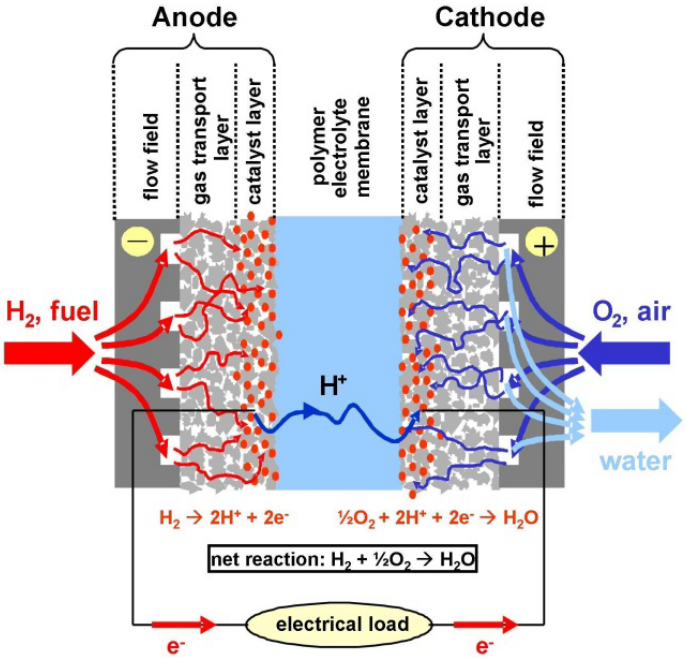

Figure 3.2: Structure of a single fuel cell [63].

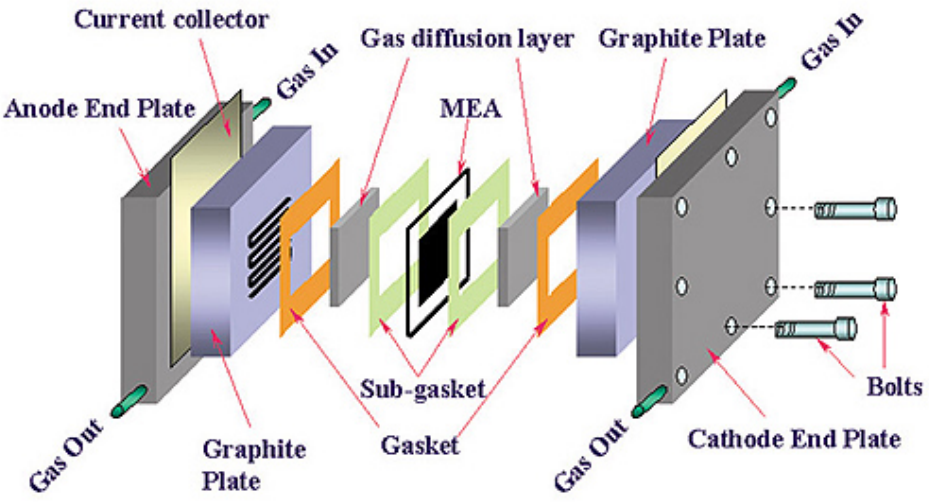

Figure 3.3: Exploded view of PEM fuel cell stack [64].

3.1.1 Membrane

The prime function of the membrane is to transport the protons from dissociated hydrogen molecules at electrode sites of the anode. Other functions include separating the anode and cathode reactants by acting as electron insulator while providing high ionic current conductivity. The most commonly used electrolyte in PEMFC is a polymer based material (Semi crystalline Teflon with perfluoro sulfonic acid [PFSA] groups) branded as Nafion®. These membranes are mostly selected due to their good availability at low cost, lesser water drag, low gas permeability, strength and flexibility, and chemical as well as thermal stability.

The ionic conductivity of PFSA membranes could reach to that of aqueous electrolytes; however they are strongly dependent on the membrane water content. Therefore the uptake of water and its distribution within the membrane becomes a defining factor for ionic conductivity of the fuel cell.

3.1.2 Catalyst Electrode layer

The catalyst layers on the anode and cathode side of the membrane promote and speed up the electrochemical reactions. The catalyst present in the layer helps in dissociating reactant molecules to generate external electronic current. Currently, platinum based catalysts are usually used, in spite of being very expensive. To ensure close contact of the three phases (electric, ionic, gas), catalyst particles are finely dispersed on an electrically conducting carbon paper. In this manner the

amount of active platinum exposed to the reactants is maximized, greatly increasing power density of the cell. The catalyst electrodes are attached to the adjacent components by spraying or coating the catalyst ink either on gas diffusion layer or the membrane and hot pressing the MEA together.

3.1.3 Gas Diffusion Layer

The gas diffusion layer (GDL), also known as the backing layer is a critical component in fuel cell assembly. The main function of a GDL is to distribute the reactant gases to and from the reaction sites while providing electronic conductivity. Additionally, its role is to minimize water flooding and maximize the electronic contact at catalyst interfaces. Since a conducting substrate is required to distribute electrons from anode to cathode, a chemically inert carbon layer is used in the manufacture of GDL layers. An ideal GDL should possess adequate hydrophobic characteristics and enhance electronic contact with low resistance, and effectively transport reactant gases to the catalyst layers. Lastly, the GDL structure should be strong enough to withstand the pressure of the tightly clamped stack cells, which is necessary to prevent leakages and in reduction of contact resistances.

3.1.4 Bipolar plates

The bipolar plate is also known as the flow field plate due to the integral design for reactant flows. The bipolar plates connect the MEA to the stack and are attached to anode on one side and cathode to the other, thus the name bipolar. Their primary role is the supply, distribution and removal of reactants and products from the stack. They also collect current from the cell terminals. In order to ensure heat removal, the bipolar plates are generally equipped with cooling channels for circulation of coolants through the stack. The bipolar plates therefore need to be high electronic conductors, impermeable with high chemical and mechanical stability, low weight and low cost with appropriate manufacturability.

3.2 Balance of Plant (BoP)

PEM fuel cells entail supplementary equipment to manage the characteristics of gases entering and leaving the system for maximum power output and to prolong the stack life. Key objectives of these BoP components include regulating fuel cell temperature, regulation of fuel and oxidant stoichiometry at anode and cathode, humidification of fuel cell and removal of liquid water from the flow fields.

Suitable regulation of these characteristics is necessary for efficient and uninterrupted fuel cell operation. Brief description of these components is as follows:

3.2.1 Humidifier

One of the key issues in PEMFC is the dehydration in the membrane. A fully hydrated membrane supports the ionic crossover between the electrodes, as well as extends its life. Therefore, reactants in the PEMFC need to be humidified before entering the stack. In the present model, a humidifier utilizes the water produced by chemical reaction inside the fuel cells to humidify the inlet air. A simple model based on mass and energy balance is implemented here. Although some empirical models could be considered, these vary over a wide range depending upon the types of humidifiers used. Due to the lack of sufficient data, it is assumed that the inlet air is optimally humidified before entering the stack. The relative humidity of air entering the cathode is set to 95% in the calculations; although other values can be chosen. This assumption could be justified as it is very close to the real operational conditions. On the anode side, there is no humidifier and the fuel is humidified by means of water crossover and its recirculation. It is observed that water crossover from cathode to anode through the membrane is adequate enough to raise the relative humidity in the anode exhaust to 100%. This recirculation, when mixed with inlet stream delivers the desired humidity into the anode of the fuel cell.

A static model of humidifier is used to add the desired amount of water into the cathode inlet stream. This model calculates the amount of water required to reach the set relative humidity value based on the air temperature at the outlet of the humidifier. The relative humidity (RH) can be defined as the ratio of partial pressures of vapour, to the partial pressure of that in the saturated mixture, at the same temperature:

$$RH = \frac{P_v}{P_{sat}} \tag{3.1}$$

Aspen custom modeller has built–in functions to calculate saturation pressures at different temperatures. The partial pressure of vapour in the air is calculated based upon the molar fraction of water in the air.

$$P_v = x_v \cdot P_{air} \tag{3.2}$$

where P_{air} is the total pressure of air. For a set RH value, this gives the molar fraction of water vapour needed at the outlet of humidifier, which in turn calculates the desired molar flow of water. Simple mass balance of all inlet and outlet streams determines the amount of water transferred from cathode exhaust to the air entering the cathode:

$$\dot{m}_{exh,in} = \dot{m}_{exh,out} - \dot{m}_{H_2O} \tag{3.3}$$

$$\dot{m}_{air,out} = \dot{m}_{air,in} + \dot{m}_{H_2O} \tag{3.4}$$

In a similar manner, a simplistic heat transfer model is used to define air temperatures at the cathode inlet. Here the assumption has been made that the cathode exhaust, which is at higher temperature than the air entering the humidifier, transfers heat at an effectiveness of 0.85. The temperature of air leaving the humidifier is determined by the following energy balance:

$$\dot{m}_{air} C_{p,air} \left(T_{air,out} - T_{air,in}\right) = 0.85 \cdot \dot{m}_{exh} C_{p,exh} \left(T_{exh,in} - T_{exh,out}\right) \tag{3.5}$$

Where subscripts *air* and *exh* denote the air stream directed towards fuel cell inlet and exhaust stream from the cathode respectively.

3.2.2 Air Blower and pumps

In the above proposed system, air blower, anode recirculation pump and water pumps are one of the BoP components which are also regulated by the control system. Aspen Dynamics ™ contains models of these units in its library as well.

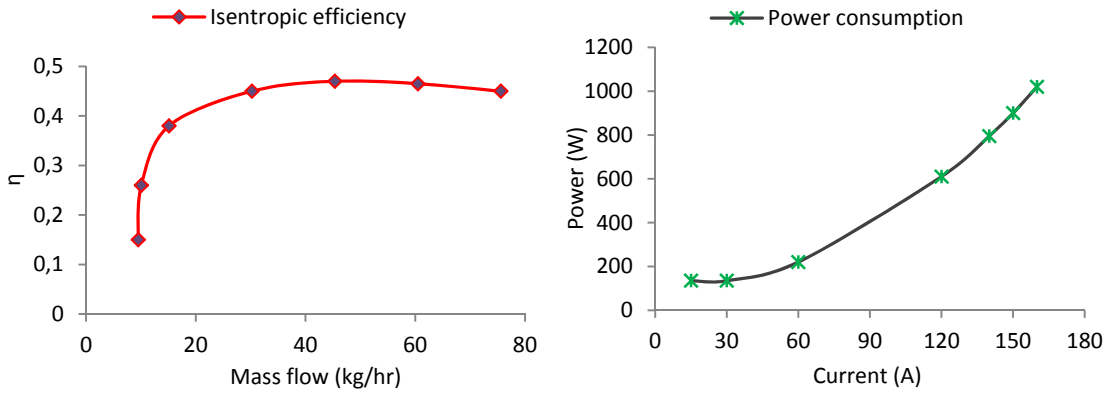

Figure 3.4: (a) Efficiency profile of air compressor versus air mass flow, (b) Power consumption of air compressor at different stack currents.

Since the nominal power of the PEMFC is only 21 kW, mass flow rates of fuel and air are very low. For example, at an average load of 10 kW, fuel and air flows are around 0.00014 kg/s and 0.0088 kg/s respectively. Therefore, very low values of isentropic efficiencies are suggested in this study, while the mechanical efficiency is set at 90%.

The efficiency of a blower ranges from 15% to 48% in the calculations based on experimental measurements. The mass flow dependent variance of isentropic efficiency can be seen in Fig. 3.4a, whereas power consumption data for different stack currents is shown in Fig. 3.4b. Similarly, calculated pump efficiencies are also very low for the cooling water circuits and are determined to be around 70%.

3.2.3 Heat Exchangers

As can be seen in Fig. 3.1, a network of heat exchangers constitutes the thermal management of the prescribed system. They extract the heat produced within the fuel cell stack and maintain the desired operating temperature which is critical for fuel cell durability and performance. Although heat exchanger models used here are predefined in Aspen Dynamics, some of the parameters have been assumed on the basis of media entering the hot and cold sides of these heat exchangers. The heat exchanger, which is connected to the internal cooling loop, has liquid water on both its hot and cold side. Therefore, a UA value of 1.0 kW/K is assumed. Whereas, UA values for air pre–cooler and radiator are approximated to be 0.05 kW/K and 0.3 kW/K respectively. In performing the simulations, the pressure drop was assumed to be 0.05 on both sides of heat exchangers. The corrected LMTD is calculated in addition to the corresponding inlet and outlet temperatures of hot and cold streams.

3.2.4 Flow valves

A valve is placed between the hydrogen tank and inlet manifold of anode which enables or disables the hydrogen supply. This regulatory valve adjusts high hydrogen pressure of the tank to the desired operating pressure of the fuel cell. Since the system does not operate on dead–end mode, the amount of hydrogen regulated by this valve equals the stoichiometric hydrogen required of the fuel cell. Stoichiometric ratio is defined as the amount of reactant supplied to the amount which is consumed in the reaction.

Flow and pressure of oxidant into the cathode is regulated by the blower. The amount of stoichiometric oxygen for the fuel cell reaction is manipulated by a

controller which regulates the electrical power of the blower, and hence compression and air flow.

3.2.5 Water trap

A knockout drum for liquid water is placed before the purge valve on the anode recirculation loop of the system. This container is simulated using a separator block in Aspen plus, which after determining phase properties of the inlet stream separates the liquid and vapour species at the outlet. Liquid water is collected at the bottom of the tank and the vapour stream is recirculated back into the anode feed. Though in simulations, all of the liquid is expelled from the stream, it is more likely to experience few liquid droplets in the recycled loop.

Chapter 4

System controls

Current research aims to build up a system which meets the requirements of actual stack running under varying load and operating conditions. As mentioned earlier that BoP components are critical for proper functioning of the stack. These components are able to regulate three major control loops in the fuel cell system: reactant supply, the water management, and the heat management. This section presents the methodology of controlling system parameters and operating conditions for the system to achieve the prescribed goals through stable operations. Classic proportional–integral (PI) controllers, which are widely used in industrial control systems, are employed to regulate different components and flow streams. Principally, these controllers calculate "error" value as the difference between a measured process variable and a desired set–point, and attempt to minimize this error by adjusting the process control inputs. Aspen Plus Dynamics has built–in PID controllers with options of specifying process and output variable ranges, tuning and filtering of controls and selection of ideal, series or parallel algorithms. Classical notation for output of the ideal PID controller employed in this study is specified as:

$$OP = K_p\left(e(t) + \frac{1}{T_i}\int_0^t e(\tau)d\tau + T_d\frac{d}{dt}e(t)\right) \tag{4.1}$$

where, OP is the controller output, K_P is the proportional gain which is set different value for different components. T_i and T_d are integral and derivative times respectively and e is the calculated error between set point and processed variable at instantaneous time t. τ is the variable of integration taking values from 0 to present time. Key parameters to be controlled in the proposed system are reactant inlet stoichiometries, inlet pressures, coolant inlet and operating temperatures of the stack. Control strategies incorporating these PIDs and regulatory mechanisms for different operating parameters are discussed

accordingly. However, optimization of these controllers is not performed in the present study. Figure 4.1 elucidates on processed and manipulated variable for different control blocks implemented in the proposed system.

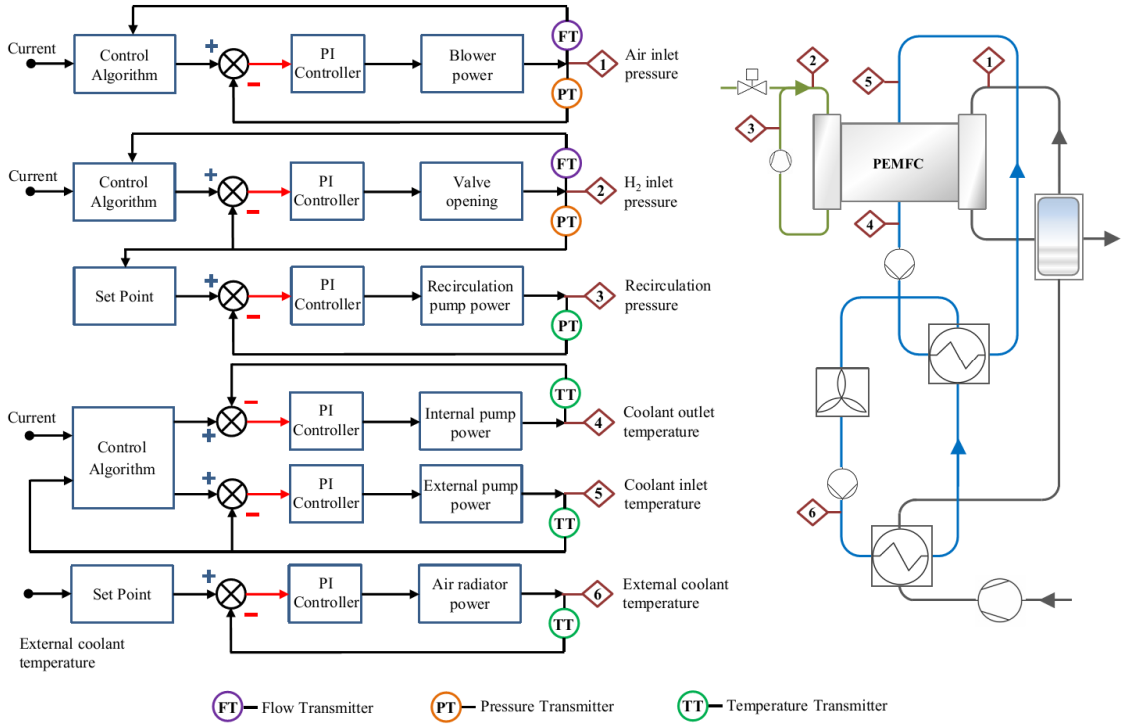

Figure 4.1: Control blocks for the PEMFC system.

4.1 Operating conditions

The principle functionality of the PEMFC stack is to provide stable electrical power over a range of operating and environmental conditions. However, fuel cell functionality is constrained within specific limitations pertaining to operational integrity and stack lifetime. Optimum fuel cell performance depends on a number of operating conditions including current density, reactant stoichiometry, relative humidity, inlet pressures, and cell temperature. Each of these conditions impacts the performance of the fuel cell individually or with combined effect.

Operating the stack below its minimum theoretical stoichiometry leads to premature durability issues. Stoichiometry is defined as the ratio of actual flow rate to the flow rate required to support the reaction. The minimum theoretical stoichiometry required to support the reaction is 1.0 for both fuel and oxidant. In

practice, higher stoichiometries, or flows, are required to ensure adequate reactant concentrations and to remove water. The fuel cell performance is not sensitive to stoichiometries at low currents because the minimum flow rates required for water removal are more than adequate to provide the necessary concentrations. At high currents, the reactant concentration at the catalyst reaction sites is the critical factor.

For high current loads, excess flows are also needed to manage the water production in the cathode and to dilute the higher nitrogen crossover to the anode. In the case of fuel starvation, damage can be done to a cell operated much below the average cell voltage. The extent of the damage increases with decreasing current density due to a higher average cell voltage. The cathode, however, is much more sensitive to air stoichiometry. As air stoichiometry is decreased at high load, cell voltage drops and the cell voltage standard deviation increases significantly. Air starvation might not cause damage to the cells, though it could lead to the appearance of individual low cell voltages. Air flow requirement increases with current and is dependent on the number of cells in the stack.

Low voltage cells can occur within the stack because of insufficient reactant concentration at catalyst reaction sites. This could be caused due to inadequate reactant stoichiometry, N_2 build–up in the anode, water blockage, and large internal leaks between anode and cathode. Over the stack lifetime, greater leaks can develop and cause operational problems. The development of internal and external leaks with lifetime operation is highly dependent on stack operating conditions. Large internal leaks have a negative impact on stack operation and system efficiency. Since the anode inlet pressure is higher than the cathode side, hydrogen will transfer to the cathode side, will not be used in the fuel cell reaction and thus will be wasted fuel. The onset of an internal leak will be accelerated by high temperature and low humidity in the cells. Temperature is also one of the key factors for dry cell operations, since at high temperature the water is in vapour state and easier to remove. Nonetheless, there still is some liquid water in the flow channels.

Over the period of stack life, there are three main ways in which external leaks can occur: gas diffusion through the external seals, overheating and seal damage due to high reactant pressures. Elevated temperatures may also trigger external leaks if operated over longer durations. Further, high pressure cycling also leads to a reduction interface pressure, resulting in an external leak.

For a system with anode recirculation, build–up of inert gases will decrease the hydrogen concentration to the point where fuel starvation spots will occur. The

crossover rate of nitrogen from the cathode to the anode is highly dependent on the operating conditions of the stack. Generally, N_2 crossover will increases with the increase in cathode pressure and cell temperatures. Ensuring the cathode pressure is lower than the anode pressure will minimize nitrogen crossover and improve cell stability. Additionally, from a safety perspective, it is preferred to operate the anode at a higher pressure than the cathode. In the event of an internal leak, hydrogen would preferentially leak to the cathode and be diluted by the air, or combine with oxygen to produce water. However, there is a maximum cross pressure limit beyond which mechanical stresses could be produced in the stack resulting in damage [62].

For a maximum service life and efficiency of the stack, *Ballard* recommends operating conditions within which the stack should operate, which are followed in this study. Figures 4.2 and 4.3 portray the graphical representation of the suggested operating parameters for the specified fuel cell stack.

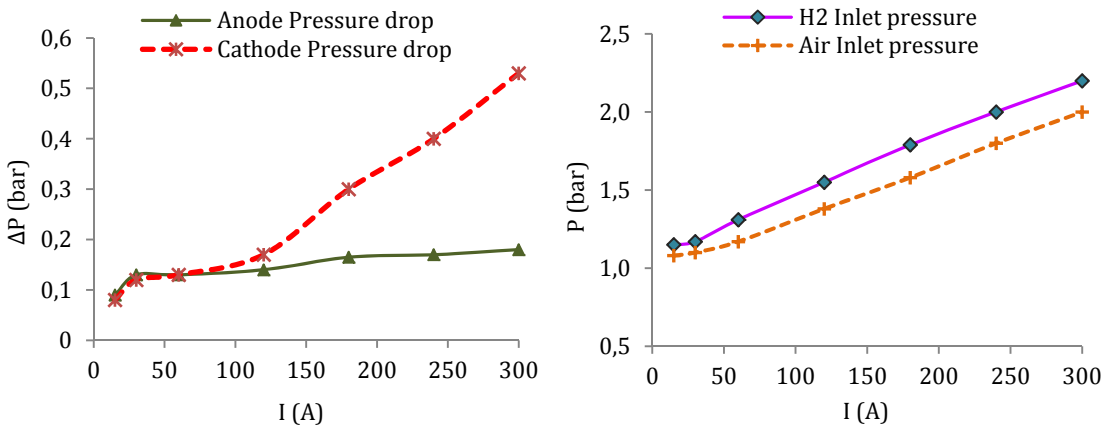

Figure 4.2: Stack data provided by Ballard (a) Nominal pressure drop within the fuel cell, (b) Inlet pressures for reactants.

During normal steady state operation, reactant pressure should be above coolant pressure whereas for short transients and during start–up, coolant pressure may exceed reactant pressure. In a system with fuel recirculation, the consumption is slightly above 1.0 stoichiometry as 1% to 2% of the flow will be required for purging.

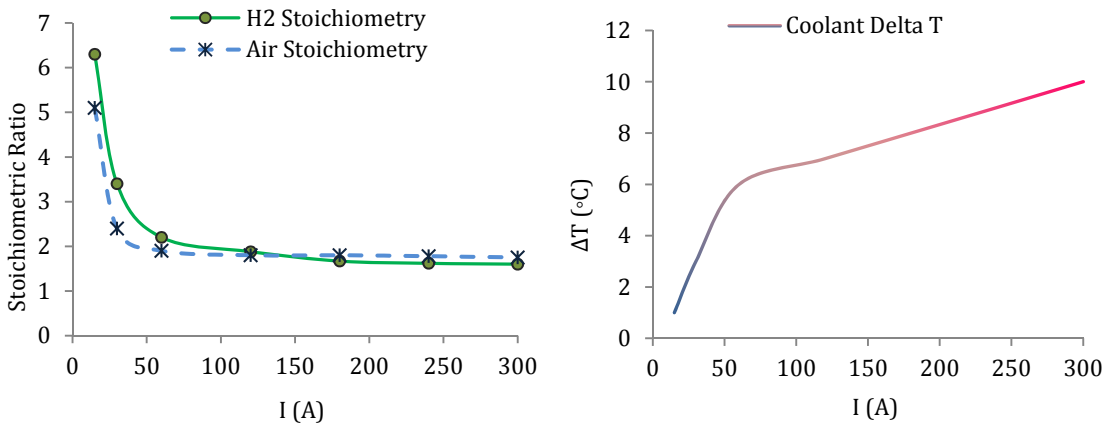

Figure 4.3: (a) Reactant stoichiometry used in the fuel cell control system, (b) Stack inlet and outlet temperature difference maintained by coolant mass flow.

4.2 Air flow control

The control loops of hydrogen and air supply mechanism should maintain the optimal reactant ratio and prevent shortages that occur during abrupt and amplified changes in the external load. It is reported in [65] that the proposed PEMFC system is not sensitive to reduction in fuel flow during load fluctuations; however if the hydrogen stoichiometry is below 1.0, then fuel starvation can cause irreversible damage to the stack. On the other hand, oxygen starvation affects the fuel cell to a greater degree and has a much larger effect on stack performance. Oxygen starvation is a complex phenomenon that occurs when oxygen partial pressure falls below the critical level outlined by the reaction stoichiometry. It greatly affects the voltage potential of the cell and can cause short circuit in severe cases. Hence, an adequate air supply is required.

Figure 4.3a shows the fuel and air stoichiometries for the selected fuel cell stack. It can be seen that at low current loads, high amounts of excess reactant flows are desired. For stack operating at low power and low pressures, water formed by the reaction in the cathode side of the cells needs to be ejected out of the stack, which is done by supplying high amounts of air. While the oxidant consumption depends on the current load, the amount of oxygen delivered to a fuel cell is directly related to the blower power. Here, data from pressure and flow sensors is transmitted to the controller where an algorithm based on data from Fig. 4.3a, translates it to be the process variable and set point for the PI controller, which regulates the blower power in order to maintain the desired oxygen ratio.

Air flow into the fuel cell is dependent on the current drawn from the stack. Figure 4.4a displays the current ramp tests against the power consumption of the air blower. Oxygen required by the fuel cell is instantly supplied by the blower which is regulated by the controls at the backend. In the PID controllers implemented here, the set–point for air flow controller is defined as the difference between the recommended air stoichiometric curves and the measured air stoichiometry from the flows at the inlet and outlet of the fuel cell stack. As can be seen in Fig. 4.4a, that the set–point is always set to 0 and the controller manipulates the blower power to coincide the process variable with the set–point. With each current change, the process variable distances from the set–point and the controller is actuated.

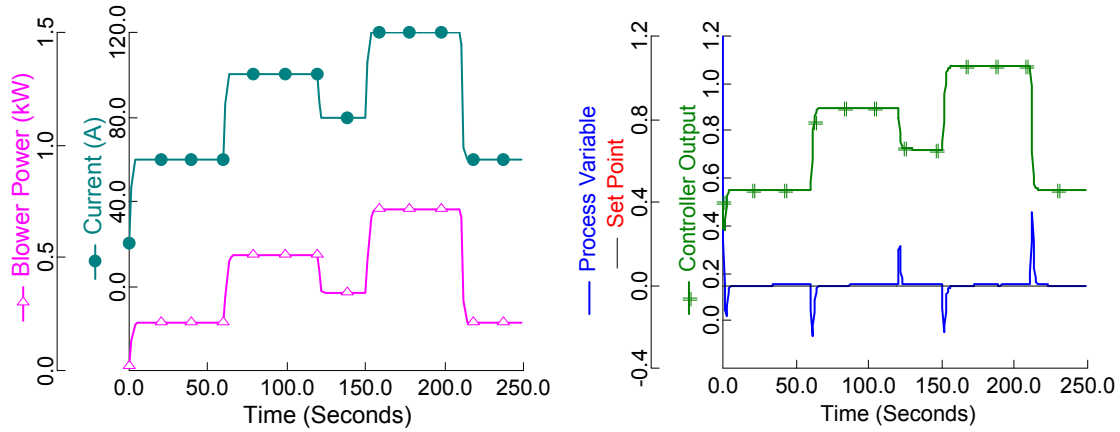

Figure 4.4: Air flow controls (a) Air compressor power versus stack current, (b) Controller output variation with change in process variable.

A similar change in the measured air stoichiometry is observed. For an abrupt current rise, air stoichiometry is reduced until the activation of control which increases power supplied to the blower and consequently delivers the required amount of air to the fuel cell stack.

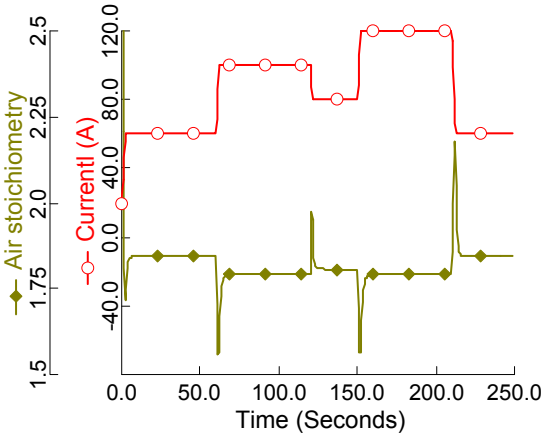

Figure 4.5: Change in O_2 stoichiometry with current drawn from stack.

4.3 Fuel flow control

Fuel starvation also causes stack damage in the form of performance degradation. When the fuel stoichiometry is lower than required there is a non–uniform fuel concentration within the stack, which leads to localized fuel starvation. Similar to the air flow control, an algorithm for controlling hydrogen flow is devised along with a PI controller, which regulates the control valve opening for optimal fuel supply at the desired pressures.

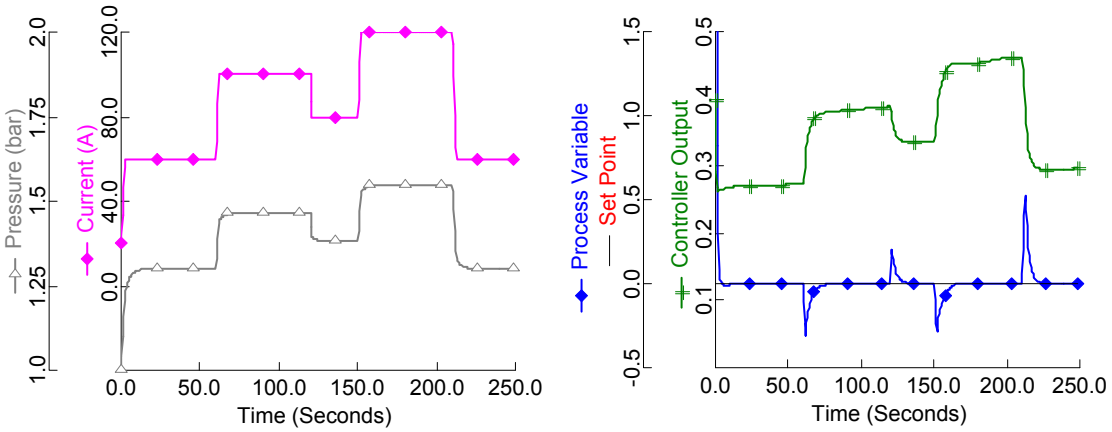

Figure 4.6: Fuel flow controls (a) Anode inlet pressure versus stack current, (b) Control input and output variables.

Figure 4.6a expresses the variation in fuel inlet pressure to the ramping of stack current. The proportional valve opens or closes to change the hydrogen flow into the stack. This control process is elucidated in Fig. 4.6b, where the output variable (valve opening position) is controlled to reach the desired fuel stoichiometry.

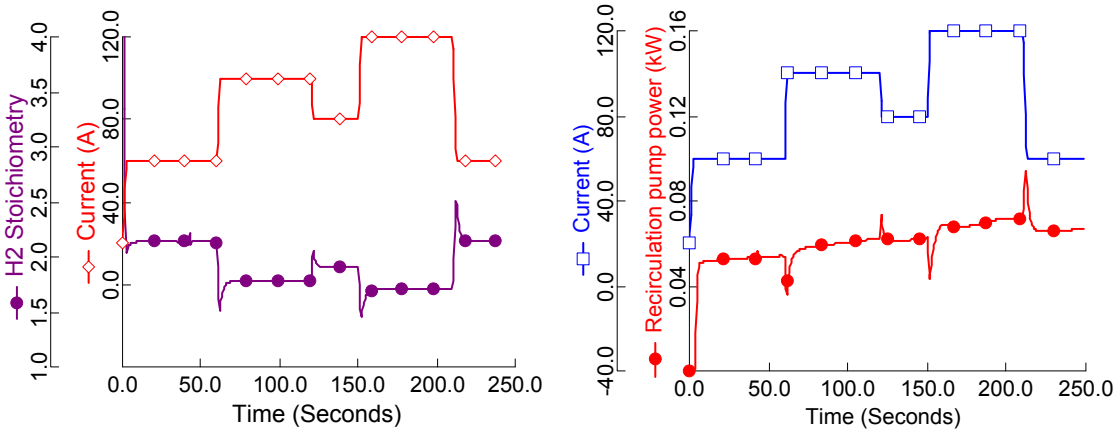

Figure 4.7: (a) Fuel stoichiometry as a function of current, (b) Power consumption of recirculation pump against stack current.

Variations in fuel stoichiometry against the drawn current can be noticed in Fig. 4.7a. Excess fuel ratio is reduced from 2.2 to 1.6 at current ramp–up from 60A to 100A. Larger current changes could induce even lower fuel stoichiometry; it is therefore always preferred to operate the fuel cell well above its stoichiometric requirements. In a similar manner, the pressures in anode recirculation loop are governed by PI controllers which collect data from anode upstream and manipulate recirculation pump power accordingly. Figure 4.7b portrays the power consumed by the recirculation pump in the same event of current change.

4.4 Temperature control

Thermal management in PEMFC systems is of vital importance, basically due to the fact that heat produced in the selected fuel cell cannot be dissipated by convection and radiation through the stack surface. A consistent and stable operation of around 70°C thus requires a liquid cooling system. Since the operating temperature of the fuel cell is not very high, a low temperature difference with the ambient requires having a large heat transfer surface.

Therefore, an efficient thermal control system becomes of substantial importance to ensure optimum system performance.

As shown in Fig. 4.1, the cooling system for the proposed fuel cell consists of internal and external cooling circuits. As mentioned earlier, the coolant mass flow rate defines the variance in the stack temperature or simply maintains the fuel cell operating temperature. In this case, temperature in the stack can be controlled by the coolant flow rate which acts as an input signal and is adjusted by the PI controller. Based on data from Fig. 4.3b, equations defining stack temperature as a set–point for controller are developed. In addition, the controller simultaneously collects data from temperature transmitter at the coolant outlet stream, which then changes the coolant flow accordingly by sending output signals to the driving pump. Employment of such algorithm in the system controller ensures a stable operation under normal steady–state conditions, however for system start–up scenario, a different approach is required. This approach is selected because at start–up sequence, temperature of the stack is equal to the ambient and the above–mentioned control strategy would not allow the stack temperature difference to increase more than 10°C and hence increase the time to reach steady–state operations, which is not desirable. In this regard, at start–up sequence, the coolant flow is restricted to a minimum value until the desired stack operating temperature is reached which is when the steady–state controls begin functioning. Though, a lower coolant flow is needed to increase the stack heat–up time at start, a very high temperature difference may cause damage to the fuel cells in the stack. Henceforth, the maximum temperature difference is limited to 17°C for this study.

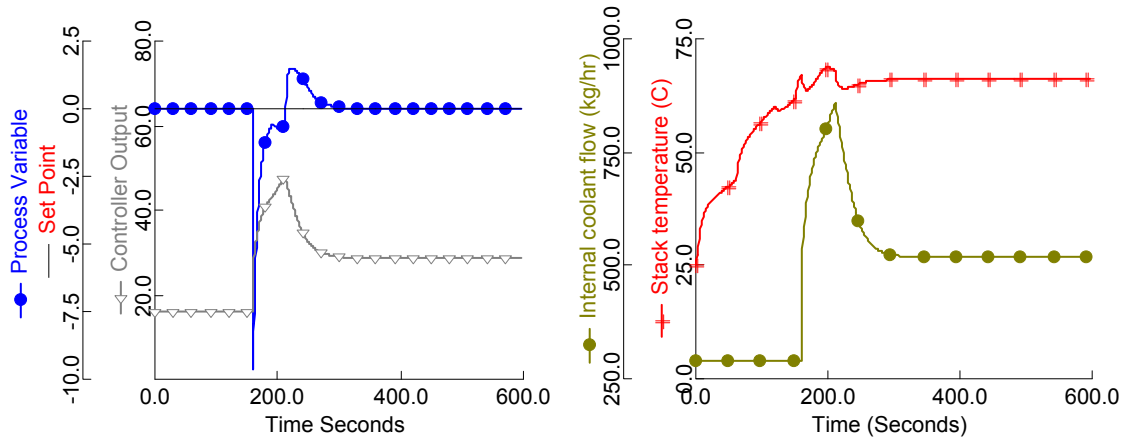

Figure 4.8: Temperature controls (a) PID controller process and output variables, (b) Stack operating temperature as a function of coolant mass flow.

Thermal controls are not actuated by stack current changes, but with temperatures of the coolant entering and leaving the system. The set–point for stack operating temperature control is set by difference between the desired coolant outlet temperatures and the measured ones. In Fig. 4.8a, it can be seen that the controller output takes longer time to reach the set–point values once it is activated, which is a common trait of thermal management in fuel cells. Coolant flow rates increase or decrease slowly in comparison to other controls, as can be observed in Fig. 4.8b.

Temperature of the coolant entering the stack can similarly be controlled by the flow of water in the external circuit. Control signal to the associated pump regulates the electrical power of the pump and hence the coolant inlet temperature into the stack. Figure 4.9a demonstrates the actuation of inlet temperature controls. Once the temperature of the coolant entering the stack reaches 61°C, flow in the external circuit is increased to maintain it. In a similar fashion, temperature of water in the external circuit is dependent on radiator fan speed. Radiator power consumption is also not directly affected by the PEMFC stack current, and is activated to cool down the external coolant to the desired temperatures (see Fig. 4.9b). For the present case, the radiator control is set to maintain the external coolant temperature to 50°C.

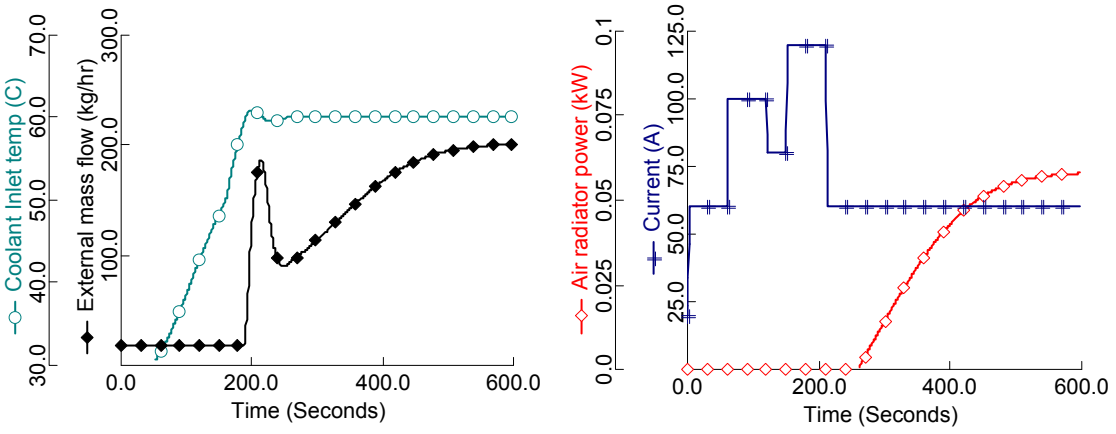

Figure 4.9: Thermal management (a) Coolant inlet temperature versus external coolant flow, (b) Power consumption graph of air radiator.

Chapter 5

Modelling of PEM Fuel Cell Stack

The PEMFC system proposed in Fig. 3.1 is constructed by using Aspen Dynamics simulation tool. As mentioned in the 1st chapter, that Aspen Dynamics contains a vast library of component models which can be configured to design and simulate various process engineering systems. However, in order to have a detailed study of intricate fuel cell phenomena, a comprehensive fuel cell model is devised. This model constitutes equations for fuel cell electrochemistry, mass and energy balances, water and nitrogen crossovers in membrane and fuel cell thermodynamics in addition to the flow models of reactants and products at fuel cell interface. Governing equations for these sub–models are discussed below:

5.1 Fuel cell Potential

5.1.1 Thermodynamic Potential

Since the fuel cell directly converts chemical energy into electrical energy, it can be described by the Gibbs free energy, which is a thermodynamic potential measuring the maximum available work from a process. For a chemical reaction, the net change in the Gibbs free energy is equal to the difference between the Gibbs free energy of products and the reactants. In case of PEMFCs, where oxygen and hydrogen are the only reactants and water as the product, change in Gibbs free energy $\Delta\bar{g}_f^0$, is calculated at standard conditions.

$$\Delta\bar{g}_f^0 = \left(\bar{g}_f^0\right)_{H_2O} - \left(\bar{g}_f^0\right)_{H_2} - \frac{1}{2}\left(\bar{g}_f^0\right)_{O_2} \tag{5.1}$$

Here, $\bar{g}_f^0$ is the specific Gibbs free energy of formation and is a function of temperature, pressure and gas phase [66].

5.1.2 Theoretical fuel cell potential

For an ideal reversible fuel cell, the maximum electrical work at a constant temperature and pressure is equal to the Gibbs free energy:

$$W_{el} = \Delta G^0 = -n \cdot F \cdot E^0 \tag{5.2}$$

where E is the ideal potential of the cell, n is the number of electrons and F is the Faraday's constant. Number of electrons for a H_2–O_2 cell reaction is 2, hence the formation for ideal fuel cell potential becomes:

$$E^0 = \frac{-\Delta G^0}{2F} \tag{5.3}$$

This potential is valid for standard temperature and pressure. However, PEM fuel cells usually operate at higher temperatures and because Gibbs free energy is a function of temperature, it decreases the cell potential to a certain extent. The actual theoretical cell potential can be accounted in the Nernst equation:

$$E = E^0 + \frac{RT}{2F} \ln\left(\frac{a_{H_2} a_{O_2}{}^{1/2}}{a_{H_2O}} \right) \tag{5.4}$$

here activity, a, is defined as:

$$a = \frac{P_i}{P_0} \tag{5.5}$$

P_i is the partial pressure of the gases and P_0 is the standard pressure. By assuming the gases are ideal, their activity is proportional to their partial pressure and the activity of liquid water is equal to 1, the Nernst equation takes the form:

$$E = E^0 + \frac{RT}{2F} \ln\left(P_{H_2} P_{O_2}{}^{1/2} \right) \tag{5.6}$$

Theoretical cell voltage is decreased when partial pressure of water vapour increases. For evaluation of temperature, T, the stack temperature is selected, as the temperature gradient of gases at inlet and outlet is reasonably low. P_{H2} and P_{O2} are average partial pressures of the hydrogen and oxygen and are given as:

$$P_{H_2} = \left(\frac{y_{H_2,out} - y_{H_2,in}}{2} \right) \overline{P}_a \tag{5.7}$$

$$P_{O_2} = \left(\frac{y_{O_2,out} - y_{O_2,in}}{2} \right) \overline{P}_c \tag{5.8}$$

Here, y is the molar fraction of the species at their respective terminals. Assuming that all of the available energy is converted into electrical power, the efficiency of a fuel cell can be stated as:

$$\eta_{rev} = \frac{\Delta G^0}{\Delta H} \tag{5.9}$$

The Change in enthalpy of formation, ΔH, is also temperature dependent and the ideal efficiency decreases with the temperature increase. The cell efficiency could be calculated based on higher or lower heating values, HHV and LHV respectively. For LHV, the water is assumed to be in vapour form, while liquid form of water is assumed for HHV calculations. HHV is usually higher than LHV because the latent heat of vaporization in the reactants and the products is accounted for as well.

$$\eta_{cell} = \frac{V_{cell}}{1.48} \text{ for HHV} \tag{5.10}$$

$$\eta_{cell} = \frac{V_{cell}}{1.25} \text{ for LHV} \tag{5.11}$$

Where V_{cell} is the average cell voltage and η_{cell} is the cell efficiency at standard temperature and pressure.

5.2 Electrochemical Model

An actual fuel cell has a lower efficiency than the ideal one because of the irreversible losses in the cell reaction. The fuel cell terminal voltage drops from the open circuit voltage and this drop in voltage is proportional to the current drawn by the electric circuit. This phenomenon is known as polarization. There are three main types of polarization: activation polarization, ohmic polarization and concentration polarization. In a practical fuel cell, the voltage drop is significantly more at low and high current densities. At low current densities, the activation polarization is predominant and at high current densities, the concentration polarization is a major cause of losses. The ohmic polarization is nothing but cell resistance and hence with increase in cell current the voltage drop increases proportionately. Low temperature fuel cells exhibit high activation polarization at

low current densities. On the other hand, high temperature fuel cells have a low activation losses and ohmic polarization is the most important cause for losses.

The thermodynamic efficiency and net power of the system are determined by the current drawn and voltage produced by the stack. The average cell voltage of a fuel cell is defined by an analytical expression:

$$V_{cell} = E - V_{act} - V_{ohmic} - V_{conc} \tag{5.12}$$

where E is the theoretical voltage, V_{act} the activation overpotential, V_{ohmic} ohmic overpotential and V_{conc} denotes concentration loss.

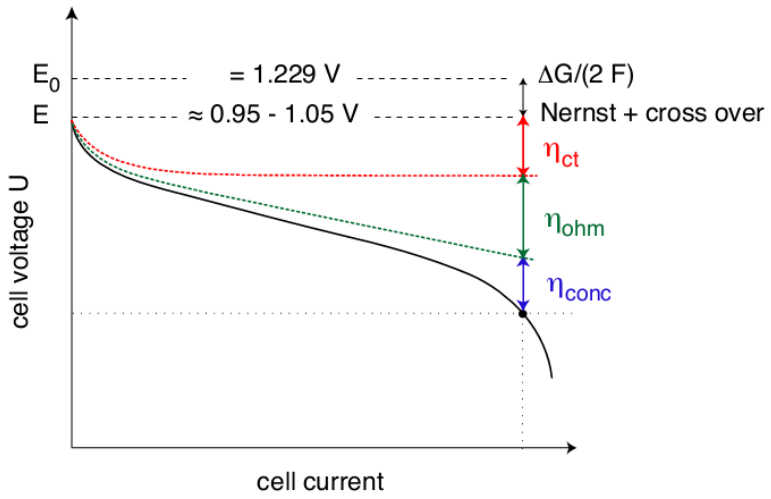

Figure 5.1: Representation of a typical Voltage–Current curve denoting different polarization dominated regions [67].

It can be seen in Fig. 5.1 that the open circuit voltage (OCV) starts far below from the Nernst potential of the cell. This is due to internal current losses as well as fuel crossover through the membrane. These aspects are further discussed in the following section and their impact on cell performance is incorporated into activation overpotential equations.

5.2.1 Activation loss

Activation overpotential is the voltage required to overcome the activation energy of the cell reactions. This occurs due to slow charge transfer reaction at the surface

of the electrodes and a proportion of the total voltage is needed in the reaction kinetics. Also, a certain amount of voltage is utilized in transportation of electrons to and from the electrodes, thereby further reducing the potential at the fuel cell terminals. The electron transfer, also referred as exchange current density is dependent on temperature and pressure of reactants. The reactions at the anode are very fast in comparison to the ones at cathode, therefore anode overpotential is sometimes neglected [68]. Reduction in activation losses can be achieved by raising the temperature, increasing the active surface of the catalysts, and increasing the amount of reactants.

The total activation losses in the cell are equal to sum of anode and cathode contributions. Knowing this and assuming equal transfer coefficients in both electrodes, the Butler–Volmer equation is simplified to Tafel slope and used in the current model:

$$V_{act} = V_{act,c} + V_{act,a} = \frac{RT}{\alpha_c F}\ln\left(\frac{i+i_{loss}}{i_{0,c}}\right) + \frac{RT}{\alpha_a F}\ln\left(\frac{i+i_{loss}}{i_{0,a}}\right) \tag{5.13}$$

Here, R is the universal gas constant and α denotes the transfer coefficients on the anode and cathode sides. The term i_{loss} accounts for the losses due to the internal current generation and fuel crossover. Although a fuel cell electrolyte is designed to conduct positive ions, some electrons cross the membrane internally. Since these electrons do not follow the external path, they give rise to internal currents. Some fuel may also diffuse through the membrane and react directly with the oxygen without producing any external current. These internal losses affect by reducing the current density by a few mA when at higher temperatures, however the voltage loss could be at least 0.2V less than the reversible voltage with PEMFC operating at normal air and pressure [66]. Here, the value for internal current density, i_{loss} is assumed to be equal to 0.002 A/cm^2 [69].

The equations below are valid for evaluating the transfer coefficients on the anode and cathode side respectively:

$$\alpha_a = \beta \cdot n_{el} \tag{5.14}$$

$$\alpha_c = (1-\beta) \cdot n_{el} \tag{5.15}$$

The symmetry factor, $\beta = 0.5$ is chosen, n_{el} is the number of electrons in the rate step of the reaction and equal to 4 for anode and 1 for cathode. The exchange current density, i_0, is also a function of temperature and catalyst activity. An

analytical expression is chosen here, which predicts the value of exchange current density at the anode and cathode [69].

$$i_{0,a} = n \cdot F \cdot k_a \cdot \exp\left(\frac{(1-\beta)\cdot n \cdot F \cdot E}{RT}\right) \tag{5.16}$$

$$i_{0,c} = n \cdot F \cdot k_c \cdot \exp\left(\frac{-\beta \cdot n \cdot F \cdot E}{RT}\right) \tag{5.17}$$

Where, k is the reaction rate coefficient and found by calibration of the model.

The equations for activation losses mentioned above have been used in the current study, though there are alternative methods which have been considered as well. According to the method proposed by Berger [70], the activation overpotential can be determined by the following equation:

$$V_{act} = \xi_1 + \xi_2 + \xi_3 \cdot T\left[\ln\left(c^*_{O_2}\right)\right] + \xi_4 \cdot T\left[\ln(i)\right] \tag{5.18}$$

The values for the constants (ξ), can be found by solving the set of equations defined below, where c^* are the concentrations of the species.

$$\xi_1 = \frac{\Delta G^0_f}{nF} - \frac{\Delta G^0_f}{\alpha_c nF} \tag{5.19}$$

$$\xi_2 = \frac{R}{\alpha_c nF}\ln\left[nFA_{cell}k_c\left(c^*_{H^+}\right)^{1-\alpha_c}\left(c^*_{H_2O}\right)^{\alpha_c}\right] + \frac{R}{nF}\ln\left[4FA_{cell}k_a\left(c^*_{H_2}\right)\right] \tag{5.20}$$

$$\xi_3 = \frac{R(1-\alpha_c)}{\alpha_c nF} \tag{5.21}$$

$$\xi_4 = -\left(\frac{R}{nF} + \frac{R}{\alpha_c nF}\right) \tag{5.22}$$

5.2.2 Ohmic Loss

Ohmic overpotential is generated by the resistance to the ionic flow in the electrolyte, resistance to the flow of electrons through the electrodes, and contact resistance at the cell terminals. Ohmic losses can be reduced by using electrodes with high electronic conductivity and thinner membranes which are conducive to high ion transfer. However, thinner membranes would increase fuel and gas crossovers, provide less structural stability and in some cases might not insulate the

electrodes, resulting in short circuit. These limitations would demand a trade–off of between reduction in ohmic losses and membrane thickness. The electrolyte and electrodes both obey Ohm's law and the formulation for the calculation of ohmic losses used in this model is presented below.

$$V_{ohmic} = \left(r_{el} + r_{ion}\right) \cdot i \tag{5.23}$$

The ionic resistance of the membrane is denoted by r_{ion} and r_{el} represents the electronic resistance in the electrodes and the contact resistance at the terminals of the bipolar plates. The electronic resistance is reported to be very low when compared to the ionic resistance in the membrane; therefore it is usually ignored in the summation of overall ohmic resistance [71]. The ionic resistance increases with the current drawn from the stack and on the contrary decreases with the cell temperature. A correlation for Nafion 117 membrane was formulated by Mann et al. [72], which is used here:

$$r_{ion} = \frac{C_1 \cdot \left[1 + 0.03i + 0.062 \cdot \left(\frac{T}{303}\right)^2 \cdot i^{2.5}\right]}{\left(\lambda_{mem} - 0.634 - 3i\right) \cdot \exp\left[C_2 \cdot \left(\frac{T - 303}{T}\right)\right]} \cdot t_m \tag{5.24}$$

where λ_{mem} is the average water content of the membrane and t_m is the membrane thickness. Other terms are correction factors for operating temperatures other than 303 K; C_1 and C_2 are fitted to be 180 and 16.4 respectively. There are however another simpler correlations reported in [67], [73]:

$$r_{ion} = \frac{t_m}{\sigma_m} \tag{5.25}$$

The membrane activity, σ_m is a function of water content and the temperature, and is determined by the following equation [67]:

$$\sigma_m = \left(0.005139\lambda_{mem} - 0.00326\right) \cdot \exp\left(1268\left(\frac{1}{303} - \frac{1}{T}\right)\right) \tag{5.26}$$

5.2.3 Concentration Loss

The concentration overpotential arises due to a reduction in the reactant concentrations at the electrode–membrane interface. At high current densities, the reactions occurring within the cell are faster. The fuel and reactants are consumed faster than they are reach the cell sites, which can be seen as a characteristic voltage

drop in the polarization curve. This drop is even more pronounced if the reactants are not pure and mixed gases are fed to the fuel cell e.g. air is used instead of oxygen [66]. One of the main reasons for such losses is product accumulation which dilutes the oxygen concentration at the catalytic layer, resulting in concentration gradients. Such an overpotential could be related to the limiting current density of the cell, which is the maximum current drawn from the cell. At these high currents, the transport of species is comparatively slower than the needed concentrations, at which case the partial pressures of these reactants reach near zero at reaction sites, consequently dropping the voltage potential to very low levels. This effect can be expressed mathematically by correlating to the limiting current densities [74], [75], and used in the present model.

$$V_{conc} = V_{conc,c} + V_{conc,a} = \frac{RT}{n_e F}\ln\left(1 - \frac{i}{i_{\lim,c}}\right) + \frac{RT}{n_e F}\ln\left(1 - \frac{i}{i_{\lim,a}}\right) \tag{5.27}$$

Limiting current densities at cathode and anode are calculated as the product of maximum current density and the stoichiometry of the reactants:

$$i_{\lim,c} = S_{O_2} \cdot i_{\max} \tag{5.28}$$

$$i_{\lim,a} = S_{H_2} \cdot i_{\max} \tag{5.29}$$

The concentration overpotential is usually prominent at high currents, which are seldom drawn from the cell for longer stack life and higher efficiencies. At average loads, these losses do not play a significant role and can be neglected in fuel cell modelling.

5.3 Membrane Transportation Sub–models

In addition to electronic and ionic transfers in PEMFCs, a number of complex transport phenomena occur in the form of gas and vapour transportation across the fuel cells. Species crossover in the MEA components is well recognized, yet detailed mechanisms of the intricate processes are not fully understood in some cases due to their complex nature. Nevertheless, most of these processes affect the performance and life cycle of the fuel cell and therefore need further diligence. Figure 5.2 provides schematic of gas and vapour transport phenomena in a typical MEA of a hydrogen fuel cell. As it can be seen in the figure, there are six basic processes of species transport across the membrane.

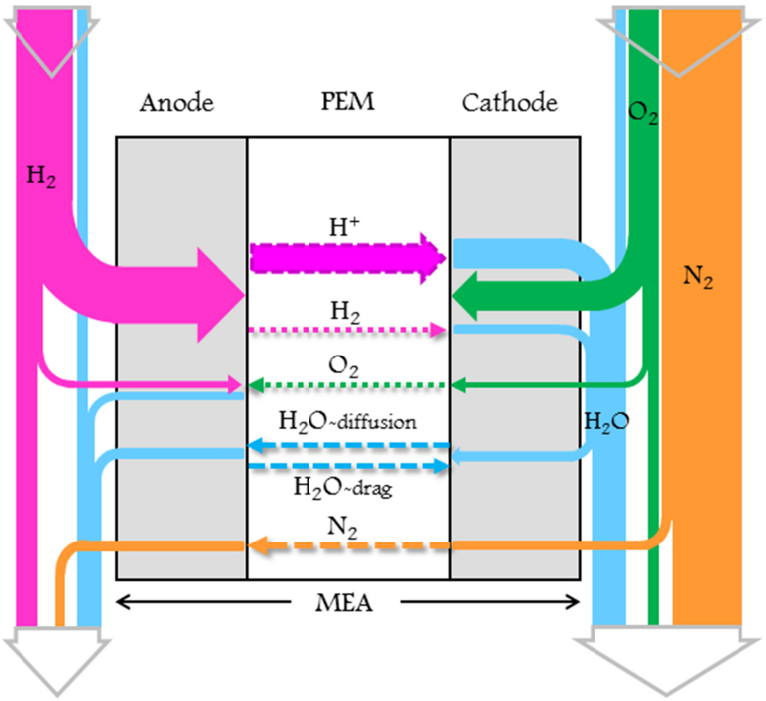

Figure 5.2: Schematic diagram of gas transport phenomena across PEM fuel cell MEA.

Conduction of protons is the primary mode of transference, which react with oxygen molecules on the cathode side to generate electrical power and water as reaction product. Some fuel and oxygen also crosses over and react to produce water without contributing to the stack power production. The losses associated to these internal crossovers have been discussed in the electrochemical model sections of this chapter. Some molecules of water are also dragged along with the hydrogen ions to the cathode, while higher water concentrations at cathode result in diffusion towards the anode of the fuel cell. Nitrogen being an inert gas remains inactive in the reactions occurring within these cells. However, some proportions of nitrogen permeate towards the anode as well. Model formulation for water transportation and nitrogen permeation through the fuel cell are presented here accordingly.

5.3.1 Water crossover

Proper management of water in PEMFCs plays a vital role in enhancing stack lifetime and in achieving higher performance goals. Drying of the membrane could result in permanent membrane damage, whereas on the contrary, high water flooding could also lead to cell reversal also resulting in permanent cell damage

[66], [76]. Drying of membrane at the anode side occurs if the fuel is not adequately hydrated and hampers the ionic flow causing additional heat generation within the cell. This in turn leads to increased dehydrating of the membrane and subsequently decreasing cell voltage output. On the other hand, PEMFCs operating at higher current densities and lower temperatures experience water flooding. When higher currents are drawn from the stack, higher amount of water is produced which saturates and condenses in the cathode, leading to clogging in flow channels restricting the air flow to the catalyst electrode layer. These cells with limited air flow channels would have a significantly less voltage potential across them, which would reduce the output stack voltage.

Nafion membranes are characterized in terms of their thickness and water uptake isotherms. In the present study, water content profiles are assumed to be linear across the membrane thickness, as suggested by [77], [78]:

$$\lambda_{mem} = \frac{\lambda_c + \lambda_a}{2} \tag{5.30}$$

The membrane water content, λ, specifies the amount of water uptake per sulfonic acid groups in the membrane and is a function of water activity at respective anode and cathode electrode interfaces. The following expressions have been used here [79]:

$$\lambda_{c\&a} = 0.043 + 17.18a_w - 39.85a_w^2 + 36a_w^3 \qquad 0 < a_w < 1 \tag{5.31}$$

$$\lambda_{c\&a} = 14 + 1.4(a_w - 1) \qquad 0 < a_w \leq 3 \tag{5.32}$$

The value of λ is equal to 14 for a perfectly hydrated membrane and in some cases could reach 22 e.g. under super saturated conditions. The water vapour activity, a_w, can be defined as the ratio of vapour partial pressures to the saturated partial pressures for both cathode and anode interfaces.

$$a_w = \frac{P_w}{P_{sat}} \tag{5.33}$$

In order to have a fully hydrated membrane, both the fuel and the air are humidified before being fed to the fuel cell. Water flows in both directions within the membrane. When the Water crosses from the anode towards the cathode, it is referred to as electro–osmotic drag. The electro–osmotic drag occurs due to the dragging of water molecules with hydrogen ions. The number of dragged molecules vary and are typically found to be in the range of 0.5– 5 water molecules per hydrogen ion [66]. Whereas, when the water travels from the cathode towards

the anode, it is called as back diffusion. This diffusion is a result of high concentration gradients across the membrane, arising due to water production at cathode side. Water flux due to electro–osmotic drag is given by:

$$J_{H_2O,drag} = 2n_{drag}\frac{i}{nF} \tag{5.34}$$

where:

$$n_{drag} = n_{drag}^{sat}\frac{\lambda_{mem}}{22} \tag{5.35}$$

The saturated electro–osmotic drag, n_{drag}^{sat}, is assumed to be 2.5 for the current study, as it has been experimentally evaluated between 2.3 to 2.7 for fully hydrated membranes in equilibrium with liquid water [67].

Back diffusion, on the other hand is calculated by diffusion parameters:

$$J_{H_2O,diffusion} = \frac{\rho_{dry}}{M_m}D_w\frac{d\lambda_{mem}}{dz} \tag{5.36}$$

Here, ρ_{dry} is the density of Nafion at dry conditions and M_m represents its molecular weight. D_w denotes the water diffusivity and z is the axis along the membrane thickness. Table 5.1 shows key figures for Nafion 117 used here:

Table 5.1: Key parameters for Nafion 117 membrane

Parameter	**Value**
Membrane thickness, $t_m\ (cm)$	0.0183
Density of dry membrane, $\rho_{dry}\ \left(g/cm^3\right)$	3.28
Molecular weight of membrane, $M_m\ (Kg/mol)$	1.1

The net water transport through the membrane is the difference of electro–osmotic drag and back diffusion:

$$J_{H_2O} = \frac{\rho_{dry}}{M_m}D_w\frac{d\lambda_{mem}}{dz} - 2n_{drag}\frac{i}{nF} \tag{5.37}$$

The diffusion coefficient is a function of temperature and water content of the membrane. The following correlation has been implemented here, which was proposed by [73], [79], [80]:

$$D_w = D_\lambda \exp\left[2416 \cdot \left(\frac{1}{303} - \frac{1}{T}\right)\right] \tag{5.38}$$

To determine the value for D_λ, the following expression suggested by Springer et al. [79], has been applied here. This equation is only valid for $\lambda > 4$, which is justified for current simulations since the membrane is adequately hydrated and membrane water content is always above 4.

$$D_\lambda = 10^{-6}\left(2.563 - 0.33\lambda_{mem} + 0.0264\lambda_{mem}^2 - 0.000671\lambda_{mem}^3\right) \tag{5.39}$$

Some authors have considered correlations which are related to the electro–osmotic drag e.g. Murahashi et al. proposed the following:

$$D_\lambda = 5.51 \times 10^{-7} \cdot n_{drag} \tag{5.40}$$

Others have applied the following equations based on experimental results and consider membrane water content only while withdrawing temperature impact on the water diffusion:

$$D_\lambda = \begin{cases} 10^{-6}, & \lambda_{mem} < 2 \\ 10^{-6}\left(1 + 2\left(\lambda_{mem} - 2\right)\right), & 2 \le \lambda_{mem} \le 3 \\ 10^{-6}\left(3 - 1.67\left(\lambda_{mem} - 3\right)\right), & 3 < \lambda_{mem} < 4.5 \\ 1.25 \times 10^{-6}, & \lambda_{mem} \ge 4.5 \end{cases} \tag{5.41}$$

5.3.2 Nitrogen crossover

For PEMFC membranes, high proton conductivity and low ionic resistance has been achieved by directing significant efforts towards minimizing membrane thickness which subsequently promotes water crossovers across it to humidify the anode side of the fuel cell. Moreover, high power density is also attributed to the membrane thickness in addition to GDL and stack assembly. Limitations for physical stability of the cell and gas crossovers have to be balanced by selection of a membrane with reasonable thickness. It is however reported by Baik and Kim [47] and Cheng et al. [81] that membrane thickness and equivalent weight does not considerably effect the gas permeability coefficients, but influence of water content in the membrane is significant enough. Mittlesteadt and Umbrell [82] suggested that in fact N_2 crossover is the sum of two parallel processes; gas diffusion through

polymer and water phase of the ionomer respectively. Their simple model was correlated to the functional form by Ahluwalia and Wang [45]. Here, a similar permeation model of [59] with a scale factor of 8 and equations with the influence of stack temperature and membrane water uptake is used.

$$K_{N_2} = \alpha_{N_2}(0.0295 + 1.21 f_v - 1.93 f_v^{\,2}) \times 10^{-11} \times \exp\left[\frac{E_{N_2}}{R}\left(\frac{1}{T_{ref}} - \frac{1}{T}\right)\right] \tag{5.42}$$

The activation energy for nitrogen, E_{N_2} is assumed to be 24 kJ/mol, α_{N_2} is scale factor, R is the universal gas constant, T_{ref} is 303K and f_v is the volumetric ratio of water in the membrane and is given by;

$$f_v = \frac{\lambda_{mem} \cdot V_w}{V_{mem} + \lambda_{mem} \cdot V_w} \tag{5.43}$$

where λ_{mem} is the membrane water content, V_{mem} and V_w are molar volumes of dry membrane and liquid water.

In a PEMFC, concentration gradient across the membrane is the driving force for N_2 diffusion from cathode to anode. Since concentration of a certain species could be related to its partial pressure in a volume, the nitrogen flux is calculated from the partial pressures of N_2 in cathode and anode of the fuel cell.

$$J_{N_2} = K_{N_2} \frac{P_{N_2,ca} - P_{N_2,an}}{t_{mem}} \tag{5.44}$$

where t_{mem} is the thickness of the membrane and is assumed to be constant in the current simulations.

5.4 Flow Modelling

For flow model of anode and cathode, the model uses mass balance to calculate the inlet and outlet properties of streams. The partial pressures of different species are determined from the properties of the gas streams entering and leaving the system, gas and water crossovers, products formed and depletion of reactants during chemical reactions within the fuel cell stack model. Faraday's law is used to predict the molar flow rate required off the reactants for a specific current:

$$\dot{n}_{H_2} = \frac{I}{nF} S_{H_2} \tag{5.45}$$

where, S_{H2} is the hydrogen stoichiometric ratio for that particular current.

Molar balance for the anode outlet is given by:

$$\dot{n}_{H_2,out} = \dot{n}_{H_2,in} - \left(\frac{i + i_{loss}}{2F} \right) A_{cell} \cdot N_{cells} \tag{5.46}$$

$$\dot{n}^{a}_{H_2O,out} = \dot{n}^{a}_{H_2O,in} + \left(J_{H_2O} \cdot A_{cell} \cdot N_{cells} \right) \tag{5.47}$$

$$\dot{n}^{a}_{N_2,out} = \dot{n}^{a}_{N_2,in} + \left(J_{N_2} \cdot A_{cell} \cdot N_{cells} \right) \tag{5.48}$$

Molar balance for the cathode outlet is summed up in the equations given below:

$$\dot{n}_{O_2,out} = \dot{n}_{O_2,in} - \frac{1}{2} \left(\frac{i + i_{loss}}{2F} \right) A_{cell} \cdot N_{cells} \tag{5.49}$$

$$\dot{n}^{c}_{H_2O,out} = \dot{n}^{c}_{H_2O,in} + \left(\frac{i + i_{loss}}{2F} \right) - \left(J_{H_2O} \cdot A_{cell} \cdot N_{cells} \right) \tag{5.50}$$

$$\dot{n}^{c}_{N_2,out} = \dot{n}^{c}_{N_2,in} - \left(J_{N_2} \cdot A_{cell} \cdot N_{cells} \right) \tag{5.51}$$

$$\dot{n}_{CO_2,out} = \dot{n}_{CO_2,in} \tag{5.52}$$

$$\dot{n}_{Ar,out} = \dot{n}_{Ar,in} \tag{5.53}$$

5.5 Heat Transfer

The total energy into the fuel cell is consumed by the electrical power output, heat removed by the coolant, heat loss at the stack surface and energy stored within the stack itself. In the current model, a lumped thermal model proposed by [27] is considered. The stack is regarded as a single thermal mass with a heat capacity. With the assumption of stack temperature being equal to the coolant temperature at the outlet, heat exchanged with the coolant and hence stack operating temperature could be determined. The energy balance between the above–mentioned modes can be given by:

$$C_t \cdot \frac{dT}{dt} = \dot{E}_{in} - \dot{E}_{out} - \dot{E}_{el} - \dot{E}_{loss} \tag{5.54}$$

where, C_t is the thermal capacitance of the stack, $\dot{E}_{in}$ is the total power delivered by the fuel to the stack (kW), $\dot{E}_{el}$ is the power consumed by the electrical load (kW), $\dot{E}_{out}$ is the heat transferred to the cooling water circulating in the stack (kW), and $\dot{E}_{loss}$ is the heat dissipated to the ambient (kW).

The subordinate components in the BoP, i.e. anode recirculation and water pumps, air blower, mixers and heat exchangers are modelled using the default mathematical models provided in Aspen Dynamics.

5.6 System Efficiency

The net power produced by the fuel cell is the product of current drawn and the voltage generated. Since, average cell voltages are calibrated to define the IV curve here, the net power produced by the stack is attained by multiplying the cell power to the number of cells in the stack:

$$P_{stack} = \left(V_{cell} \cdot I\right) \cdot N_{cells} \tag{5.55}$$

For specific power output simulations at steady–state, the current (I) is assumed to be constant, which calculates the flow rates of reactants based on the stoichiometry. The voltage is determined by the electrochemical equations summarized above. However, in case of transient analysis, the current and voltage models are independent and are determined by the system controls.

Usually stack efficiency is calculated by the following equation:

$$\eta_{stack} = \frac{P_{stack}}{\dot{n}_{fuel} \cdot LHV} \tag{5.56}$$

However, since the fuel cell operates at higher stoichiometry, it is futile to calculate the stack efficiency based on inlet and outlet conditions. Efficiency calculated in this method will be lower than the actual stack performance. On the other hand, cell efficiency will be a more suitable parameter to gauge the fuel cell performance. In the present model, average cell voltage is determined, which is one of the performance parameters, therefore stack efficiency is assessed on cell efficiency. Another approach has been used here, in which the efficiency is determined by the

difference of amount of fuel entering and leaving the system, as the fuel is recirculated back into the anode feed:

$$\eta_{stack} = \frac{P_{stack}}{\left(\dot{n}_{fuel,in} - \dot{n}_{fuel,out}\right) \cdot LHV} \tag{5.57}$$

Overall system efficiency is defined as the ratio of net electrical power and net calorific value of the hydrogen supplied to the system.

$$\eta_{sys} = \frac{P_{net}}{\dot{n}_{fuel} \cdot LHV} \eta_{inv} \tag{5.58}$$

Here, η_{inv} is the power conditioning efficiency of the inverters and is assumed to be 96%. Net electrical power is the difference of power produced by the stack and power consumed by all the auxiliary components:

$$P_{net} = P_{stack} - \left(P_{blower} + P_{pumps} + P_{radiator}\right) \tag{5.59}$$

5.7 Model Validation

Simulations for the prescribed system were carried out and reliability of the suggested model is verified and corroborated against design validation data provided by fuel cell stack manufacturer, *Ballard Power Systems* [62]. Model characteristics of the same system at various operating temperatures and power loads have been studied in Hosseinzadeh and Rokni [65]. Figure 5.3a represents adaptation of the devised model which corresponds to the polarization curve obtained from operational data associated with the given PEMFC stack.

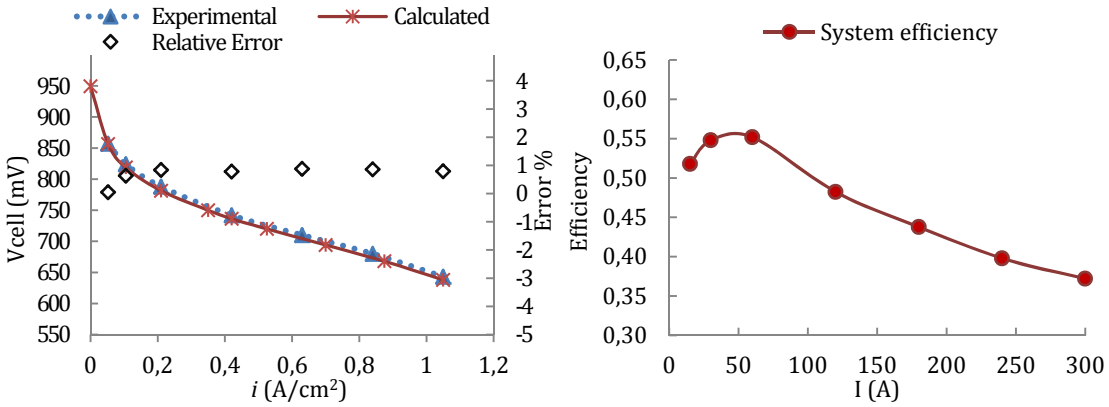

Figure 5.3: (a) Comparison of stack operational data and calculated polarization curves for PEM fuel cell with relative error, (b) System efficiency profile at operating current range.

As a convention here, the plots are demonstrated with both current and current densities, which correspond to the same values on the x–axis. The calculated relative error shows a good agreement between the model and data provided. As suggested by the manufacturer, stack temperature range of 60–70°C has been used in simulations of the current system. Selection of other parameters and operating conditions is based upon table 3.1.

Figure 5.3b exhibits profile of overall system efficiency at corresponding currents. A general trend of decreasing efficiencies with increasing loads can be observed, which is characterised by an increase in ohmic overpotentials in the stack and high power consumption of BoP for cooling of the system. However an exception to the contrary can be noticed at very low currents, where high parasitic losses in BoP render the system efficiency to be lower as well. Nevertheless, higher stack efficiencies at low loads assist the system efficiency to be not as low when compared to that at higher currents. The system operates at maximum efficiency at 25% of the nominal stack power, i.e. at a power load of 5.2 kW and current withdrawal of approximately 60 A.

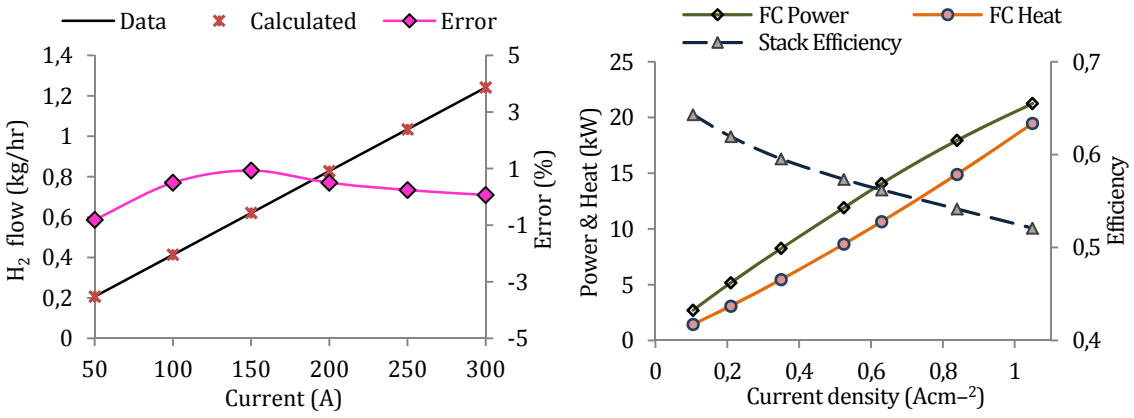

Figure 5.4: (a) Calculated H_2 consumption versus Ballard data with relative error, (b) Heat and power generation with stack efficiency at corresponding current densities.

Hydrogen consumption for different operating loads is compared to the provided experimental data as well, see Fig. 5.4a. Fuel utilization is found to be an excellent match with the present model. In Fig. 5.4b, profiles for heat and power generated by the stack are presented. At higher current densities, stack efficiency tends to decrease, which is due to higher ohmic and concentration resistances. Power production is subsequently declined with higher heat generation.

Chapter 6

Exergy analysis of Fuel Cell Stack

6.1 Overview

As described in previous chapters, PEM fuel cells are electrochemical devices which generate electricity at relatively higher power density and conversion efficiency. However, like any other device, PEMFC are also subject to thermodynamic irreversibilities that occur during the cell operations. Therefore, these irreversibilities need to be assessed, analysed and consequently reduced to ensure efficient operation of PEM fuel cells. An elementary approach to cater these issues is the energy analysis of the system or component. However in an energy analysis, which is based on the first law of thermodynamics, the loss in quality of energy is ignored and all forms of energy are considered to be equivalent. On the other hand, exergy analysis, based on the first and second law of thermodynamics, shows the thermodynamic imperfections of a process, which comprises of all energy losses and irreversibilities. One of the implications of 2^{nd} law of thermodynamics is that there is always some exergy destroyed when a process involves a temperature change, which can be attributed to overall entropy increase of the system plus its surroundings.

In order to evaluate measures to reduce exergy losses, one needs to have knowledge of the processes that cause these losses. In the fuel cell stack, five processes can be distinguished in which the exergy losses occur: heat generation and transfer between the stack and its surrounding environment, mixing of species in inlet and outlet streams, chemical reactions occurring within the fuel cells, and polarization losses [83]. In a fuel cell system, other irreversibilities in the BoP components are also present; such as blowers, humidifier, heat exchangers, etc. Since, fuel cells are electrochemical devices and contain no mechanical parts, friction and losses associated with it are a non–issue. The chemical energy of the fuel is directly converted to electrical power output and heat is produced as a by–product of this

chemical reaction. Moreover, polarization losses due to ohmic resistances in the cells and electronic circuit are converted to heat as well.

In this study, an exergy analysis of a PEM fuel cell stack is performed to investigate the effects of thermodynamic irreversibilities on the performance of PEMFC. One of the objectives is to investigate the effects of various parameters such as operating temperatures, current densities and reactant relative humidity on stack start–up, which is a vital issue in automotive applications itself. Here, an exergetic analysis on the fuel cell stack is conducted in time. The scope is not to investigate irreversibility in the surrounding components.

6.2 Laws of thermodynamics and PEM fuel cells

A fuel cell generates electrical power ($\dot{W}$) through chemical reactions between the reactants and a certain amount of heat is released ($\dot{Q}$) at a constant operating temperature (T_f). The maximum amount of work that an internally reversible fuel cell delivers can be written as:

$$\dot{W}_{\max} = \dot{W}_{\text{int}\,rev} - \left(T_{FC} - T_0\right)\cdot \dot{n}_f \cdot \Delta\overline{S}_{reaction} \tag{6.1}$$

Here, $\dot{W}_{\text{int}\,rev}$ is the work done by the fuel cell without presence of internal losses, $\Delta\overline{S}_{reaction}$ is the entropy change due to the reaction, and $\dot{n}_f$ is the number of moles of fuel. The electric power output and efficiency of internally reversible fuel cell can be derived by the energy and entropy balance over the control volume and are given by:

$$\dot{W}_{\text{int}\,rev} = -\dot{n}_f \cdot \Delta\overline{H}_{reaction} + \dot{n}_f \cdot T_{FC} \cdot \Delta\overline{S}_{reaction} = -\dot{n}_f \cdot \Delta\overline{G}_{reaction} \tag{6.2}$$

$$\eta_{\text{int}\,rev} = \frac{\Delta\overline{G}_{reaction}}{\Delta\overline{H}^{0}_{reaction}} \tag{6.3}$$

where, $\Delta\overline{H}_{reaction}$ and $\Delta\overline{G}_{reaction}$ are enthalpy and Gibbs free energy of the reactions. Hence, the maximum power that can be generated by any reversible fuel cell is given by:

$$\dot{W}_{\max} = -\dot{n}_f \left\{-\Delta\overline{G}_{reaction} - \left(T_{FC} - T_0\right)\cdot \Delta\overline{S}_{reaction}\right\} \tag{6.4}$$

It is observed in the equation above that external irreversibilities associated with the reactants to reach the fuel cell operating temperature from the ambient and

those linked to cooling the product from fuel cell temperature to the ambient are expressed in the second part of right side of the equation. In an ideal case, where it is assumed that the incoming reactants and released products are at their dead state (environment conditions), the maximum work produced by the fuel cell is demonstrated by [84]:

$$\dot{W}_{0,\max} = \dot{n}_f \left(-\Delta \overline{G}^0_{reaction} \right) \tag{6.5}$$

In this case the maximum first law efficiency is given by Eq. 6.6, which is independent of fuel cell temperature.

$$\eta_{0,\max} = \frac{\Delta \overline{G}^0_{reaction}}{\Delta \overline{H}^0_{reaction}} \tag{6.6}$$

In practice, the fuel cell like any other device is accomplished with internal irreversibility. Efficiency of the fuel cell decreases with temperature, which is due to external irreversibility. This drop cannot be overcome by elimination of internal losses (activation, ohmic and concentration overpotentials). However, coupling a fuel cell with external devices can extract more power from the system. Since, PEMFC usually operate at low temperatures, heat generated within these modules is of little or no use. On the other hand, SOFC operate in a range of 700–900°C and thereby can be used as a topping cycle with a Stirling engine, gas or steam turbines. For this particular reason, SOFC have higher exergetic efficiencies when compared to PEMFC.

Table 6.1: Maximum achievable voltage and efficiency for H_2–O_2 fuel cells at different temperatures

Temperature (°C)	ΔG_o (kJ mol^{-1})	Max EMF (V)	Efficiency Limit
25 (liquid)	–237.2	1.23	83%
80 (liquid)	–228.2	1.18	80%
100	–225.2	1.17	79%
200	–220.4	1.14	77%
400	–210.3	1.09	74%
600	–199.6	1.04	70%
800	–188.6	0.98	66%
1000	–177.4	0.92	62%

6.3 Exergy balance in PEM fuel cell

In context of the presented argument, a general exergy balance diagram of PEM fuel cell can be plotted as shown in Figure 6.1. Here, $\dot{E}x_{mass}$, $\dot{E}x_{heat}$, $\dot{E}x_{work}$ and $\dot{E}x_{st}$ are exergy transfer by mass, heat, work and exergy stored in the fuel cell respectively.

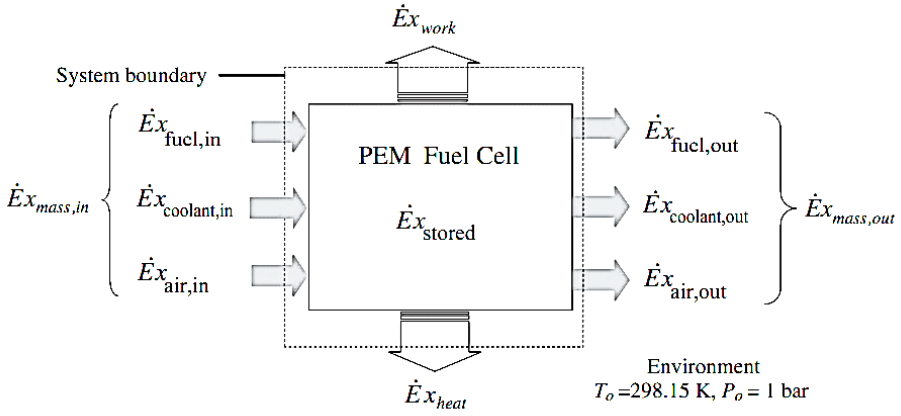

Figure 6.1: Schematic of exergy balance for a PEM fuel cell stack.

Thermodynamic concepts and their applicability for the current study are derived from the literature [85]. General energy and exergy balance of a system are written as follows:

$$\dot{E}_{st} = \dot{E}_{in} - \left(\dot{E}_{out} + \dot{W}_{FC} + \dot{E}_{loss}\right) \tag{6.7}$$

$$\dot{E}x_{D} = \dot{E}x_{mass,in} - \left(\dot{E}x_{mass,out} + \dot{E}x_{work} + \dot{E}x_{heat} + \dot{E}x_{st}\right) \tag{6.8}$$

where, $\dot{E}_{st}$ and $\dot{E}x_{D}$ are the stored energy respective exergy destruction rate, due to irreversibilities in the fuel cell stack. It is evident from the above equation that inlet exergy should be larger than outlet exergy and some part of it will be destroyed within the stack, which is one of the implications of 2nd law of thermodynamics.

While,

$$\dot{E}x_{mass,in} = \sum_i n_i e_i^t \tag{6.9}$$

Here e_i^t is the total exergy of the flow stream (kJ/kmol), n is the molar flow rate and i denotes the number of inlet or outlet streams.

$\dot{E}x_{work}$ is equal to the electrical power produced ($\dot{W}$); which incorporates all the internal reversibilities i.e. polarization losses. In case of fuel cells, heat transfer with the surroundings is only the heat loss to the ambient:

$$\dot{E}x_{heat} = \left(1 - \frac{T_0}{T_{FC}}\right)\dot{Q}_{loss} \tag{6.10}$$

The last term on right of Eq. (6.8), $\dot{E}x_{st}$ is the exergy stored in the fuel cell stack and is given by:

$$\dot{E}x_{st} = \left(\frac{dT_{FC}}{dt}\right)\frac{\dot{E}_{st}}{T_{FC}} \tag{6.11}$$

Exergetic efficiency of the stack is defined as the ratio of total electrical power produced to the available exergy, which is this case is determined using:

$$\eta_{ex} = \left(\frac{\dot{W}}{\dot{E}x_{mass,in} - \dot{E}x_{mass,out}}\right) \tag{6.12}$$

Generally, it is a point of interest to minimize entropy generation in a system and thereby, reduce the destruction of exergy. In the exergy analysis of the proposed system, entropy generation rate can be calculated by:

$$\dot{S}_{gen} = \left(\frac{\dot{E}x_D}{T_0}\right) \tag{6.13}$$

The total exergy of any flow stream is further broken down into physical and chemical exergies. Kinetic and potential exergies are neglected here.

$$e^t = e^{ph} + e^{ch} \tag{6.14}$$

Physical exergy is associated with the temperature and pressure of the reactants and the products in the fuel cell system. Simply, it is the amount of useful work that a substance can deliver when brought reversibly from its state to the "restricted dead state". Physical exergies can be described by their enthalpy and entropy states as below:

$$e^{ph} = (h - h_0) - T_0(s - s_0) \tag{6.15}$$

In the current study, restricted dead states are the same as surrounding environment conditions i.e. 25°C and 1 bar of pressure.

The chemical exergy is associated with the departure of the chemical composition of a system from that of the environment. The components of the media in the system are first converted to reference compounds or products and eventually diffuse to the environment which in this case is also the dead state. Since, inlet and outlet flows are a mixture of gases, the exergy of the gaseous mixtures is calculated by using:

$$e_i^{ch} = \sum y_i e_i^0 + RT_0 \cdot \sum y_i \ln(y_i) \tag{6.16}$$

Here, e_i^0 is the standard molar chemical exergy for component species. The following table 6.2, displays these exergy values, which are taken from literature [86]. Enthalpies and entropies at specific conditions are calculated using Aspen Dynamics' built–in functions.

Table 6.2. Standard molar chemical exergy, of substances at 298.15 K and 1 bar.

Species	Formula	Exergy (kJ/kmol)
Hydrogen	H_2	236,100
Nitrogen	N_2	720
Oxygen	O_2	3970
Water (Vapour)	H_2O (g)	9500
Water (Liquid)	H_2O (l)	900

6.4 Simulation results

Equations characterising exergy of the PEMFC described above are implemented in Aspen Custom Modeler™ in addition to the electrochemical, thermal, feed flow and water transportation equations to constitute a dynamic fuel cell model. The developed fuel cell component is then incorporated into Aspen Dynamics program to evaluate intrinsic exergetic losses during transients and steady–state as well. Thermodynamic and exergetic efficiencies along with net power of the system are determined by current drawn and voltage produced by the stack. The total energy into the fuel cell is consumed by the electrical power output, heat removed by the coolant, heat loss at the stack surface and energy stored by the stack itself. In the current model, a lumped thermal model proposed by [27] is considered.

6.4.1 Exergy efficiency of PEM Fuel Cell

The exergy efficiency of the fuel cell is calculated from the ratio of power produced to the available energy. In a system with fuel recirculation and higher fuel stoichiometries, the stack efficiency has very low values compared to the system efficiency, because a high percentage of fuel is wasted. Here, average cell efficiency is considered to be the stack efficiency in order to compare it with exergetic efficiency. Fig. 6.2a shows the energy and exergy efficiency profiles for average operating current loads for the described system. A general decreasing trend of both exergy and energy can be observed, though exergy efficiency of the stack is higher than the energy efficiency.

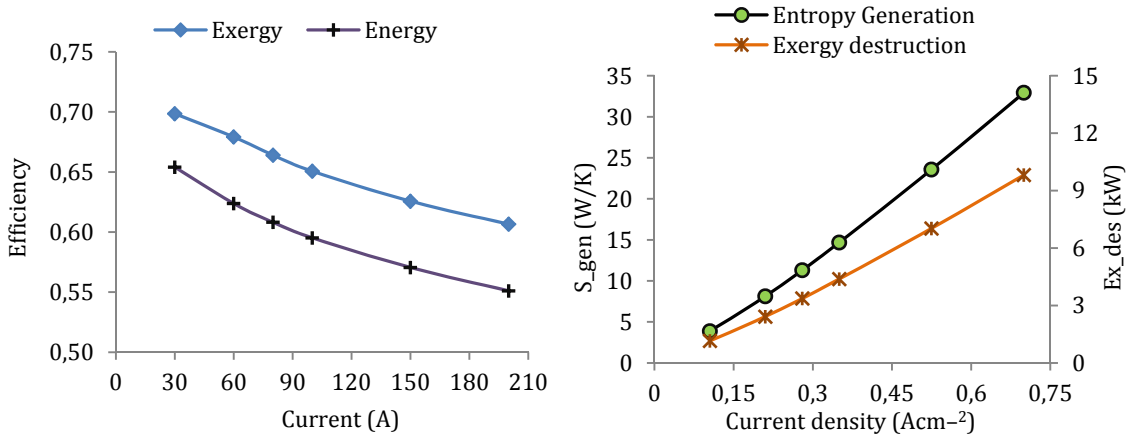

Figure 6.2: (a) Energy and exergy efficiency of PEMFC at different current loads, (b) Exergy destruction and entropy generation at increasing current densities.

Exergy destruction associated with the performance of fuel cell at increasing current loads is represented in Fig. 6.2b. At higher currents, the stack efficiency decreases; this raises the amount of entropy generation in the fuel cell.

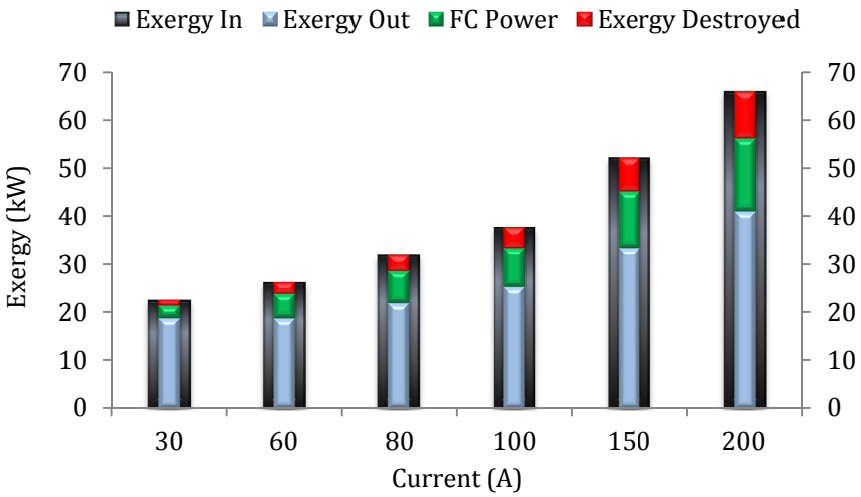

Figure 6.3: Total exergy entering and leaving the fuel cell stack at different operating currents with the amount of fuel cell power produced and exergy destroyed.

Figure 6.3 portrays the exergy balance for the fuel cell stack, where the amount of exergy entering the stack is divided into electric power generation, exergy loss and exergy leaving the system in the form of outgoing streams.

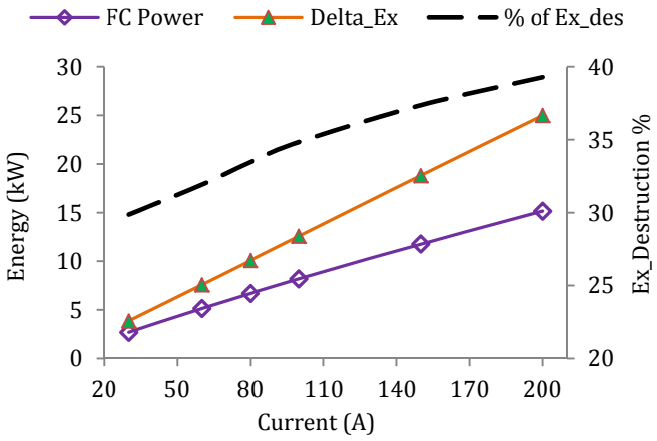

Figure 6.4: Percentage of exergy destruction at corresponding FC power production.

Exergy destroyed by PEM fuel cells operating at higher loads is comparatively higher to that of lower load conditions. This can be noticed in Fig. 6.4, where the exergy

destruction ratio to the inlet power increases from 32% to 39% with increasing currents from 30A to 200A.

6.4.2 Effect of stack current

The described system model is designed with a control oriented approach so that it emulates a real time PEMFC operation. Input parameters, recommended by the stack manufacturer such as operating temperatures, pressures and reactant stoichiometries are embedded in the system controls and the system operates more or less at the optimum. However, control strategies related to thermal and water management play an important role in design of optimal stack behaviour in transient conditions. Therefore, simulations are carried out to study the dynamic response of the stack towards the influencing parameters.

Different start–up cases were investigated to analyse energetic and exergetic efficiencies and factors affecting them. Currents of 40 and 100 A are applied for two start–up scenarios. Initial stack temperature is that of surrounding conditions, here 25°C is used. Figure 6.5 shows that at high current start–ups, both energy and exergy efficiencies of the system decrease. At steady–state, exergetic efficiency of the stack is found to be 70% and 66% when applied current is changed from 40 to 100 A.

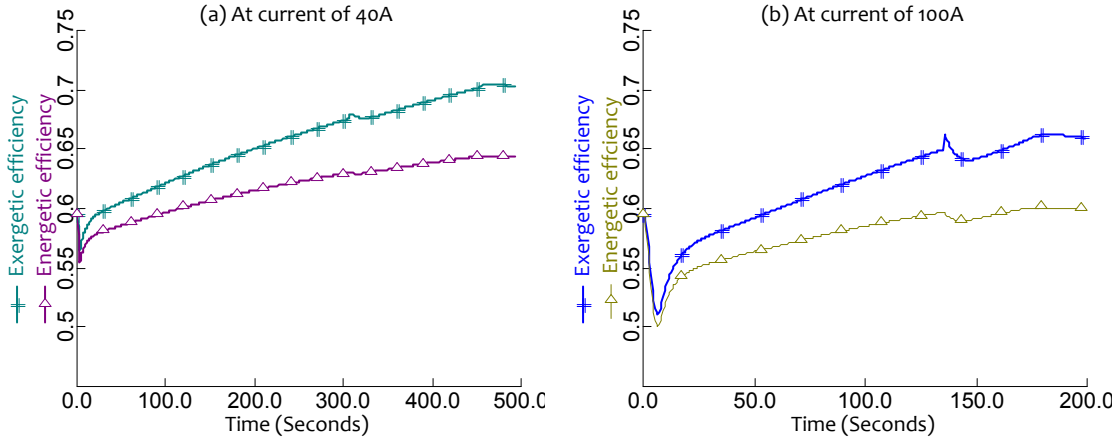

Figure 6.5: Energy and exergy efficiency of stack at system start–up: (a) at current of 40A, (b) at current of 100A.

It can be observed that besides initial fluctuations at the start–up, the exergetic efficiency rises steadily until the stack reaches stable operating conditions. This is due to the fact that voltage generated in the fuel cell rises steadily with the operating temperature of the stack. This dependency is discussed later in the following section. Another noticeable observation is the slope of elevation in these efficiencies. The gap between energy and exergy efficiency increases with time as stack temperature is raised from cold state. This is due to the direct proportionality between physical exergies of the component species and the temperature of the fuel cell.

6.4.3 Influence of operating temperature

The power generation capability of a PEMFC tends to be prominent with increasing operating temperatures, as portrayed in Fig. 6.6. This is mainly due to the rise in the cell voltage, which is a function of Gibbs free energy, and described in Nernst equation [65]. Gibbs free energy is also a function of reactant partial pressures and the operating temperature. However, in the present study, effects of partial pressures are not discussed. It is evident from the Fig. 6.6a, that an increase of temperature from 25°C to 65°C raises the voltage from 0.63 to 0.80 V. Low cell voltages for the same amount of power would require high current densities; leading to greater mass flow rates of the reactants. This will result in increased difference between the total exergies of the reactants and the products, hence lower the exergetic efficiency as demonstrated by [38].

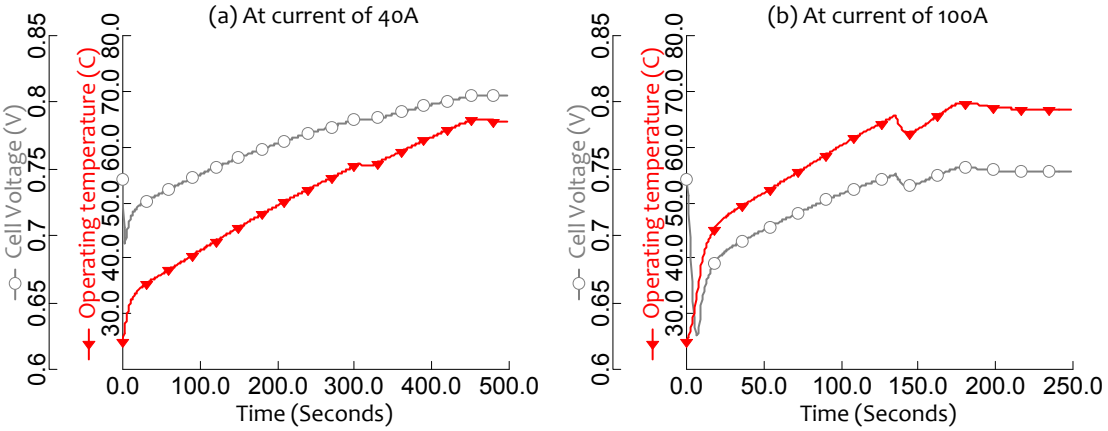

Figure 6.6: Cell voltages and stack temperature at system start–up: (a) at current of 40A, (b) at current of 100A.

In contrast, higher operating temperatures produce more voltage potential across the electrodes, consequently generating higher power output from the system. So far, the influence of fuel cell operating temperature on energy and exergy efficiency has been well established for start-up case, which is also dependant on other varying operating factors. However, the magnitude of impact of any parameter on the system is fully understood when it is subject to variation at steady-state operations.

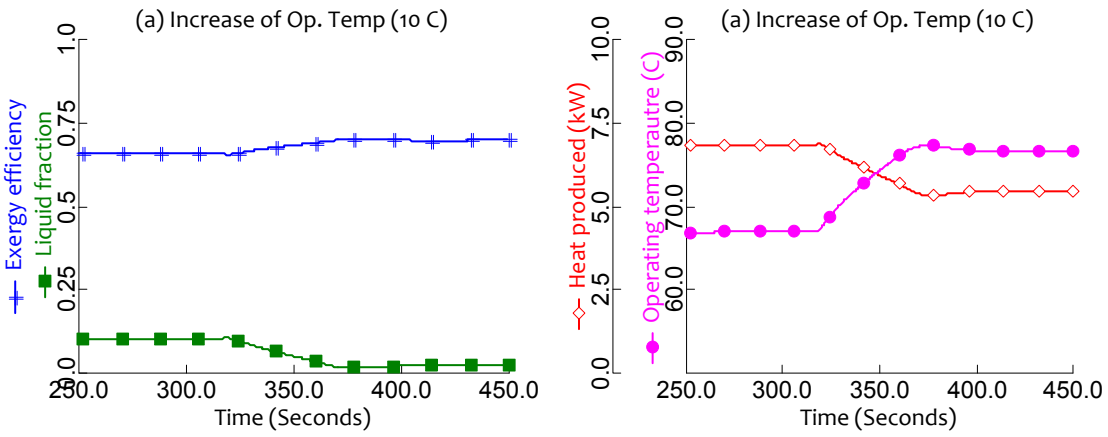

Figure 6.7: Effect of increase in stack operating temperature by 10°C (a) Exergetic efficiency and liquid water fraction, (b) heat produced by the FC stack.

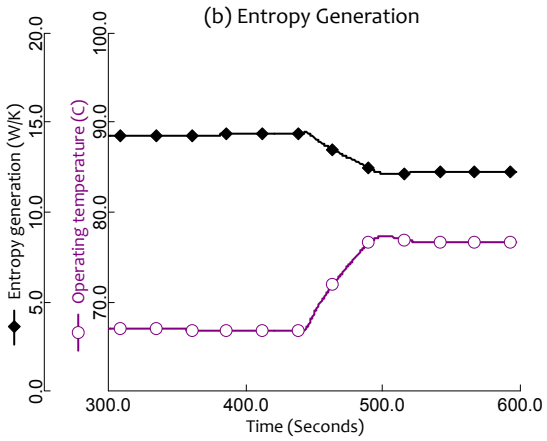

Figure 6.8: Entropy generation in the stack with change in stack operating temperature.

Here, variation of operating temperature and its effect on other parameters is investigated. Fig. 6.7a depicts the increase in exergetic efficiency and water vapour with temperature increment from 67°C to 77°C at a current load of 100A. The amount of liquid water at cathode is decreased to only 2% from the previous 10 %, thereby reducing the heat generation in the stack (Fig. 6.7b). The change in entropy generation within the fuel cell with changing operating temperatures is shown in Fig 6.8. Results show that the entropy production decreases with the increase of operating temperature. In addition to the factors above, at higher temperatures reaction kinetics is faster and irreversibilities associated to activation polarization are considerably lowered, thereby reducing entropy generation in the fuel cell.

6.4.4 Impact of ambient temperature

It is interesting to reason if increase in operating temperature is beneficial to PEMFC, then how the system would react to variations in the surrounding temperature. Fig. 6.9 portrays the effects of ambient temperature on exergetic efficiency and entropy generation when a start–up current of 60A is drawn from the system. It can be observed in Fig. 6.9a, that at 25°C ambient temperature, the start–up exergetic efficiency is around 1% higher than to that of 15°C ambient temperature in Fig. 6.9b.

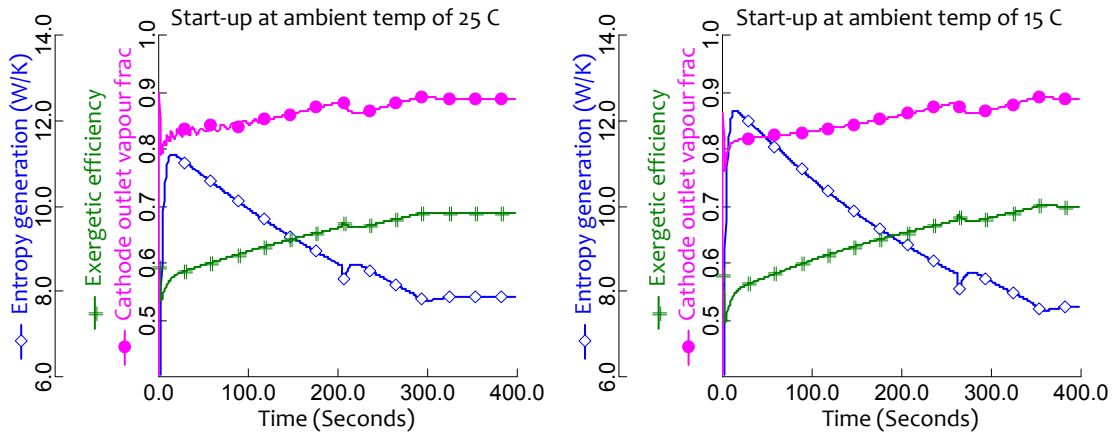

Figure 6.9: Effect of ambient temperature on entropy generation and exergetic efficiency; (a) ambient temperature of 25°C and (b) 15°C respectively.

This is due to the amount of water condensation in the fuel cell cathode which has been discussed previously. With a same current withdrawal of 60A, more water is saturated when the surrounding temperature is lower. In the present case, 20% of liquid water is present at cathode exhaust at 25°C, whereas 24% of water saturation occurs at 15°C ambient temperature. Additionally, potential difference generated across fuel cells is lower, hence a lower efficiency at start–up. In a similar observation, it can be noted that entropy generated in system at 25°C is around 11.2 W/K.

On the other hand, entropy generation is determined to be 12.3 W/K at 15°C start–up. Although there is a negative impact of lower ambient temperature on the initial stage of fuel cell operations, steady–state operations show a positive effect. Exergetic efficiency and destruction of exergy are found to be very close for both cases, when the system operates at steady–state conditions. Increase in exergetic efficiency for cold surroundings mounts to 1.5% to that of 25°C, while a 6% reduction in entropy generation is observed when ambient is at 15°C. Furthermore, its takes more time for the system to reach stable operations.

6.4.5 Effect of liquid water

Water management is a critical issue in PEM fuel cells and has significant impact on overall performance of the stack. Removal of water from cathode is dependent on stack temperature and pressure drop. Fuel cell water production increases with current and is also dependent on the number of cells in the stack. Fig 6.10a shows the start–up of the system at 40A. The amount of liquid water at cathode outlet is around 17 % when stack operating temperature is close to the ambient and lowers gradually as the stack reaches steady–state. On the other hand, when the stack is operating at 100 A, the amount of liquid water percentage at cathode outlet is 23% approximately, which is higher than to when compared to 40A simulation. This affects the exergetic efficiency of the fuel cell in a negative way. An abrupt decrease at start–up can be seen in both figures below, although it is much prominent at higher current densities, see Fig. 6.10b. This is the result of lower stack temperatures at the starting sequence and higher current densities. The most critical factor in lower exergetic efficiencies at start–up is the amount of heat produced by condensation of water and chemical reactions occurring at the cathode. As the system tends towards stability, increase in operating temperature reduces liquid water at the outlet, thereby decreasing heat generation. Liquid fractions at anode outlet are very low when compared to cathode outlet. They are calculated to be in the range of 1.5 to 2.0 % for both 40A and 100A current scenarios discussed above.

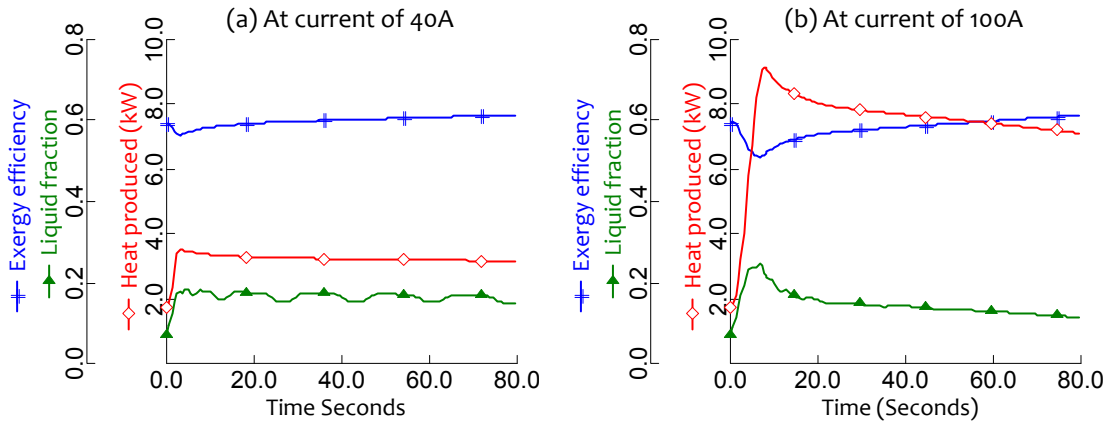

Figure 6.10: Heat produced by liquid water and its effect on exergetic efficiency at system start–up: (a) at current of 40A, (b) at current of 100A.

6.5 Summary

In this chapter, energetic and exergetic performances of PEMFC stack were evaluated in time, considering the first and second law of thermodynamics and associated irreversibilities were identified. Exergy analysis of PEMFC was conducted for start–up case, in order to identify effect of underlying operating parameters. Results show that the largest exergy destruction takes place when system is started at high–currents and low ambient conditions. Also, cell voltages increase with increasing stack temperature. Moreover, entropy generation is reduced at high operating temperatures and with low presence of liquid water in the cathode outlet. Furthermore, low ambient temperatures increase the exergetic efficiency slightly when operating at steady state temperatures. Moreover, presence of liquid water at cathode outlet is also one of the main contributors in high entropy generation in the fuel cell stack. At high current start–ups, saturated water accounts for almost quarter of the total cathode exhaust, generating additional heat to be removed from the stack.

Chapter 7

System Analysis on Start–up

7.1 Premise

In order to make hydrogen powered fuel cell vehicles commercially viable, there are many challenges which need to be overcome. The durability of PEMFCs is one of these challenges that need to be catered to prolong the engine life to that of currently used ICE vehicles. A common failure mode for automotive fuel cells is the voltage degradation, which can be mainly attributed to voltage cycling during transient operations, fuel starvation, and during system startup and shutdown [87], [88]. Due to these start–up and shutdown cycles over a long period, the fuel cell electrodes develop carbon corrosion which is one of the root causes for voltage degradation [89].

Other issues point towards the practicality of fuel cell automobiles. The user will expect to drive the vehicle almost immediately after turning it on, implying a short warm–up time. However, environmental conditions dictate the heating times for these fuel cells. Lower ambient temperatures impede the quick start–up by either freezing of the residual water in the stack at sub–zero temperatures and secondly the temperature–dependent performance of the fuel cell until it reaches higher steady–state operating temperatures. Many key parameters that affect the start–up operations of the fuel cell have been reported in the open literature; such as ambient temperatures, water content in the membrane, operating loads and corresponding current densities, reactant stoichiometry, and water saturation within fuel cell. As already described in the literature review, a very large volume of research has been conducted on cold starts with many propositions of methodologies to prevent water freezing in the fuel cells; however, there is still a need for models elaborating further details of the intricate processes and mechanisms of local transport phenomena on the performance of the fuel cells when starting at normal operating temperatures.

Building on these needs, a start–up analysis is performed for the described PEMFC system, starting at ambient temperature of 25°C and the focus has been set to evaluate the effects of key parameters till the system reaches steady–state operating temperatures. Thereby, a complete control–oriented system–level dynamic model is proposed in this chapter which incorporates all necessary BoP components for a PEMFC fuel cell stack by including electrochemical, thermal, feed flows and water transportation models and a detailed control strategy. In totality, here a sizable focus has been set for (i) comprehensive control strategy regulating hydrogen and air feed flows, coolant inlet and fuel cell stack operating temperatures, (ii) thermal model with liquid coolant circuit incorporated in it which takes into account reactant and product phase changes, (iii) Thermal management including effects of coolant controls and heat exchangers on fuel cell stack performance, and (iv) Water management and effects of water crossover on anode recirculation loop and fuel cell relative humidity.

7.2 System start–up

Fuel cell start–up sequence could be defined as the time required by a system to reach stable conditions, which is achieved when the voltage and consequently power reach a stationary value. Normally, the optimal operating temperature of a PEM fuel cell is reported to be in the range of 60–80°C. Within this range, chemical reactions occurring inside the fuel cell are relatively fast and facilitate removal of water produced by these reactions. Whereas, at low temperatures, there is a considerable rise in kinetic and ohmic losses in addition to reactant transport losses caused by a high rate of water condensation [34]. Lower membrane conductivity is also associated to these temperatures. Thus, it is necessary to elevate the stack operating temperature as soon as possible during the start–up in order to meet the external load requirements.

When the fuel cell is in standby stage i.e. when no current is drawn, auxiliary components such as air blower, coolant pumps, radiator fan and hydrogen inlet valve are closed. At system start–up, all of these components are switched on and fuel valve is opened. Power from the stack is drawn only when the current load is applied on the stack. In the current simulations, values of stream flows are initialized to be non–zeros. In this way, a realistic start–up sequence could be imitated and furthermore initial zero–condition in Aspen Dynamics could be avoided. Initial temperature of the stack is assumed to be equal to ambient temperature (25°C) and a start–up power load is introduced by ramping of current at a rate of 20 A/sec.

Operating temperature of the stack is maintained around 60–70°C with a pressure range of 1.1–2.2 bar. Maximum power produced from the described stack is 21.2 kW corresponding to a current of 300A; however it is generally operated at lower current ranges to attain higher efficiencies by reducing ohmic and concentration overpotentials within the fuel cell stack. Other parameters and operating conditions are selected from chapter 4.

7.2.1 Stack warm–up periods

Different start–up strategies are compared and the results are summarized below. Currents at 40, 60, 80 and 100 amperes are drawn and heat–up times for these four cases are presented in the Fig. 7.1. At start, the flow in cooling circuits is set to the lowest since it is desired to raise the stack temperature to its optimal operation. Coolant flow in the internal circuit is fixed to 290 kg/hr as recommended by the manufacturer. Flow in the internal cooling circuit increases, once the stack temperature difference increases by 15°C. Flow in external circuit is regulated to maintain stack inlet temperature of internal cooling circuit. Air flow in radiator is started to maintain temperature of external cooling loop to around 50°C. As can be seen in the figure below, when the stack is started at current of 40A at a ramp rate of 20 A/s, it takes approximately 425 seconds to reach stable operating temperature.

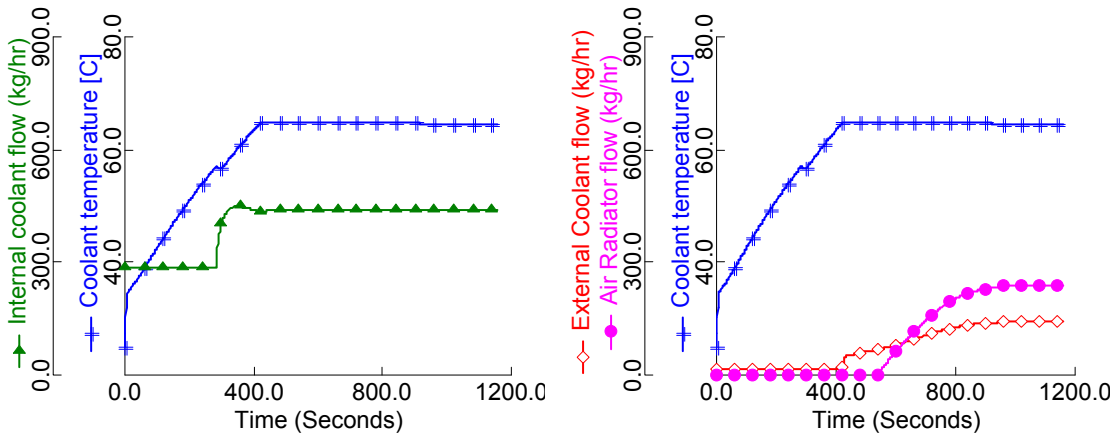

Figure 7.1: Start–up at 40A; (a) Stack heat–up times and corresponding coolant flow rate, (b) Flow rates in external cooling circuit and air radiator.

The heat–up time for 60, 80 and 100 A is determined to be 300, 220 and 175 seconds respectively. The heat–up time becomes shorter as the applied current is increased. High current densities at the cell surface result in a larger amount of heat generation in a relatively short time, which rapidly raises the temperature of the cells.

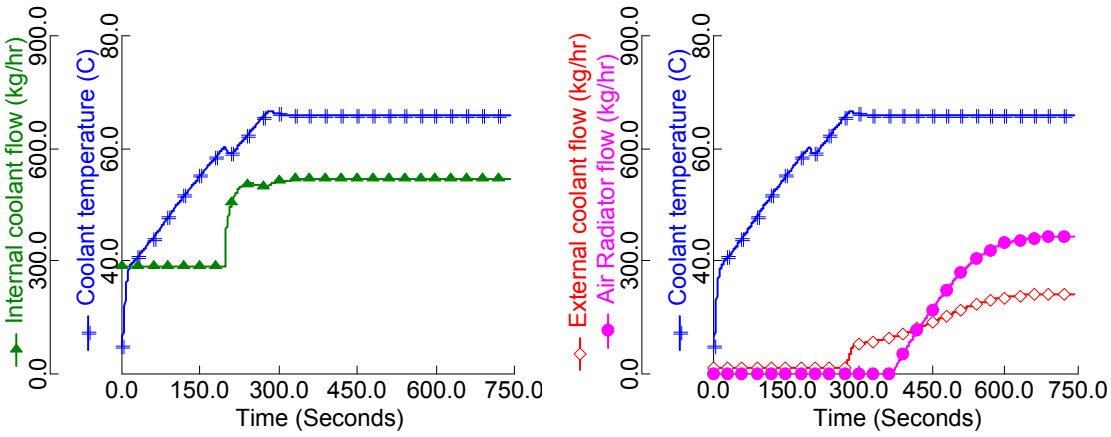

Figure 7.2: Start–up at 60A; (a) heat–up time and coolant flow, (b) External cooler and radiator flow rates.

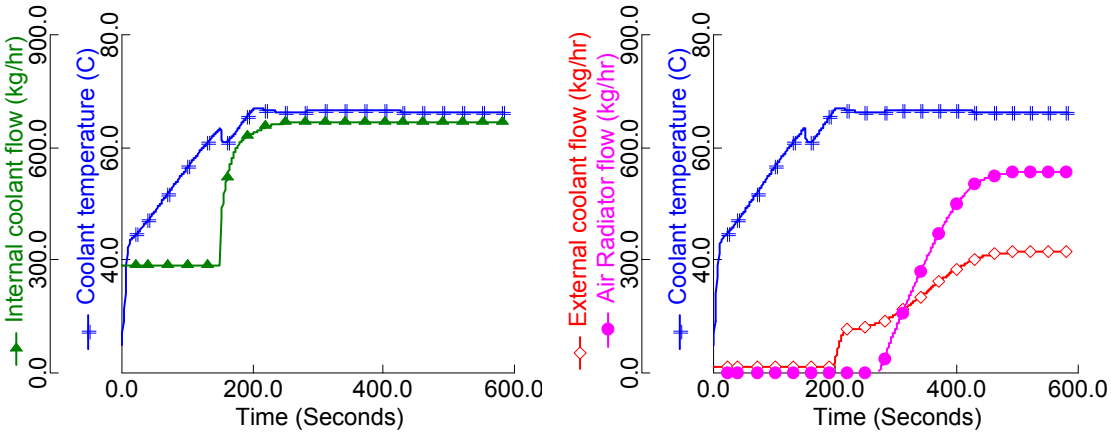

Figure 7.3: Start–up at 80A; (a) heat–up time and coolant flow, (b) External cooler and radiator flow rates.

Accordingly, the flow rates in the internal and external circuit are increased to maintain the stack operating temperature. Once, the temperature of external cooling circuit reaches the control value, air radiator is actuated to expel the heat from the system. Figures 7.2, 7.3 and 7.4 further exemplify the heating times with corresponding coolant flow rates at currents of 60A, 80A and 100A respectively.

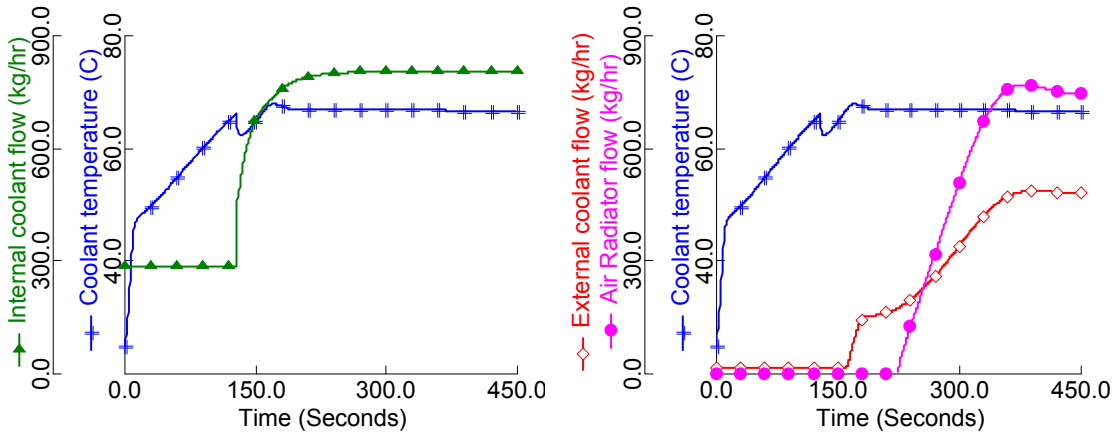

Figure 7.4: Start–up at 100A; (a) Stack heat–up times and corresponding coolant flow rate, (b) Flow rates in external cooling circuit and air radiator.

7.2.2 Power generation and system efficiency

Generally, stack efficiency is higher to that of the complete system with BoP. However, in a system with fuel recirculation, stack efficiency is attributed to fuel stoichiometry, though there is no considerable effect on the system efficiency. When the actual and stoichiometric mass flow of hydrogen differ least then less fuel is wasted and stack efficiency is at its maximum. The same argument could be generalized for system efficiency as well. This is because at higher air mass flows, power consumption of auxiliary components increases.

Different start–up cases were investigated to analyse the system efficiency, net power output and auxiliary power consumptions. Currents of 60 and 100 A are applied for two start–up scenarios. Overall efficiency of the system is as much affected by blower and radiator fan, as by the fuel cell stack itself. Fig. 7.5b shows that at high current start–ups, power generated from the stack increases. However, efficiency of the system decreases. As can be seen in the figure, system efficiency decreases from 55% to 50% when applied current is changed from 60 to 100 A. During start–up, power consumption of coolant pumps and air radiator is very low

when compared to that of the air blower (Fig. 7.5c). Therefore, auxiliary power consumption is dominated by the air blower. It is observed that power consumed by the air blower increases during start–up and becomes constant after a few seconds. Also, power produced by the stack increases at a sound pace and becomes stable once steady state is reached. This elevation in the stack power is due to the fact that the operating temperature of fuel cell increases till it reaches the desired optimal temperature.

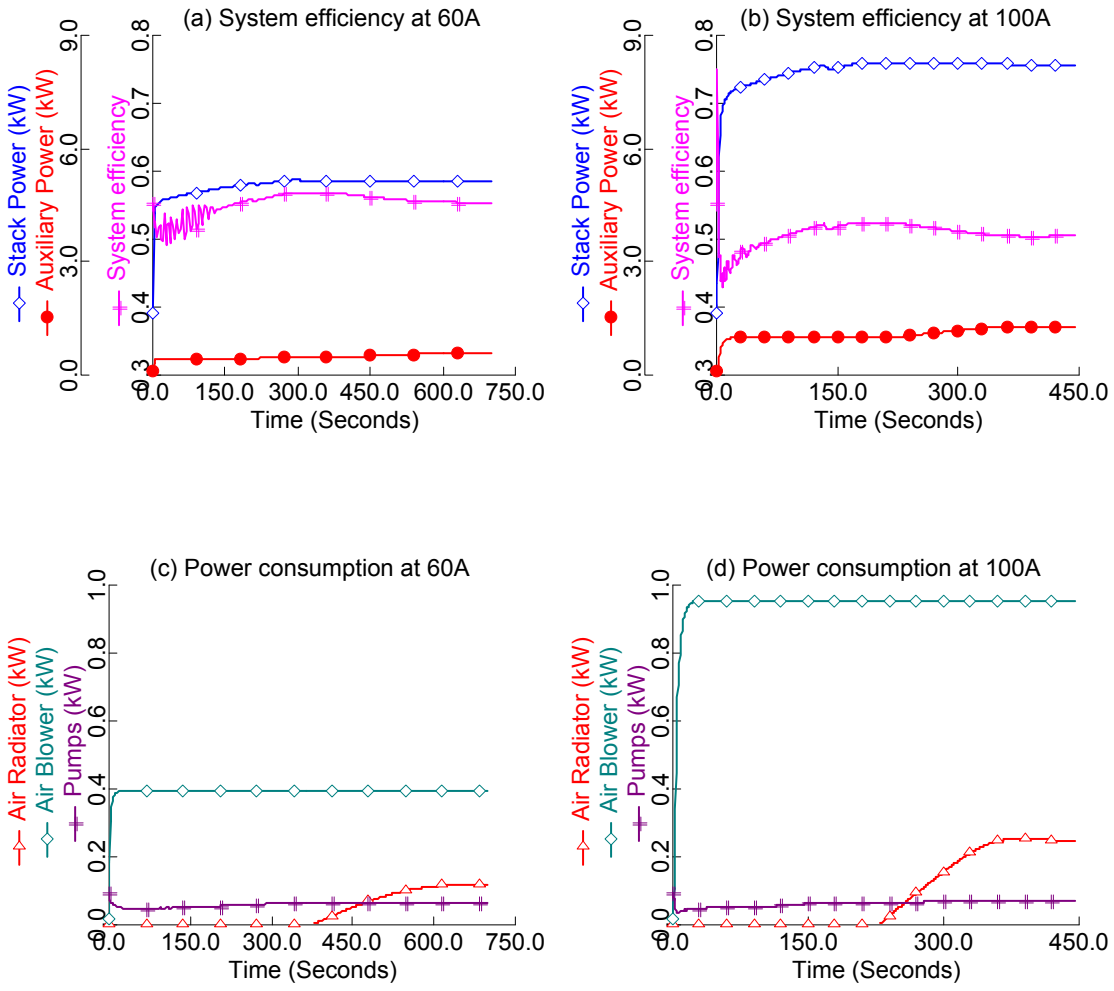

Figure 7.5: System efficiency and stack power; (a) at start–up current of 60A (b) at start–up current of 100A, auxiliary power consumption at start–up of 60A (c) and 100A (d) respectively.

As seen in Fig. 7.5c and 7.5d, radiator fan is shut off at the start sequence, but is activated once temperatures in the external cooling circuit are high enough to be cooled down. Air flow in the radiator can be regarded as a linear function of its electrical power and therefore once it is started by the controller, the system efficiency decreases. Since, at high temperatures heat production in the stack is quite high, the radiator fan consumes around 250 W for a current withdrawal of 100 A, whereas it only requires approximately 125 W when current is at 60 A.

7.2.3 Cell voltage at start–up sequence

Potential difference generated across the fuel cell is dependent on factors such as current density, reactant partial pressures and temperature at which cell reactions occur. Figure 8 elucidates some of these underlying factors which affect the voltage and consequently power output of the stack. Here, during the PEMFC start sequence, current is ramped to 80 A at a rate of 20 A/s. Since current density and reactant pressures are regulated at very fast rate, they follow a constant profile along the time axis.

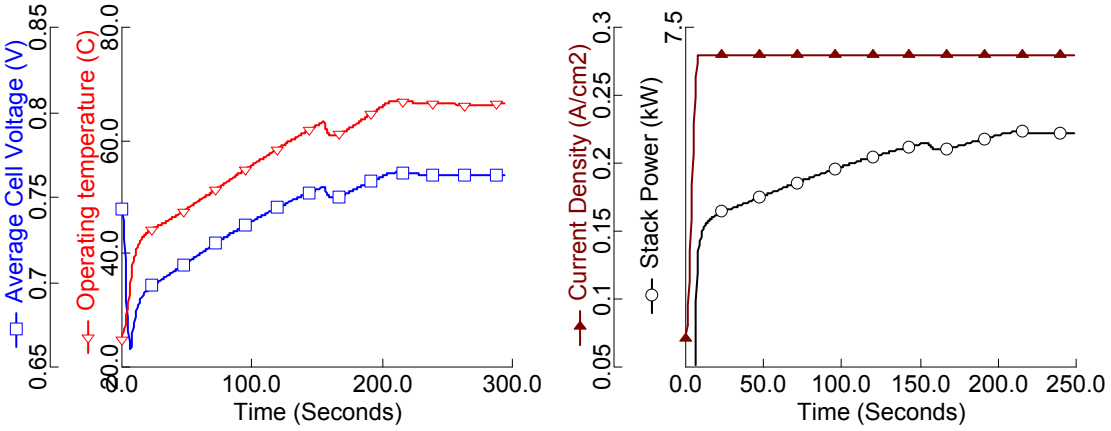

Figure 7.6: (a) Cell voltage as a function of operating temperature with start–up current of 80A, (b) Stack power versus cell current density.

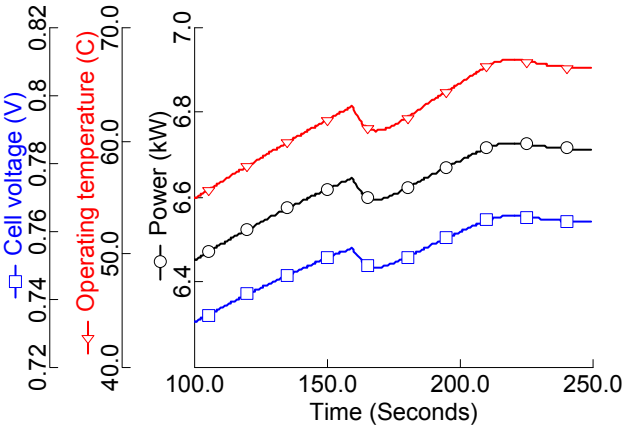

Figure 7.7: Effect of sudden temperature drop on voltage and power.

However, the stack temperature, which is attributed to the coolant mass flows, keeps on increasing until it reaches the desired operating temperature. As can be seen in Fig. 7.6a, cell voltage increases with the operating temperature. This fact is due to the reason being fast reaction kinetics at the electrodes of individual cell sites. It can be observed that the voltage reduces abruptly when simulation time is around 160 seconds. At this stage, the decrease in cell temperature and voltage is caused by the sudden increase in coolant flow into the stack, which maintains the stack operating temperature. In a similar manner, power produced by the stack also increases and decreases with cell voltage, see Fig. 7.6b. Nevertheless, Fig. 7.7 shows a detailed view of the aforementioned instance of time. Evidently power produced by the stack responds to a similar trend to that of voltage against operating temperature of the stack.

In terms of voltage overpotentials, the voltage drop is characterized by activation, ohmic and concentration losses. At start–up, activation polarization is the dominant factor in voltage losses. Figure 7.8 displays the activation overpotential with current ramp (20A/s) till it reaches 80A in 4 seconds. The peak of activation loss can be observed at this instance of time. Since, exchange current density is dependent on temperature and pressure of reactants; as temperature of the stack rises, the overpotential tends to decline and becomes constant at steady–state conditions. Ohmic overpotential, on the other hand increases with the current drawn from the stack.

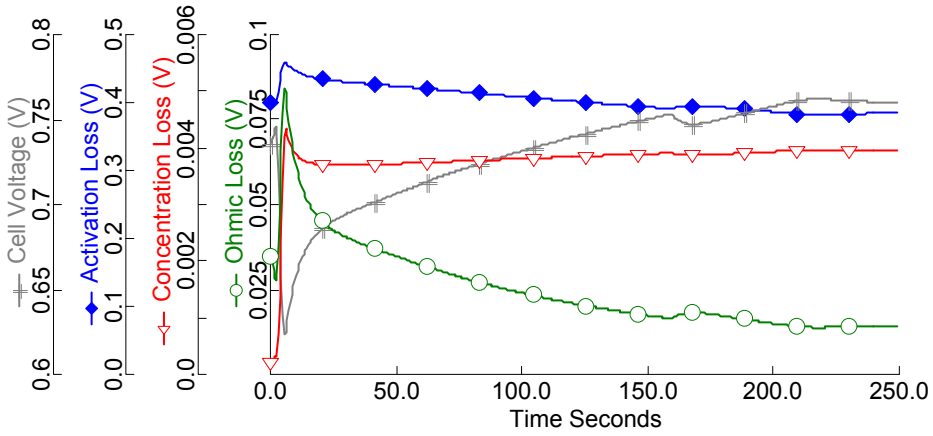

Figure 7.8: Contribution of different losses in cell voltage reduction.

With the increase in cell temperature, ionic resistance drops to very low values. Concentration losses, which arise by the deficiency of reactants at reaction sites, do not affect the voltage to a considerable extent. The current ramp up becomes stable within a few seconds of start–up and does not fluctuate after that, therefore the mass transfer overpotential does not contribute to the voltage drop effectively.

7.2.4 Fuel and oxidant flows

This section caters analysis of reactant flows into the fuel cell and investigates their effect on cell performance as well as on adjacent streams. Cell performance is not sensitive to fuel stoichiometry; whereas the cathode is more sensitive to air stoichiometry. For this reason, simulations are carried out by employing operating conditions and parameters mentioned previously (chapter 4). A start–up current of 60 A is used in this case. Figure 7.9 specifically portrays flow behaviour of fuel and air into and out of anode and cathode channels respectively. It is observed that fuel entering the stack contains water i.e. the fuel is humidified. Since, fuel from anode exhaust is recirculated; it adds more unutilized hydrogen and water to the inlet stream.

Composition of hydrogen in the entrance becomes stable after initial regulation. However, the amount of water keeps on increasing due to the increase in stack's temperature and water cross–over from cathode. This occurrence shows similar incremental trends as in case of stack temperature in Fig 7.1. Anode outlet flows show similar trends, though the amount of hydrogen at the outlet is reduced as it is consumed in the cell reactions.

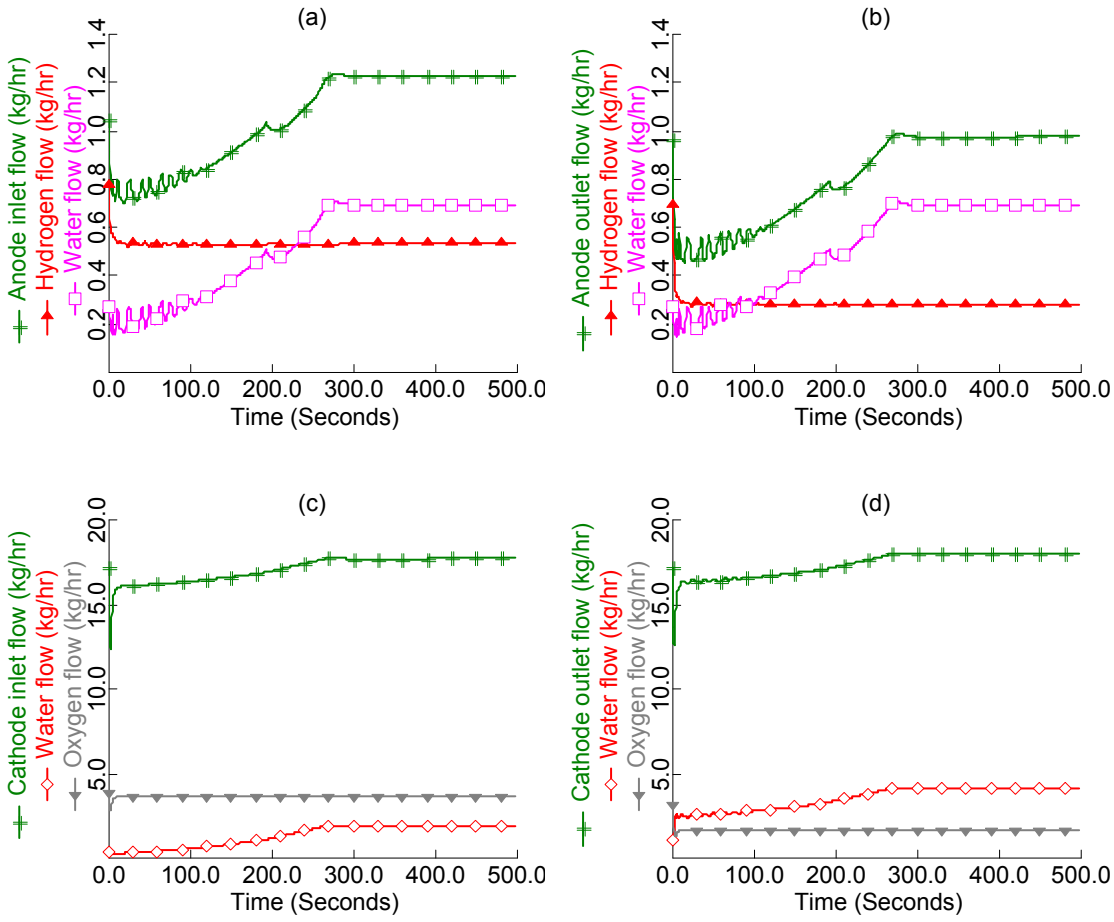

Figure 7.9: Fuel and air flows at inlet and outlet of the stack: (a) Fuel flow at anode inlet, (b) Fuel flow at anode outlet, (c) Air flow at cathode inlet and (d) Air flow at cathode outlet.

Air flow into the cell can also be seen to increase with time (Fig. 7.9c). As temperature of the stack increases, more water is needed to maintain the humidity at the desired level; here, a constant relative humidity of inlet air is assumed. Oxygen and nitrogen remain more or less constant throughout the heat-up time. Once, the stack reaches its steady-state, the air flow becomes constant. At cathode outlet (Fig. 7.9d), the total flow increases correspondingly, however the oxygen content is lower as it is consumed in the reaction as well, whereas water flow is increased. The additional water in the outlet is the product of fuel cell reaction. Higher stoichiometries for both fuel and oxidant are maintained to manage this water production in the cathode and to dilute nitrogen crossover to the anode.

7.2.5 Air humidification effects

In PEMFC systems, adequate hydration is necessary to facilitate ionic conduction in the membrane and to avoid physical degradation over its extended usage. Cell drying depends on a number of operating conditions including current density, reactant flow rate, gas composition, relative humidity, inlet pressure, and cell temperature. Dry operation will lead to stack performance degradation and eventually, internal leaks. On the other hand, excess water accumulation in the fuel cell might cause water flooding at the cathode region which is also not desirable. Inlet humidities also contribute to liquid water saturation in the fuel cell, which is reported in [90].

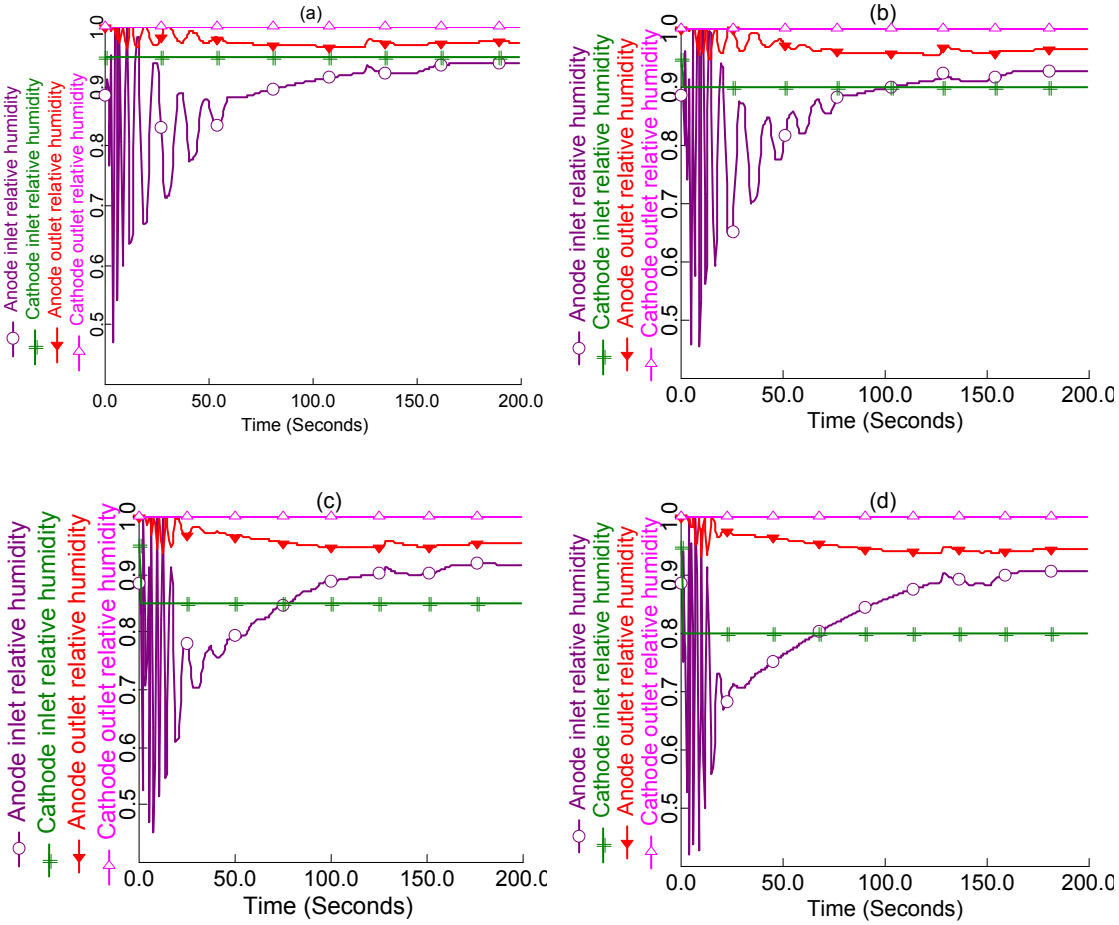

Figure 7.10: Effect of air inlet relative humidity on fuel inlet and outlet: (a) Air inlet humidity of 95%, (b) 90%, (c) 85% and (d) 80% respectively.

As mentioned above, the proposed system in this study utilizes an external humidifier to moisten incoming air, whereas anode side is not humidified. Recirculation of fuel serves the humidification purpose on the anode side of the fuel cell. Here, the role of the inlet relative humidity at the cathode of fuel cell electrodes and its interaction with adjacent flows is discussed and a comparison is presented by a systematic analysis of these results. A constant relative humidity of 95%, 90%, 85% and 80% is selected at a start–up current of 120A for the present simulations. Fig. 7.10 depicts relative humidity states at electrode inlet and outlets respectively. The recirculation stream mixing with anode inlet stream contains approximately 1% liquid water droplets.

It can be witnessed that anode inlet humidity increases from 90% to 94% when cathode inlet air is humidified from 80% to 95%. Similarly, relative humidity at anode exhaust is increased from 95% to 98%. It can be seen that time taken to reach these humidity levels is more when air inlet humidity is kept lower. Since, water is produced at the cathode; it is fully saturated at the outlet of the fuel cell.

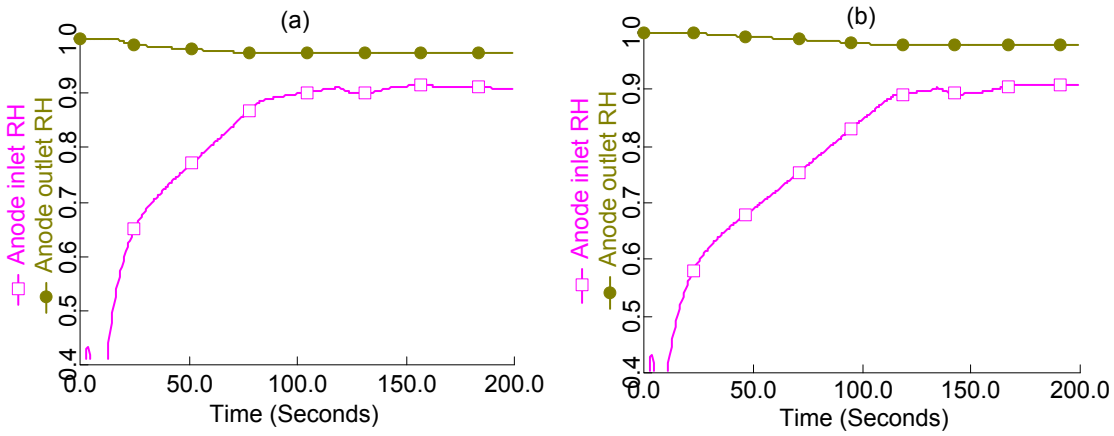

Figure 7.11: Relative humidity of fuel at inlet and outlet: (a) with 1–2% liquid at anode inlet (b) with no liquid at anode inlet.

While liquid droplets are not wanted in anode streams as they could cause water flooding in the stack, they affect the humidity levels in the anode. Figure 7.11 elaborates on the time taken by the fuel cell to reach the maximum humidity levels in the anode side. It can be noticed that the fuel cell reaches maximum humidity levels within 100 s when the anode recirculation stream contains liquid water. On the other hand, in the case where all the liquid water is assumed to be trapped by

the knockout drum, the time required to reach highest humidity increases to approximately 130 s.

7.2.6 Water saturation at cathode

Removal of water from the cathode is dependent on stack temperature and pressure drop. Temperature is the more critical factor, since at high temperatures water will be in the vapour state and easier to remove. Stack water production increases with current and is also dependent on the number of cells. The exact amount of liquid water product depends on the cathode outlet temperature. Figure 7.12 provides information on the amount of liquid water at inlet and outlet of the cathode channel. Fig. 7.12a shows the start–up of the system at 40A. As seen, the amount of liquid water at cathode outlet is around 17 % when stack operating temperature is close to the ambient and lowers to 11% when the stack reaches steady–state at 65°C.

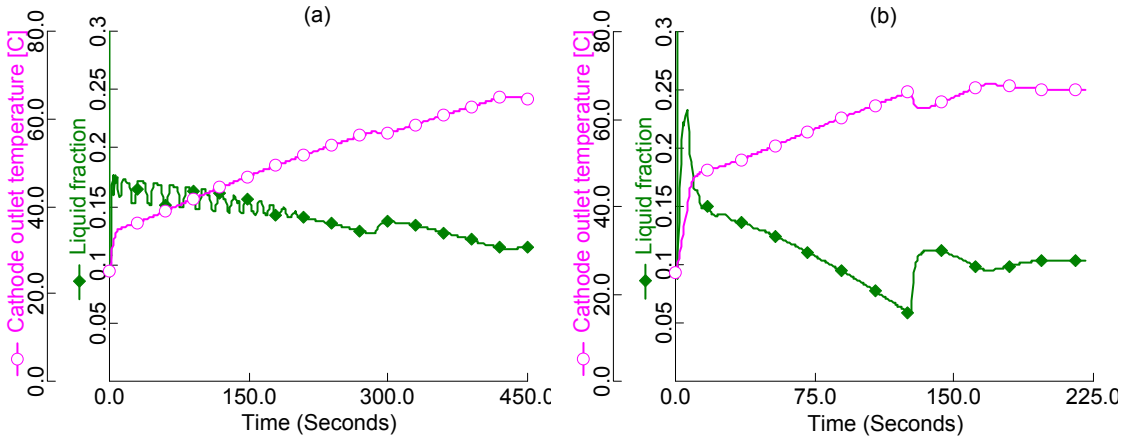

Figure 7.12: Percentage of liquid water at cathode outlet; (a) at start–up current of 40A and (b) at start–up current of 100A.

On the other hand, when the stack is operating at 100 A (Fig. 7.12b), the amount of liquid water percentage at cathode outlet is 23% approximately, which is much higher than the case with 40A start–up. This is because of higher current densities at start–up sequence when the stack temperatures are very low. When higher currents are drawn, reactions within the fuel cell are accelerated which demand more intake of fuel and oxidant. Consequently these reactions produce more water when compared to production at low currents. Since the stack temperature

is low at start–up, higher percentage of produced water is saturated at the fuel cell cathode. At low currents, water removal is the dominant factor and reactant stoichiometries are determined by the minimum flow rates required for water removal which in the present case are more than adequate to provide the necessary concentrations. At steady–state when stack operating temperature is around 67°C, liquid water fraction in the outlet air is determined to be around 11%. Liquid fractions at anode outlet are very low when compared to cathode outlet. They are calculated to be in the range of 1.5 to 2.0 % for both 40A and 100A current scenarios discussed above.

7.3 Summary

This chapter encompassed the dynamic analysis of PEMFC system during start–up sequence. Main contributions of the suggested model are attributed to system response methodology, which incorporates stack thermal behaviour in addition to fuel cell electrochemistry, water crossover, mass and energy balances. It is observed that system efficiency and voltage output are higher at low power start–ups but for the fuel cell stack it takes longer time to reach stable operating conditions. Furthermore, air radiator consumes more power at high currents once the system is stable and due to this fact, system efficiency is reduced. In addition, it is shown that cathode inlet water levels are adequate enough to humidify fuel stream, which is recirculated into the anode. Finally, amount of liquid water in the cathode outlet is considerably higher, at high current density start–ups, while water removal from cathode exhaust requires additional attention at low stack operating temperatures. While high start–up current densities cause issues at cathode, humidity levels increase faster reducing the dry cell operating times.

Chapter 8

Transitory load changes –System Analysis

8.1 Overview

As a power source for automotive applications, PEMFC systems are usually subject to inflexible operating requirements when compared to stationary applications. These systems have to operate at varying conditions related to temperatures, pressures, power load and humidity. PEMFC dynamics are influenced by reactant flows, heat management and water content in the streams as well as within the fuel cell itself. All the auxiliary components, such as air and fuel supply system which include compressors and control valves, and the thermal control system which consists of heat exchangers, coolant pumps and air radiators need to be controlled for optimum operation of fuel cell when the system experiences varying load changes. Understanding the transient behaviour of a PEMFC therefore becomes very beneficial in dynamic modelling of these power modules at a system–level. Most of the studies available in literature focus on transient response of fuel cell stack under different operating conditions; primarily on individual component analysis. Therefore, a need for a control–oriented dynamic system model is identified, which simulates a fuel cell stack under multiple varying operating conditions and changing auxiliary components outputs. Dynamic characteristics of PEMFC are also attributed to the heat management and water transportation, which are critical issues and need to be optimized for efficient operations and improve durability of the fuel cell stack. Investigations for effects of heat exchangers on fuel cell stack performance and water crossover on anode recirculation operations are therefore selected to be one of the primary objectives here.

This chapter aims at analysis and investigation of a complete PEMFC system and studies its transient response to varying load and operating conditions. Effects of

system controls and other components on the fuel cell performance are also investigated. A thermal management strategy has been designed and its dynamic impact on fuel cell stack has been conveyed here as well. Analysis of water crossover in the fuel cell and its impact on anode recirculation operations has been conducted and suitable findings are reported. Moreover, two–phase characteristics of concerning material streams are determined which provide suitable insight to saturated water issues in the fuel cell stack.

8.2 Results and discussion

In practice, the fuel cell is coupled with a battery and load management is attributed to the operational strategy of the two combined. Therefore, external load changes are not directed towards the fuel cell module straight away. The battery acts as a buffer between the fuel cell and the external load, unless under special circumstances when it reaches its lowest charge levels. This is when the fuel cell becomes fully responsible for providing all the external power in addition to charging the battery. Present simulations are carried out without the battery component and load changes are assumed to be for the case when only the fuel cell stack is affected. Results for transitory effects under variable load changes (when a current corresponding to a specific power load is drawn from the stack and varied at any occurrence of time) are discussed below:

8.2.1 Voltage loss during load change

An instance of load change, when current is ramped from 60 A to 100 A at a rate of 20 amperes per second and vice versa, is presented in Fig. 8.1a and its effects on cell voltage are examined. It can be observed that the cell voltage reduces abruptly with current surge and vice versa. This decline in voltage potential at increase of current density is attributed to the cell overpotentials. Fig. 8.1b elucidates the losses that account for the voltage drop in individual cells. When the current is ramped up from 60A to 100A, there is a certain lag between the consumption of reactants and the supply. The time taken by the air blower and fuel valve to provide additional air results in concentration overpotential, however the magnitude of mass transfer loss is not considerably high to be the dominant factor. This is due to the fact that current range of 100A equals current density of 0.35 Acm^{-2}, which is well beyond the region governed by concentration losses.

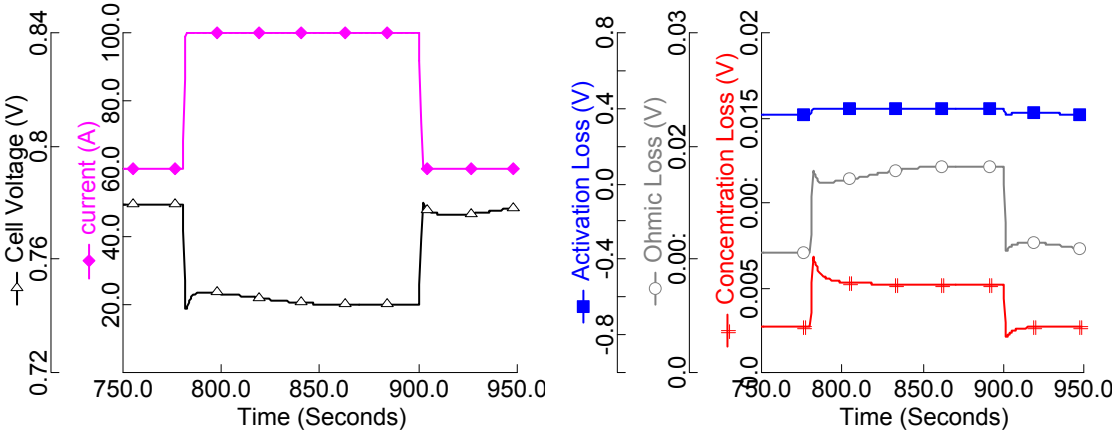

Figure 8.1: (a) Voltage change with stack current, (b) Variation in overpotentials at transitory change of 60–100–60A.

It can be similarly observed that ohmic losses also increase with current density. At the current ramp–up, the ohmic overpotential surges, however it can be noticed that it decreases slightly and then gradually increase to become stable. Actually, this is because of the temperature dependency of membrane ionic resistance. Effect of operating temperature is further discussed in detail in the proceeding section.

8.2.2 Thermal management of the system

Besides current density, cell voltage is also a function of operating temperature and pressure. Since, pressures of the reactants are already regulated; here we will discuss temperature dependency of developed potential differences in the cell. Voltage increases with the elevation of operating temperature. This is due to fast reaction kinetics at the electrodes of individual cell sites when operating at higher temperatures. At the same instance of current ramp as more current is drawn; more heat is produced by the reactions at cell sites, thus elevating the stack temperature. Consequently, the voltage also increases after the initial dip and follows the decreasing profile with the stack temperature as it is controlled towards the desired operating temperature. The opposite could also be observed when the current is reduced back to 60A.

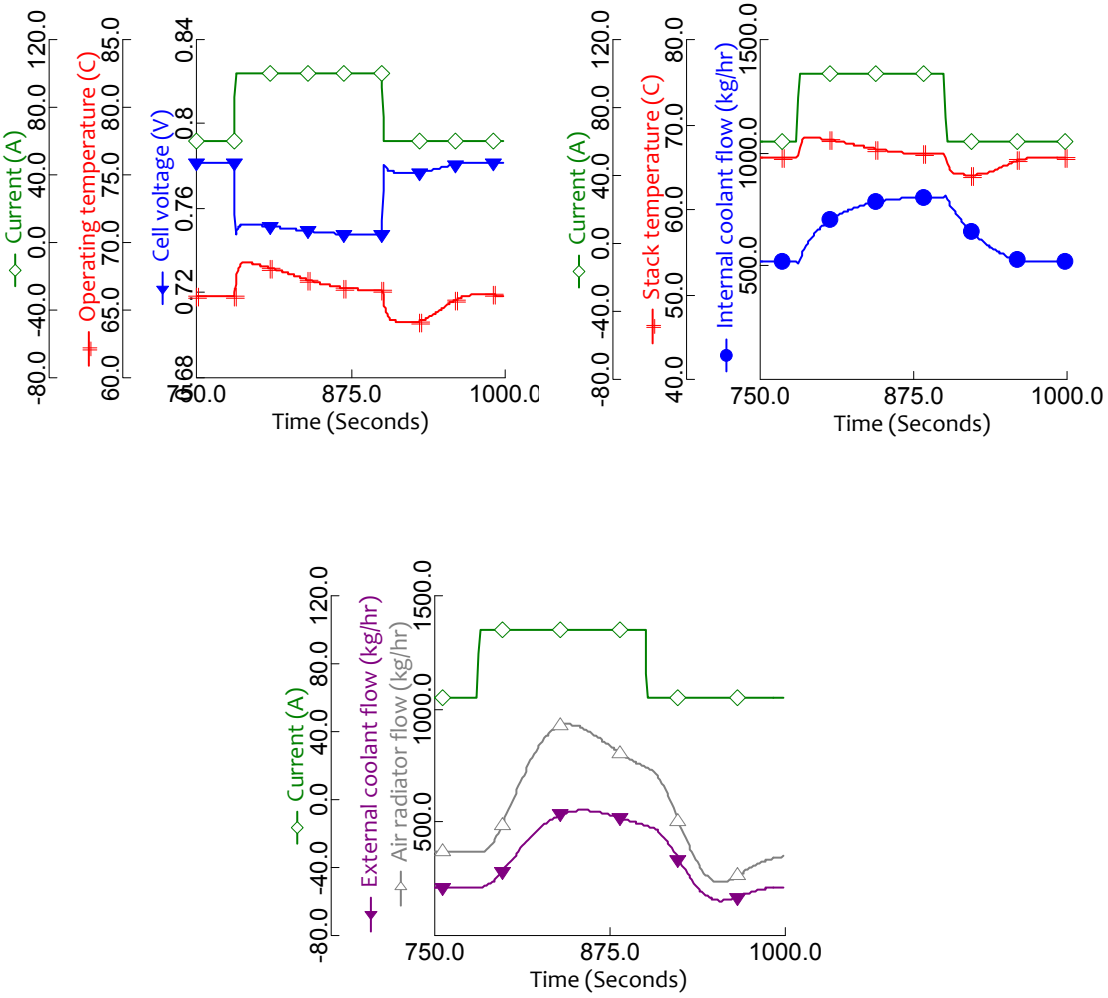

Figure 8.2: Current ramp–up from 60–100A and vice versa: (a) Changes in cell voltages and operating temperature, (b) Changes in coolant flow rate to maintain the fuel cell operating temperature, (c) variation in external cooling flows and air radiator.

Since, temperature affects the voltage and overall system efficiency, it becomes important to have a stable operating temperature and therefore an efficient thermal management system. Figure 8.2b shows the variation in coolant flow rates with temperatures. Similarly, it can also be seen in the Fig. 8.2c, that coolant flow rates in both cooling circuits and an air radiator maintain the temperature of the stack, though it is very slow compared to the reaction kinetics affecting the stack voltage. Thermal control strategy and regulation of air radiator, internal and external cooling circuits has already been detailed in chapter 4. Ramping of current increases the operating temperature of stack thereby actuating controls to contemplate this increase. Flow in the internal cooling circuit, which is coupled with the fuel cell stack is increased to extract heat and maintain the desired

temperature difference between the stack inlet and outlet. Flow in the external cooling circuit is pumped up to retain the inlet temperature to 60°C. Air flow in radiator is also increased to maintain temperature of external cooling loop around 50°C by rejecting the heat to the surroundings. Rate of coolant flows in respective streams is associated with the power consumed by coolant pumps and air radiator which ultimately affects the overall system efficiency. It is also observed that air radiator being a liquid–gas heat exchanger has the slowest reaction time out of the three. Since temperature controls are slow compared to electrochemical reactions, overall thermal control strategy has a fair impact on stack voltage which undergoes frequent load changes.

8.2.3 System efficiency and power consumption

As can be seen in the Fig. 8.3a, when the stack current is altered from 60A to 100A, there is a reduction in system efficiency, mainly due to the associated voltage drop. Overall efficiency of the system is as much affected by air blower and radiator fan, as by the fuel cell stack itself. It can be observed that power produced by the stack increases with current drawn. Also, power consumed by auxiliary components increases, thereby reducing system efficiency from 55.5% to 50%. Once decreased, there is an abrupt rise in efficiency due to increase in voltage and it fluctuates at around 50% mark due to slow temperature controls and fluctuating power consumption by air radiator.

Figure 8.3b displays the power generated by the fuel cell stack and consumption of BoP components. Auxiliary power consumption is around 11–16% of the power produced. Fig. 8.4a elaborates on power consumption in the air supply. Being a major consumer in the system, power consumption of air blower rises with increase in current and this incremental profile can be associated to the increased mass flow of air required to maintain oxidant stoichiometry in the fuel cell. After the initial rise, power consumption of air blower becomes constant; however the consumption graph of air radiator takes more time to become stable (Fig. 8.4b). This is due to the fact that flow in air radiator is manipulated to control the temperature and is a slow process. Together, air blower and radiator consume 10% to that of stack power, whereas a coolant and recirculation pumps account for 1.0–1.3% when operating at 60A.

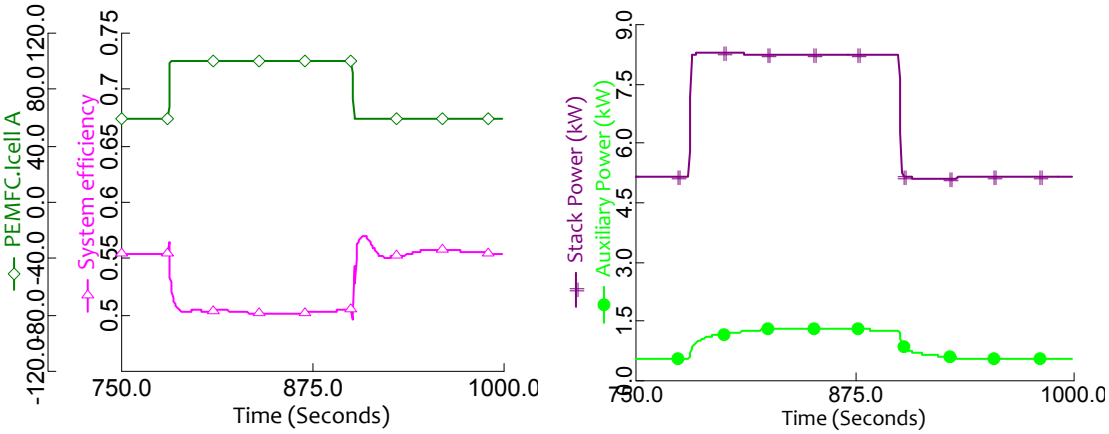

Figure 8.3: (a) System efficiency variation with load change, (b) stack power output and auxiliary power consumption.

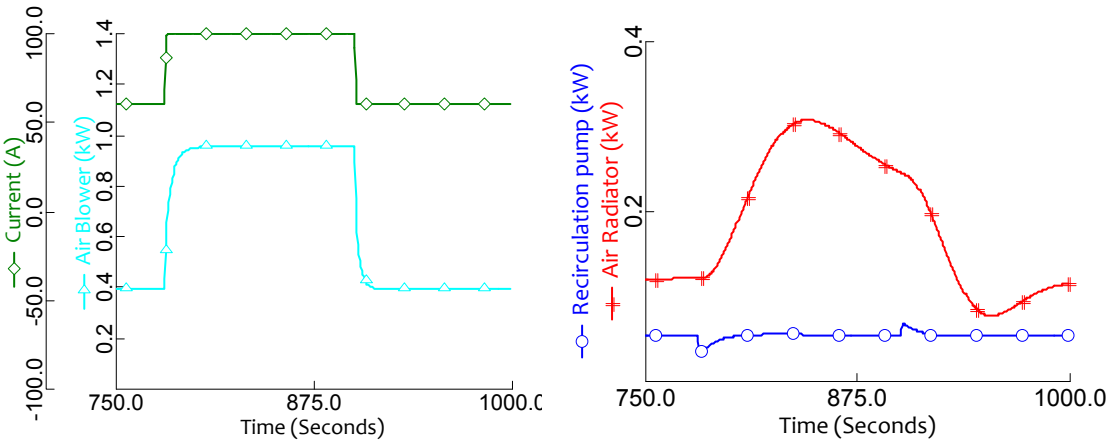

Figure 8.4: Auxiliary power consumption versus current; (a) Air blower power, (b) Air radiator and recirculation consumption.

Whereas, at higher currents of 100 A, power consumed by air blower and radiator constitutes 15% of the total stack power. For a swift temperature control and a thermally stable operation, air radiator requires more power or a larger heat exchanger area which would further reduce efficiency during these load variations. Power consumption of coolant pumps is not shown in the above figure because increase in internal and external coolant flows affects the auxiliary power consumption to a very small extent as compared to air compressor and radiator. Anode recirculation pump also consumes very low power; however the peaks at current surge are a noticeable detail, which is addressed later in the results.

8.2.4 Water management during load changes

In PEMFCs, water management is a fundamental issue since the performance of fuel cell is strongly influenced by its internal water distribution. Figure 8.5a shows net water diffusion in the cell when current is changed from 60A to 100A and back. In the figure, positive values for water crossover designate transportation of water from cathode to anode of the fuel cell and vice versa. With increasing currents, more water is produced in the cathode which supports back–diffusion towards the anode until the system reaches back to steady–state and there is almost no net water crossover. Some negative peaks are also observed at the start of current change, which are due to electro–osmotic drag. As more current is drawn, there is a rapid increase in hydrogen ion flux towards the cathode, thereby supporting water crossover through electro–osmotic drag. Back–diffusion rate is increased with the production of water on the cathode side and subsequently water flux is directed towards fuel cell anode. The reverse can said to be true when current is ramped down from 100 A to 60A.

Effect of water distribution can also be observed in anode inlet and outlet relative humidity. Whereas for the cathode, since it is assumed that air enters at a constant relative humidity of 95%, the outlet humidity is always above 100%. Therefore, results for only anode are discussed here.

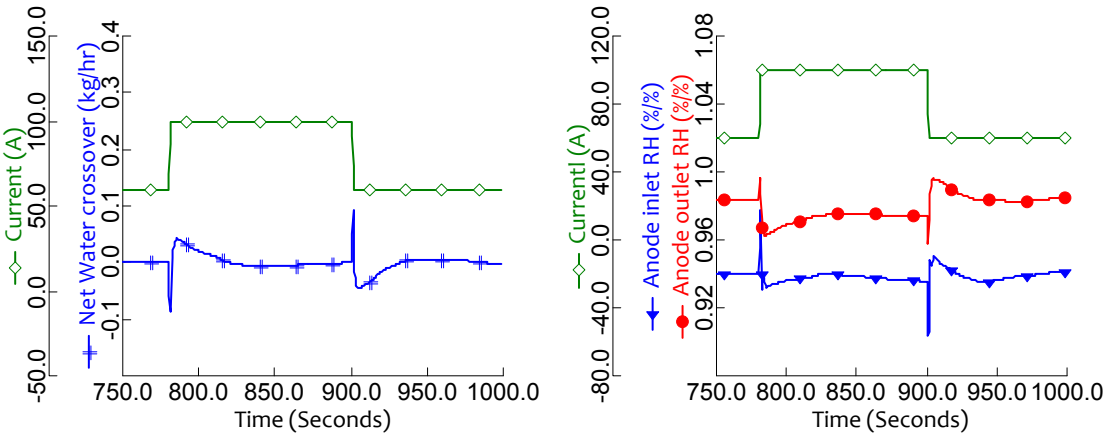

Figure 8.5: Current ramp–up from 60–100A and vice versa: (a) Water crossover through PEMFC membrane, (b) Effect of water transportation on anode RH.

From Fig. 8.5b, it could be further observed that relative humidity at anode outlet decreases with a current surge, though an abrupt increase is detected at the start of this change. Sudden ramping of the current consumes more hydrogen, leaving higher molar fraction and partial pressure of water in the anode, thus the peak of high relative humidity. With the rise in stack temperature, water activity on anode side is reduced and water diffusion from cathode increases and consequently stabilizes to almost zero net–water crossover with the control of operating temperature. Factors contributing to the water crossover in the membrane are elaborated in Fig. 8.6. The membrane water content, which is the measure of amount of water per sulfonic group in the membrane, is a function of water activity in the anode and cathode of the fuel cell. Since, the air entering the cathode is humidified and contains additional water produced during cell reactions; it is close to the maximum. Here, the average water activity at cathode is not exactly 1, as the humidity levels at the inlet are around 95%. On the other hand, water activity at the anode reduces with the increase in current. This raises the gradient for back diffusion from the cathode towards the fuel cell anode. Fig. 8.6b depicts the average membrane content and back diffusion coefficient for water transportation across the membrane. The diffusion coefficient is a function of temperature as well as water content (see Eq. 5.39 and 5.40). As the membrane water content is linearly stable, the diffusion profile inclines more towards the cell temperature variations. The transportation phenomena in the fuel cell become fairly complex with co–dependence of many parameters on temperature and hydration of the membrane.

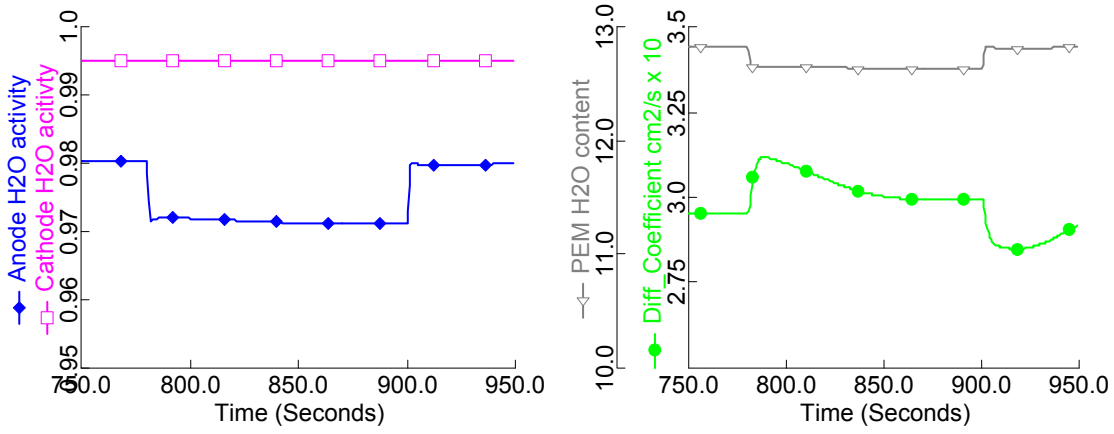

Figure 8.6: Current ramp–up from 60–100A and vice versa: (a) Water activity in fuel cell, (b) Back diffusion coefficient for water in membrane.

Water removal from a fuel cell cathode is also dependent on stack temperature and pressure drop. Temperature is the dominant factor of the two, and the amount of saturated water depends on the cathode outlet temperature. Inlet humidity also contributes to liquid water saturation in the fuel cell, as reported in Wong et al. [90]. Figure 8.7 provides information on the amount of liquid water at outlet of the cathode channel for two different current surge amplitudes.

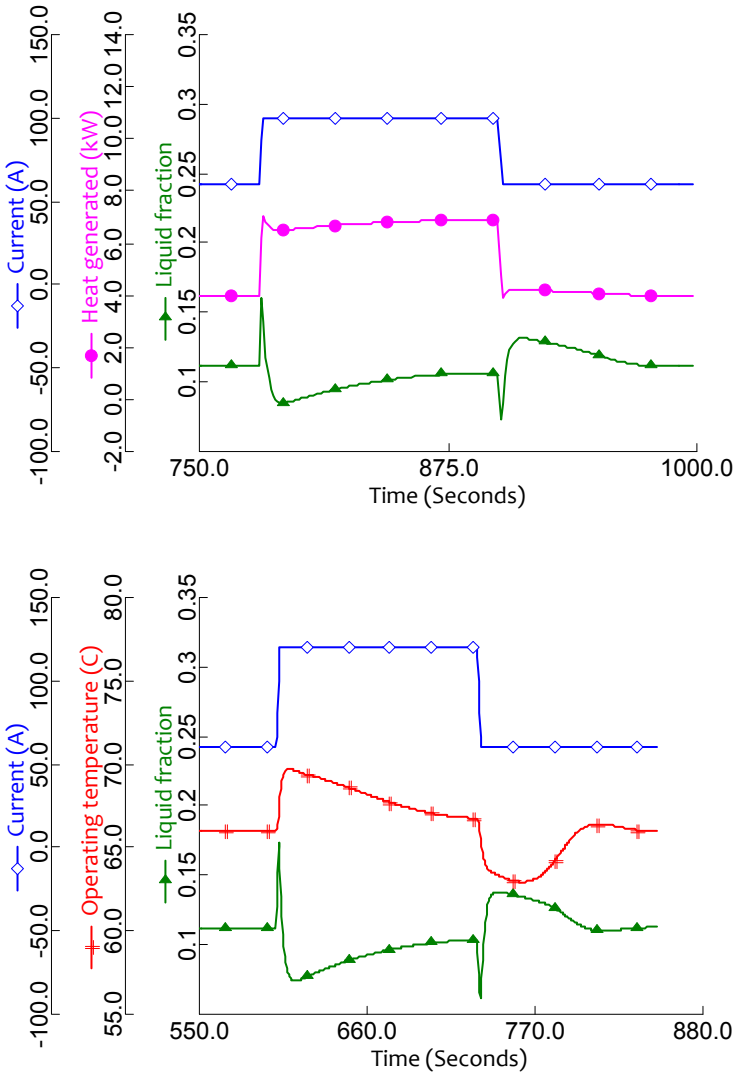

Figure 8.7: Liquid water at cathode outlet; (a) Current ramp–up from 60A to 100A and vice versa, (b) Current ramp–up from 60A to 120A and back.

It can be seen in Fig. 8.7a, that there is an abrupt increase in amount of liquid water at cathode when the current is ramped from 60A to 100A. When higher

currents are drawn, reactions within the fuel cell are accelerated which demand more intake of fuel and oxidant. Consequently these reactions produce more water when compared to production at low currents. Since the stack temperature does not elevate till that instance, higher percentage of produced water is saturated at fuel cell cathode. Heat produced by cell reactions then elevates the stack temperature, thereby reducing saturated water at the outlet. Moreover, condensation of water at cell sites produces additional heat which rapidly increases the stack temperature. It can be further noticed in Fig. 8.7a that heat produced in the stack lowers as water liquid fractions drop. On the other hand, when current is reduced back to 60A, a similar but opposite profile is observed and the amount of liquid water tends to increase with a sink in stack temperature. Therefore, at low temperatures and currents, water removal is a dominant factor and stoichiometries are determined by the minimum flow rates required for water removal which in the present case are more than adequate to provide the necessary concentrations. Figure 8.7b shows water saturation results when ramping of current is set from 60A to 120A instead. Although the data profile is analogous to that of Fig. 9a, it is noted that amplitude of these peaks is higher when compared. Apparently, the amount of liquid water at cathode exit is same for both cases when the fuel cell is operating at steady state. Heat produced by condensation requires additional flow of coolant to maintain stack operating temperature, yet it does not affect the system efficiency to a greater extent as liquid pumps do not consume that much power. As there is no external humidification apparatus for fuel and recirculation of anode exhaust aides in humidifying the anode, water crossover has a significant impact on anode operations which are discussed below.

8.2.5 Stream properties at fuel cell ports

Figure 8.8 depicts the variations in reactant inlet flows when the load on fuel cell is varied. It is interesting to notice the fluctuations in the anode inlet and outlet. When the current is ramped up from 60A to 100A, more hydrogen is consumed increasing the utilization factor at that instance. This can be seen in Fig. 8.8b where mass flow at anode exhaust suddenly decreases. Changes in temperature can also be noted at these current surges as the air stream is cooled by external cooling circuit. Control of fuel stoichiometry takes some time to readjust to the desired level. Although, anode outlet flow is disturbed by fuel stoichiometry, it is also affected by the water content in anode outlet (70% mass fraction), which depends on the net water crossover within the cell. Initial peaks at both load changes are also attributed to the electro–osmotic drag which is a function of current density. Since anode inlet is supported by recirculation from anode exhaust, the changes within the stack influence it considerably. In Fig. 8.8a, fuel flow at anode inlet

follows a similar trend to that of anode exhaust, as well as the inlet temperature. Rapid reduction in temperature is due to lower volume of recirculation which is at around 69°C whereas dry hydrogen from the tank is at 25°C. Fluctuations in water content at anode inlet disturb fuel flow controls and relative humidity constantly; they remain within acceptable ranges however. Figure 8.8c shows the fuel stoichiometry changes and power consumed by recirculation pump, which are affected by the depletion of hydrogen at anode cell sites and water diffusion during the current surges.

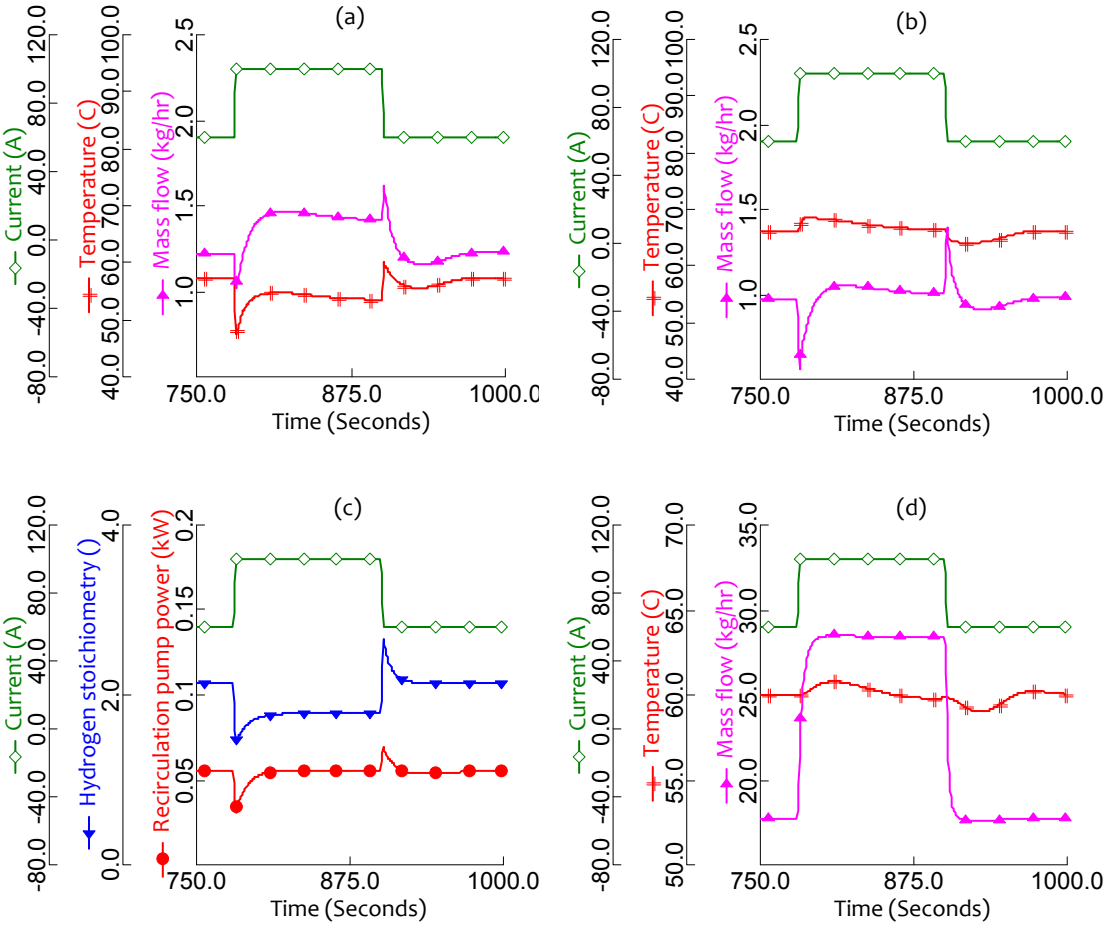

Figure 8.8: Current ramp–up from 60–100A and vice versa:, (a) Stream properties at anode inlet and (b) outlet respectively, (c) Effect on fuel stoichiometry and recirculation pump, (d) Air flow into the cathode.

On cathode side (Fig. 8.8d), as expected, the air flow which is regulated by a controller increases when the current is ramped up and steadies along with the system. There is no specific temperature control of inlet air in this model, though external coolant flows manipulate the air temperature which is further preheated

by the humidifier before entering the stack. Air temperature varies around 60°C which is equal to the controlled temperature for coolant entering the stack; however temperature difference at anode inlet is significantly higher during these load variations. Such temperature gradients incur adverse effects as they form thermal stresses in the stack with co–flow configuration and reduce its life cycle.

8.3 Summary

Main contributions of this chapter are ascribed to the dynamic system responses to the transitory load changes, which is characterized mainly by heat management and water transportation within the fuel cell. It is observed that thermal management strategy greatly influences voltage output and system efficiency which increase with stack operating temperature. Power consumed by liquid coolant pumps is minimal and have no considerable effect on system efficiency, whereas air radiator consumes most of the power in thermal management system. A 5% increase in power consumption of air blower and radiator is observed during load variations for the cases presented here. Furthermore, water crossover in the fuel cell has shown a significant impact on PEMFC anode operations. Anode inlet flows, humidity and recirculation pump are influenced by net water diffusion during load changes. Temperature changes at anode inlet are considerably higher during load variations and have a negative impact as they generate thermal stresses in the stack and reduce its lifetime. Also, amount of saturated water at cathode is dependent on operating temperature which apparently pertains to thermal management strategy of the system.

Chapter 9

Nitrogen crossover & anode purging methodologies

9.1 Premise

In a typical PEMFC, hydrogen is fed into the anode of the fuel cell stack and oxygen/air into the cathode, while the water produced from cell reactions is ejected out of the cathode outlet. Since the current generated in the fuel cell is directly attributed to the rate of electrochemical reactions i.e. the number of electrons dispatched per mole of hydrogen at anode and the number of moles of oxygen for reduction at cathode, power produced by the stack is associated to the rate at which the fuel and oxidant are supplied. Ideally, all of the hydrogen and oxygen needed for any specific power of the fuel cell stack would be consumed and only water and unused nitrogen of the air would leave the system. However, not all hydrogen and oxygen delivered at the reaction stoichiometry reaches the cell sites which can cause fuel starvation, leading to irreversible damage to the stack in addition to a lower power output [65]. Therefore, higher stoichiometries of reactants are fed into the system. In most systems, the unused hydrogen exceeding the fuel stoichiometry is recirculated back into the feed stream, which serves in humidification of the fuel and also increases the system efficiency.

As already mentioned, one of the benefits of PEMFCs is their high power density which is essential for portable applications. Recent advancements in manufacturing have made these stacks more compact by significantly reducing the thickness of MEA, though it enhances gas crossover across the membrane resulting in current losses within the fuel cell itself. One of these gases is nitrogen from the air, which permeates from the cathode to anode and gets concentrated in the anode due to recirculation. Similarly, water produced on the cathode side is also transported towards the anode through the membrane. This build–up of nitrogen and water reduces the concentration of hydrogen in anode channels and obstructs

hydrogen molecules to reach cell reaction sites effectively, which adversely affects the voltage developed in the cell [44], [48] . Also, H_2 starved areas are developed within the fuel cell which can also result in carbon corrosion [91], [92]. Furthermore, additional flow of these crossed over gases increases the power consumption of recirculation pump, thereby adding to the efficiency loss due to the voltage drop. In most systems with anode recirculation, N_2 build–up is usually avoided by frequently purging a certain percentage of the anode outlet gas before mixing it with the inlet stream. An alternative approach is to continuously bleed a small fraction of the recirculation stream. While both mentioned approaches release some portions of nitrogen as well as water vapour from the recirculated stream, it also purges unused hydrogen. In this context, the amount purge fraction and time intervals of these purging techniques are of particular interest to the authors. An optimum strategy would cease the build–up of N_2 with a compromise of minimum H_2 wastage. Although, there are a few publications dealing with nitrogen crossovers and associated purge processes, but to the best of authors' knowledge, there is no available study on intricate details of nitrogen crossovers and the effect of purge cycles on the fuel cell performance during transient operations.

This chapter covers the dynamic characteristics of the PEMFC system operating with purge cycles, and investigate its performance during transitory load changes. N_2 accumulation in fuel cell anode and its effect on system performance is investigated, and in view of this buildup, different purging strategies are assessed. At last, an alternate method for nitrogen detection and automatic purging is proposed and compared with conventional methods during different stages of external load changes. This model could be regarded as a basic foundation in design and optimization of purge cycles for automotive systems running PEMFCs.

9.2 Simulation results and discussion

Using the PEMFC stack data and control parameters summarized in chapter 4, simulations for the system are carried out using Aspen Dynamics program. Reliability of the fuel cell model and dynamic behaviour of the system under consideration have already been reported in authors' previous studies [93], [94] and [95]. These studies have reported transient response of different components of the system as well as their mutual dependencies on control strategies, thermal management and water transportation of the fuel cell stack under different operating scenarios; such as system start–up and during transitory load changes. Here, simulation results for the effect of nitrogen crossover and associated purging

of anode recirculation are presented. Stack temperature range of 60–70°C has been used in simulations of the current system.

9.2.1 Gas Buildup at anode

Based on the permeability of N_2 and partial pressure gradient across the membrane, simulations for the prescribed system were conducted and corroborated against validation data by stack manufacturer [62]. Fig. 9.1 presents the simulated net nitrogen crossover in the fuel cell stack against the provided experimental data. The corresponding relative error advocates a reasonable agreement between the simulations and stack trial data.

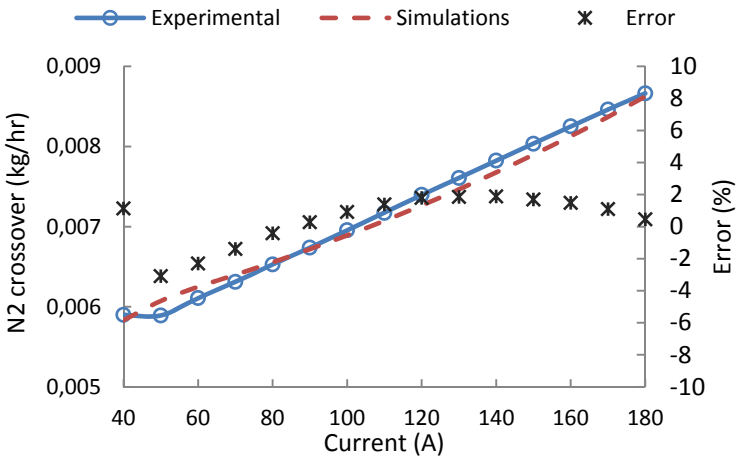

Figure 9.1: Calculated nitrogen crossover rates against provided experimental data.

Current drawn from the fuel cell is set to a constant 120 A with no purging of the anode recirculation loop. Since pure H_2 is used as the fuel, there is no presence of nitrogen in anode inlet of the fuel cell at the start–up. Fig. 9.2a shows the N_2 crossover from the cathode to anode side of the fuel cell during the start–up operations of the stack. It is observed that as the temperature and water uptake of the membrane increases, N_2 permeance increases, thereby increasing nitrogen crossover from the cathode to the anode side of the cell. An abrupt decline in temperature is noticed at around 120 s, which is due to the control initializations of coolant flows to maintain the stack operating temperature. Details of the control setup and thermal management of the system are reported in [93]. N_2 permeance decreases with the sudden reduction in temperature and subsequently reducing the crossover at that instant of time. However, as the system stabilizes to steady state, the permeance becomes constant but N_2 crossover tends to decrease as

can be seen in Fig. 9.2b. This is due to the fact that N_2 accumulation in the anode reduces the concentration gradient across the cells.

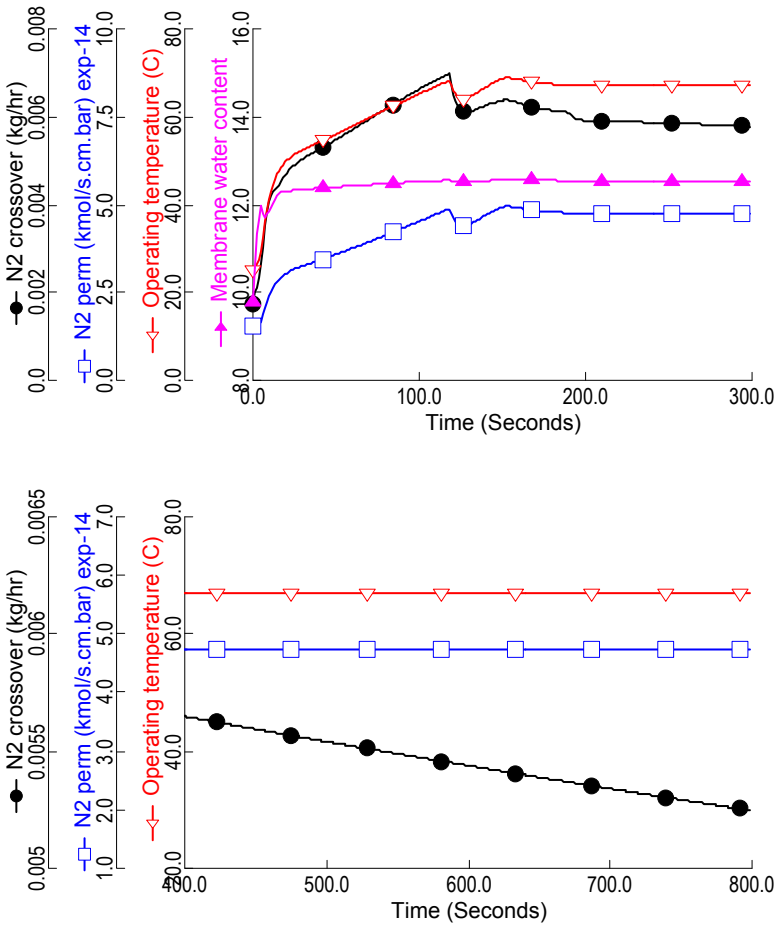

Figure 9.2: N_2 permeance and crossover rate at (a) fuel cell start–up and (b) Steady–state operations.

Depletion of hydrogen in the anode due to nitrogen accumulation leads to a slow decay of the cell voltage. Fig. 9.3a represents the voltage decay due to increase in N_2 fractions and corresponding decrease in H_2 concentrations in the fuel inlet. Although voltage decay shows a linear relation with nitrogen accumulation, its impact over extended operations results in hydrogen starved regions in the cell resulting in increased cathode overpotential and resistive losses [60]. Another issue related to anode recirculation is the accumulation of water, which clogs flow fields and results in lower concentrations of H_2 as well. Fig. 9.3b points to the gradual increase in liquid water at anode outlet.

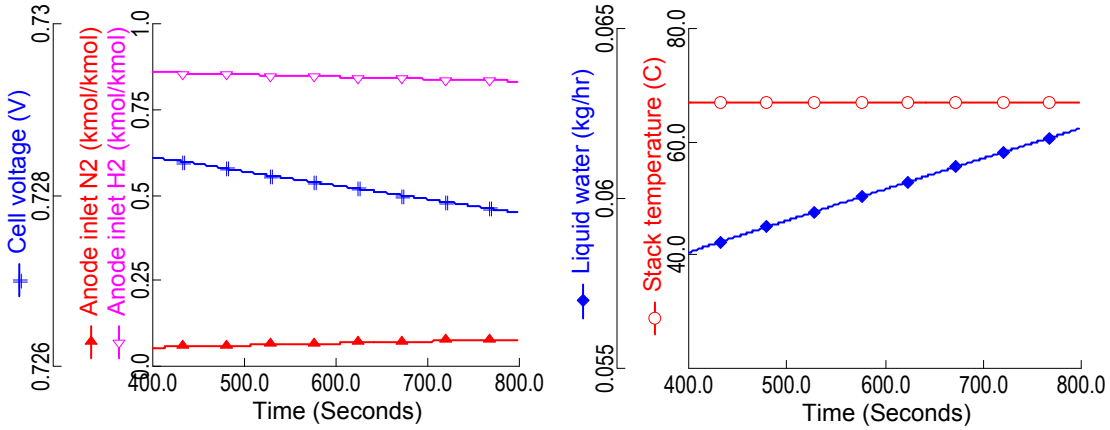

Figure 9.3: (a) Cell voltage decay due to N_2 buildup and (b) Increment in liquid water at anode exhaust.

9.2.2 Anode outlet bleed

As shown above, N_2 accumulation could lead to dilution of hydrogen in the fuel. Moreover, power consumption of recirculation pump increases due to additional flow of nitrogen and water vapour. One way of preventing accumulation of these gases is venting of anode exhaust often called as bleeding. Figure 9.4a presents different percentages of anode bleed and nitrogen accumulation at anode inlet.

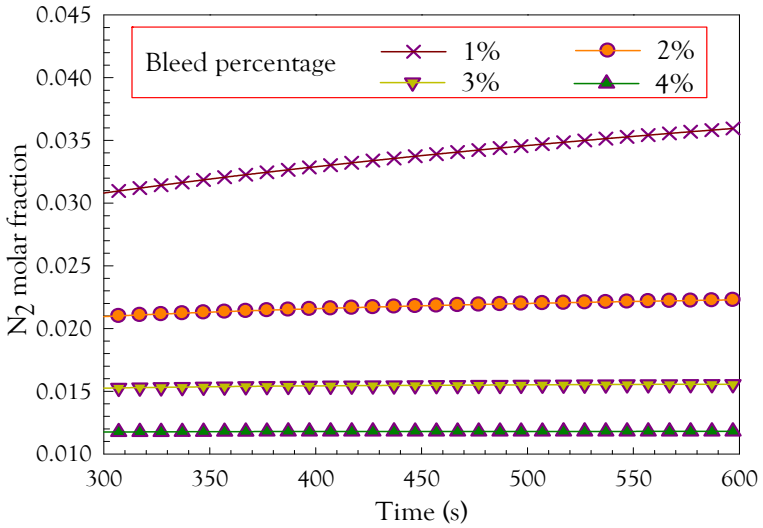

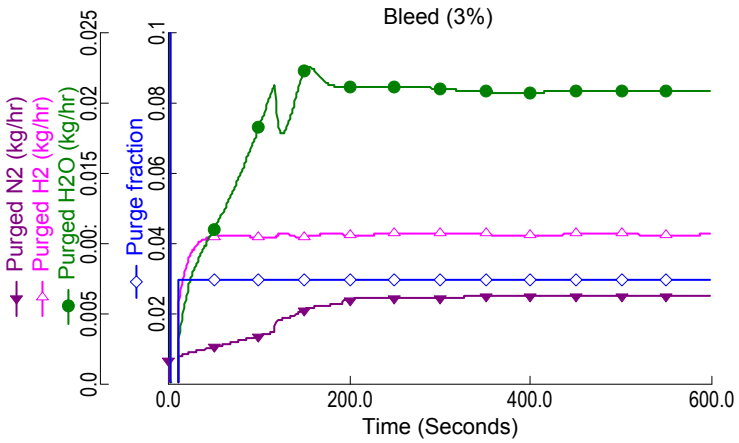

Figure 9.4: (a) N_2 levels for different bleed fractions at anode inlet and (b) Composition of bleed stream from system start–up.

It can be seen that N_2 keeps on increasing when the vent out fraction is 1% and remains constant around 3% of the anode exhaust. At this bleed rate, molar N_2 remains close to 1.5% of the fuel entering the stack. Fig. 9.4b shows the constituent flow rates of 3 % vented stream. A large amount of water is also vented along with nitrogen. A constant loss of hydrogen at a rate of 0.011 kg/hr (2% of the supplied fuel) would suffice to prevent gas accumulation in anode of the PEMFC.

9.2.3 Anode outlet purge

A purge of the anode recirculation is another method to reduce nitrogen and water levels in the fuel inlet. A purge is initiated by opening of a solenoid valve placed at the anode outlet. This valve opens for a short duration (purge time), removing a portion of gases in the stream. The time between these purges is referred to as purge interval. Though any combination of these could be assumed, here arbitrary values of 0.6s, 0.3s, 0.9s and 60s of purge valve opening time, opening duration, valve closing time and purge interval are selected respectively. Here, a steady state analysis is conducted by drawing a current of 120 A and the valve opening is set to purge 20% of the exhaust stream. Modelling of the valve and its pressure effects have been neglected here as it falls out of the scope of study. However, [53] have studied the behaviour of pressure during purge process and reported a uniform distribution of pressures for short purge times as used in current simulations. In addition, it is reported that fluctuations in anode pressure due to frequent purging, also supports liquid water removal from the channels.

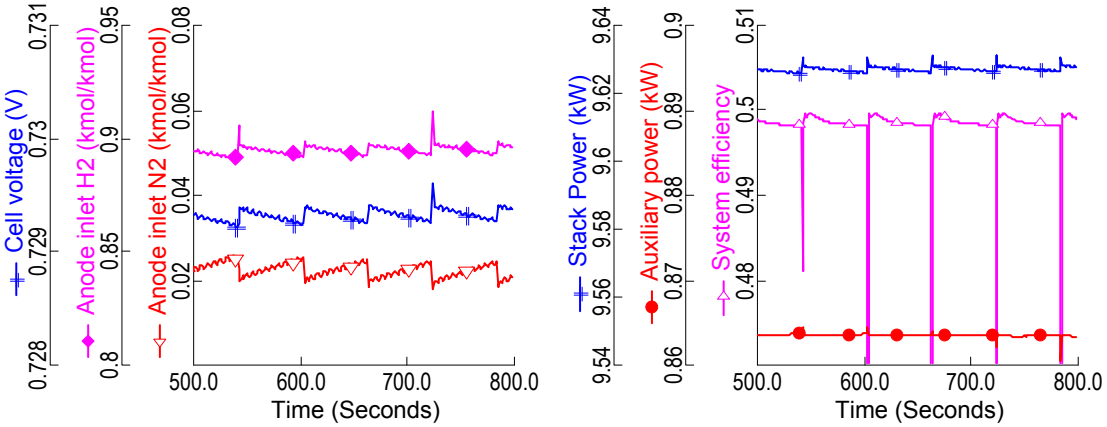

Figure 9.5: Performance of Fuel cell for fixed purge interval of 60 s; (a) Voltage rejuvenation with semi–stable profile and (b) system efficiency and power during purge sequences.

Fig. 9.5a shows a semi–stable cell voltage during these purge events. As soon as the purge is initiated, it removes both liquid water and nitrogen gas and recovers the voltage drop caused by reduced active cell sites. N_2 and H_2 fractions could also be noticed to change with each purge. During the purge intervals, there is a steady buildup of nitrogen which gradually decays the cell voltage which lowers the efficiency. This can be seen in Fig. 9.5b where efficiency of the system increases with each purge and slowly lowers before the next purge event. It is also noticed that there is an abrupt decline in the system efficiency at purge instances. This is due to the fact that unused hydrogen leaving the purge valve reduces the recyclable amount, thus these drop lines. Change in power consumption of auxiliary components is minimal as only low–power recirculation pump is affected by the purge. Since the total purge time is only 1.8 s and purge interval is 60 s, it is cumbersome to determine the average efficiency lost for long durations of fuel cell operations. Nonetheless, amount of H_2 vented to the atmosphere could be determined to assess the economics of the operations. Fig. 9.6 explicates that around 0.08 kg/hr of H_2 is wasted per purge event with interval of 60 s, which accounts for 1.2% of the total fuel supplied to the system.

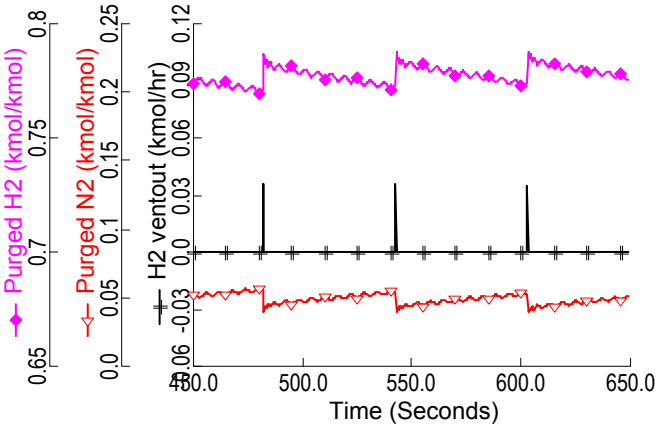

Figure 9.6: Molar fractions at purge routines and H_2 vent out rate.

9.2.4 Automatic Anode purge

As mentioned earlier that in addition to reducing the fuel cell voltage, enrichment of nitrogen could lead to corrosion of the electrodes. With the ageing of the cell membrane it tends to get thinner and due to the degradation, micro cracks and pinhole regions are generated which further increase N_2 crossover. Another approach simulated in the present investigation is the use of an automatic control for optimization of purge intervals. For practical diagnosis of fuel cell systems, nitrogen at anode inlet could be detected by arc emission spectroscopy methods. Signal from these detectors is transmitted to the controller, where it adjusts the parameters for effective purges. An optimum purge sequence would prevent N_2 buildup at a minimum expense of released hydrogen. Optimization of the purge routine could be carried out by manipulation of many variables such as valve opening and closing times, purge time, purge interval and purge stream fractions. Simulations for different combinations of these variables for different power loads would require tremendous amount of time and effort. For the sake of comparison purposes, only purge intervals are chosen to be the manipulated variable in the present simulations.

According to [62], molar N_2 fraction of 5% or less has no or minimal effect on stack life. A purge initiation limit of 3% has been set i.e. the purge event will occur only when N_2 molar concentration of 3% or more is detected at anode inlet. Simulations for two different currents are carried out here. Voltage recovery and efficiency profiles for automatic purging are found to be similar to that of fixed time interval as the purge process is same. However, N_2 crossover in the cell changes with current density as reported by [44]. Typically N_2 crossover increases

with current density, as more heat is produced to raise the temperatures and increase nitrogen permeance. Yet in a system such as the one under investigation, system controls maintain the temperature of the stack and prevent excessive gas crossovers. Also, stoichiometric ratios of anode determine the flow rate of supplied H_2 and are inversely proportional to the N_2 concentration in the anode exit stream [47].

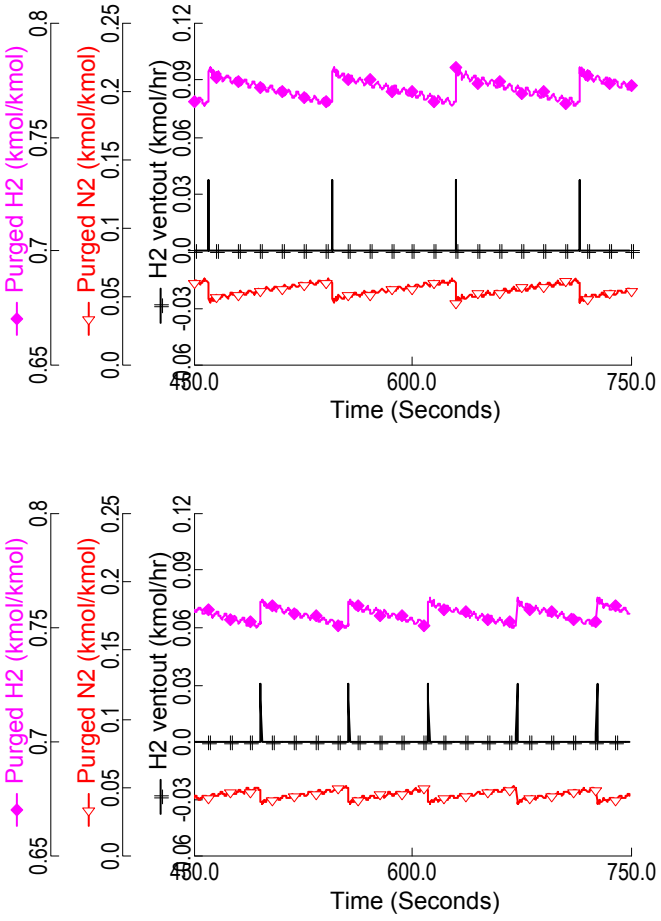

Figure 9.7: Automatic purge intervals and corresponding molar fractions of purges stream; (a) at drawn current of 120 A, and (b) 60 A.

Figure 9.7a shows N_2 and H_2 levels in anode recirculation after purging and corresponding flow rate of hydrogen purged to the atmosphere. When the current drawn during steady state operation is 120 A, H_2 is purged at a rate of 0.08 kg/hr, similar to the rate at fixed interval purge in Fig. 9.6. However, automatic purging interval is found to be around 85 s, saving 15 s per purge. In Fig. 9.7b, when the

current is drawn at 60 A, H_2 purge rate is reduced to 0.06 kg/hr and purge interval is found to be 55 s. This is due to the fact that H_2 flow rate at a low current density is relatively smaller compared to that at a high current density, so is the anode exit flow rate. Therefore, low currents will result in a high N_2 levels in the anode exhaust which will require frequent purging. Fuel losses associated with these purges are reduced to 0.8% of the total fuel being fed to the system. Based on the data from table 3.1, higher stoichiometric ratios are used at low currents.

9.2.5 Anode purge at load changes

PEMFC systems have to operate at varying load and operating conditions when used in automotive applications. Nitrogen concentration would vary with changing loads which requires an efficient purging strategy to cater these dynamics. For this particular simulation, current load is changed from 120A to 60A and vice versa at 380 s and 410 s respectively. Results for different purging methods are presented in Fig. 9.8 and Fig. 9.9.

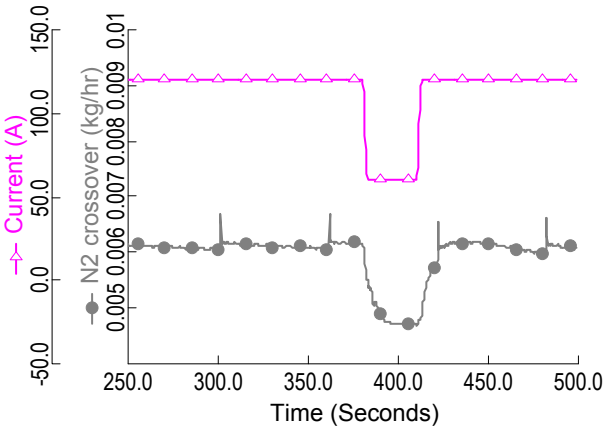

Figure 9.8: N_2 crossover through membrane for fixed purge interval routine during load changes from 120A to 60A and vice versa.

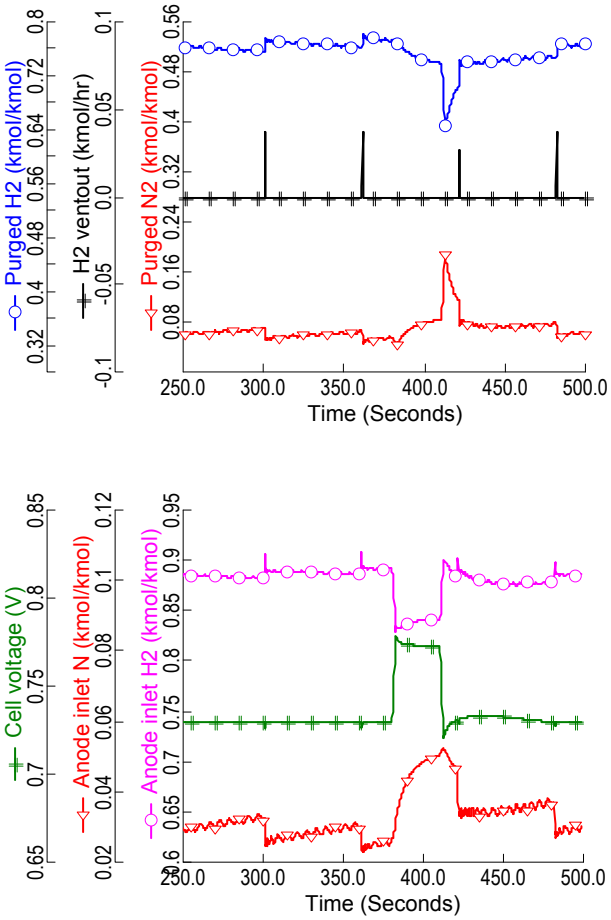

Figure 9.9: Effect of load changes of 120–60–120 A on fixed purge interval; (a) H_2 purge rate (b) N_2 concentration at anode inlet and cell voltage.

Fig. 9.8 portrays nitrogen crossover during the load changes for a fixed purge interval of 60 s. As the current is decreased, nitrogen flux towards the anode is reduced. N_2 concentration at anode exit also decreases as shown in Fig. 9.9a. However, N_2 levels at anode inlet tend to increase (Fig. 9.9b). As explained above, this is attributed to the low residual flows of H_2 at low current densities. On the other hand, when the current is elevated to 120A at 410 s, sudden shortage of H_2 is observed until the time taken by flow valves to adjust. Reduced stoichiometry of hydrogen results in N_2 concentration spike as well. Voltage change as a function of current density is evident in the figure, though voltage revival during purges is not that pronounced.

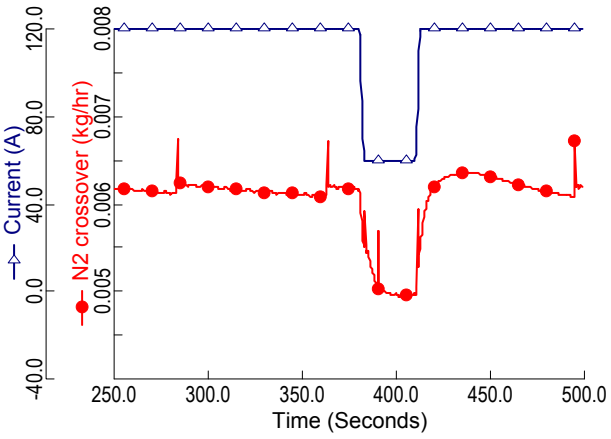

Figure 9.10: N_2 crossover through membrane for automatic purge interval sequence during load changes from 120 A to 60 A and vice versa.

Effects of load changes to the nitrogen crossover and system performance during automatic purge are reported in Fig. 9.10. Nitrogen crossover shows similar trend when compared to fixed time interval. When the current is lowered to 60 A, low residual H_2 increases nitrogen levels at anode exit. As the molar N_2 concentration reaches 3%, automatic purge control activates the purge process. Here again, only purge intervals are varied for automatic purging.

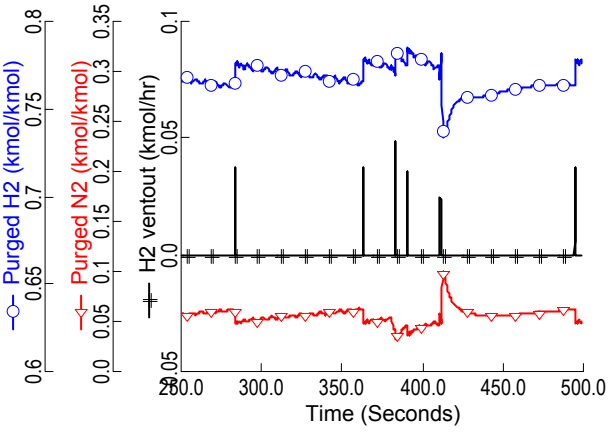

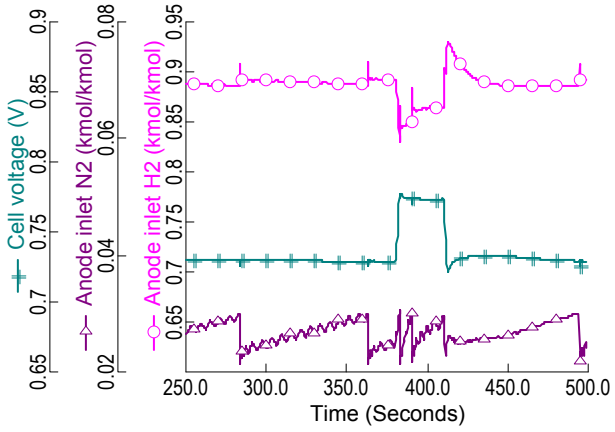

Figure 9.11: Effect of load changes of 120–60–120 A on automatic purge interval; (a) H_2 purge rate (b) N_2 concentration at anode inlet and cell voltage.

It can be seen in Fig. 9.11a that several instances of purge occur between 380–410 s. Purge rate of H_2 varies with the unused fuel at the anode exit. Unlike fixed time interval, N_2 concentrations at anode inlet are retained to lower levels for automatic purge controls (Fig. 9.11b).

Based on the results discussed above, the applicability of nitrogen detectors and automatic purge shows promise as a diagnostic tool for prediction of gas crossovers and act as a building block for devising purge strategies depending upon the load and mode of application.

9.3 Summary

A study on dynamics of nitrogen crossovers in PEMFC system with recirculation was conducted and its effects on purging strategy were discussed in chapter. The results exhibit that with pure recirculation, voltage and system efficiency declines due to nitrogen accumulation in fuel cell. Different purging methodologies were simulated to address hydrogen dilution issue at reaction sites. Anode bleed out of 3% is found to be the limit for prevention of N_2 buildup and retains the concentration levels to less than 1%. Also, cell voltage degrades linearly with N_2 buildup and rejuvenates at purge sequences. An alternate strategy for automatic initiation of anode recirculation purge by employing nitrogen detectors was simulated. Using the same purge time for various cases, it is shown that purge interval is lowered for low currents mainly due to low H_2 residual flows rates.

Moreover, during transient load changes, automatic purge catered well to prevent nitrogen levels from rising when compared to a fixed purge interval strategy.

Chapter 10

Concluding remarks

10.1 General summary

The fuel cell technology is one of the potential candidates for future transportation systems. In order to do so, fuel cells have to be developed to the extent that they are a viable alternative to current ICE vehicles in the near future. In addition to be cost effective, FCVs have to ensure reliability and durability when running under inflexible operating conditions. The need for transient analysis of such systems becomes of prime importance in order to make fuel cells a practical option for automobiles in the near future.

In the above context, the aim of this research was to investigate the dynamic behaviour of a PEMFC system in order to improve system efficiency when it is operating at different loads and operating conditions. A successful operation of fuel cell would require proper handling of four main sub–systems; fuel and oxidant supply, thermal and water management, and power conditioning modules.

These sub–systems need well–suited operating conditions which are controlled by the auxiliary components and hence define the overall system performance and effect the lifetime of the fuel cell stack. Current research was focused towards addressing these issues, firstly by developing a PEMFC stack model and then construction of the entire system with integrated controls to emulate a fuel cell system operating under varying operating conditions and influence of external parameters. System analyses were conducted for start–up sequence and transitory load changes. Issues related to water and thermal management were investigated with emphasis on species crossover mechanisms across the fuel cell. Finally, study on different purging strategies was conducted in order to cater to water management of the system.

10.2 Summary of analysis

10.2.1 Modelling of the PEM fuel cell system

The fuel cell model developed accommodates equations with electrochemical, thermal, feed flow and species crossover models in addition to two–phase calculations at fuel cell electrodes. Power output is calculated based on individual voltage and current models with time varying external loads, reactant pressures and stoichiometries, stack operating temperatures and reactant humidity levels. For fuel cell voltage, the polarization curve was created on the basis of Nernst voltage with activation, ohmic and concentration losses. Mass and energy conservation equations with electrochemical relations were used to calculate flow rates, concentrations and partial pressures of species in the reactant and product streams. In order to shed light on the complex interplay of different transport phenomena, detailed water and nitrogen crossover models were incorporated in the fuel cell stack model. A simple humidifier model comprising of heat and mass balance was built to achieve 95% humidity levels at cathode inlet of the fuel cell. The fuel was humidified by recirculation of anode exhaust.

The prime function of the PEMFC stack is to provide stable and uninterrupted power supply over a range of operating and environmental conditions. However, fuel cell functionality is constrained within specific limitations pertaining to operational integrity and stack lifetime. Optimum fuel cell performance depends on a number of operating conditions including current density, reactant stoichiometry, relative humidity, inlet pressures, and cell temperature. Each of these conditions is at the behest of proper interaction between the controlling auxiliary component and the fuel cell stack. Here, a control system was designed and demonstrated with the ability to predict the dynamic requirements of PEM fuel cell system during simultaneous changes of load and operating conditions.

Simulations for the prescribed system were carried out and reliability of the suggested model was verified and corroborated against design validation data, which were found to be in excellent agreement. Polarization curves, fuel consumption and power output profiles were found to be in accordance with the validation. Heat produced by the stack was also investigated by exergetic analysis of the PEMFC stack and associated irreversibilities were identified. From the preliminary results, a general conclusion could be drawn concerning the fuel cell exergetic efficiency, which depends on reactant pressures, operating temperatures, polarization overpotentials, current density and reactant stoichiometries. It was deduced that stack start–up at high current densities reduces exergetic efficiency in

the initial instances, while the efficiency of the fuel cell can be increased through increasing the fuel cell operating temperature and voltages. Moreover, entropy generation is reduced at high operating temperatures and with low presence of liquid water in the cathode outlet. Also, low ambient temperatures increase the exergetic efficiency slightly when operating at steady state temperatures. However, exergy destruction is higher at low start–up temperatures.

10.2.2 Start–up analysis of fuel cell system

In Proton Exchange Membrane Fuel Cells (PEMFC) systems, dynamic behaviour of a start–up is of particular importance to ensure a short start–up time and an efficient operation. A start–up analysis was performed for the described PEMFC system, starting at ambient temperature of 25°C and the focus had been set to evaluate the effects of key parameters till the system reaches steady–state operating temperatures. Key contributions of the suggested model are attributed to system response methodology, which incorporates stack thermal behaviour in addition to fuel cell electrochemistry, water crossover, mass and energy balances. It was observed that system efficiency and voltage output are higher at low power start–ups but for the fuel cell stack it takes longer time to reach stable operating conditions. In the context of fuel cell durability, quick start–ups to reach stable operating temperatures would allow high performance of the fuel cell and limit the operation time in the low performance states. Higher current density start–up would reduce the warming up times for the stack, though the load management during start–up would have to be properly managed. Another issue related to high currents is the water saturation at cathode, which is considerably higher at high current density start–ups. Removal of liquid water from cathode exhaust thus requires additional attention at low stack operating temperatures. Furthermore, air radiator consumes more power at high currents once the system is stable and due to this fact, system efficiency is reduced. In the proposed system, only air is humidified while the fuel is supposed to be adequately moistened by water crossover through the cell and recycling of humidified exhaust. Simulations were carried out to assess the extent of humidification in anode by assuming different humidity levels of inlet air. It was determined that cathode inlet water levels are adequate enough to humidify fuel stream. Though it is undesirable to have liquid droplets in the recirculating stream, their presence tends to increase the relative humidity at a faster pace. Small amounts of liquid water in anode would reduce the dry operational conditions, but negatively affect the recirculation pumps.

10.2.3 System response during transitory load changes

As a power source for automotive applications, fuel cell systems usually operate at continuously varying external requirements related to temperatures, pressures, power load and humidity. PEMFC dynamics are influenced by reactant flows, heat management and water content in the streams as well as within the fuel cell itself. The power output from a fuel cell module is a combination of battery and the fuel cell stack. Changes to the external load are handled by the battery with fuel cell charging it until it reaches minimum set charge state from where the fuel cell is responsible for providing power to the external load and for charging the battery as well. Regardless of the size of the battery and load handling management of the system, only load changes to the fuel cell stack were simulated here. Main contributions are ascribed to the dynamic system responses to the transitory load changes, which is characterized mainly by heat management and water transportation within the fuel cell. It was observed that the thermal management strategy greatly influences voltage output and system efficiency which increase with stack operating temperature. Moreover, slow temperature controls affect the stability of fuel cell operations. The changes in external load were few and far, only to study the thermal controls. With the changes occurring more than a minute apart, temperature changes stabilization was approximated to be within 30 seconds. High coolant mass flow rates were initiated in order to contemplate fast electrochemical changes in the stack. With very high variations in coolant flow rates, power consumed by liquid coolant pumps is minimal and had no considerable effect on system efficiency. On the other hand, air radiator consumes more during load changes. A 5% increase in power consumption of air blower and radiator is observed during load variations for the cases presented here. Furthermore, water crossover in the fuel cell has shown a significant impact on PEMFC anode operations. Anode inlet flows, humidity and recirculation pump are influenced by net water diffusion during load changes. Temperature changes at anode inlet are considerably higher during load variations and have a negative impact as they generate thermal stresses in the stack and reduce its lifetime. Also, amount of saturated water at cathode is dependent on operating temperature which apparently pertains to thermal management strategy of the system.

10.2.4 Effect of nitrogen crossover on purging strategy

Recent advancements in manufacturing of PEMFC stacks have made them more compact by significantly reducing the thickness of MEA. On the contrary, thin membranes enhances gas crossover across the cell resulting in current losses within the fuel cell itself. Nitrogen and water produced on the cathode side are both

transported towards the anode through the membrane and reduce the concentration of hydrogen in anode channels and obstructs hydrogen molecules to reach cell reaction sites effectively, which adversely affects the voltage developed in the cell. Here, model for nitrogen crossover and its build–up anode was developed and its effects on fuel cell performance and anode recirculation were simulated, and associated purging strategies were discussed. Nitrogen crossover model was found to be in excellent agreement with the experimental data provided by the stack manufacturer. The results exhibited that with pure recirculation, voltage and system efficiency declined due to nitrogen accumulation in fuel cell. Purging of anode recirculation is one of the approaches to relieve the stream off nitrogen and unwanted water. However, unutilized fuel is also wasted with each purge. Different purging methodologies were simulated to address hydrogen wastage during purging and dilution in the fuel cell. For continuous bleeding of anode exhaust, a bleed–out of 3% was found to be the limit for prevention of N_2 buildup. Concentration levels of nitrogen were also retained less than 1%. Apparently, cell voltage degraded linearly with N_2 buildup and rejuvenated at purge sequences. These results are limited to partial fuel starvation only and do not take into account the dilution of hydrogen in extreme conditions. An alternate strategy for automatic initiation of anode recirculation purge by employing nitrogen detectors was simulated. For practical diagnosis of fuel cell systems, nitrogen at anode inlet could be detected and signal from these detectors is transmitted to the controller, where it adjusts the parameters for effective purges. An optimum purge sequence would prevent N_2 buildup at a minimum expense of released hydrogen. Using the same purge time for various cases, it is shown that purge interval is lowered for low currents mainly due to low H_2 residual flows rates. Moreover, during transient load changes, automatic purge catered well to prevent nitrogen levels from rising when compared to a fixed purge interval strategy. Build–up of nitrogen during fixed purges is further increased if load changes are frequent. Whereas nitrogen detection method proved to be feasible for predicting gas crossovers during purge sequences at different loads and can be used as a base for optimizing and development of anode purge strategies for PEMFC systems.

10.3 Improvements for future work

This work has treated some of the technical aspects of modelling a PEM fuel cell system and controlling it to predict its behaviour with time. Even though this model can be useful in optimizing and designing operational strategies for different load cycles such as system start–up and purging states in PEMFC systems, several parameters need to be validated with experimental data from an actual fuel

cell test bench. Most of the focus was inclined towards fuel cell stack in the current research; however an extensive model validation from experimental setup would certainly help in verification of individual auxiliary components and make the model more insightful. The humidifier model used in this study is fairly simple and uses a fixed input of relative humidity and calculates amount of water needed for humidification by mass balance while the heat transfer is determined by the energy balance. The dynamic effects of the actual humidifier are therefore needed to simulate the actual humidity levels and temperature of the air entering the fuel cell stack.

Within all the areas covered in this dissertation, more knowledge is required in order to fully understand the inner workings of the fuel cell stack. Many challenges still exist in understanding the precise mechanisms of transportation in the fuel cell. Complex diffusion phenomena, such as water and nitrogen crossover occurring within the stack require further deliberation. A multi–dimensional model would be beneficial in determining these parameters in addition to several spatially distributed variables. Pressure drops within the flow fields and temperature distribution in the fuel cell is not uniform, which vary the current density along the cell surface. Since, current density is a key parameter in defining the performance of the fuel cell, information on its distribution would help in identifying fuel starvation problems in more detail and predict transient behaviour closer to the actual fuel cell.

Several controls were implemented in the system under investigation, which could emulate the system response to a favourable extent. However, only PID controllers with simple feedback loop were mostly incorporated with no tuning or optimization conducted in this research. In conjunction with experimental evaluation, advanced control strategies will further enhance the ability of this system. Moreover, an extended exergy analysis of all the underlying components is expected to help in identifying inefficient components during steady–state as well as transient conditions, and contribute in a more robust control strategy of the system.

Out of the several interesting plans, it is intended to extend the model with the addition of battery and power conditioning component models. Currently, the system efficiencies are calculated to be optimistically higher, because losses in the external terminals and power conditioning components such as the inverter have not been accounted for. Instead, a fixed value is assumed. A battery model in connection with the fuel cell stack would be able to simulate load distribution on these components and assist in studying the load management of the system. Similarly, for detailed modelling of the purge process, there is need for a dynamic

model of purge valve. Finally, there is always a room for improvement in research and the author considers it more than anyone as a motivation for further work.

Bibliography

1 Renewable Energy Sources and Climate Change Mitigation. ; 2012.

2 Key World Energy Statistics. Paris: ; 2012.

3 Aspentech. Aspen plus dynamics. 2012.http://www.aspentech.com/products/aspen–dynamics.aspx

4 Hwang J–J, Kuo J–K, Wu W, Chang W–R, Lin C–H, Wang S–E. Lifecycle performance assessment of fuel cell/battery electric vehicles. *International Journal of Hydrogen Energy* 2013; 38:3433–3446.

5 Honda's FCX fuel cell concept vehicle. *AutoTechnology* 2007; 7.

6 Friedlmeier G, Friedrich J, Panik F. Test Experiences with the DaimlerChrysler Fuel Cell Electric Vehicle NECAR 4. *Fuel Cells* 2001; 1:92–96.

7 Thomas CE. Fuel cell and battery electric vehicles compared. *International Journal of Hydrogen Energy* 2009; 34:6005–6020.

8 Houchins C, Kleen GJ, Peterson D, Garland NL, Ho DL, Marcinkoski J, *et al.* U.S. doe progress towards developing low–cost, high performance, durable polymer electrolyte membranes for fuel cell applications. *Membranes* 2012; 2:855–878.

9 Rodrigues A, Amphlett JC, Mann RF, Peppley BA, Roberge PR. Carbon monoxide poisoning of proton–exchange membrane fuel cells. *IECEC–97* –

proceedings of the thirty–second intersociety energy conversion engineering conference, vols 1–4 1997; :768–773.

10 Baschuk, Li X. Carbon monoxide poisoning of proton exchange membrane fuel cells. *International Journal of Energy Research* 2001; 25:695–713.

11 Ballard Power Systems. 2013.http://www.ballard.com/about–ballard/fuel–cell–education–resources/how–a–fuel–cell–works.aspx

12 Gelfi, Stefanopoulou, Pukrushpan, Peng H. Dynamics of low–pressure and high–pressure fuel cell air supply systems. 2003.

13 McCain BABA, Stefanopoulou AGAG, Kolmanovsky IVI V. On the dynamics and control of through–plane water distributions in PEM fuel cells. *Chemical Engineering Science* 2008; 63:4418–4432.

14 Ceraolo M, Miulli C, Pozio A. Modelling static and dynamic behaviour of proton exchange membrane fuel cells on the basis of electro–chemical description. *Journal of Power Sources* 2003; 113:131–144.

15 Amphlett JC, Mann RF, Peppley BA, Roberge PR, Rodrigues A. A model predicting transient responses of proton exchange membrane fuel cells. *Journal of Power Sources* 1996; 61:183–188.

16 Yerramalla S, Davari A, Feliachi A. Dynamic modeling and analysis of polymer electrolyte fuel cell. *2002 IEEE Power Engineering Society Summer Meeting, Vols 1–3, Conference Proceedings* 2002; :82–86.

17 Pathapati PR, Xue X, Tang J. A new dynamic model for predicting transient phenomena in a PEM fuel cell system. *Renewable Energy* 2005; 30:1–22.

18 Jia J, Wang Y, Li Q, Cham YT, Han M. Modeling and Dynamic Characteristic Simulation of a Proton Exchange Membrane Fuel Cell. *IEEE Transactions on Energy Conversion* 2009; 24:283–291.

19 Hu G, Fan J, Chen S, Liu Y, Cen K. Three–dimensional numerical analysis of proton exchange membrane fuel cells (PEMFCs) with conventional and interdigitated flow fields. *Journal of Power Sources* 2004; 136:1–9.

20 Kim K, Wang M, Von Spakovsky MR, Nelson DJ. Dynamic synthesis/design and operation/control optimization under uncertainty of a PEMFC system.

ASME International Mechanical Engineering Congress and Exposition, Proceedings 2009; 8:679–689.

21 Li Y, Xu S, Yang Z, Li Y. Experiment and simulation study on cold start of automotive PEMFC. *International Conference on Electric Information & Control Engineering ICEICE,* Wuhan 2011; :2166–2170.

22 Yan Q, Toghiani H, Lee Y–W, Liang K, Causey H. Effect of sub–freezing temperatures on a PEM fuel cell performance, startup and fuel cell components. *Journal of Power Sources* 2006; 160:1242–1250.

23 Mangold M, Piewek S, Klein O, Kienle A. A model for the freeze start behavior of a pem fuel cell stack. *Journal of Fuel Cell Science and Technology* 2011; 8.

24 Meng H. A PEM fuel cell model for cold–start simulations. *Journal of Power Sources* 2008; 178:141–150.

25 Sundaresan M, Moore RM. PEM Fuel Cell Stack Cold Start Thermal Model. *Fuel Cells* 2005; 5:476–485.

26 Vasu G, Tangirala AK. Control–orientated thermal model for proton–exchange membrane fuel cell systems. *Journal of Power Sources* 2008; 183:98–108.

27 Khan MJ, Iqbal MT. Modelling and analysis of electrochemical, thermal, and recetant flow dynamics for a PEM fuel cell system. *Fuel Cells* 2005; 5:463–475.

28 Shan Y, Choe S–Y. Modeling and simulation of a PEM fuel cell stack considering temperature effects. *Journal of Power Sources* 2006; 158:274–286.

29 Del Real AJ, Arce A, Bordons C. Development and experimental validation of a PEM fuel cell dynamic model. *Journal of Power Sources* 2007; 173:310–324.

30 Ahn J–W, Choe S–Y. Coolant controls of a PEM fuel cell system. *Journal of Power Sources* 2008; 179:252–264.

31 Jung J–H, Ahmed S. Dynamic model of PEM fuel cell using real–time simulation techniques. *Journal of Power Electronics* 2010; 10:739–748.

32 Asghari S, Akhgar H, Imani BF. Design of thermal management subsystem for a 5kW polymer electrolyte membrane fuel cell system. *Journal of Power Sources* 2011; 196:3141–3148.

33 Beicha A. Modeling and simulation of proton exchange membrane fuel cell systems. *Journal of Power Sources* 2012; 205:335–339.

34 Park S–K, Choe S–Y. Dynamic modeling and analysis of a 20–cell PEM fuel cell stack considering temperature and two–phase effects. *Journal of Power Sources* 2008; 179:660–672.

35 Blomen LJMJ. Review of an energy and exergy analysis of a fuel cell system. *Journal of Power Sources* 1993; 41:239–252.

36 Saidi MH, Ehyaei MA, Abbasi A. Optimization of a combined heat and power PEFC by exergy analysis. *Journal of Power Sources* 2005; 143:179–184.

37 Barbir F, Gómez T. Efficiency and economics of proton exchange membrane (PEM) fuel cells. *International Journal of Hydrogen Energy* 1997; 22:1027–1037.

38 Kazim A. Exergy analysis of a PEM fuel cell at variable operating conditions. *Energy Conversion and Management* 2004; 45:1949–1961.

39 Kazim. Exergoeconomic analysis of a PEM electrolyser at various operating temperatures and pressures. *International Journal of Energy Research* 2005; 29:539–548.

40 Mert SO, Dincer I, Ozcelik Z. Exergoeconomic analysis of a vehicular PEM fuel cell system. *Journal of Power Sources* 2007; 165:244–252.

41 Miansari M, Sedighi K, Amidpour M, Alizadeh E, Miansari M. Experimental and thermodynamic approach on proton exchange membrane fuel cell performance. *Journal of Power Sources* 2009; 190:356–361.

42 Leo TJ, Durango JA, Navarro E. Exergy analysis of PEM fuel cells for marine applications. *Energy* 2010; 35:1164–1171.

43 Uyanga E, Sevjidsuren G, Bumaa B, Sangaa D, Altantsog P. Exergy analysis of NEXA™ PEM fuel cell module. 2011; 1:256–260.

44 Kocha SS, Deliang Yang J, Yi JS. Characterization of gas crossover and its implications in PEM fuel cells. *AIChE Journal* 2006; 52:1916–1925.

45 Ahluwalia RK, Wang X. Buildup of nitrogen in direct hydrogen polymer–electrolyte fuel cell stacks. *Journal of Power Sources* 2007; 171:63–71.

46 Catalano J, Myezwa T, De Angelis MG, Baschetti MG, Sarti GC. The effect of relative humidity on the gas permeability and swelling in PFSI membranes. *International Journal of Hydrogen Energy* 2012; 37:6308–6316.

47 Baik KD, Kim MS. Characterization of nitrogen gas crossover through the membrane in proton–exchange membrane fuel cells. *International Journal of Hydrogen Energy* 2011; 36:732–739.

48 Weber. Gas–crossover and membrane–pinhole effects in polymer–electrolyte fuel cells. *Journal of the Electrochemical Society* 2008; 155:B521–31.

49 Pukrushpan JT, Peng H, Stefanopoulou AG. Control–Oriented Modeling and Analysis for Automotive Fuel Cel Systems. *Journal of Dynamic Systems Measurement & Control* 2004; 126.

50 Zhu WH, Payne RU, Tatarchuk BJ. Critical flow rate of anode fuel exhaust in a PEM fuel cell system. *Journal of Power Sources* 2006; 156:512–519.

51 Tang Y, Yuan W, Pan M, Li Z, Chen G, Li Y. Experimental investigation of dynamic performance and transient responses of a kW–class PEM fuel cell stack under various load changes. *Applied Energy* 2010; 87:1410–1417.

52 Zhai S, Zhou S, Sun P, Chen F, Niu J. Modeling study of anode water flooding and gas purge for PEMFCs. *Journal of Fuel Cell Science and Technology* 2012; 9.

53 Gou J, Pei P, Wang Y. The dynamic behavior of pressure during purge process in the anode of a PEM fuel cell. *Journal of Power Sources* 2007; 162.

54 Wang X, Tajiri K, Ahluwalia RK. Water transport during startup and shutdown of polymer electrolyte fuel cell stacks. *Journal of Power Sources* 2010; 195:6680–6687.

55 Karimäki H, Pérez LC, Nikiforow K, Keränen TM, Viitakangas J, Ihonen J. The use of on–line hydrogen sensor for studying inert gas effects and

nitrogen crossover in PEMFC system. *International Journal of Hydrogen Energy* 2011; 36:10179–10187.

56 Promislow K, St–Pierre J, Wetton B. A simple, analytic model of polymer electrolyte membrane fuel cell anode recirculation at operating power including nitrogen crossover. *Journal of Power Sources* 2011; 196:10050–10056.

57 Hou Y, Shen C, Yang Z, He Y. A dynamic voltage model of a fuel cell stack considering the effects of hydrogen purge operation. *Renewable Energy* 2012; 44:246–251.

58 Müller EA, Kolb F, Guzzella L, Stefanopoulou AG, McKay DA. Correlating nitrogen accumulation with temporal fuel cell performance. *Journal of Fuel Cell Science and Technology* 2010; 7:210131–2101311.

59 Siegel JB, Bohac S V, Stefanopoulou AG, Yesilyurt S. Nitrogen Front Evolution in Purged Polymer Electrolyte Membrane Fuel Cell with Dead–Ended Anode. *Journal of the Electrochemical Society* 2010; 157:B1081–93.

60 Yesilyurt S, Siegel JB, Stefanopoulou AG. Modeling and Experiments of Voltage Transients of Polymer Electrolyte Membrane Fuel Cells With the Dead–Ended Anode. *Journal of Fuel Cell Science and Technology* 2012; 9.

61 Choi JW, Hwang Y–S, Seo J–H, Lee DH, Cha SW, Kim MS. An experimental study on the purge characteristics of the cathodic dead–end mode PEMFC for the submarine or aerospace applications and performance improvement with the pulsation effects. *International Journal of Hydrogen Energy* 2010; 35:3698–3711.

62 Ballard Mark9 SSL. Product manual and integration guide. 2008.

63 Eikerling Research Group, SFU. 2013.http://www.sfu.ca/eikerlingresearch/overview/

64 Scientific Computing World. 2013.http://www.scientific–computing.com /features/feature.php?feature_id=126

65 Hosseinzadeh E, Rokni M. Development and validation of a simple analytical model of the Proton Exchange Membrane Fuel Cell (PEMFC) in a

fork–lift truck power system. *International journal of green energy* 2013; 10:523–543.

66 Larminie J, Dicks A. *Fuel cell systems explained*. Chichester, West Sussex: J. Wiley; 2003.

67 Spiegel C. *Designing and building fuel cells*. New York: McGraw–Hill; 2007.

68 Liu H, Laconti AB, Gasteiger HA, Zhang J. Factors impacting chemical degradation of perfluorinated sulfonic acid ionomers. *ECS Transactions* 2005; 1:283–293.

69 Santarelli MG, Torchio MF, Cochis P. Parameters estimation of a PEM fuel cell polarization curve and analysis of their behavior with temperature. *Journal of Power Sources* 2006; 159:824–835.

70 Bockris JO. Handbook of fuel cell technology – Editor Carl Berger. Prentice–Hall, 1968; $318.50. *Electrochimica Acta* 1969; 14:925–926.

71 Santarelli MG, Torchio MF. Experimental analysis of the effects of the operating variables on the performance of a single PEMFC. *Energy Conversion and Management* 2007; 48.

72 Mann RF, Amphlett JC, Hooper MAI, Jensen HM, Peppley BA, Roberge PR. Development and application of a generalised steady–state electrochemical model for a PEM fuel cell. *Journal of Power Sources* 2000; 86:173–180.

73 Zhang L, Pan M, Quan S. Model predictive control of water management in PEMFC. *Journal of Power Sources* 2008; 180:322–329.

74 Spinelli P, Francia C, Ambrosio EP, Lucariello M. Semi–empirical evaluation of PEMFC electro–catalytic activity. *Journal of Power Sources* 2008; 178:517–524.

75 Haji S. Analytical modeling of PEM fuel cell i–V curve. *Renewable Energy* 2011; 36:451–458.

76 Wang X, Nguyen T V, Hussey DS, Jacobson DL. Experimental study of relative permeability of porous media used in PEM fuel cells. *ECS Transactions* 2010; 33:1151–1162.

77 Martins LS, Ordonez JC, Vargas JVC. Experimental validation of a simplified pemfc simulation model. *ES2009: Proceedings Of The Asme 3rd International Conference On Energy Sustainability, Vol 1* 2009; :305–314.

78 Gurau V, Barbir F, Liu H. Analytical solution of a half–cell model for PEM fuel cells. *Journal of the Electrochemical Society* 2000; 147:2468–2477.

79 Springer TE, Zawodzinski TA, Gottesfeld S. Polymer Electrolyte Fuel–Cell model. *Journal of the Electrochemical Society* 1991; 138:2334–2342.

80 Nishiyama E, Murahashi T. Permeability of a PEMFC gas diffusion layer based on morphology. *ECS Transactions* 2011; 41:2021–2031.

81 Cheng X, Zhang J, Tang Y, Song C, Shen J, Song D, *et al.* Hydrogen crossover in high–temperature PEM fuel cells. *Journal of Power Sources* 2007; 167:25–31.

82 Mittelsteadt C, Umbrell M. Gas Permeability in Perfluorinated Sulfonic Acid Polymer Electrolyte Membranes. *Meeting abstracts– electrochemical society* – 2005.

83 Groot A De, Woudstra N. Exergy analysis of a fuel–cell system. *Journal of the Institute of Energy* 1995; 68.

84 Wright SE. Comparison of the theoretical performance potential of fuel cells and heat engines. *Renewable Energy* 2004; 29:179–195.

85 Bejan A. *Advanced engineering thermodynamics*. Hoboken,N.J.: Wiley; 2006.

86 Bejan A, Tsatsaronis G, Moran M. *Thermal design and optimization*. New York: Wiley–Interscience; 1996.

87 Mathias, Makharia, Gasteiger, Conley, Fuller, Gittleman, *et al.* Two fuel cell cars in every garage? *Electrochemical Society Interface* 2005; 14:24–35.

88 Yu PT, Kocha S, Paine L, Gu W, Wagner FT. The effects of air purge on the degradation of PEM fuel cells during startup and shutdown procedures. *2004 AIChE Spring National Meeting, Conference Proceedings* 2004; :521–527.

89 Patterson TW, Darling RM. Damage to the cathode catalyst of a PEM fuel cell caused by localized fuel starvation. *Electrochemical and Solid–State Letters* 2006; 9:A183–A185.

90 Wong KH, Loo KH, Lai YM, Tan S–C, Tse CK. A theoretical study of inlet relative humidity control in PEM fuel cell. *International Journal of Hydrogen Energy* 2011; 36:11871–11885.

91 Reiser CA, Bregoli L, Patterson TW, Yi JS, Yang JD, Perry ML, *et al.* A reverse–current decay mechanism for fuel cells. *Electrochemical and Solid–State Letters* 2005; 8:A273–A276.

92 Meyers JP, Darling RM. Model of carbon corrosion in PEM fuel cells. *Journal of the Electrochemical Society* 2006; 153:A1432–A1442.

93 Rabbani A, Rokni M. Dynamic characteristics of an automotive fuel cell system for transitory load changes. *Sustainable Energy Technologies and Assessments* 2013; 1.http://dx.doi.org/10.1016/j.seta.2012.12.003

94 Rabbani A, Rokni M. Start–up Analysis of a PEM Fuel Cell System in Vehicles. *International Journal of Green Energy* 2013;11:1–21.

95 Hosseinzadeh E, Rokni M, Rabbani A, Mortensen HH. Thermal and water management of low temperature Proton Exchange Membrane Fuel Cell in fork–lift truck power system. *Applied Energy* 2013; 104:434–444.

Appendix A

Aspen Dynamics Modelling Language

A.1. PEM Fuel Cell component model

Model - PEMFC

```
1   Model PEMFC
2
3
4     PARAMETER Comp USES StringParameter
5         Valid As StringSet;
6     End
7
8     PARAMETER Crossover USES StringParameter
9       Valid as stringset(["Yes","No"]);
10      value:"Yes";
11    End
12
13
14  // Allow for mapping of names used in simulator to those in the model
15
16    CompH2                As Comp (Description:"Component name for hydrogen");
17    CompO2                As Comp (Description:"Component name for oxygen");
18    CompH2O               As Comp (Description:"Component name for water");
19    CompN2                As Comp (Description:"Component name for nitrogen");
20    CompH3N               As Comp (Description:"Component name for ammonia");
21    N2_Cross              As Crossover  (Description:"Select Nitrogen Crossover");
22    Water_Cross           As Crossover  (Description:"Select Water Crossover");
23    CompH2.Valid : ComponentList;
24    CompO2.Valid : ComponentList;
25    CompH2O.Valid: ComponentList;
26    CompN2.Valid : ComponentList;
27    CompH3N.Valid: ComponentList;
28    CompH2 : "H2";
29    CompO2 : "O2";
30    CompH2O: "H2O";
31    CompN2 : "N2";
32    CompH3N: "H3N";
33
34    CompListAnode         As StringSet ([CompH2, CompH2O, CompN2]);
35    CompListCathode       As StringSet ([CompO2, CompH2O, CompN2]);
36    CompListInertA        As StringSet (ComponentList - CompListAnode);
37    CompListInertC        As StringSet (ComponentList - CompListCathode);
38    CompListInert         As StringSet (ComponentList - CompListAnode - CompListCathode);
39
40
41  // Ports
42    In_A          As Input        MoleFractionPort;
```

```
43      In_C          As Input        MoleFractionPort;
44      Out_A         As Output       MoleFractionPort;
45      Out_C         As Output       MoleFractionPort;
46      Cool_In       As Input        MoleFractionPort;
47      Cool_Out      As Output       MoleFractionPort;
48      Work          As Output               WorkPort;
49      Heat          As Output               HeatPort;
50
51    // Parameters
52      Faraday             As  RealParameter             (Description:"Faraday constant (C/mol)", 96487);
53      R                   As  RealParameter             (Description:"Gas constant (J/molK)", 8.314);
54
55    // Fixed variables
56      Tnot     As Temperature          (Description:"Ambient temperature", Fixed);
57      TnotK    As Temperature_abs      (Description:"Ambient temperature", 298.15);
58      Pnot     As Pressure             (Description:"Ambient pressure", Fixed);
59      DPcool   As Press_Diff           (Description:"Pressure loss cooling circuit", Fixed, 0.1);
60      Ncells   As Notype               (Description:"Number of cells in stack", Fixed, 110);
61      Acell    As Area                 (Description:"Active area of the cell", Fixed, 0.02858);
62      A_st     As Area                 (Description:"Stack surface area", Fixed, 0.5);
63      h_conv   As heat_trans_coeff     (Description:"heat transfer coeff for air", Fixed, 0.005);
64      tm       As Length               (Description:"Membrane thickness", Fixed, 0.000183);
65      EN2      As Constant             (Description:"N2 Activation energy for permeation", Fixed, 24000);
66      Alpha    As Constant             (Description:"N2 permeation scaling factor", Fixed, 8.0);
67      Voc      As Output Voltage       (Description:"Cell open circuit potential", 1.1);
68      DX       As Notype               (Description:"Correction factor for mean values", Fixed, 0.2);
69      Rho_D    As Dens_mass            (Description:"Density of dry  Nafion", Fixed, 3280);
70      MWn      As Molweight            (Description:"Molar mass of Nafion", Fixed, 1100);
71      ne       As Constant             (Description:"Number of electrons transferred", Fixed, 2.0);
72      Iin      As Current_density      (Description:"internal loss, current density", Fixed, 0.002);
73      Icell    As Input,Output Current (Description:"Cell Current", Fixed, 1);
74      ILoss    As Current              (Description:"Current lost to internal crossovers", 0.5);
75      Imax     As Current_density      (Description:"Maximum current density", Fixed, 1.2);
76      n_a      As Constant             (Description:"n_a", Fixed, 2.0);
77      n_c      As Constant             (Description:"n_c", Fixed, 1.0);
78      B        As Constant             (Description:"B", Fixed, 0.5);
79      TStep    As TimeSec              (Description:"Time step of one second", Fixed, 1.0);
80      Em_H2    As Enth_mol             (Description:"Specific molar chemical exergy of Hydrogen", Fixed, 0.2361);
81      Em_O2    As Enth_mol             (Description:"Specific molar chemical exergy of Oxygen", Fixed, 0.003970);
82      Em_H2Og  As Enth_mol             (Description:"Specific molar chemical exergy of Water(g)", Fixed, 0.009500);
83      Em_H2Ol  As Enth_mol             (Description:"Specific molar chemical exergy of Water(l)", Fixed, 0.0008842);
84      Em_N2    As Enth_mol             (Description:"Specific molar chemical exergy of Nitrogen", Fixed, 0.000720);
```

```
85      Em_CO2   As Enth_mol              (Description:"Specific molar chemical exergy of CO2", Fixed, 0.019870);
86      Em_AR    As Enth_mol              (Description:"Specific molar chemical exergy of Argon", Fixed, 0.011640);
87
88    // Variables with arrays
89      Nfain(CompListAnode)       As Flow_mol_low    (Description:"Molar flow rate at anode inlet");
90      Nflain(CompListAnode)      As Flow_mol_low    (Description:"Liquid molar flow rate at anode inlet");
91      Nfcin(CompListCathode)     As Flow_mol_low    (Description:"Molar flow rate at cathode inlet");
92      Nflcin(CompListCathode)    As Flow_mol_low    (Description:"Liquid molar flow rate at cathode inlet");
93      Nfaout(CompListAnode)      As Flow_mol_low    (Description:"Molar flow rate at anode outlet");
94      Nflaout(CompListAnode)     As Flow_mol_low    (Description:"Liquid molar flow rate at anode outlet");
95      Nfcout(CompListCathode)    As Flow_mol_low    (Description:"Molar flow rate at cathode outlet");
96      Nflcout(CompListCathode)   As Flow_mol_low    (Description:"Liquid molar flow rate at cathode outlet");
97      NfaInert(CompListInerta)   As Flow_mol_low    (Description:"Anode inert components flow rate");
98      NfcInert(CompListInertc)   As Flow_mol_low    (Description:"Cathode inert components flow rate");
99      Nfcoolin(ComponentList)    As Flow_mol        (Description:"Molar flow rate at cooling inlet");
100     Nfcoolout(ComponentList)   As Flow_mol        (Description:"Molar flow rate at cooling outlet");
101     MW(ComponentList)          As Molweight       (Description:"Molecular weights");
102     GFE(ComponentList)         As Gibbs_mol_vap   (Description:"Gibbs free energy of components");
103     GFnot(ComponentList)       As Gibbs_mol_vap   (Description:"Gibbs free energy of components at 25 C");
104     Xw (ComponentList)         As Molefraction    (Description:"Vapour Quality", Fixed, 0);
105     Ppain(CompListAnode)       As Pressure        (Description:"Partial pressure at anode inlet", 0.5);
106     Ppcin(CompListCathode)     As Pressure        (Description:"Partial pressure at cathode inlet", 0.5);
107     Ppaout(CompListAnode)      As Pressure        (Description:"Partial pressure at anode outlet", 0.5);
108     Ppcout(CompListCathode)    As Pressure        (Description:"Partial pressure at cathode outlet", 0.5);
109     Paav(ComponentList)        As Pressure        (Description:"Average pressures in anode", 0.5);
110     Pcav(ComponentList)        As Pressure        (Description:"Average pressures in cathode", 0.5);
111     MDOTain(ComponentList)     As Flow_mass       (Description:"Mass flow rate at anode inlet");
112     MDOTcin(ComponentList)     As Flow_mass       (Description:"Mass flow rate at cathode inlet");
113     MDOTaout(ComponentList)    As Flow_mass       (Description:"Mass flow rate at anode inlet");
114     MDOTcout(ComponentList)    As Flow_mass       (Description:"Mass flow rate at cathode inlet");
115     Spain(ComponentList)       As Hidden Pressure (Description:"Satutation pressures at anode inlet", 0.5);
116     Spcin(ComponentList)       As Hidden Pressure (Description:"Satutation pressures at cathode inlet", 0.5);
117     Spout(ComponentList)       As Hidden Pressure (Description:"Satutation pressures at outlet", 0.5);
118     Spnot(ComponentList)       As Hidden Pressure (Description:"Satutation pressures at st conditions", 0.5);
119     Yain(CompListAnode)        As Molefraction    (Description:"Anode inlet gas mole fraction");
120     Ycin(CompListCathode)      As Molefraction    (Description:"Cathode inlet gas mole fraction");
121     Yaout(CompListAnode)       As Molefraction    (Description:"Anode outlet gas mole fraction");
122     Ycout(CompListCathode)     As Molefraction    (Description:"Cathode outlet gas mole fraction");
123     Yai(ComponentList)         As Molefraction    (Description:"Anode inlet vapor composition");
124     Yci(ComponentList)         As Molefraction    (Description:"Cathode inlet vapor composition");
125     Ycooli(ComponentList)      As Molefraction    (Description:"Coolant inlet vapor composition");
126     Xai(ComponentList)         As Molefraction    (Description:"Anode inlet liquid composition");
```

```
127     Xci(ComponentList)        As Molefraction    (Description:"Cathode inlet liquid composition");
128     Xcooli(ComponentList)     As Molefraction    (Description:"Coolant inlet liquid composition");
129     Yao(ComponentList)        As Molefraction    (Description:"Anode outlet vapor composition");
130     Yco(ComponentList)        As Molefraction    (Description:"Cathode outlet vapor composition");
131     Ycoolo(ComponentList)     As Molefraction    (Description:"Coolant outlet vapor composition");
132     Xao(ComponentList)        As Molefraction    (Description:"Anode outlet liquid composition");
133     Xco(ComponentList)        As Molefraction    (Description:"Cathode outlet liquid composition");
134     Xcoolo(ComponentList)     As Molefraction    (Description:"Coolant outlet liquid composition");
135
136   // Other variables
137     SH2           As Input,Output Notype       (Description:"Inlet stoichiometry of Hydrogen", 1.6);
138     SO2           As Input,Output Notype       (Description:"Inlet stoichiometry of Oxygen", 1.8);
139     S_Ratio       As Input,Output Notype       (Description:"stoichiometric Ratios", 0.9);
140     Tcell         As Temperature_abs           (Description:"Stack temperature", Rateinitial, 298.15);
141     Tain          As Input,Output Temperature  (Description:"Anode inlet temperature", 61);
142     Tcin          As Input,Output Temperature  (Description:"Cathode inlet temperature", 61);
143     Tcoolin       As Input,Output Temperature  (Description:"Cooling water inlet temperature", 61);
144     Tcoolout      As Input,Output Temperature  (Description:"Cooling water outlet temperature", 69);
145     Taout         As Input,Output Temperature  (Description:"Anode Outlet temperature", 69);
146     Tcout         As Input,Output Temperature  (Description:"Cathode Outlet temperature", 69);
147     DeltaT        As Input,Output Temp_diff    (Description:"Operating temperature", 0);
148     Top           As Input,Output Temperature  (Description:"Operating temperature", Rateinitial, 25);
149     TopK          As Temperature_abs           (Description:"Operating temperature", 342.15);
150     Pa            As Pressure                  (Description:"Average Pressure at anode", 1.92);
151     Pc            As Pressure                  (Description:"Average Pressure at cathode", 1.6);
152     DPa           As Press_Diff                (Description:"Pressure loss at anode", 0.15);
153     DPc           As Press_Diff                (Description:"Pressure loss at cathode",  0.4);
154     Pain          As Input,Output Pressure     (Description:"Pressure at anode inlet", 2.0);
155     Pcin          As Input,Output Pressure     (Description:"Pressure at cathode inlet", 1.8);
156     Paout         As Input,Output Pressure     (Description:"Pressure at anode outlet", 1.85);
157     Pcout         As Input,Output Pressure     (Description:"Pressure at cathode outlet", 1.4);
158     Pcoolin       As Input,Output Pressure     (Description:"Pressure at cooling water intlet", 1.0);
159     Pcoolout      As Input,Output Pressure     (Description:"Pressure at cooling water outlet", 1.0);
160     RHOain        As Dens_mol_vap              (Description:"Anode inlet vapor density");
161     RHOaout       As Dens_mol_vap              (Description:"Anode outlet vapor density");
162     RHOcin        As Dens_mol_vap              (Description:"Cathode inlet vapor density");
163     RHOcout       As Dens_mol_vap              (Description:"Cathode outlet vapor density");
164     RHOlain       As Dens_mol_liq              (Description:"Anode inlet liquid density");
165     RHOlaout      As Dens_mol_liq              (Description:"Anode outlet liquid density");
166     RHOlcin       As Dens_mol_liq              (Description:"Cathode inlet liquid density");
167     RHOlcout      As Dens_mol_liq              (Description:"Cathode outlet liquid density");
168     RHOcoolin     As Dens_mol_liq              (Description:"Cooling circuit inlet liquid density");
```

```
169     RHOcoolout    As Dens_mol_liq             (Description:"Cooling circuit outlet liquid density");
170     P_Gen         As  Output Power            (Description:"Total power", 16.5);
171     H_Gen         As  Output Energy_rate      (Description:"Heat produced", 14.0);
172     NfTain        As  Flow_mol                (Description:"Molar flow rate at anode inlet", 0.8);
173     NfTcin        As  Flow_mol                (Description:"Molar flow rate at cathode inlet", 5.0);
174     NfTaout       As  Flow_mol                (Description:"Molar flow rate at anode inlet", 1.0);
175     NfTcout       As  Flow_mol                (Description:"Molar flow rate at cathode inlet", 4.0);
176     MDain         As Input,Output Flow_mass   (Description:"Total mass flow rate at anode inlet");
177     MDcin         As Input,Output Flow_mass   (Description:"Total mass flow rate at cathode inlet");
178     MDaout        As Input,Output Flow_mass   (Description:"Total mass flow rate at anode outlet");
179     MDcout        As Input,Output Flow_mass   (Description:"Total mass flow rate at cathode outlet");
180     MWfin         As Molweight                (Description:"Average Molecular weight of fuel at inlet", 3.5);
181     MWfout        As Molweight                (Description:"Average Molecular weight of fuel at outlet", 5.0);
182     MWain         As Molweight                (Description:"Average Molecular weight of air at inlet", 27.5);
183     MWaout        As Molweight                (Description:"Average Molecular weight of air at outlet", 25.0);
184     MWcoolin      As Molweight                (Description:"Average Molecular weight of coolant at inlet",27.5);
185     MWcoolout     As Molweight                (Description:"Average Molecular weight of coolant at outlet",25.0);
186     SatPain       As Pressure                 (Description:"Water saturation pressure at anode inlet", 0.2);
187     SatPcin       As Pressure                 (Description:"Water saturation pressure at cathode inlet", 0.2);
188     SatPout       As Pressure                 (Description:"Outlet water vapor saturation pressure", 0.3);
189     SatPnot       As Pressure                 (Description:"Water vapor saturation pressure at st conditions", 0.3);
190     Pwain         As Pressure                 (Description:"Anode inlet water vapor pressure", 0.12);
191     Pwaout        As Pressure                 (Description:"Anode outlet water vapor pressure", 0.27);
192     Pwcin         As Pressure                 (Description:"Cathode inlet water vapor pressure", 0.2);
193     Pwcout        As Pressure                 (Description:"Cathode outlet water vapor pressure", 0.27);
194     awa           As Notype                   (Description:"Water activity at anode", 0.94);
195     awc           As Notype                   (Description:"Water activity at cathode", 0.99);
196     PO2           As Pressure                 (Description:"Average Partial pressure of O2", 0.23);
197     PH2           As Pressure                 (Description:"Average Partial pressure of H2", 1.8);
198     PaH2O         As Pressure                 (Description:"Average Anode Partial pressure of H2O", 1.8);
199     PcH2O         As Pressure                 (Description:"Average Cathode Partial pressure of H2O", 1.8);
200     Lmda_a        As Notype                   (Description:"Water content at anode", 10.8);
201     Lmda_c        As Notype                   (Description:"Water content at cathode", 12.9);
202     Lmda_mem      As Notype                   (Description:"Water content in membrane");
203     DC            As Diffus_vap               (Description:"Diffusion coefficient for water in cell");
204     Ja            As flux_mol                 (Description:"Molar flux for water from anode");
205     Jc            As flux_mol                 (Description:"Molar flux of water from cathode");
206     Jnet          As flux_mol                 (Description:"Net Molar flux of water in the cell");
207     Jnetn         As Flow_mol_low             (Description:"Net Molar flow of water in the cell");
208     Jnetm         As flow_mass_low            (Description:"Net Mass flow of water across the cell");
209     Jst           As Flow_mol                 (Description:"Net Molar flow of water across the stack");
210     Jmst          As Flow_mass                (Description:"Net Mass flow of water across the stack");
```

```
211     JH2          As flux_mol                (Description:"Molar flux of Hydrogen in Anode");
212     JO2          As flux_mol                (Description:"Molar flux of Oxygen in Cathode");
213     Gstan        As Free_energy             (Description:"Standard Gibbs free energy for reaction");
214     Greal        As Free_energy             (Description:"Real Gibbs free energy for reaction");
215     Gnot         As Free_energy             (Description:"Gibbs free energy for reaction at 25 C");
216     Ioa          As Current_density         (Description:"Anode exchange current density");
217     Ioc          As Current_density         (Description:"Cathode exchange current density", 1.9E-7);
218     Icd          As Current_density         (Description:"Average current density", 0.8);
219     Ilim_a       As Current_density         (Description:"Anode limiting current density");
220     Ilim_c       As Current_density         (Description:"Cathode limiting current density");
221     It           As Input,Output Current    (Description:"Total current");
222     Icell2       As Input,Output Current    (Description:"Calculated current");
223     Vcell        As Input,Output Voltage    (Description:"Cell potential", 0.65);
224     Vnrst        As Voltage                 (Description:"Nernst Cell potential", 1.17);
225     Vnot         As Voltage                 (Description:"Standard Nernst Cell potential at 25 C", 1.17);
226     Vact         As Voltage                 (Description:"Activation overpotential", 0.4);
227     Vact_a       As Voltage                 (Description:"Anode Activation overpotential", 0.0);
228     Vact_c       As Voltage                 (Description:"Cathode Activation overpotential", 0.4);
229     Vohmic       As Voltage                 (Description:"Ohmic overpotential", 0.1);
230     Vconc_a      As Voltage                 (Description:"Anode concentration overpotential", 0.001);
231     Vconc_c      As Voltage                 (Description:"Cathode concentration overpotential", 0.001);
232     Vconc        As Voltage                 (Description:"Total concentration overpotential", 0.001);
233     Vstack       As Voltage                 (Description:"Stack voltage");
234     Relec        As Resistance              (Description:"Electrical resistance in the cell", 0.0);
235     Rionic       As Resistance              (Description:"Ionic resistance in the cell");
236     Rion         As Resistance              (Description:"Ionic resistance in the cell, (ohm-cm2");
237     gTest        As Free_energy             (Description:"Gibbs energy deviation");
238     A_a          As Constant                (Description:"A_a", 1.0);
239     A_c          As Constant                (Description:"A_c", 0.5);
240     EtaCell      As Input,Output Notype     (Description:"Average cell efficiency", 0.5);
241     AFR          As Input,Output Notype     (Description:"Air to Fuel Ratio");
242     RHain        As Notype                  (Description:"Relative humidity at Anode Inlet", 0.95);
243     RHcin        As Notype                  (Description:"Relative humidity at Cathode Inlet", 0.92);
244     RHaout       As Notype                  (Description:"Relative humidity at Anode Outlet", 1.0);
245     RHcout       As Notype                  (Description:"Relative humidity at Cathode Outlet", 1.0);
246     VFa          As Vapfraction             (Description:"Anode inlet vapor fraction", 1);
247     VFc          As Vapfraction             (Description:"Cathode inlet vapor fraction", 1);
248     VFcool       As Vapfraction             (Description:"Coolant inlet vapor fraction", 1);
249     LFa          As Liqfraction             (Description:"Anode inlet liquid fraction", 1);
250     LFc          As Liqfraction             (Description:"Cathode inlet liquid fraction", 1);
251     LFcool       As Liqfraction             (Description:"Coolant inlet liquid fraction", 1);
252     Hva          As Enth_mol_vap            (Description:"Anode vapor inlet molar enthalpy");
```

```
253     Hvc           As Enth_mol_vap          (Description:"Cathode vapor inlet molar enthalpy");
254     Hvcool        As Enth_mol_vap          (Description:"Coolant vapor inlet molar enthalpy");
255     Hla           As Enth_mol_liq          (Description:"Anode liquid inlet molar enthalpy");
256     Hlc           As Enth_mol_liq          (Description:"Cathode liquid inlet molar enthalpy");
257     Hlcool        As Enth_mol_liq          (Description:"Coolant liquid inlet molar enthalpy");
258     VFao          As Vapfraction           (Description:"Anode outlet vapor fraction", 1);
259     VFco          As Vapfraction           (Description:"Cathode outlet vapor fraction", 1);
260     VFcoolo       As Vapfraction           (Description:"Coolant outlet vapor fraction", 1);
261     LFao          As Liqfraction           (Description:"Anode outlet liquid fraction", 1);
262     LFco          As Liqfraction           (Description:"Cathode outlet liquid fraction", 1);
263     LFcoolo       As Liqfraction           (Description:"Coolant outlet liquid fraction", 1);
264     Hvao          As Enth_mol_vap          (Description:"Anode vapor outlet molar enthalpy");
265     Hvco          As Enth_mol_vap          (Description:"Cathode vapor outlet molar enthalpy");
266     Hvcoolo       As Enth_mol_vap          (Description:"Coolant vapor outlet molar enthalpy");
267     Hlao          As Enth_mol_liq          (Description:"Anode liquid outlet molar enthalpy");
268     Hlco          As Enth_mol_liq          (Description:"Cathode liquid outlet molar enthalpy");
269     Hlcoolo       As Enth_mol_liq          (Description:"Coolant liquid outlet molar enthalpy");
270     Cplin         As Cp_mol                (Description:"Specific heat capacity of liquid water at inlet");
271     Cplout        As Cp_mol                (Description:"Specific heat capacity of liquid water at outlet");
272     Cplave        As Cp_mol                (Description:"Average Specific heat capacity of liquid water");
273     Ein           As Energy_rate           (Description:"Energy in");
274     Eout          As Energy_rate           (Description:"Energy out");
275     Eloss         As Energy_rate           (Description:"Energy lost");
276     Est           As Energy_rate           (Description:"Energy stored");
277     Egen          As Energy_rate           (Description:"Energy generated");
278     E_delta       As Energy_rate           (Description:"Energy difference between inlet and outlet");
279     S_ain         As Entr_mol              (Description:"Entropy at Anode inlet");
280     S_aout        As Entr_mol              (Description:"Entropy at Anode outlet");
281     S_cin         As Entr_mol              (Description:"Entropy at Cathode inlet");
282     S_cout        As Entr_mol              (Description:"Entropy at Cathode outlet");
283     S_coolin      As Entr_mol              (Description:"Entropy at Coolant inlet");
284     S_coolout     As Entr_mol              (Description:"Entropy at Coolant outlet");
285     Snot_ain      As Entr_mol              (Description:"Standard Entropy at Anode inlet");
286     Snot_aout     As Entr_mol              (Description:"Standard Entropy at Anode outlet");
287     Snot_cin      As Entr_mol              (Description:"Standard Entropy at Cathode inlet");
288     Snot_cout     As Entr_mol              (Description:"Standard Entropy at Cathode outlet");
289     Snot_coolin   As Entr_mol              (Description:"Standard Entropy at Coolant inlet");
290     Snot_coolout  As Entr_mol              (Description:"Standard Entropy at Coolant outlet");
291     SD_ain        As Entr_mol              (Description:"Entropy difference at Anode inlet");
292     SD_aout       As Entr_mol              (Description:"Entropy difference at Anode outlet");
293     SD_cin        As Entr_mol              (Description:"Entropy difference at Cathode inlet");
294     SD_cout       As Entr_mol              (Description:"Entropy difference at Cathode outlet");
```

```
295     SD_coolin     As Entr_mol          (Description:"Entropy difference at Coolant inlet");
296     SD_coolout    As Entr_mol          (Description:"Entropy difference at Coolant outlet");
297     Hnot_ain      As Enth_mol          (Description:"Standard Enthalpy at Anode inlet");
298     Hnot_aout     As Enth_mol          (Description:"Standard Enthalpy at Anode outlet");
299     Hnot_cin      As Enth_mol          (Description:"Standard Enthalpy at Cathode inlet");
300     Hnot_cout     As Enth_mol          (Description:"Standard Enthalpy at Cathode outlet");
301     Hnot_coolin   As Enth_mol          (Description:"Standard Enthalpy at Coolant inlet");
302     Hnot_coolout  As Enth_mol          (Description:"Standard Enthalpy at Coolant outlet");
303     HD_ain        As Enth_mol          (Description:"Enthalpy difference at Anode inlet");
304     HD_aout       As Enth_mol          (Description:"Enthalpy difference at Anode outlet");
305     HD_cin        As Enth_mol          (Description:"Enthalpy difference at Cathode inlet");
306     HD_cout       As Enth_mol          (Description:"Enthalpy difference at Cathode outlet");
307     HD_coolin     As Enth_mol          (Description:"Enthalpy difference at Coolant inlet");
308     HD_coolout    As Enth_mol          (Description:"Enthalpy difference at Coolant outlet");
309     S_In          As notype            (Description:"Total Entropy at inlet");
310     S_Out         As notype            (Description:"Total Entropy at outlet");
311     Delta_S       As notype            (Description:"Entropy difference for inlet & outlet");
312     S_Gen         As notype            (Description:"Entropy generation");
313     Exrg_Des      As power             (Description:"Exergy destruction");
314     Mol_Entr      As Entr_mol          (Description:"Entropy at Anode inlet");
315     E_ph_ain      As Enth_mol          (Description:"Physical exergy at anode inlet");
316     E_ph_aout     As Enth_mol          (Description:"Physical exergy at anode outlet");
317     E_ph_cin      As Enth_mol          (Description:"Physical exergy at cathode inlet");
318     E_ph_cout     As Enth_mol          (Description:"Physical exergy at cathode outlet");
319     E_ph_coolin   As Enth_mol          (Description:"Physical exergy at coolant inlet");
320     E_ph_coolout  As Enth_mol          (Description:"Physical exergy at coolant outlet");
321     E_ch_ain      As Enth_mol          (Description:"Chemical exergy at anode inlet");
322     E_ch_aout     As Enth_mol          (Description:"Chemical exergy at anode outlet");
323     E_ch_cin      As Enth_mol          (Description:"Chemical exergy at cathode inlet");
324     E_ch_cout     As Enth_mol          (Description:"Chemical exergy at cathode outlet");
325     E_ch_coolin   As Enth_mol          (Description:"Chemical exergy at coolant inlet");
326     E_ch_coolout  As Enth_mol          (Description:"Chemical exergy at coolant outlet");
327     E_chv_ain     As Enth_mol          (Description:"Chemical exergy of vapour at anode inlet");
328     E_chv_aout    As Enth_mol          (Description:"Chemical exergy of vapour at anode outlet");
329     E_chv_cin     As Enth_mol          (Description:"Chemical exergy of vapour at cathode inlet");
330     E_chv_cout    As Enth_mol          (Description:"Chemical exergy of vapour at cathode outlet");
331     E_chv_coolin  As Enth_mol          (Description:"Chemical exergy of vapour at coolant inlet");
332     E_chv_coolout As Enth_mol          (Description:"Chemical exergy of vapour at coolant outlet");
333     E_chl_ain     As Enth_mol          (Description:"Chemical exergy of liquid at anode inlet");
334     E_chl_aout    As Enth_mol          (Description:"Chemical exergy of liquid at anode outlet");
335     E_chl_cin     As Enth_mol          (Description:"Chemical exergy of liquid at cathode inlet");
336     E_chl_cout    As Enth_mol          (Description:"Chemical exergy of liquid at cathode outlet");
```

```
337     E_chl_coolin  As Enth_mol                (Description:"Chemical exergy of liquid at coolant inlet");
338     E_chl_coolout As Enth_mol                (Description:"Chemical exergy of liquid at coolant outlet");
339     Ex_ain        As Enth_mol                (Description:"Total exergy at anode inlet");
340     Ex_cin        As Enth_mol                (Description:"Total exergy at cathode inlet");
341     Ex_aout       As Enth_mol                (Description:"Total exergy at anode outlet");
342     Ex_cout       As Enth_mol                (Description:"Total exergy at cathode outlet");
343     Ex_coolin     As Enth_mol                (Description:"Total exergy at coolant inlet");
344     Ex_coolout    As Enth_mol                (Description:"Total exergy at coolant outlet");
345     Ex_In         As Energy_rate             (Description:"Total exergy into the system");
346     Ex_Out        As Energy_rate             (Description:"Total exergy out of the system");
347     Ex_Dest       As Energy_rate             (Description:"Exergy destroyed in the system");
348     Ex_Q          As Energy_rate             (Description:"Exergy of heat transfer in the system");
349     Ex_st         As Energy_rate             (Description:"Exergy stored in the system");
350     Ex_Delta      As Energy_rate             (Description:"Exergy difference between inlet and outlet");
351     Eta_X         As Input,Output notype     (Description:"Exergetic efficiency");
352     Vmem          As Vol_mol                 (Description:"Molar Volume of nafion");
353     Vw            As Vol_mol                 (Description:"Molar Volume of liquid water");
354     fv            As notype                  (Description:"Fraction of water in membrane");
355     knot          As Permeation_Coeff        (Description:"Maximum permeance for nitrogen", fixed, 1E-14);
356     kn2           As Permeation_Coeff        (Description:"Permeance for nitrogen");
357     Jn2           As Flow_mol_low            (Description:"Net Molar flow of nitrogen across the cell");
358     Jn2st         As Flow_mol_low            (Description:"Net Molar flow of nitrogen across the stack");
359     Jn2m          As Flow_mass_low           (Description:"Net Mass flow of nitrogen across the cell");
360     Jn2mst        As Flow_mass_low           (Description:"Net Mass flow of nitrogen across the stack");
361     Test1         As Input,Output notype     (Description:"Test Value",  1.0) ;
362     Test2         As Input,Output notype     (Description:"Test Value",  1.0) ;
363     Test3         As Input,Output notype     (Description:"Test Value",  1.0) ;
364     Col           As Output notype           (Description:"Charge of electricity in Amp-hrs");
365
366
367   // Total charge
368     Col = Icell * Time;
369
370   // Molecular weights of the components
371     Calling_MW:                   Call (MW) = pMolWeights();
372     Mol_Vol_Nafion:               Vmem * Rho_D = MWn;
373     Mol_Vol_LiqH2O:               Vw * 1000 = 18.0156;
374
375   // Ambient Conditions
376     TnotK = Tnot + 273.15;
377
378   // Operating Temperature
```

```
379     Delta_Temperature:            DeltaT = Cool_Out.T - Cool_In.T;
380     Cell_temperature:             Tcell = TopK;
381
382   // Temperature of outlet gases
383     Temp_Op_Kelvin:               TopK = Top + 273.15;
384
385   // Anode intlet conditions
386     In_A_Flash:                   Call (Yai, Xai, VFa, Hva, Hla) = Pflash (In_A.T, In_A.P, In_A.z);
387     In_A_Temperature:             Tain = In_A.T;
388     In_A_Pressure:                Pain = In_A.P;
389     In_A_H2_molflow:              Nfain("H2") = In_A.F * In_A.z("H2");
390     In_A_water_molflow:           Nfain("H2O") = In_A.F * In_A.z("H2O");
391     In_A_N2_molflow:              Nfain("N2") = In_A.F * In_A.z("N2");
392     In_A_inert_molflow:           NfaInert(CompListInerta) = In_A.F * In_A.z(CompListInerta);
393     In_A_Liquid_fraction:         LFa = 1 - VFa;
394     In_A_liquid_flow_rate:        Nflain("H2O") = Nfain("H2O") * LFa;
395                                   In_A.V.Lower: -1e35;
396
397   // Cathode intlet conditions
398     In_C_Flash:                   Call (Yci, Xci, VFc, Hvc, Hlc) = pFlash (In_C.T, In_C.P, In_C.z);
399     In_C_Temperature:             Tcin = In_C.T;
400     In_C_Pressure:                Pcin = In_C.P;
401     In_C_O2_molflow:              Nfcin("O2") = In_C.F * In_C.z("O2");
402     In_C_water_molflow:           Nfcin("H2O") = In_C.F * In_C.z("H2O");
403     In_C_N2_molflow:              Nfcin("N2") = In_C.F * In_C.z("N2");
404     In_C_inert_molflow:           NfcInert(CompListInertc) = In_C.F * In_C.z(CompListInertc);
405     In_C_Liquid_fraction:         LFc = 1 - VFc;
406     In_C_liquid_flow_rate:        Nflcin("H2O") = Nfcin("H2O") * LFc;
407                                   In_C.V.Lower: -1e35;
408
409   // Coolant inlet conditions
410     Cool_in_Flash:                Call (Ycooli, Xcooli, VFcool, Hvcool, Hlcool) = Pflash (Cool_In.T, Cool_In.P,
    Cool_In.z);
411     Cool_in_Temperature:          Tcoolin = Cool_In.T;
412     Cool_in_Pressure:             Pcoolin = Cool_In.P;
413     Cool_in_molflows:             Nfcoolin(ComponentList) = Cool_In.F * Cool_In.z;
414     Cool_in_Cp:                   Call (Cplin) = pCp_Mol_Liq (Cool_In.T, Cool_In.P, Cool_In.z);
415     Cool_in_Liq_fraction:         LFcool = 1 - VFcool;
416
417   // Anode outlet conditions
418     Out_A_Flash:                  Call (Yao, Xao, VFao, Hvao, Hlao) = pFlash (Out_A.T, Out_A.P, Out_A.z);
419     Out_A_Total_molflow:          Out_A.F = Sigma(Nfaout) + Sigma(NfaInert);
```

```
420     Out_A_Temperature:          Out_A.T = Top;
421     Out_A_Pressure:             Out_A.P = Paout;
422     Out_A_H2_molflow:           Out_A.z("H2") * Max(1e-5,Out_A.F) = Max(Nfaout("H2"));
423     Out_A_O2_molflow:           Out_A.z("O2") * Max(1e-5,Out_A.F) = Max(NfaInert("O2"));
424     Out_A_water_molflow:        Out_A.z("H2O") * Max(1e-5,Out_A.F) = Max(Nfaout("H2O"));
425     Out_A_N2_molflow:           Out_A.z("N2") * Max(1e-5,Out_A.F) = Max(Nfaout("N2"));
426
427                                 For i in CompListInert Do
428     Out_A_inert_molflow:         Out_A.z(i) * Max(1e-5,Out_A.F) = Max(NfaInert(i));
429                                 EndFor
430     Out_A_Enthalpy:             Call (Out_A.h) = pEnth_mol (Out_A.T, Out_A.P, Out_A.z);
431     Out_A_Vapor_Density:        Call (RHOaout) = pDens_Mol_Vap (Out_A.T, Out_A.P, Yao);
432     Out_A_Liquid_Density:       Call (RHOlaout) = pDens_Mol_liq (Out_A.T, Out_A.P, Xao);
433     Out_A_Liquid_fraction:      LFao = 1 - VFao;
434     Out_A_mass_bal:             Out_A.V * (RHOaout*VFao +RHOlaout*LFao) = 1;
435     Hydrogen_flow5:             Nfaout("H2") = Nfain("H2") - ((Icell+ILoss)*Ncells*3.6)/(ne*Faraday);
436     Out_A_liquid_flow_rate:     Nflaout("H2O") = Nfaout("H2O") * LFao;
437
438                                 If (N2_Cross=="Yes") Then
439                                   Nfaout("N2") = Nfain("N2") + Jn2st;
440                                  Else
441                                   Nfaout("N2") = Nfain("N2");
442                                 Endif
443
444                                 If (Water_Cross=="Yes") Then
445                                   Nfaout("H2O") = Nfain("H2O") + Jst;
446                                  Else
447                                   Nfaout("H2O") = Nfain("H2O");
448                                 Endif
449
450   // Cathode outlet connection
451     Out_C_Flash:                Call (Yco, Xco, VFco, Hvco, Hlco) = pFlash (Out_C.T, Out_C.P, Out_C.z);
452     Out_C_Total_molflow:        Out_C.F = Sigma(Nfcout) + Sigma(NfcInert);
453     Out_C_Temperature:          Out_C.T = Top;
454     Out_C_Pressure:             Out_C.P = Pcout;
455     Out_C_H2_molflow:           Out_C.z("H2") * Max(1e-5,Out_C.F) = Max(NfcInert("H2"));
456     Out_C_O2_molflow:           Out_C.z("O2") * Max(1e-5,Out_C.F) = Max(Nfcout("O2"));
457     Out_C_water_molflow:        Out_C.z("H2O") * Max(1e-5,Out_C.F) = Max(Nfcout("H2O"));
458     Out_C_N2_molflow:           Out_C.z("N2") * Max(1e-5,Out_C.F) = Max(Nfcout("N2"));
459
460                                 For i in CompListInert Do
461     Out_C_inert_molflow:         Out_C.z(i) * Max(1e-5, Out_C.F) = Max(NfcInert(i));
```

```
462                                 EndFor
463     Out_C_Enthalpy:             Call (Out_C.h) = pEnth_mol (Out_C.T, Out_C.P, Out_C.z);
464     Out_C_Vapor_Density:        Call (RHOcout) = pDens_Mol_Vap (Out_C.T, Out_C.P, Yco);
465     Out_C_Liquid_Density:       Call (RHOlcout) = pDens_Mol_liq (Out_C.T, Out_C.P, Xco);
466     Out_C_Liquid_fraction:      LFco = 1 - VFco;
467     Out_C_mass_bal:             Out_C.V * (RHOcout*VFco +RHOlcout*LFco) = 1;
468     Oxygen_flow6:               Nfcout("O2") = Nfcin("O2") - (0.5*(Icell+Iloss)*Ncells*3.6)/(ne*Faraday);
469     Out_C_liquid_flow_rate:     Nflcout("H2O") = Nfcout("H2O") * LFco;
470
471                                 If (N2_Cross=="Yes") Then
472                                   Nfcout("N2") = Nfcin("N2") - Jn2st;
473                                  Else
474                                   Nfcout("N2") = Nfcin("N2");
475                                 Endif
476
477                                 If (Water_Cross=="Yes") Then
478                                   Nfcout("H2O") = Nfcin("H2O") - Jst + ((Icell+ILoss)*Ncells*3.6)/(ne*Faraday);
479                                  Else
480                                   Nfcout("H2O") = Nfcin("H2O") + ((Icell+ILoss)*Ncells*3.6)/(ne*Faraday);
481                                 Endif
482
483   // Coolant outlet conditions
484     Cool_out_Flash:             Call (Ycoolo, Xcoolo, VFcoolo, Hvcoolo, Hlcoolo) =  Pflash (Cool_Out.T, Cool_Out.P
      , Cool_Out.z);
485     Cool_out_Temperature:       Top = Cool_Out.T;
486     Cool_out_Pressure:          Cool_Out.P = Cool_In.P - DPcool;
487     Cool_out_molfrac:           Cool_Out.z = Cool_In.z;
488     Cool_out_enthalpy:          Call (Cool_Out.h) = pEnth_mol (Cool_Out.T, Cool_Out.P, Cool_Out.z);
489     Cool_out_density:           Call (RHOcoolout) = pDens_Mol_Liq (Cool_Out.T, Cool_Out.P, Cool_Out.z);
490     Cool_out_mass_bal:          Cool_Out.V * RHOcoolout = 1;
491     Cool_out_Liq_fraction:      LFcoolo = 1 - VFcoolo;
492     Cool_out_Cp:                Call (Cplout) = pCp_Mol_Liq (Cool_Out.T, Cool_Out.P, Cool_Out.z);
493     Average_cooling_Cp:         Cplave  * 2 = Cplin + Cplout;
494     Coolant_flow_bal:           Cool_Out.F = Cool_In.F;
495
496   // Mass flows of inlet and outlet streams
497     Molar_mass_In_A:            Call (MWfin) = pMolWeight(In_A.z);
498     Molar_mass_In_C:            Call (MWain) = pMolWeight(In_C.z);
499     Molar_mass_Out_A:           Call (MWfout) = pMolWeight(Out_A.z);
500     Molar_mass_Out_C:           Call (MWaout) = pMolWeight(Out_C.z);
501     Molar_mass_CoolIn:          Call (MWcoolin) = pMolWeight(Cool_In.z);
502     Molar_mass_CoolOut:         Call (MWcoolout) = pMolWeight(Cool_Out.z);
```

```
503
504     In_A_Massflows:                MDOTain = In_A.F * In_A.z * MW;
505     In_A_Total_massflow:           MDain = Sigma(MDOTain);
506     In_C_Massflows:                MDOTcin = In_C.F * In_C.z * MW;
507     In_C_Total_massflow:           MDcin = Sigma(MDOTcin);
508     Out_A_Massflows:               MDOTaout = Out_A.F * Out_A.z * MW;
509     Out_A_Total_massflow:          MDaout = Sigma(MDOTaout);
510     Out_C_Massflows:               MDOTcout = Out_C.F * Out_C.z * MW;
511     Out_C_Total_massflow:          MDcout = Sigma(MDOTcout);
512
513   // Air to Fuel Ratio
514     Air_to_fuel_Ratio:             AFR * MDain = MDcin;
515
516   // Stoichiometric Constraints
517     Hydrogen_stoichiometry:        SH2 = Nfain("H2") / (Nfain("H2")-Nfaout("H2"));
518     Oxygen_stoichiometry:          SO2 = Nfcin("O2") / (Nfcin("O2")-Nfcout("O2"));
519
520   // Pressure losses
521     DeltaP_Anode:                  If (Icell <= 10.0) then
522                                      DPa = 0.05;
523                                    Else
524                                      DPa = 0.205945-0.10676*EXP((-1.3973E-10)*(Icell^(4.016)));
525                                    Endif
526
527     DeltaP_Cathode:                If (Icell <= 10.0) then
528                                      DPc = 0.05;
529                                    Else
530                                      DPc = 0.0996335 - 6.88E-04*Icell + 3.580E-05*(Icell^2) - 1.864E-07*(Icell^3) +
    2.922E-10*(Icell^4);
531                                    Endif
532     Ploss_In_A:                    Paout = Pain - DPa;
533     Ploss_In_C:                    Pcout = Pcin - DPc;
534     Ave_Pressure_anode:            Pa * 2 = (Pain + Paout);
535     Ave_Pressure_cathode:          Pc * 2 = (Pcin + Pcout);
536
537   // Partial pressures
538     PartialP_In_A:                 Ppain = In_A.z * Max(1e-5,Pain);
539     PartialP_In_C:                 Ppcin = In_C.z * Max(1e-5,Pcin);
540     PartialP_Out_A:                Ppaout = Out_A.z * Max(1e-5,Paout);
541     PartialP_Out_C:                Ppcout = Out_C.z * Max(1e-5,Pcout);
542
543   // Average Partial Pressures
```

```
544     Ave_An_pressureH2:            2 * PH2 = Ppain("H2") + Ppaout("H2");
545     Ave_An_pressureH2O:           2 * PaH2O = Ppain("H2O") + Ppaout("H2O");
546     Ave_Ca_pressureO2:            2 * PO2 = Ppcin("O2") + Ppcout("O2");
547     Ave_Ca_pressureH2O:           2 * PcH2O = Ppcin("H2O") + Ppcout("H2O");
548
549     Ave_Pressures_An:             2 * Paav = Ppain + Ppaout;
550     Ave_Pressures_Ca:             2 * Pcav = Ppcin + Ppcout;
551
552   // Water saturated vapor pressures
553     Sat_pressures_Out:            Call (Spout) = pVap_Pressures (Top);
554     Sat_pressures_In_A:           Call (Spain) = pVap_Pressures (Tain);
555     Sat_pressures_In_C:           Call (Spcin) = pVap_Pressures (Tcin);
556     Sat_pressures_st  :           Call (Spnot) = pVap_Pressures (Tnot);
557
558     Sat_pressure_In_A:            SatPain = Spain("H2O");
559     Sat_pressure_In_C:            SatPcin = Spcin("H2O");
560     Sat_pressure_Out:             SatPout = Spout("H2O");
561     Sat_pressure_st :             SatPnot = Spnot("H2O");
562
563   // Relative Humidities of inlet and outlet streams
564                                   If (Ppain("H2O") > SatPain) then
565                                     RHain = 1.0;
566                                    Else
567     Rel_humidity_In_A:              RHain * SatPain = Ppain("H2O");
568                                   Endif
569
570                                   If (Ppcin("H2O") > SatPcin) then
571                                      RHcin = 1.0;
572                                     Else
573     Rel_humidity_In_C:               RHcin * SatPcin = Ppcin("H2O");
574                                   Endif
575
576                                   If (Ppaout("H2O") > SatPout) then
577                                      RHaout = 1.0;
578                                     Else
579     Rel_humidity_Out_A:              RHaout * SatPout = Ppaout("H2O");
580                                   Endif
581
582                                   If (Ppcout("H2O") > SatPout) then
583                                      RHcout = 1.0;
584                                     Else
585     Rel_humidity_Out_C:              RHcout * SatPout = Ppcout("H2O");
```

```
                                Endif

// Water activity at electrodes
  Water_activity_a:             awa = DX * (RHain) + (1 - DX) * (RHaout);
  Water_activity_c:             awc = DX * (RHcin) + (1 - DX) * (RHcout);

// Water Cross-Over calculations
  Water_content_a:              Lmda_a = 0.043 + 17.18 * awa - 39.85 *(awa^2) + 36 *(awa^3);
  Water_content_c:              Lmda_c = 0.043 + 17.18 * awc - 39.85 *(awc^2) + 36 *(awc^3);
  Water_content_mem:            Lmda_mem * 2 = (Lmda_a + Lmda_c);
  Diffusion_coeff:              DC = 10E-6*(EXP((2416.0*((1.0/303)-1.0/TopK))))*(2.563-0.33*Lmda_c+0.0264*(Lmda_c^
2)-0.000671*(Lmda_c^3));
  Diffusion_anode:              Ja * (22.0*Faraday) = (2.5*Icd*lmda_a) *10;
  Diffusion_cathode:            Jc * (MWn * tm) = Rho_D * DC * 1E-4*(lmda_c-lmda_a);
  Net_diffusion_flux:           Jnet = Jc - Ja;
  Net_diffusion_flow:           Jnetn = Jnet * Acell * 3600;
  Net_diff_massflow:            Jnetm = Jnet * MW("H2O")* Acell * 3600;  //conversion of (mol/scm^2) to (kg/hr)
  Total_water_crossover:        Jst = Jnetn * Ncells;
  Total_water_masscross:        Jmst = Jst * MW("H2O");

// Nitrogen Cross-Over calculations
  Water_frac_membrane:          fv = (Lmda_mem * Vw)/(Lmda_mem*Vw + Vmem);
  N2_permeance:                 kn2 = Alpha * knot * (0.0295 + (1.21*fv) - 1.93*(fv^2)) * EXP((EN2/R)*((1/303)-(1/
TopK)));
  N2cross_mol_flow:             Jn2 * tm = kn2 * 3600 * (Pcav("N2") - Paav("N2")) * Acell * 100;
  N2cross_mass_flow:            Jn2m = Jn2 * MW("N2");
  N2molarcross_stack:           Jn2st = Jn2 * Ncells;
  N2masscross_stack:            Jn2mst = Jn2m * Ncells;

// Reagent Fluxes
  H2_Flux:                      JH2 * Acell * 3600 =  Nfain(CompH2);
  O2_Flux:                      JO2 * Acell * 3600 =  Nfcin(CompO2);

// Current density in the cell
  Total_current:                It *(3600) = ne * Faraday * (Nfain("H2")-Nfaout("H2"))*1000;
  Current_density:              Icd * (Acell*10000) = Icell;
  Calculated_current:           Icell2 * Ncells = It;
  Current_Loss:                 ILoss = Iin * Acell * 10000;
  Limiting_current_dens_A:      Ilim_a = SH2 * Imax;
  Limiting_current_dens_C:      Ilim_c = SO2 * Imax;

// Gibbs free energy
```

```
626     Calling_gibbs:                Call (GFE) = pGibbs_Mol_IDLGAS (Top, In_C.z);
627     Standard_gibbs:               Gstan =1E6 * (GFE("H2O") - GFE("H2") - 0.5*GFE("O2"));
628     Gibbs_deviation:              gTest = (R * (TopK) * LOGe(1/((PH2^(1))*(PO2^(0.5)))));
629     Calc_gibbs_energy:            Greal = Gstan + (R * (TopK) * LOGe(1/((PH2^(1))*(PO2^(0.5)))));
630
631     Calling_gibbs_not:            Call (GFnot) = pGibbs_Mol_IDLGAS (Tnot, In_C.z);
632     Standard_gibbs_not:           Gnot = 1E6 * (GFnot("H2O") - GFnot("H2") - 0.5*GFnot("O2"));
633
634   // Nernst Potential of the cell
635     Nernst_potential:             Vnrst * (ne*Faraday) = (-Greal);
636     Standard_potential:           Vnot * (ne*Faraday) = (-Gnot);
637
638   // Activation Overpotential
639     Constant_Aa:                  A_a = (1-B)* n_a;
640     Constant_Ac:                  A_c = (1-B)* n_c;
641     Exh_current_Density:          Ioc = 0.6 * Faraday * EXP((-B)*n_c*Faraday * 1.1/(R*TopK));
642     Act_anode:                    Vact_a = 0.00000001;
643     Act_cathode:                  Vact_c * (A_c * Faraday) = R * (TopK) * LOGe((Icd+Iin)/(Max(1.9E-7,Ioc)));
644     Act_overpotential:            Vact = Vact_a + Vact_c;
645
646   // Ohmic Overpotential
647     Electronic_resistance:        Relec = 0.00000001;
648     Ionic_resistance:             Rion = (180*(1+0.03*(Icd+Iin)+0.06*(TopK/303)^2*(Icd+Iin)^2.5)*(tm*100)/((Lmda_mem
    -0.63-3*(Icd+Iin))*EXP(16.4*((TopK-303)/TopK))));
649     Ionic_resist_ohms:            Rionic * (Acell*10000) = Rion;
650     Ohmic_overpotential:          Vohmic = (Icd + Iin ) * Acell *10000 * (Relec + Rionic);
651
652   // Concentration Overpotential
653     Conc_overpotential_Anode:     Vconc_a = ((-R*TopK)/(ne*Faraday)) * LOGe((1 - (Icd/Ilim_a)));
654     Conc_overpotential_Cathode:   Vconc_c = ((-R*TopK)/(ne*Faraday)) * LOGe((1 - (Icd/Ilim_c)));
655     Conc_overpotential:           Vconc = Vconc_a + Vconc_c;
656
657   // Fuel Cell Stack Power
658     Cell_voltage:                 Vcell = Vnrst - Vact - Vohmic - Vconc;
659     Stack_voltage:                Vstack = Vcell * Ncells;
660     Power_Stack:                  P_Gen * 1000 = Vcell * Icell * Ncells;
661     Cell_efficiency:              EtaCell * 1.25 = Vcell;
662
663   // WorkPort Connections
664     Work_power:                   Work.W = P_Gen;
665     Work_speed:                   Work.Speed = 0;
666
```

```
667   // HeatPort Connections
668     Heat_Generated:              -Heat.Q = (In_A.h*In_A.F + In_C.h*In_C.F - Out_A.h*Out_A.F - Out_C.h*Out_C.F) +
    Egen;
669     Heat_Produced:                H_Gen = -Heat.Q;
670
671   // Energy Balance
672     Energy_in:                   Ein = (In_A.h*In_A.F + In_C.h*In_C.F + Cool_In.h *Cool_In.F);
673     Energy_out:                  Eout = (Out_A.h*Out_A.F + Out_C.h*Out_C.F + Cool_Out.h * Cool_Out.F);
674     Energy_difference:           E_Delta = Ein - Eout;
675     Energy_generated:            Egen * 10E5 = -P_Gen * 3600;
676     Energy_loss:                 Eloss * 10E5 = -(h_conv*A_st*(TopK - TnotK)*3600);
677     Energy_stored:               Est * 10E5 = -(6000*0.04*0.75*$Tcell);
678     Energy_Balance:              Eout = Ein + Egen + Eloss + Est;
679
680   // Entropy Generation
681     Entropy_Anode_In:            Call (S_ain) = pEntr_mol (In_A.T, In_A.P, In_A.z);
682     Entropy_Cathode_In:          Call (S_cin) = pEntr_mol (In_C.T, In_C.P, In_C.z);
683     Entropy_Anode_Out:           Call (S_aout) = pEntr_mol (Out_A.T, Out_A.P, Out_A.z);
684     Entropy_Cathode_Out:         Call (S_cout) = pEntr_mol (Out_C.T, Out_C.P, Out_C.z);
685     Entropy_Coolant_In:          Call (S_coolin) = pEntr_mol (Cool_In.T, Cool_In.P, Cool_In.z);
686     Entropy_Coolant_Out:         Call (S_coolout) = pEntr_mol (Cool_Out.T, Cool_Out.P, Cool_Out.z);
687
688     Total_Entropy_In:            S_In * 3600 = S_ain*In_A.F + S_cin*In_C.F + S_coolin*Cool_In.F;
689     Total_Entropy_Out:           S_Out * 3600 = S_aout*Out_A.F + S_cout*Out_C.F + S_coolout*Cool_Out.F;
690     Entropy_Change:              Delta_S = S_Out - S_In;
691     Exegy_destroyed:             Exrg_Des = S_Gen *(TnotK);
692     Generated_entropy:           S_Gen * TnotK * 3600 = Ex_Dest *10E8;  // (W/K)
693
694                                  SD_ain = S_ain - Snot_ain;
695                                  SD_cin = S_cin - Snot_cin;
696                                  SD_aout = S_aout - Snot_aout;
697                                  SD_cout = S_cout - Snot_cout;
698                                  SD_coolin = S_coolin - Snot_coolin;
699                                  SD_coolout = S_coolout - Snot_coolout;
700
701                                  HD_ain = In_A.h - Hnot_ain;
702                                  HD_cin = In_C.h - Hnot_cin;
703                                  HD_aout = Out_A.h - Hnot_aout;
704                                  HD_cout = Out_C.h - Hnot_cout;
705                                  HD_coolin = Cool_In.h - Hnot_coolin;
706                                  HD_coolout = Cool_Out.h - Hnot_coolout;
707
```

```
708
709   // Exergy Balance
710     St_Entropy_Anode_In:          Call (Snot_ain) = pEntr_mol (Tnot, Pnot, In_A.z);
711     St_Entropy_Cathode_In:        Call (Snot_cin) = pEntr_mol (Tnot, Pnot, In_C.z);
712     St_Entropy_Anode_Out:         Call (Snot_aout) = pEntr_mol (Tnot, Pnot, Out_A.z);
713     St_Entropy_Cathode_Out:       Call (Snot_cout) = pEntr_mol (Tnot, Pnot, Out_C.z);
714     St_Entropy_Coolant_In:        Call (Snot_coolin) = pEntr_mol (Tnot, Pnot, Cool_In.z);
715     St_Entropy_Coolant_Out:       Call (Snot_coolout) = pEntr_mol (Tnot, Pnot, Cool_Out.z);
716
717     St_Enthalpy_Anode_In:         Call (Hnot_ain) = pEnth_mol (Tnot, Pnot, In_A.z);
718     St_Enthalpy_Cathode_In:       Call (Hnot_cin) = pEnth_mol (Tnot, Pnot, In_C.z);
719     St_Enthalpy_Anode_Out:        Call (Hnot_aout) = pEnth_mol (Tnot, Pnot, Out_A.z);
720     St_Enthalpy_Cathode_Out:      Call (Hnot_cout) = pEnth_mol (Tnot, Pnot, Out_C.z);
721     St_Enthalpy_Coolant_In:       Call (Hnot_coolin) = pEnth_mol (Tnot, Pnot, Cool_In.z);
722     St_Enthalpy_Coolant_Out:      Call (Hnot_coolout) = pEnth_mol (Tnot, Pnot, Cool_Out.z);
723
724     Ph_Exergy_Anode_In:           E_ph_ain = (In_A.h - Hnot_ain) - ((TnotK)*(S_ain - Snot_ain)/10E5);
725     Ph_Exergy_Anode_Out:          E_ph_aout = (Out_A.h - Hnot_aout) - ((TnotK)*(S_aout - Snot_aout)/10E5);
726     Ph_Exergy_Cathode_In:         E_ph_cin = (In_C.h - Hnot_cin) - ((TnotK)*(S_cin - Snot_cin)/10E5);
727     Ph_Exergy_Cathode_Out:        E_ph_cout = (Out_C.h - Hnot_cout) - ((TnotK)*(S_cout - Snot_cout)/10E5);
728     Ph_Exergy_Coolant_In:         E_ph_coolin = (Cool_In.h - Hnot_coolin) - ((TnotK)*(S_coolin - Snot_coolin)/10E5);
729     Ph_Exergy_Coolant_Out:        E_ph_coolout = (Cool_Out.h - Hnot_coolout) - ((TnotK)*(S_coolout - Snot_coolout)/
    10E5);
730
731     Ch_Ex_V_Anode_In:             E_chv_ain = (Yai("H2")*Em_H2 + Max(1e-5,Yai("H2O"))*Em_H2Og) + (R*(TnotK)*(Yai(
    "H2")*LOGe(Yai("H2")) + Max(1e-5,Yai("H2O"))*LOGe(Max(1e-5,Yai("H2O"))))/10E5);
732     Ch_Ex_V_Anode_Out:            E_chv_aout = (Yao("H2")*Em_H2 + Yao("H2O")*Em_H2Og) + (R*(TnotK)*(Yao("H2")*LOGe(
    Yao("H2")) + Yao("H2O")*LOGe(Yao("H2O")))/10E5);
733     Ch_Ex_V_Cathode_In:           E_chv_cin = (Yci("H2O")*Em_H2Og+Yci("N2")*Em_N2+Yci("O2")*Em_O2) + (R*(TnotK)*(Yci
    ("O2")*LOGe(Yci("O2"))+Yci("N2")*LOGe(Yci("N2"))+Yci("H2O")*LOGe(Yci("H2O")))/10E5);
734     Ch_Ex_V_Cathode_Out:          E_chv_cout = (Yco("H2O")*Em_H2Og+Yco("N2")*Em_N2+Yco("O2")*Em_O2) + (R*(TnotK)*(
    Yco("O2")*LOGe(Yco("O2"))+Yco("N2")*LOGe(Yco("N2"))+Yco("H2O")*LOGe(Yco("H2O")))/10E5);
735     Ch_Ex_V_Coolant_In:           E_chv_coolin  = (Ycooli("H2O")*Em_H2Og) + (R*(TnotK)*(Ycooli("H2O")*LOGe(Ycooli(
    "H2O")))/10E5);
736     Ch_Ex_V_Coolant_Out:          E_chv_coolout = (Ycoolo("H2O")*Em_H2Og) + (R*(TnotK)*(Ycoolo("H2O")*LOGe(Ycoolo(
    "H2O")))/10E5);
737
738     Ch_Ex_L_Anode_In:             E_chl_ain = Em_H2Ol;
739     Ch_Ex_L_Anode_Out:            E_chl_aout = Em_H2Ol;
740     Ch_Ex_L_Cathode_In:           E_chl_cin = Em_H2Ol;
741     Ch_Ex_L_Cathode_Out:          E_chl_cout = Em_H2Ol;
742     Ch_Ex_L_Coolant_In:           E_chl_coolin = Em_H2Ol;
```

```
743     Ch_Ex_L_Coolant_Out:          E_chl_coolout = Em_H2Ol;
744
745     Ch_Exergy_Anode_In:           E_ch_ain = E_chv_ain*VFa + E_chl_ain*(1-VFa);
746     Ch_Exergy_Anode_Out:          E_ch_aout = E_chv_aout*VFao + E_chl_aout*(1-VFao);
747     Ch_Exergy_Cathode_In:         E_ch_cin = E_chv_cin*VFc + E_chl_cin*(1-VFc);
748     Ch_Exergy_Cathode_Out:        E_ch_cout = E_chv_cout*VFco + E_chl_cout*(1-VFco);
749     Ch_Exergy_Coolant_In:         E_ch_coolin = E_chv_coolin*VFcool + E_chl_coolin*(1-VFcool);
750     Ch_Exergy_Coolant_Out:        E_ch_coolout = E_chv_coolout*VFcoolo + E_chl_coolout*(1-VFcoolo);
751
752     Total_Exergy_Anode_In:        Ex_ain = E_ph_ain + E_ch_ain;
753     Total_Exergy_Cathode_In:      Ex_cin = E_ph_cin + E_ch_cin;
754     Total_Exergy_Anode_Out:       Ex_aout = E_ph_aout + E_ch_aout;
755     Total_Exergy_Cathode_Out:     Ex_cout = E_ph_cout + E_ch_cout;
756     Total_Exergy_Coolant_In:      Ex_coolin = E_ph_coolin + E_ch_coolin;
757     Total_Exergy_Coolant_Out:     Ex_coolout = E_ph_coolout + E_ch_coolout;
758
759     Exergy_In     :               Ex_In = (Ex_ain*In_A.F + Ex_cin*In_C.F + Ex_coolin*Cool_In.F);
760     Exergy_Out    :               Ex_Out = (Ex_aout*Out_A.F + Ex_cout*Out_C.F + Ex_coolout*Cool_Out.F);
761     Exergy_Heat   :               Ex_Q = (1 - ((TnotK)/(TopK)))* (-Eloss);
762     Exergy_stored :               Ex_st = ($Tcell/(Tcell))*(-Est);
763     Exergy_Destroyed2:            Ex_Dest = Ex_In - Ex_Out - (-Egen) - Ex_Q - Ex_st;
764     Exergy_difference:            Ex_Delta = Ex_In - Ex_Out;
765     Exergetic_efficiency:         Eta_X = (P_Gen * 0.0036) / (Ex_In - Ex_Out);
766
767
768   End
```

A.2. Humidifier component model

Model - Humidifier

```
1   Model Humidifier
2
3   Parameter Comp Uses StringParameter
4         Valid As StringSet;
5     End
6
7   // Allow for mapping of names used in simulator to those in the model
8
9     CompH2      As Hidden Comp (Description:"Component name for hydrogen");
10    CompO2      As Hidden Comp (Description:"Component name for oxygen");
11    CompH2O     As Hidden Comp (Description:"Component name for water");
12    CompN2      As Hidden Comp (Description:"Component name for nitrogen");
13    CompCO2     As Hidden Comp (Description:"Component name for carbon dioxide");
14    CompAR      As Hidden Comp (Description:"Component name for argon");
15    CompH2.Valid : ComponentList;
16    CompO2.Valid : ComponentList;
17    CompH2O.Valid: ComponentList;
18    CompN2.Valid : ComponentList;
19    CompCO2.Valid: ComponentList;
20    CompAR.Valid : ComponentList;
21    CompH2 : "H2";
22    CompO2 : "O2";
23    CompH2O: "H2O";
24    CompN2 : "N2";
25    CompCO2: "CO2";
26    CompAR : "AR";
27
28  // Ports
29
30    In_Exh        As Input        MoleFractionPort;
31    In_Air        As Input        MoleFractionPort;
32    Out_Exh       As Output       MoleFractionPort;
33    Out_Air       As Output       MoleFractionPort;
34
35  // Parameters
36
37    RHair         As  RealParameter (Description:"Relative humidity of air out",                  0.95);
38
39  // Input variables
40
41    MWein         As  Molweight     (Description:"Average Molecular weight of exhaust at inlet",  3.5);
42    MWeout        As  Molweight     (Description:"Average Molecular weight of exhaust at outlet", 5.0);
```

```
43      MWain          As  Molweight      (Description:"Average Molecular weight of air at inlet",       27.5);
44      MWaout         As  Molweight      (Description:"Average Molecular weight of air at outlet",      25.0);
45      SatPain        As  Pressure       (Description:"Water saturation pressure at air inlet",         0.2);
46      SatPein        As  Pressure       (Description:"Water saturation pressure at exhaust inlet",     0.2);
47      SatPaout       As  Pressure       (Description:"Water saturation pressure at air outlet",        0.3);
48      SatPeout       As  Pressure       (Description:"Water saturation pressure at exhaust outlet",    0.3);
49      RHain          As  Notype         (Description:"Relative humidity of Air in",                    0.95);
50      RHein          As  Notype         (Description:"Relative humidity of Exhaust in",                0.92);
51      RHaout         As  Notype         (Description:"Relative humidity of Air out",          Fixed,   0.95);
52      RHeout         As  Notype         (Description:"Relative humidity of Exhaust out",               1.0);
53      Cpa_in         As  Cp_mol         (Description:"Specific heat of air inlet");
54      Cpa_out        As  Cp_mol         (Description:"Specific heat of air outlet");
55      Cpe_in         As  Cp_mol         (Description:"Specific heat of exhaust inlet");
56      Cpe_out        As  Cp_mol         (Description:"Specific heat of exhaust outlet");
57      RHOaout        As  Dens_mol_vap   (Description:"Air outlet vapor density", Free);
58      RHOeout        As  Dens_mol_vap   (Description:"Exhaust outlet vapor density", Free);
59      Ntr            As  Flow_mol       (Description:"Molar flow rate of transferred water");
60      Mtr            As  Flow_mass      (Description:"Mass flow rate of transferred water");
61      Temp_Aout      As  Temperature    (Description:"Outlet temperature of Air",             Fixed,    50);
62      DeltaP         As  Pressure       (Description:"Pressure drop in humidifier",           Fixed, 0.05);
63
64    // Variables with arrays
65
66      MW(ComponentList)        As Hidden Molweight  (Description:"Molecular weights");
67      MDOTain(ComponentList)   As Hidden Flow_mass  (Description:"Mass flow rate at air inlet");
68      MDOTein(ComponentList)   As Hidden Flow_mass  (Description:"Mass flow rate at exhaust inlet");
69      MDOTaout(ComponentList)  As Hidden Flow_mass  (Description:"Mass flow rate at air inlet");
70      MDOTeout(ComponentList)  As Hidden Flow_mass  (Description:"Mass flow rate at exhaust inlet");
71      MDain                    As Flow_mass         (Description:"Total mass flow rate at air inlet");
72      MDein                    As Flow_mass         (Description:"Total mass flow rate at exhaust inlet");
73      MDaout                   As Flow_mass         (Description:"Total mass flow rate at air outlet");
74      MDeout                   As Flow_mass         (Description:"Total mass flow rate at exhaust outlet");
75      Nfain(ComponentList)     As Hidden Flow_mol   (Description:"Molar flow rate at air inlet");
76      Nfein(ComponentList)     As Hidden Flow_mol   (Description:"Molar flow rate at exhaust inlet");
77      Nfaout(ComponentList)    As Hidden Flow_mol   (Description:"Molar flow rate at air outlet");
78      Nfeout(ComponentList)    As Hidden Flow_mol   (Description:"Molar flow rate at exhaust outlet");
79      Ppain(ComponentList)     As Hidden Pressure   (Description:"Partial pressure at air inlet");
80      Ppein(ComponentList)     As Hidden Pressure   (Description:"Partial pressure at exhaust inlet");
81      Ppaout(ComponentList)    As Hidden Pressure   (Description:"Partial pressure at air outlet");
82      Ppeout(ComponentList)    As Hidden Pressure   (Description:"Partial pressure at exhaust outlet");
83      SPain(ComponentList)     As Hidden Pressure   (Description:"Saturation pressures of components at air inlet");
84      SPein(ComponentList)     As Hidden Pressure   (Description:"Saturation pressures of components at air outlet");
```

```
85      SPaout(ComponentList)   As Hidden Pressure   (Description:"Sat pressures of components at exhaust inlet");
86      SPeout(ComponentList)   As Hidden Pressure   (Description:"Sat pressures of components at exhaust inlet");
87      Test                    As Notype            (Description:"Test Value",  1.0) ;
88
89    // Molecular weights of the components
90
91      Calling_MW:                       Call (MW) = pMolWeights();
92
93      Molar_mass_In_Air:                Call (MWain) = pMolWeight(In_Air.z);
94      Molar_mass_In_Exh:                Call (MWein) = pMolWeight(In_Exh.z);
95      Molar_mass_Out_Air:               Call (MWaout) = pMolWeight(Out_Air.z);
96      Molar_mass_Out_Exh:               Call (MWeout) = pMolWeight(Out_Exh.z);
97
98    // Air inlet conditions
99
100     In_Air_molflows:                  Nfain(ComponentList) =  In_Air.F * In_Air.z(ComponentList);
101                                       In_Air.V.Lower: -1e35;
102
103   // Exhaust inlet conditions
104
105     In_Exh_molflows:                  Nfein(ComponentList) =  In_Exh.F * In_Exh.z(ComponentList);
106                                       In_Exh.V.Lower: -1e35;
107
108   // Air outlet conditions
109
110     Out_Air_Temperature:              Out_Air.T = Temp_Aout;
111     Out_Air_Pressure:                 Out_Air.P = In_Air.P - DeltaP;
112                                       Nfaout(ComponentList - CompH2O) = Nfain(ComponentList - CompH2O);
113                                       Nfaout(CompH2O) = Nfain(CompH2O)+ Ntr;
114                                       Out_Air.F = Sigma(Nfaout);
115                                       Out_Air.z * Out_Air.F = Nfaout;
116
117     Out_Air_Enthalpy:                 Call (Out_Air.h) = pEnth_mol (Out_Air.T, Out_Air.P, Out_Air.z);
118     Out_Air_Density:                  Call (RHOaout) = pDens_Mol_Vap (Out_Air.T, Out_Air.P, Out_Air.z);
119                                       Out_Air.V * RHOaout = 1;
120
121   // Exhaust outlet conditions
122
123     Out_Exh_Pressure:                 Out_Exh.P = In_Exh.P - DeltaP;
124                                       Nfeout(ComponentList - CompH2O) = Nfein(ComponentList - CompH2O);
125                                       Nfeout(CompH2O) = Nfein(CompH2O)- Ntr;
126                                       Out_Exh.F = Sigma(Nfeout);
```

```
127                                   Out_Exh.z * Out_Exh.F = Nfeout;
128
129     Out_Exh_Enthalpy:             Call (Out_Exh.h) = pEnth_mol(Out_Exh.T, Out_Exh.P, Out_Exh.z);
130     Out_Exh_Density:              Call (RHOeout) = pDens_Mol_Vap (Out_Exh.T, Out_Exh.P, Out_Exh.z);
131                                   Out_Exh.V * RHOeout = 1;
132
133   // Water transferred to the air
134
135     MTR_transfer:                 Mtr = Ntr * MW(CompH2O);
136
137   // Partial pressures
138
139                                   Ppain("H2O") * In_Air.F = In_Air.P * Nfain("H2O");
140                                   Ppein("H2O") * In_Exh.F = In_Exh.P * Nfein("H2O");
141                                   Ppaout("H2O") * Out_Air.F = Out_Air.P * Nfaout("H2O");
142                                   Ppeout("H2O") * Out_Exh.F = Out_Exh.P * Nfeout("H2O");
143
144   // Water saturated vapor pressures
145
146     Sat_pressure_In_Air:          Call (SPain) = pVap_Pressures (In_Air.T);
147     Sat_pressure_In_Exh:          Call (SPein) = pVap_Pressures (In_Exh.T);
148     Sat_pressure_Out_Air:         Call (SPaout) = pVap_Pressures(Out_Air.T);
149     Sat_pressure_Out_Exh:         Call (SPeout) = pVap_Pressures (Out_Exh.T);
150
151                                   SatPain  = SPain(CompH2O);
152                                   SatPein  = SPein(CompH2O);
153                                   SatPaout = SPaout(CompH2O);
154                                   SatPeout = SPeout(CompH2O);
155
156   // Relative Humidities
157
158     RHair_in:                     RHain * SatPain = Ppain("H2O");
159     RHair_out:                    RHaout * SatPaout = Ppaout("H2O");
160     RHexh_in:                     RHein * SatPein = Ppein("H2O");
161     RHexh_out:                    RHeout * SatPeout = Ppeout("H2O");
162
163
164   // Mass flows of inlet and outlet streams
165
166     In_Air_Massflows:             MDOTain = In_Air.F * In_Air.z * MW;
167     In_Air_Total_massflow:        MDain = Sigma(MDOTain);
168
```

```
169     In_Exh_Massflows:               MDOTein = In_Exh.F * In_Exh.z * MW;
170     In_Exh_Total_massflow:          MDein = Sigma(MDOTein);
171
172     Out_Air_Massflows:              MDOTaout = Out_Air.F * Out_Air.z * MW;
173     Out_Air_Total_massflow:         MDaout = Sigma(MDOTaout);
174
175     Out_Exh_Massflows:              MDOTeout = Out_Exh.F * Out_Exh.z * MW;
176     Out_Exh_Total_massflow:         MDeout = Sigma(MDOTeout);
177
178
179   // Heat Transfer and Balance
180
181     call (Cpa_in) = pCp_Mol_Vap (In_Air.T, In_Air.P, In_Air.z);
182     call (Cpa_out) = pCp_Mol_Vap (Out_Air.T, Out_Air.P, Out_Air.z);
183     call (Cpe_in) = pCp_Mol_Vap (In_Exh.T, In_Exh.P, In_Exh.z);
184     call (Cpe_out) = pCp_Mol_Vap (Out_Exh.T, Out_Exh.P, Out_Exh.z);
185     0.85 *(MDein+MDeout)*(Cpe_in+Cpe_out)*(In_Exh.T-Out_Exh.T)=(MDain+MDaout)*(Cpa_in+Cpa_out)*(Out_Air.T-In_Air.T);
186
187   End
```

A.3. Control system codes

Model - Controller

```
1   Model Controller
2   // Use special controller flowsheet routing
3     IsController : True;
4
5   // Input/output variables
6     Input1      as input  control_signal (fixed, description:"Icell");
7     Input2      as input  control_signal (fixed, description:"SH2");
8     Input3      as input  control_signal (fixed, description:"SO2");
9     Input4      as input  control_signal (fixed, description:"Anode inlet pressure");
10    Input5      as input  control_signal (fixed, description:"Cathode inlet pressure");
11    Input6      as input  control_signal (fixed, description:"Coolant inlet temperature");
12    Input7      as input  control_signal (fixed, description:"Coolant outlet temperature");
13    Input8      as input  control_signal (fixed, description:"H2 inlet flow");
14
15    Output1_     as output control_signal (description:"Output signal1");
16    Output2_     as output control_signal (description:"Output signal2");
17    Output3_     as output control_signal (description:"Output signal3");
18    Output4_     as output control_signal (description:"Output signal4");
19    Output5_     as output control_signal (description:"Output signal5");
20    Output6_     as output control_signal (description:"Output signal6");
21    Output7_     as output control_signal (description:"Output signal7");
22
23  // Equations
24
25  // Anode stoichiometry balance
26    Output1_ = Input2 - (9.674527-8.154*EXP(-98.1898*(Input1^(-1.74))));
27
28  // Cathode stoichiometry balance
29    Output2_ = Input3 - (5.681865-3.896622*EXP(-23664.825*(Input1^(-3.484))));
30
31  // Anode pressure balance
32    Output3_  = 3.01026 - 1.91167*(EXP(-6.2568E-4*(Input1^1.2657))) - Input4;
33
34  // Cathode pressure balance
35    Output4_  = 2.854 - 1.794*(EXP(-1.525E-4*(Input1^1.488))) - Input5;
36
37  // Stack Delta T balance
38     Del_T   as Temp_diff   (Description:"Operating temperature");
39
40     if (Input1 <= 0) then
41         Del_T = 0;
42       elseif (Input1 > 0 AND Input1 < 60) then
```

```
43          Del_T = 6.2021/(1+32.13557*EXP(-0.114 * Input1));
44        elseif (Input1 >= 60) then
45          Del_T = 5 + (0.016666667 * Input1);
46        else
47          Del_T = 10;
48      endif
49
50      if (Input6 <= 50) then
51         Output5_ = 0;
52       else
53         Output5_ = Del_T - (Input7 - Input6);
54      endif
55
56
57    // Stack inlet temperature
58       Output6_ = Input6;
59
60    // Compressor Efficiency
61       Output7_ = (0.5267*Input1)/(26.83+Input1);
62
63    End
```

Model - Purge_Control

```
Model Purge_Control

  IsController : True;

// Parameters
  Parameter SelectType uses StringParameter
    valid as stringset(["Auto","Time","Amp-S","Bleed","None"]);
    value : "Time";
  end;

  Select  as SelectType  (description:"Select purging method");

END
```

Task - Purge_Ctrl

```
Task Purge_Ctrl runs at 2

  If (Selector.Select=="Time") Then
      Ramp (Purge_Valve.sf("RC2"), 0.8, 0.01/60);
        Wait 0.005;
      Ramp (Purge_Valve.sf("RC2"), 1.0, 0.015/60);
      Restart after 1;
    Elseif (Selector.Select=="Amp-S") Then
      Ramp (Purge_Valve.sf("RC2"), 0.8, 0.01/60);
    Elseif (Selector.Select=="Bleed") Then
      Ramp (Purge_Valve.sf("RC2"), 0.96, 0.02/60);
    ElseIf (Selector.Select=="Auto") Then
  Endif

End
```

A.4. Aspen Tasks, feed streams & efficiency

Model - Feed

```
1   Stream Feed
2
3   /* Vapor feed model to calculate feed molar enthalpy and molar volume */
4
5     rhov_in as Dens_mol_vap       (Description:"Molar Vapor density");
6     Inlet as Output MoleFractionPort;
7     Inlet.F.spec: Fixed;
8     Inlet.T.spec: Fixed;
9     Inlet.P.spec: Fixed;
10    Inlet.Z.spec: Fixed;
11    call (Inlet.h) = pEnth_mol (Inlet.T, Inlet.P, Inlet.z);
12    call (rhov_in) = pDens_Mol_vap (Inlet.T, Inlet.P, Inlet.z);
13    Inlet.v = 1/rhov_in;
14    Inlet.v.Lower:-1e35;
15
16  End
```

Model - Liq_Feed

```
1   Stream Liq_Feed
2
3   /* Liquid feed model to calculate feed molar enthalpy and molar volume */
4
5     rhov_in as Dens_mol_Liq       (Description:"Molar Vapor density");
6     Inlet as Output MoleFractionPort;
7     Inlet.F.spec: Fixed;
8     Inlet.T.spec: Fixed;
9     Inlet.P.spec: Fixed;
10    Inlet.Z.spec: Fixed;
11    call (Inlet.h) = pEnth_mol (Inlet.T, Inlet.P, Inlet.z);
12    call (rhov_in)     = pDens_Mol_Liq (Inlet.T, Inlet.P, Inlet.z);
13    Inlet.v = 1/rhov_in;
14    Inlet.v.Lower:-1e35;
15
16  End
```

Task - Startup

```
1   Task Startup runs once when time == 0.0
2
3    SRamp (Purge_valve.sf("RC2"), 1, 2/60);
4    SRamp (PEMFC.Icell, 120, 6/60);
5
6    wait for time == 6.333;
7      SRamp (PEMFC.Icell, 60, 3/60);
8
9    wait for time == 6.833;
10     SRamp (PEMFC.Icell, 120, 3/60);
11
12  End
```

Model - Efficiency

```
1   Model Efficiency
2
3   // Use special controller flowsheet routing
4     IsController : True;
5
6   // Input/output variables
7     LHV         as input  control_signal (fixed, description:"LHV");
8     M_Flow      as input  control_signal (fixed, description:"Mass flow");
9     Net_Pin     as input  control_signal (fixed, description:"Net Power");
10
11    Eta     as output control_signal (description:"System Efficiency");
12    Fuel_E  as power                 (Description:"Fuel energy in KW");
13    Net_P   as power;
14
15  // Equations
16    Net_P = -Net_Pin;
17    Fuel_E * 3.6 = LHV * M_Flow;
18    Eta * Fuel_E = (Net_P);
19
20  End
```

Appendix B

Paper I

Rabbani A, Rokni M, Hosseinzadeh E, Mortensen H. “Start–up Analysis of a PEM Fuel Cell System in Vehicles”, International Journal of Green Energy, 2013; 11: 1–21.

Start–up Analysis of a PEM Fuel Cell System in Vehicles

Abid Rabbani[1], Masoud Rokni[1], Elham Hosseinzadeh[1] and Henrik Hilleke Mortensen[2]

1. Thermal Energy Section, Department of Mechanical Engineering, Technical University of Denmark, 2800 Kgs. Lyngby, Denmark.
2. H2Logic A/S, 7400 Herning, Denmark.

ABSTRACT

Addressing large load fluctuation in automotive applications, dynamic analysis of a Polymer Electrolyte Membrane Fuel Cell system is conducted here. Operations of a comprehensive system–level control–oriented fuel cell model with all necessary auxiliary components are demonstrated and simulation results for start–up scenario are presented. It is shown that system stability is influenced by slow thermal management controls. High loads at start–up affect voltage and system efficiency adversely. Cathode inlet water levels are found to be adequate for humidification of recirculated fuel stream. Liquid water at cathode outlet is considerably higher at high current density start–ups, pertaining to water removal issues.

Keywords: *Dynamic simulation, System modeling, fuel cell, PEMFC, water crossover.*

1 Introduction

Hydrogen is expected to play a major role in future energy economy. Fuel cells have shown a significant potential as an efficient solution for harnessing energy of hydrogen. Therefore, fuel cells are recognized to be one of the future power supply systems. The proton exchange membrane fuel cell (PEMFC) currently appears to be the preferred fuel cell for a variety of mobile applications, mainly due to its relatively low operating temperature, quick start–up, high power density and efficiency, system robustness and low degradation due to corrosion.

Fuel cell operating requirements in vehicles are more inflexible than stationary applications. These systems have to operate at varying conditions related to temperatures, pressures, power load and humidity. All the auxiliary components constitute the balance of plant (BoP). These auxiliary components, such as air and fuel supply system which include air blower (compressor) and control valves, and the thermal control system which comprises of heat exchangers, coolant pumps and air radiators are essential for successful operation of the fuel cell system. Therefore, system level dynamic

modelling becomes a useful tool in analysis of PEMFC systems. Such studies help in improving system efficiency, design development and optimization of control strategies. Very few researchers have reported on dynamic modelling of complete PEMFC systems along with their BoP. Whereas, steady–state models of these systems are present in abundance. A few others have studied these system components individually, where most of the research focuses on the fuel cell or the stack itself.

A number of PEM fuel cell models are available in the literature. (Ceraolo, Miulli and Pozio, 2003) developed a simplistic dynamic model based on cathode kinetics. (Amphlett et al., 1996) extended their previous steady–state model and presented a generalized transient model. Another bulk dynamic model catering to inverter load effects is presented by (Yerramalla, Davari and Feliachi, 2002). (Pathapati, Xue and Tang, 2005) developed a complete fuel cell model that included effects of double charge layers at cell sites along with mass and energy balance equations for the gases and the dynamics of flow and pressure in the channels. (Jia et al., 2009) also followed suit and developed a dynamic model in MATLAB/Simulink to investigate fuel cell transient electrical responses under various operating conditions. Though these models provide valuable understanding of intricate fuel cell operations, they are mostly aimed at design and optimization of individual cell components and operating parameters without going into system level analysis.

Multi–dimensional models on the other hand, disseminate complex characteristics of reactant flows and charge transportation within fuel cells. (Hu et al., 2004) represented a three–dimensional computational PEM fuel cell model with conventional and inter–digitized flow fields. Another three–dimensional mixed–domain PEM fuel cell model of (Kim et al., 2009), which integrates intrinsic transport mechanisms, has been applied to investigate effects of the fully coupled transport phenomena. These models might be useful in predicting cell or stack performance, however due to high computational times and limitations to integrate with BoP components, these models are not suitable for system–level modelling.

Of all publications in open literature, relatively few studies account for control–oriented PEMFC models. (Pukrushpan, Peng and Stefanopoulou, 2004) presented a transient dynamic model, which includes in–blower flow and inertia dynamics, manifold filling dynamics, reactant partial pressures and membrane humidity. A control–oriented thermal dynamic model is also proposed by (del Real, Arce and Bordons, 2007). (Ahn and Choe, 2008) investigated temperature effects on the overall system performance and suggested strategies for coolant controls. Issues related to temperature dynamics are also dealt and studied by (Vasu and Tangirala, 2008), which could predict the effects of temperature and feed flows on system transient behaviour. From a control perspective, it is important to develop a complete model that emulates the real behaviour of PEMFC stack when subject to varying operating conditions. Therefore, a need to develop a system–level model is identified that responds to dynamic effects of all the necessary BoP components which is lacking in the aforementioned studies.

While some researchers such as (Shan and Choe, 2006) and (Park and Choe, 2008) presented a transient stack model and analysed the temperature distribution on fuel cells, management of stack temperature by coolant flow controls becomes vital in efficient operations and reliable performance of the fuel cell system. (Khan and Iqbal, 2005) proposed a transient model to predict efficiency in terms of voltage output and heat losses by including heat transfer coefficients for the stack and an energy balance. (Jung and Ahmed, 2010) developed a thermal stack model based on real–time simulator in MATLAB/ Simulink environment. (Asghari, Akhgar and Imani, 2011) also designed a thermal management system for a PEMFC which is oriented towards the flow fields within the stack. Again these studies concentrate on the stack level without looking into dynamic characteristics that are influenced by auxiliary components.

Start–up behaviour of PEMFC stacks at sub–zero temperatures has been studied and reported by few researchers. (Youcai Li et al., 2011) conducted experiments and validated their model based on the results. (Yan et al., 2006) investigated effects of sub–freezing temperatures on fuel cell performance and start–up. A model for freeze start is also developed by (Mangold et al., 2011) and compared to experimental data. (Meng, 2008) and (Sundaresan and Moore, 2005) both proposed thermal models for cold start of PEMFC. However, start–up behaviour of a stack above the freezing temperatures which accounts for multiple varying operating conditions and changing auxiliary components outputs has not been reported to a greater extent.

Building on these modelling studies, a complete control–oriented system–level dynamic model is proposed in this paper which incorporates all necessary BoP components for a PEMFC fuel cell stack by including electrochemical, thermal, feed flows and water transportation models and a detailed control strategy. In totality, this work differs from previous studies such that here a sizable focus has been set for (i) comprehensive control strategy regulating hydrogen and air feed flows, coolant inlet and fuel cell stack operating temperatures, (ii) thermal model with liquid coolant circuit incorporated in it which takes into account reactant and product phase changes, (iii) Thermal management including effects of coolant controls and heat exchangers on fuel cell stack performance, and (iv) Water management and effects of water crossover on anode recirculation loop and fuel cell relative humidity.

Thus the objective of this study aims at design and modelling of a complete system that incorporates all the essential auxiliary components with comprehensive control strategies in order to emulate a real PEMFC system. Here, the focus is on the start–up sequence of the proposed system.

2 System Configuration

Figure 1 shows the schematics of fuel cell system analysed in this study. It includes all the components in the system, such as PEMFC stack, air blower and humidifier, pumps, heat exchangers and radiator for the cooling circuit, flow valves and controllers. Compressed air is cooled and humidified before entering the cathode side of the stack. On the other side, pressurized hydrogen from storage tank is fed to the anode of fuel

cell. Since a higher fuel stoichiometry is maintained, anode exhaust is recirculated back to the feed stream via a recirculation pump.

Heat produced in the stack is absorbed by the coolant which circulates in a circuit associated with the stack and a heat exchanger. An external cooling loop, connected to the aforementioned heat exchanger, in turn cools the water in the internal circuit.

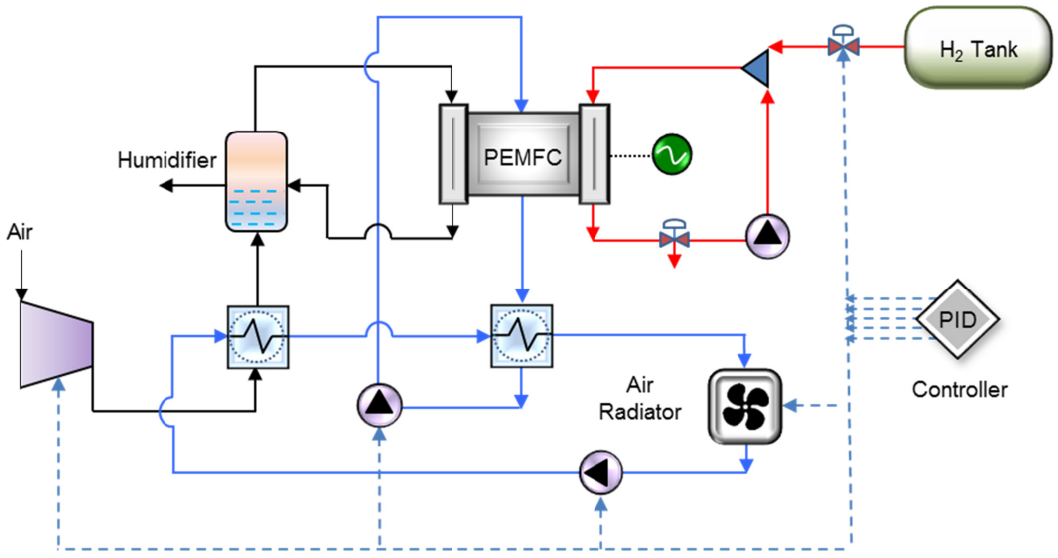

Figure 1. Schematic of a complete PEM fuel cell system with auxiliary components.

This circuit also comprises of a heat exchanger to precool the blown air and an air radiator for heat rejection from the system. Flow of water is regulated by pumps in the respective circuits. In order to ensure a stable operation of the system, a control system is needed to regulate flows, temperatures and pressures in the feed streams, cooling circuits and plant components. Therefore, in the present study, PID controllers are deployed to emulate the system in real time and thereby analyse response characteristics under varying operating conditions. Aspen Plus dynamics (Aspentech 2012) comprises of built–in PID controllers and manipulators. Combinations of these components are used to devise controls for entire system. These controllers collect data from various component inlet and outlets which are regarded as pressure, temperature and flow transmitters, and manipulate the corresponding components to reach the desired state. Due to this fact, current system responses and its behaviour are attributed to the formulated control strategy which is based on fuel cell stack limitations and recommendations by the manufacturer. Component properties related to these limitations are discussed in the following subsections whereas intricate details of system controls are dealt in the relevant section later.

2.1 Fuel Cell stack

In this study, a Ballard fuel cell stack (Ballard Mark9 SSL, 2008) has been specifically adapted. The model, which is based on equations adopted by (Hosseinzadeh and Rokni, 2012), contains some parameters which are attributed to the physical characteristics of the system, as well as on operating conditions and membrane properties. Some of these parameters which are obtained below in this section for the Ballard stack are shown in Table 1. Current research aims to build up a system which meets the requirements of actual stack running under recommended conditions.

Table 1. Parameter estimation for Ballard Fuel cell stack

Parameter	**Value**
Number of electrons transferred per mole of fuel, n_e $\left(mol_e/mol_{fuel}\right)$	2
Number of electrons for the reaction rate, n_{el} $\left(mol_e/mol_{fuel}\right)$	1 for cathode and 4 for anode
Internal current density, i_n $\left(A/cm^2\right)$	0.002
Symmetry factor, β	0.5
Membrane thickness, t_m (cm)	0.0183
Density of the membrane–dry condition, ρ_{dry} $\left(g/cm^3\right)$	3.28
Molecular weight of membrane, M_m (Kg/mol)	1.1

During normal steady state operation, reactant pressure should be above coolant pressure whereas for short transients and during start–up, coolant pressure may exceed reactant pressure. It is recommended to operate the anode at a higher pressure than the cathode. Nitrogen crosses over from the cathode to anode as cathode pressure increases relative to the anode pressure. Ensuring that cathode pressure is lower than the anode pressure will minimize nitrogen crossover and improve cell stability. In a system with fuel recirculation, the consumption will be slightly above 1.0 stoichiometry as 1% to 2% of the flow will be required for purging. In the present study, purge occurrences are neglected. For a maximum service life and efficiency of the stack, Ballard recommends operating conditions within which the stack should operate, (Ballard Mark9 SSL, 2008), which are followed in this study. Figure 2 reports recommended reactant inlet pressures and nominal pressure drops within the fuel cell stack.

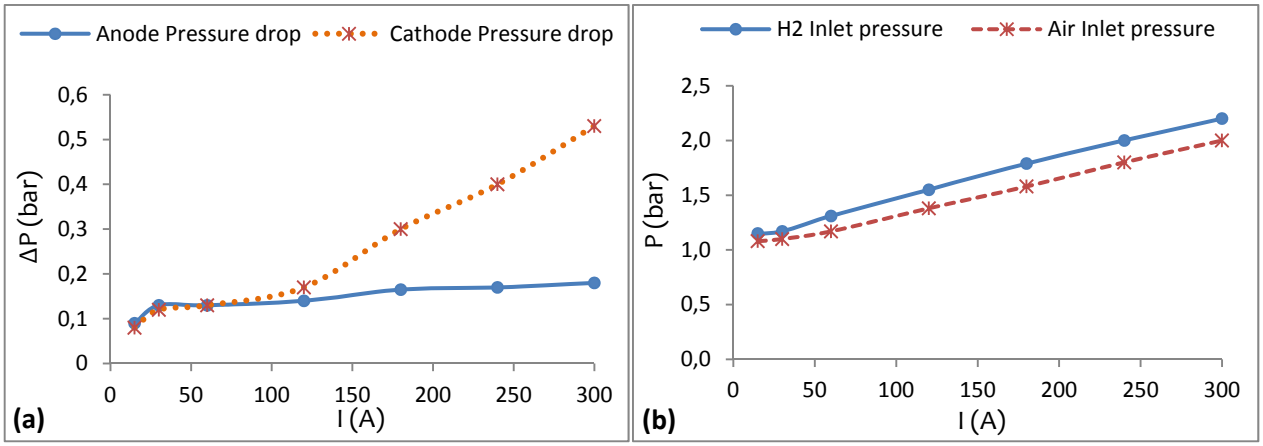

Figure 2. Stack data provided by Ballard (a) Nominal pressure drop within the fuel cell, (b) Inlet pressures for reactants.

2.2 Humidifier

One of the key issues in PEMFC is the dehydration in the membrane. A fully hydrated membrane supports the ionic crossover between the electrodes, as well as extends its life. Therefore, reactants in the PEMFC need to be humidified before entering the stack. In the present model, a humidifier utilizes the water produced by chemical reaction inside the fuel cells to humidify the inlet air. A simple model based on mass and energy balance is implemented here. Although some empirical models could be considered, these vary over a wide range depending upon the types of humidifiers used. Due to the lack of sufficient data, it is assumed that the inlet air is optimally humidified after passing through the humidifier. The relative humidity of air entering the cathode is set to 95% in the calculations; although other values can be chosen. This assumption could be justified as it is very close to the real operational conditions. On the anode side, there is no humidifier and the fuel is humidified by means of water crossover and its recirculation. It is observed that water cross–over from cathode to anode through the membrane is adequate enough to raise the relative humidity in the anode exhaust to 100%. This recirculation, when mixed with inlet stream delivers the desired humidity into the anode of the fuel cell.

2.3 Reactant feed systems

The fuel cell system is composed of blowers, pumps and valves that regulate flows of material streams. A valve is placed between the hydrogen tank and inlet manifold of anode which enables or disables the hydrogen supply. This regulatory valve adjusts high hydrogen pressure of the tank to the desired operating pressure of the fuel cell. Since the system does not operate on dead–end mode, the amount of hydrogen regulated by this valve equals the stoichiometric hydrogen required of the fuel cell. Stoichiometric

ratio is defined as the amount of reactant supplied to the amount which is consumed in the reaction.

Flow and pressure of oxidant into the cathode is regulated by the blower. The amount of stoichiometric oxygen for the fuel cell reaction is manipulated by a controller which regulates the electrical power of the blower, and hence compression and air flow.

2.4 Heat Exchangers and thermal management system

As can be seen in Fig.1 a network of heat exchangers constitute the thermal management of the prescribed system. They extract the heat produced from the cell stack and maintain the selected operating temperature which is essential for performance and durability of the fuel cell. Although heat exchanger models used here are predefined in Aspen Dynamics, some of the parameters have been assumed on the basis of media entering the hot and cold sides of these heat exchangers. The heat exchanger, which is connected to the internal cooling loop, has liquid water on both its hot and cold side. Therefore, a UA value of 1.0 kW/K is assumed. Whereas, UA values for air pre–cooler and radiator are approximated to be 0.05 kW/K and 0.3 kW/K respectively. In performing the simulations, the pressure drop was assumed to be 0.05 on both sides of heat exchangers. The corrected LMTD is calculated in addition to the corresponding inlet and outlet temperatures of hot and cold streams.

2.5 Pumps and Blowers

In the above proposed system, air blower, anode recirculation pump and water pumps are one of the BoP components which are also regulated by the control system. Aspen Dynamics ™ contains models of these units in its library as well. Since the nominal power of the PEMFC is only 21 kW, mass flow rates of fuel and air are very low. Therefore, very low values of isentropic efficiencies are suggested in this paper. The efficiency of a blower ranges from 15% to 40% in the calculations, depending on the air mass flow. Calculated pump efficiencies are also very low for the cooling water circuits and are determined to be around 70%.

3 Methodology

The characteristics of the PEMFC system described above are implemented in Aspen Plus Dynamics ™ (Aspentech 2012) which is a simulation tool for process modelling and energy system analysis. It is a component based simulation tool with a built–in unit operation modules library. The component library includes models of heat exchangers, reactors, turbo machinery, decanters and separators, pressure relief valves, controllers along with utility components and manipulators. These components are built upon by a standard set of equations representing their physical properties, such as isentropic and mechanical efficiencies in blowers and turbines. Also, user–based–custom–models can be imported into the program.

In Aspen plus Dynamics, the physical model of the complete system is devised by connecting the relevant component models through work, heat or material streams and by defining operating conditions for the system. The numerical solvers then convert these inputs into set of dynamic mathematical equations to be solved simultaneously. These equations include mass and energy conservation for all units and connecting streams, as well as relations for thermodynamic properties of the fluids involved. In addition, the program has the ability to run steady–state, initialization and dynamic simulations for the same model by changing model or module specifications. Occurrences of disturbances and operation constraints can be enforced by adding control modules to the constructed system. An implicit integrator ensures stable solution of the dynamic simulation and varies the integration step to ensure simulation accuracy.

The PEMFC stack model presented in this study is based on a model developed by (Hosseinzadeh and Rokni, 2012). They built a steady–state model for the same Ballard fuel cell stack (Ballard Mark9 SSL, 2008) which is under investigation in the present study. That study presented the effectiveness, validation and reliability of the model at different operating conditions and conducted sensitivity analysis for effects of coolant temperatures, humidity and reactant stoichiometry on system operations. However, system behaviour at start–up and varying operating conditions was not studied, which would have provided a detailed insight into transient performance of the system. In contrast to their steady–state model, here a dynamic model of the prescribed system is developed in Aspen Custom Modeller. This model constitutes equations for fuel cell electro–chemistry, mass and energy balances, water crossover in membrane and fuel cell thermodynamics. The model is implemented into ASPEN Plus Dynamics and system controls are implemented in order to ensure stable operation of the plant during load changes.

The thermodynamic efficiency and net power of the system are determined by the current drawn and voltage produced by the stack. The average cell voltage of a fuel cell is defined by an analytical expression:

$$V_{cell} = E - \eta_{act} - \eta_{ohmic} - \eta_{conc} \tag{1}$$

where E is the theoretical voltage, η_{act} the activation overpotential, η_{ohmic} ohmic overpotential and η_{conc} denotes concentration loss. Theoretical voltage is usually expressed by Nernst equation (Spiegel, 2007):

$$E = \frac{-\Delta \bar{g}_f^0}{n_e F} + \frac{RT}{n_e F} \ln\left(\frac{a_{H_2O}}{a_{H_2} a_{O_2}^{0.5}} \right) \tag{2}$$

where a is the activity of the species. Here the assumption of all reactants being ideal follows that the activity of the gases is equal to their partial pressures and the activity of liquid water is equal to 1. Then we have:

$$E = \frac{-\Delta \bar{g}_f^0}{n_e F} + \frac{RT}{n_e F} \ln\left(P_{H_2}^{-1} P_{O_2}^{-0.5} \right) \tag{3}$$

n_e is the number of electrons transferred per mole of fuel which here is hydrogen in the present case. Therefore, $n_e = 2$ is set; according the reactions taking place on the cathode side.

Change in Gibbs free energy $\Delta\bar{g}_f^0$ for the reaction below, is calculated at standard pressure but is still a function of temperature.

$$\Delta\bar{g}_f^0 = \left(\bar{g}_f^0\right)_{H_2O} - \left(\bar{g}_f^0\right)_{H_2} - \frac{1}{2}\left(\bar{g}_f^0\right)_{O_2} \tag{4}$$

The total activation losses in the cell are equal to sum of anode and cathode contributions. Knowing this and assuming equal transfer coefficients in both electrodes, the Butler–Volmer equation is simplified as:

$$\eta_{act} = \eta_{act,c} + \eta_{act,a} = \frac{RT}{\alpha_c F}\ln\left(\frac{i+i_n}{i_{0,c}}\right) + \frac{RT}{\alpha_a F}\ln\left(\frac{i+i_n}{i_{0,a}}\right) \tag{5}$$

According to the base model, the value for internal current density, i_n is assumed to be equal to $0.002\,A/cm^2$. The equations below are valid for evaluating the transfer coefficients on the anode and cathode side respectively:

$$\alpha_a = \beta \cdot n_{el} \tag{6}$$

$$\alpha_c = (1-\beta)\cdot n_{el} \tag{7}$$

The symmetry factor, $\beta = 0.5$ is chosen, n_{el} is equal to 4 for anode and 1 for cathode, see (Santarelli, Torchio and Cochis, 2006).

For exchange current density i_0, an analytical expression is chosen here, which predicts the value of exchange current density at the anode and cathode separately.

$$i_{0,a} = n_{el}\cdot F\cdot k_a \cdot \exp\left(\frac{(1-\beta)\cdot n_{el}\cdot F\cdot E}{RT}\right) \tag{8}$$

$$i_{0,c} = n_{el}\cdot F\cdot k_c \cdot \exp\left(\frac{-\beta\cdot n_{el}\cdot F\cdot E}{RT}\right) \tag{9}$$

The net water transport through the membrane is a combination of these two effects; electro osmotic drag and back diffusion and is given as:

$$J_{H_2O} = 2n_{drag}\frac{i}{2F} - \frac{\rho_{dry}}{M_m}D_\lambda\frac{d\lambda}{dz} \tag{10}$$

Another parameter needed for calculation of net water flux is water diffusion which is a function of membrane water content, λ. Here, the expression suggested by (Springer, Zawodzinski and Gottesfeld, 1991) is used:

$$D_{\lambda>4} = 10^{-6}\exp\left[2416\cdot\left(\frac{1}{303}-\frac{1}{T}\right)\right]\cdot\left(2.563 - 0.33\lambda + 0.0264\lambda^2 - 0.000671\lambda^3\right) \tag{11}$$

The total energy into the fuel cell is consumed by the electrical power output, heat removed by the coolant, heat loss at the stack surface and energy stored within the stack itself. In the current model, a lumped thermal model proposed by (Khan and Iqbal, 2005) is considered. The stack is regarded as a single thermal mass with a heat capacity.

With the assumption of stack temperature being equal to the coolant temperature at the outlet, heat exchanged with the coolant and hence stack operating temperature could be determined. The energy balance between the above–mentioned modes can be given by:

$$C_t \cdot dT/dt = \dot{P}_{in} - \dot{P}_{out} - \dot{P}_{el} - \dot{Q}_{loss} \quad (12)$$

where, C_t is the thermal capacitance of the stack, $\dot{P}_{in}$ is the total power delivered by the fuel to the stack (kW), $\dot{P}_{el}$ is the power consumed by the electrical load (kW), $\dot{P}_{out}$ is the heat transferred to the cooling water circulating in the stack (kW), and $\dot{Q}_{loss}$ is the heat dissipated to the ambient (kW).

The subordinate components in the BoP, i.e. anode recirculation and water pumps, air blower, mixers and heat exchangers are modelled using the default mathematical models provided in Aspen Plus Dynamics.

4 Control System

This section presents the methodology of controlling system parameters and operating conditions for the system to have a stable operation. Classic proportional–integral (PI) controllers, which are widely used in industrial control systems, are employed to regulate different components and flow streams. Principally, these controllers calculate "error" value as the difference between a measured process variable and a desired set–point, and attempt to minimize this error by adjusting the process control inputs. Aspen Plus Dynamics has built–in PID controllers with options of specifying process and output variable ranges, tuning and filtering of controls and selection of ideal, series or parallel algorithms. Classical notation for output of the ideal PID controller employed in this study is specified as:

$$OP = K_p\left(e(t) + \frac{1}{T_i}\int_0^t e(\tau)d\tau + T_d\frac{d}{dt}e(t)\right) \quad (13)$$

where, OP is the controller output, K_p is the proportional gain which is set different value for different components. T_i and T_d are integral and derivative times respectively and e is the calculated error between set point and processed variable at instantaneous time t. τ is the variable of integration taking values from 0 to present time. Control strategies incorporating these PIDs and regulatory mechanisms for different operating parameters are discussed accordingly.

Key parameters to be controlled in the proposed system are reactant inlet stoichiometries, inlet pressures, coolant inlet and operating temperatures of the stack. The control loops of hydrogen and air supply system should maintain the optimal reactant ratio and prevent shortages that might occur during abrupt changes in the load current. It is reported in (Hosseinzadeh and Rokni, 2012) that the aforementioned PEMFC system is not sensitive to reduction in fuel flow during load fluctuations; however if the hydrogen stoichiometry is below 1.0, then fuel starvation can cause irreversible damage to the stack. On the other hand, oxygen starvation affects the fuel

cell to a greater degree and has a much larger effect on stack performance. Hence, an adequate air supply is required.

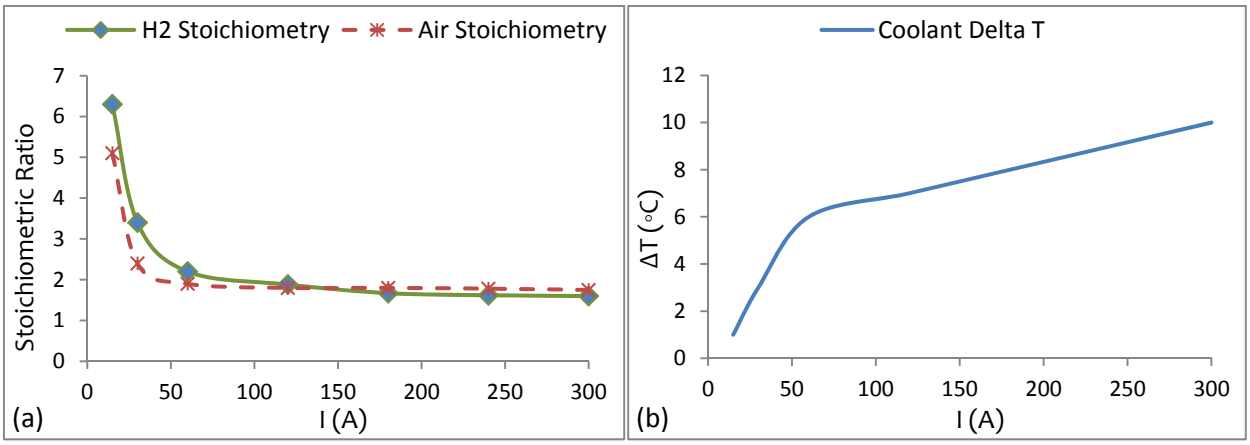

Figure 3. (a) Reactant stoichiometry used in the fuel cell control system, (b) Stack inlet and outlet temperature difference maintained by coolant mass flow.

Figure 3(a) shows the fuel and air stoichiometries for the selected fuel cell stack which are proposed by Ballard and in Fig. 3(b), recommended temperature difference between stack inlet and outlet is displayed. It can be seen that at low current loads, high amounts of excess reactant flows are desired. This is due to the fact that at low power consumption and low pressures, water is formed by the reaction in the cathode side of the cells and it needs to be ejected out of the stack, which is done by supplying high amounts of air. While the amount of oxygen consumed depends on the stack current, the amount of oxygen supplied to a fuel cell is directly related to the blower power. Here, data from pressure and flow sensors is transmitted to the controller where an algorithm based on Fig. 3(a) translates it to be the process variable and set point for the PI controller, which regulates the blower power in order to maintain the desired oxygen ratio. Similarly, an algorithm for controlling hydrogen flow is devised along with a PI controller, which regulates the control valve opening for optimal fuel supply at the desired pressures. Pressures in anode recirculation loop are governed by PI controllers which collect data from anode upstream and manipulate recirculation pump power accordingly. Figure 4 elucidates on processed and manipulated variable for different control blocks implemented in the proposed system.

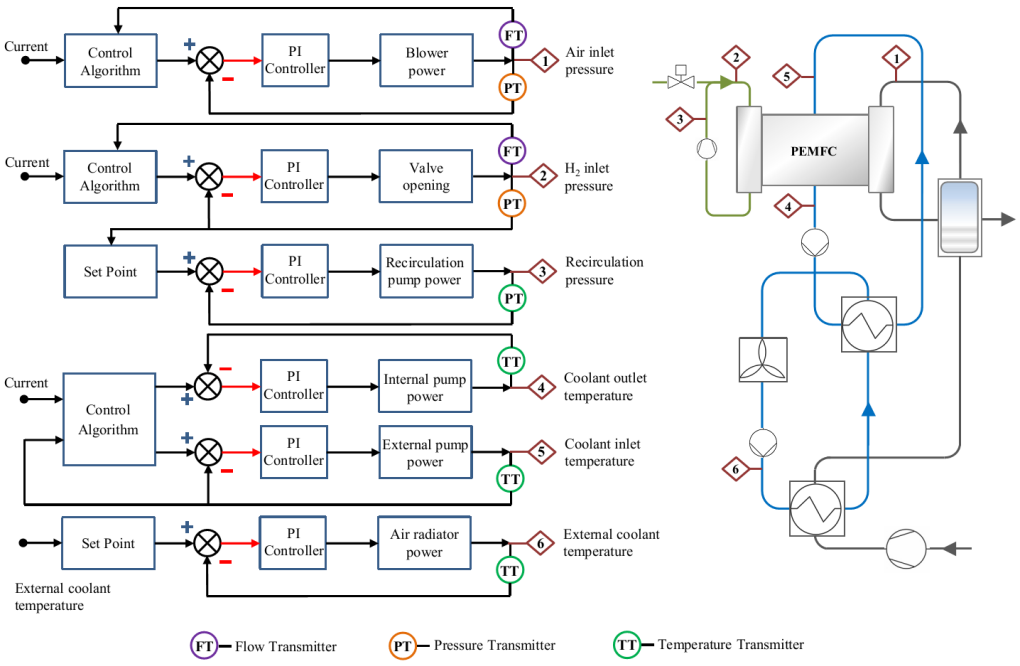

Figure 4. Control blocks for the PEMFC system.

Thermal management in PEMFC systems is of vital importance, basically due to the fact that heat produced in the selected fuel cell cannot be dissipated by convection and radiation through the stack surface. A consistent and stable operation of around 70 °C thus requires a liquid cooling system. Since the operating temperature of the fuel cell is not very high, a low temperature difference with the ambient requires having a large heat transfer surface. Therefore, an efficient thermal control system becomes of substantial importance to ensure optimum system performance.

As shown in Fig. 4, the cooling system for the proposed fuel cell consists of internal and external cooling circuits. As mentioned earlier, the coolant mass flow rate defines the variance in the stack temperature or simply maintains the fuel cell operating temperature. In this case, temperature in the stack can be controlled by the coolant flow rate which acts as an input signal and is adjusted by the PI controller. Based on data from Fig. 3(b), equations defining stack temperature as a set–point for controller are developed. In addition, the controller simultaneously collects data from temperature transmitter at the coolant outlet stream, which then changes the coolant flow accordingly by sending output signals to the driving pump. Employment of such algorithm in the system controller ensures a stable operation under normal steady–state conditions, however for system start–up scenario, a different approach is required. This is due to the fact that, at start–up sequence, temperature of the stack is equal to the ambient and the above–mentioned control strategy would not allow the stack temperature difference to increase more than 10 °C and hence increase the time to reach steady–state operations, which is not desirable. In this regard, at start–up sequence, the coolant flow is restricted to a minimum value until the desired stack

operating temperature is reached which is when the steady–state controls begin functioning. Though, a lower coolant flow is needed to increase the stack heat–up time at start, a very high temperature difference may cause damage to the fuel cells in the stack. Henceforth, the maximum temperature difference is limited to 17 °C for all scenarios here.

Temperature of the coolant entering the stack can similarly be controlled by the flow of water in the external circuit. Control signal to the associated pump regulates the electrical power of the pump and hence the coolant inlet temperature into the stack. In a similar fashion, temperature of water in the external circuit is dependent on radiator fan speed. PI controllers are used to regulate the fan speed as well.

5 Simulations

Reliability of the suggested model is verified by running simulations at different power loads when the system reaches steady–state. Fig. 5 depicts adaptation of the devised model which corresponds to the polarization curve obtained from the data provided by the manufacturer (Ballard Mark9, SSL 2008) associated with the given PEMFC stack. As suggested by the manufacturer, stack temperature range of 60–70°C has been used in simulations of the current system. Model characteristics of the same system at higher temperatures have been studied in (Hosseinzadeh and Rokni, 2012), and show a good agreement with the stack data.

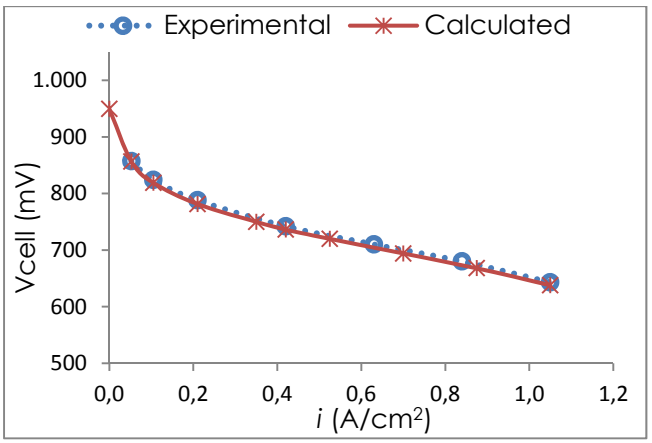

Figure 5. Comparison of calculated polarization curve compared to the corresponding data from the manufacturer (Ballard).

Start–up sequence

In case of PEMFC, dynamic behaviour of a start–up is of particular importance to ensure a short start–up time and an efficient operation. Fuel cell start–up sequence could be defined as the time required by a system to reach stable conditions, which is achieved when the voltage and consequently power, reach a stationary value. Normally,

the optimal operating temperature of a PEM fuel cell is reported to be in the range of 60–80°C. Within this range, chemical reactions occurring inside the fuel cell are relatively fast and facilitate removal of water produced by these reactions. Whereas, at low temperatures, there is a considerable rise in kinetic and ohmic losses in addition to reactant transport losses caused by a high rate of water condensation (Park and Choe, 2008). Thus, it is necessary to elevate the working temperature of a stack as quickly as possible to meet the demands of the required load power.

When the fuel cell is in standby stage i.e. when no current is drawn, auxiliary components such as air blower, coolant pumps, radiator fan and hydrogen inlet valve are closed. At system start-up, all of these components are switched on and fuel valve is opened. Power from the stack is only drawn when current load is applied on the stack. In the current simulations, values of stream flows are initialized to be non-zeros. In this way, a realistic start-up sequence could be imitated and furthermore initial zero-condition in Aspen Dynamics could be avoided. Initial temperature of the stack is assumed to be equal to ambient temperature (25°C) and a start-up power load is introduced by ramping of current at a rate of 20 A/sec. Other parameters and operating conditions are selected from section 3.

5.1 Thermal management of the system

Different start-up strategies are compared and there results are summarized below. Currents at 40, 60, 80 and 100 amperes are drawn and heat-up times for these four cases are presented in the Fig. 6 At start, the flow in cooling circuits is set to the lowest since it is desired to raise the stack temperature to its optimal operation. Coolant flow in the internal circuit is fixed to 290 kg/hr as recommended by the manufacturer. Flow in the internal cooling circuit increases, once the stack temperature difference increases by 15 °C. Flow in external circuit is regulated to maintain stack inlet temperature of internal cooling circuit. Air flow in radiator is started to maintain temperature of external cooling loop to around 50 °C.

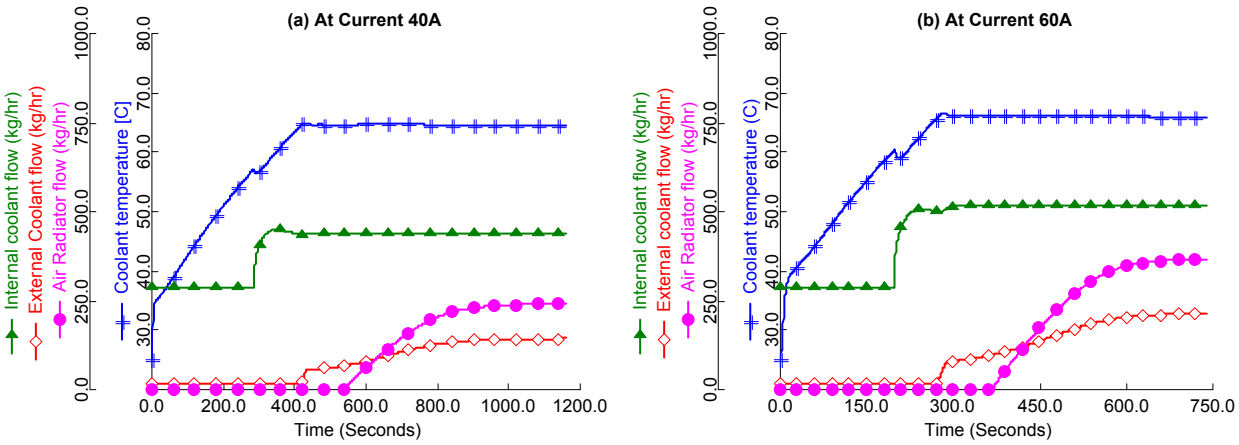

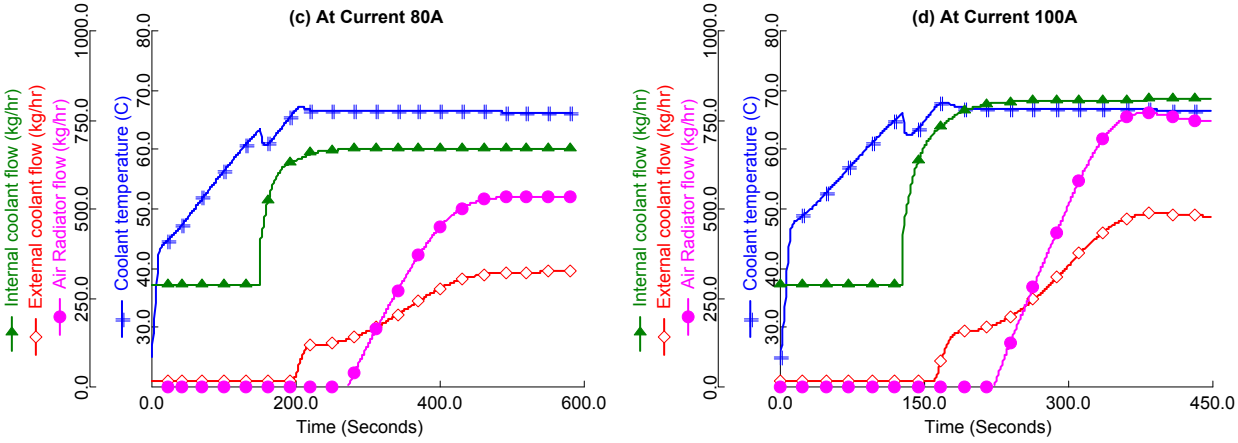

Figure 6. Stack heat–up times and corresponding coolant and radiator air mass flows: (a) at start–up current of 40A (b) at start–up current of 60A (c) at start–up current of 80A (d) at start–up current of 100A.

As can be seen in the figure below, when the stack is started at current of 40A at a ramp rate of 20 A/s, it takes approximately 425 seconds to reach stable operating temperature. The heat–up time for 60, 80 and 100 A is determined to be 300, 220 and 175 seconds respectively. The heat–up time becomes shorter as the applied current is increased. Because of the high current density, a large amount of heat is produced in a short time and the temperature rises rapidly through the cells.

5.2 Power generation and system efficiency

Generally, stack efficiency is higher to that of the complete system with BoP. However, in a system with fuel recirculation, stack efficiency is attributed to fuel stoichiometry, though there is no considerable effect on the system efficiency. When the actual and stoichiometric mass flow of hydrogen differ least then less fuel is wasted and stack efficiency is at its maximum. The same argument could be generalized for system efficiency as well. This is because at higher air mass flows, power consumption of auxiliary components increases.

Different start–up cases were investigated to analyse the system efficiency, net power output and auxiliary power consumptions. Currents of 60 and 100 A are applied for two start–up scenarios. Overall efficiency of the system is as much affected by blower and radiator fan, as by the fuel cell stack itself. Fig. 7b, shows that at high current start–ups, power generated from the stack increases. However, efficiency of the system decreases. As can be seen in the figure, system efficiency decreases from 55% to 50% when applied current is changed from 60 to 100 A. During start–up, power consumption of coolant pumps and air radiator is very low when compared to that of the air blower (Fig. 7c). Therefore, auxiliary power consumption is dominated by the air blower. It is observed that power consumed by the air blower increases during start–up

and becomes constant after a few seconds. Also, power produced by the stack increases at a sound pace and becomes stable once steady state is reached. This eleviation in the stack power is due to the fact that the operating temperature of fuel cell increases till it reaches the desired optimal temperature.

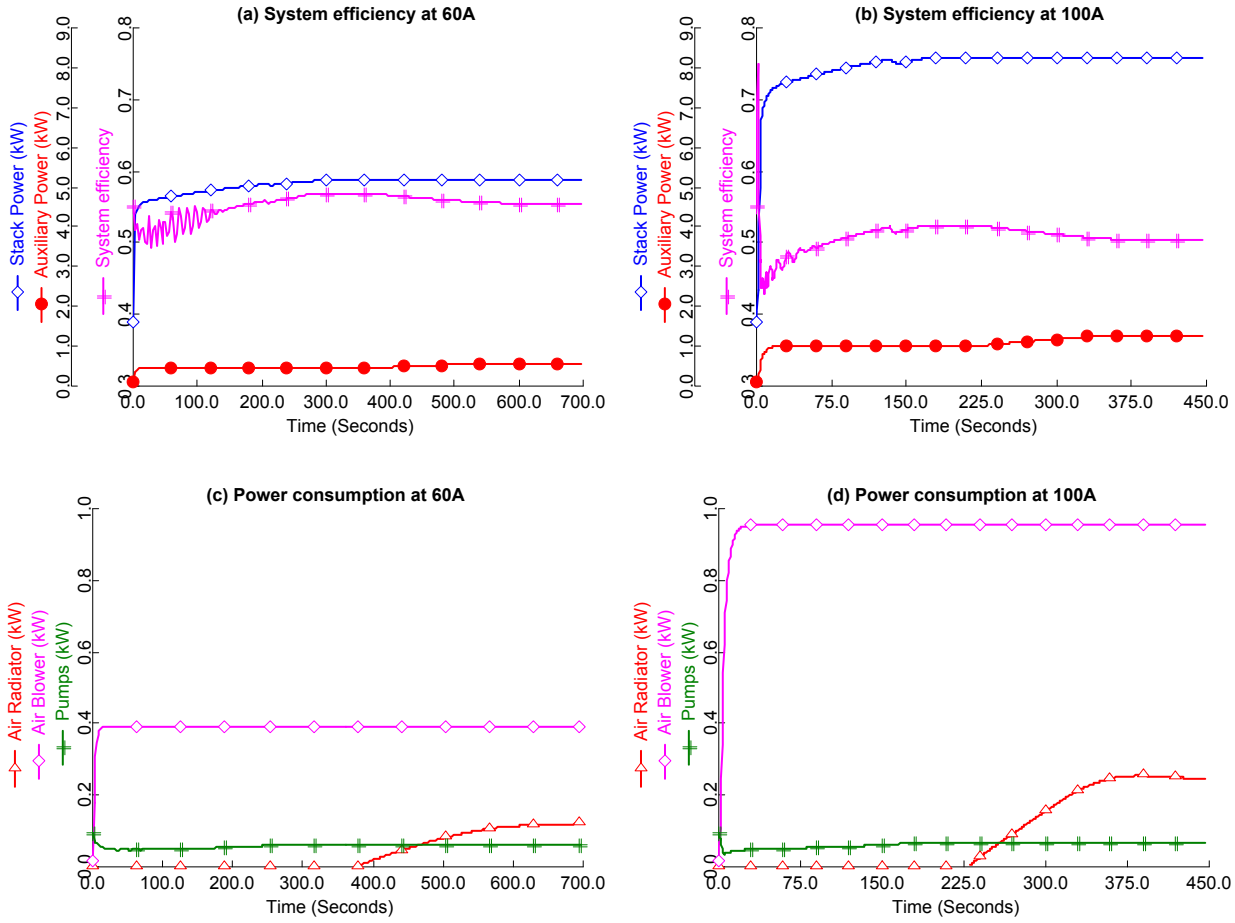

Figure 7. System efficiency and stack power (a) at start–up current of 60A (b) at start–up current of 100A, auxiliary power consumption at start–up of 60A (c) and 100A (d) respectively.

As seen in Fig. 7c and 7d, radiator fan is shut off at the start sequence, but is activated once temperatures in the external cooling circuit are high enough to be cooled down. Air flow in the radiator can be regarded as a linear function of its electrical power and therefore once it is started by the controller, the system efficiency decreases. Since, at high temperatures heat production in the stack is quite high, the radiator fan consumes around 250 W for a current withdrawal of 100 A, whereas it only requires approximately 125 W when current is at 60 A.

5.3 Cell voltage

Potential difference generated across the fuel cell is dependent on factors such as current density, reactant partial pressures and temperature at which cell reactions occur. Figure 8 elucidates some of these underlying factors which affect the voltage and consequently power output of the stack. Here, during the PEMFC start sequence, current is ramped to 80 A at a rate of 20 A/s. Since current density and reactant pressures are regulated at very fast rate, they follow a constant profile along the time axis. However, the stack temperature, which is attributed to the coolant mass flows, keeps on increasing until it reaches the desired operating temperature. As can be seen in Fig.8a, cell voltage increases with the operating temperature. This fact is due to the reason being fast reaction kinetics at the electrodes of individual cell sites. It can be observed that the voltage reduces abruptly when simulation time is around 160 seconds. At this stage, the decrease in cell temperature and voltage is caused by the sudden increase in coolant flow into the stack, which maintains the stack operating temperature. In a similar manner, power produced by the stack also decreases with voltage drop, although it is not that distinct in Fig. 8a. Nevertheless, Fig. 8b shows a detailed view of the aforementioned instance of time. Evidently power produced by the stack responds to a similar trend to that of voltage against operating temperature of the stack.

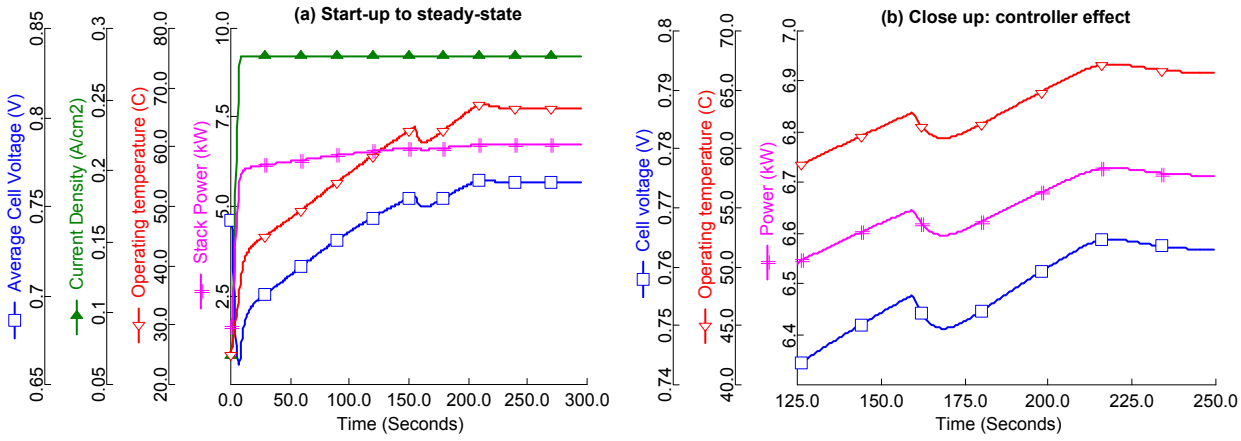

Figure 8. (a) Cell voltage as a function of stack operating temperature with start–up current of 80A, (b) Effect of sudden temperature drop on voltage and power.

5.4 Fuel and oxidant flows

This section caters analysis of reactant flows into the fuel cell and investigates their effect on cell performance as well as on adjacent streams. Cell performance is not sensitive to fuel stoichiometry; on the other hand, cathode is significantly more sensitive to air stoichiometry. Therefore, simulations are carried out by employing operating conditions and parameters mentioned previously (in section 3.1). A start–up current of

60 A is used in this case. Figure 9 specifically portrays flow behaviour of fuel and air into and out of anode and cathode channels respectively.

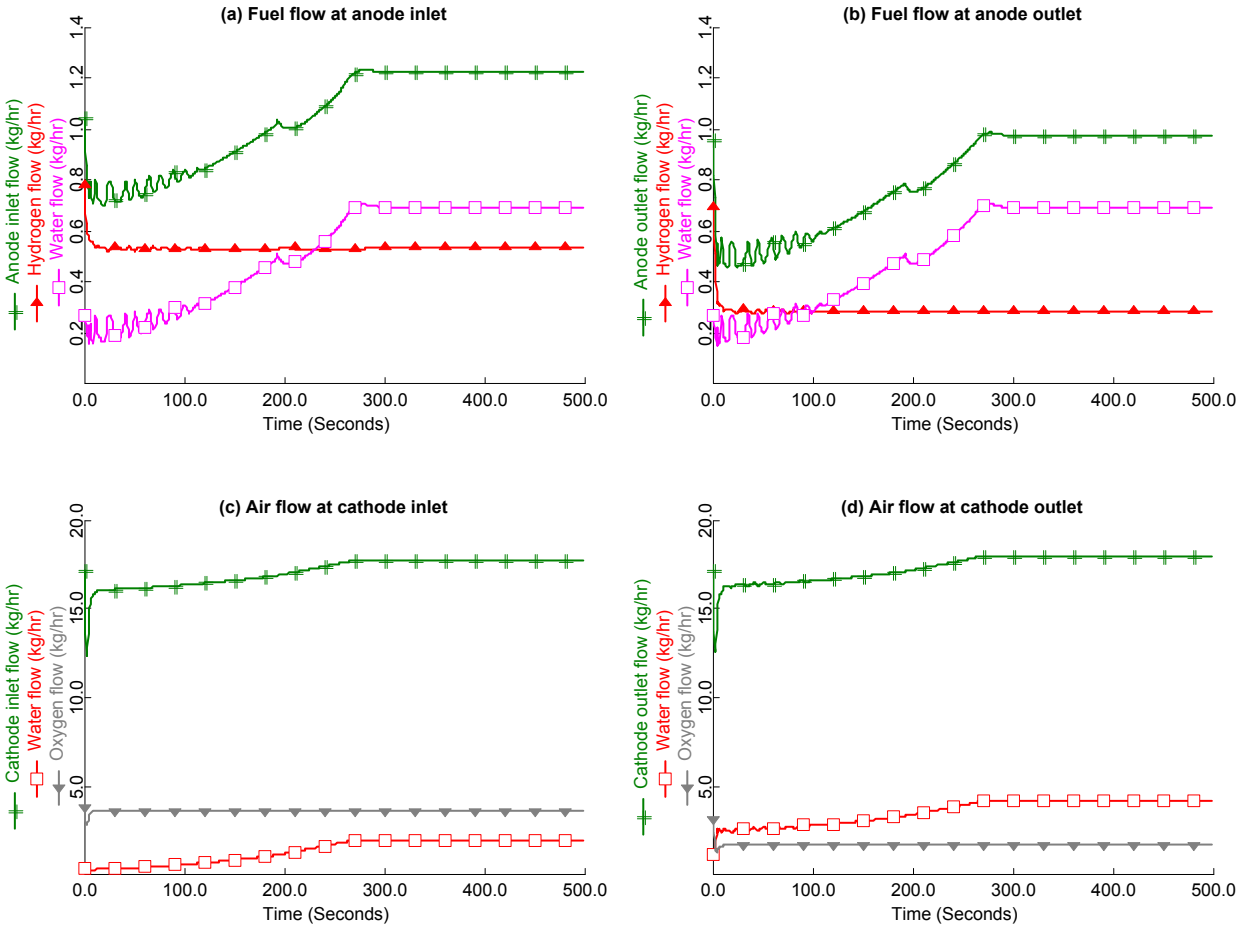

Figure 9. Fuel and air flows at inlet and outlet of the stack: (a) Fuel flow at anode inlet, (b) Fuel flow at anode outlet, (c) Air flow at cathode inlet and (d) Air flow at cathode outlet.

It is observed that fuel entering the stack contains water i.e. the fuel is humidified. Since, fuel from anode exhaust is recirculated; it adds more unutilized hydrogen and water to the inlet stream. Composition of hydrogen in the entrance becomes stable after initial regulation. However, the amount of water keeps on increasing due to the increase in stack's temperature and water cross–over from cathode. This occurrence shows similar incremental trends as in case of stack temperature in Fig 6. Anode outlet flows show similar trends, though the amount of hydrogen at the outlet is reduced as it is consumed in the cell reactions.

Air flow into the cell can also be seen to increase with time. As temperature of the stack increases, more water is needed to maintain the humidity at the desired level; here, a constant relative humidity of inlet air is assumed. Oxygen and nitrogen remain more or less constant throughout the heat–up time. Once, the stack reaches its steady–state,

the air flow becomes constant. At cathode outlet, the total flow increases correspondingly, however the oxygen content is lower as it is consumed in the reaction as well, whereas water flow is increased. The additional water in the outlet is the product of fuel cell reaction. Higher stoichiometries for both fuel and oxidant are maintained to manage this water production in the cathode and to dilute nitrogen crossover to the anode.

5.5 Air humidification effects

In PEMFC systems, sufficient hydration is essential to facilitate ionic conduction for an efficient cell operation and to avoid physical degradation of the membrane. Cell drying depends on a number of operating conditions including current density, reactant flow rate, gas composition, relative humidity, inlet pressure, and cell temperature. Dry operation will lead to stack performance degradation and eventually, internal leaks. However, when excess water accumulates in the fuel cell, water flooding might be resulted at the cathode region which is also not desirable. Inlet humidities also contribute to liquid water saturation in the fuel cell, which is reported in (Wong et al. 2011). As mentioned above, the proposed system in this study utilizes an external humidifier to moisten incoming air, whereas anode side is not humidified. Recirculation of fuel serves the humidification purpose on the anode side of the fuel cell.

Here, the role of the inlet relative humidity at the cathode of fuel cell electrodes and its interaction with adjacent flows is discussed and a comparison is presented by a systematic analysis of these results. A constant relative humidity of 95%, 90%, 85% and 80% is selected at a start–up current for the present simulations. Fig. 10 depicts relative humidity states at electrode inlet and outlets respectively.

It can be witnessed that anode inlet humidity increases from 90% to 94% when cathode inlet air is humidified from 80% to 95%. Similarly, relative humidity at anode exhaust is increased from 95% to 98%. It can be seen that time taken to reach these humidity levels is more when air inlet humidity is kept lower. Since, water is produced at the cathode; it is fully saturated at the outlet of the fuel cell.

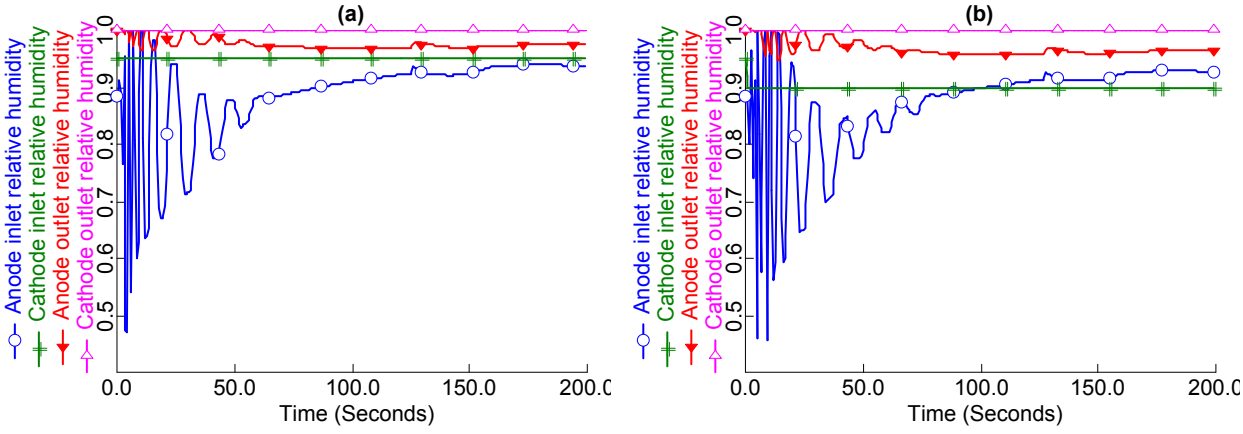

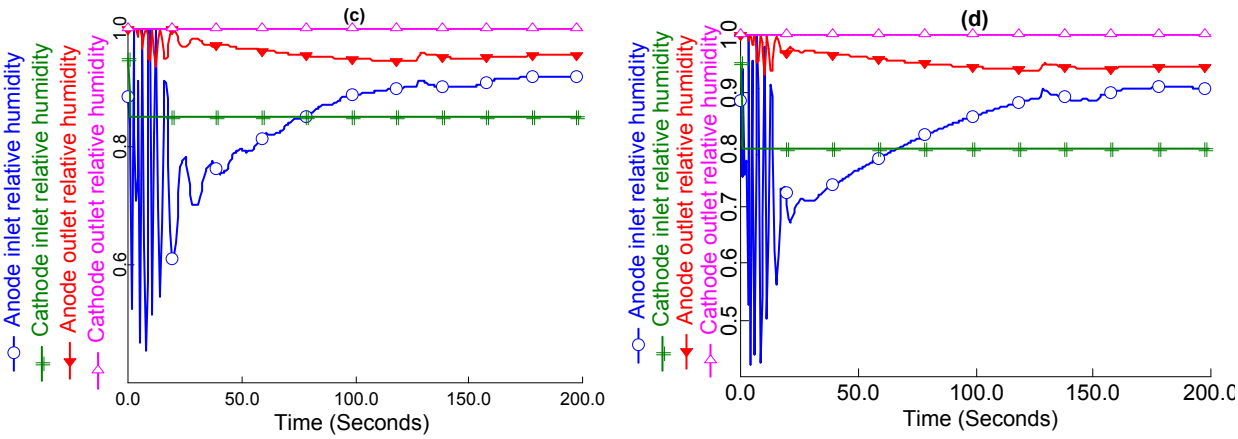

Figure 10. Effect of air inlet relative humidity on fuel inlet and outlet: (a) Air inlet humidity of 95%, (b) 90%, (c) 85% and (d) 80% respectively.

5.6 Water saturation at cathode

Water management is a critical issue since the performance of PEM fuel cell is strongly influenced by its internal water distribution. Removal of water from the cathode is dependent on stack temperature and pressure drop. Temperature is the more critical factor, since at high temperatures water will be in the vapour state and easier to remove. Stack water production increases with current and is also dependent on the number of cells. The exact amount of liquid water product depends on the cathode outlet temperature. Figure 11 provides information on the amount of liquid water at inlet and outlet of the cathode channel. Fig. 11a shows the start–up of the system at 40A. As seen, the amount of liquid water at cathode outlet is around 17 % when stack operating temperature is close to the ambient and lowers to 11% when the stack reaches steady–state at 65 °C.

On the other hand, when the stack is operating at 100 A, the amount of liquid water percentage at cathode outlet is 23% approximately, which is much higher than the case with 40A start–up. This is because of higher current densities at start–up sequence when the stack temperatures are very low. When higher currents are drawn, reactions within the fuel cell are accelerated which demand more intake of fuel and oxidant. Consequently these reactions produce more water when compared to production at low currents. Since the stack temperature is low at start–up, higher percentage of produced water is saturated at the fuel cell cathode. At low currents, water removal is the dominant factor and reactant stoichiometries are determined by the minimum flow rates required for water removal which in the present case are more than adequate to provide the necessary concentrations. At steady–state when stack operating temperature is around 67 °C, liquid water fraction in the outlet air is determined to be around 11%.

Liquid fractions at anode outlet are very low when compared to cathode outlet. They are calculated to be in the range of 1.5 to 2.0 % for both 40A and 100A current scenarios discussed above.

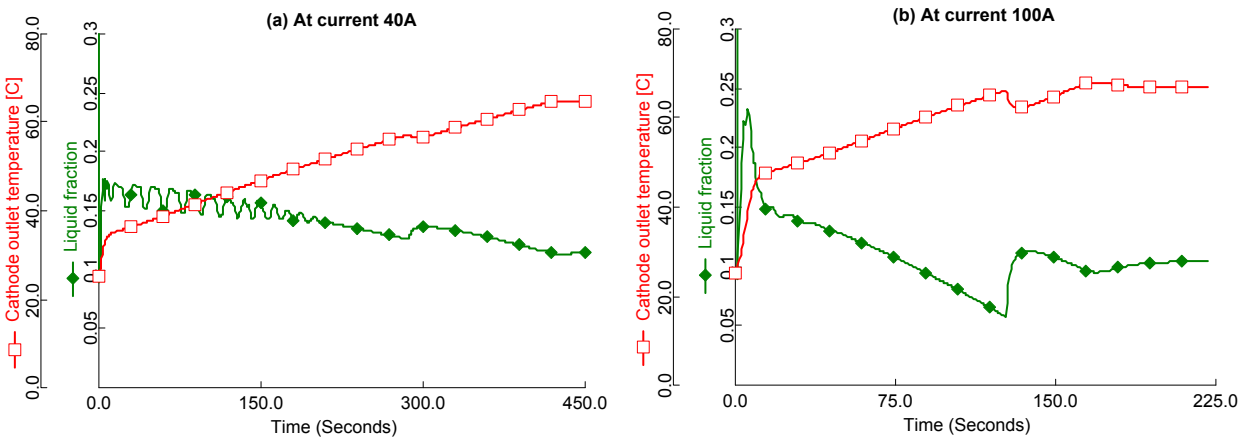

Figure 11. Percentage of liquid water at cathode outlet: (a) at start–up current of 60A and (b) at start–up current of 100A.

6 Conclusions

In this work, a comprehensive dynamic model of a fuel cell system along with the all necessary BoP components is presented. The objective of the proposed study is to design and demonstrate a control system which has the ability to predict the dynamics of PEM fuel cell system during simultaneous changes of operating conditions. Main contributions of the suggested model are attributed to system response methodology, which incorporates stack thermal behaviour in addition to fuel cell electrochemistry, water crossover, mass and energy balances. Emulation of the presented system shows that the results are in good agreement with the manufacturer's data. It is observed that system efficiency and voltage output are higher at low power start–ups but for the fuel cell stack it takes longer time to reach stable operating conditions. Also, slow temperature controls as opposed to fast electrochemical changes, affect fuel cell stability. Furthermore, air radiator consumes more power at high currents once the system is stable and due to this fact, system efficiency is reduced. In addition, it is shown that cathode inlet water levels are adequate enough to humidify fuel stream, which is recirculated into the anode. Finally, amount of liquid water in the cathode outlet is considerably higher, at high current density start–ups, while water removal from cathode exhaust requires additional attention at low stack operating temperatures. Thus, the presented model can be used for optimizing and designing operational strategies for PEMFC systems for automotive applications.

Acknowledgement

The authors would like to thank the Danish Energy Agency for financial support and our industrial partner, H2Logic, for their collaboration and technical support.

References

Ahn, Jong–Woo and Song–Yul Choe. 2008. Coolant controls of a PEM fuel cell system. *Journal of Power Sources* 179, Nr. 1: 252–264.

Amphlett, J C, R F Mann, B A Peppley, P R Roberge and A Rodrigues. 1996. A model predicting transient responses of proton exchange membrane fuel cells. *Journal of Power Sources* 61, Nr. 1–2: 183–188.

Asghari, Saeed, Hooman Akhgar and Bagher Faghih Imani. 2011. Design of thermal management subsystem for a 5kW polymer electrolyte membrane fuel cell system. *Journal of Power Sources* 196, Nr. 6: 3141–3148.

Aspentech. 2012. Aspen plus dynamics. http://www.aspentech.com/products/aspen–dynamics.aspx

Ballard Mark9 SSL. 2008. Product manual and integration guide.

Ceraolo, M, C Miulli and A Pozio. 2003. Modelling static and dynamic behaviour of proton exchange membrane fuel cells on the basis of electro–chemical description. *Journal of Power Sources* 113, Nr. 1: 131–144.

Hosseinzadeh, Elham and Masoud Rokni. 2012. Development and validation of a simple analytical model of the Proton Exchange Membrane Fuel Cell (PEMFC) in a fork–lift truck power system. *International journal of green energy* To be publ.

Hu, Guilin, Jianren Fan, Song Chen, Yongjiang Liu and Kefa Cen. 2004. Three–dimensional numerical analysis of proton exchange membrane fuel cells (PEMFCs) with conventional and interdigitated flow fields. *Journal of Power Sources* 136, Nr. 1: 1–9.

Jia, J, Y Wang, Q Li, Y T Cham and M Han. 2009. Modeling and Dynamic Characteristic Simulation of a Proton Exchange Membrane Fuel Cell. *IEEE Transactions on Energy Conversion* 24, Nr. 1: 283–291.

Jung, Jee–Hoon and Shehab Ahmed. 2010. Dynamic model of PEM fuel cell using real–time simulation techniques. *Journal of Power Electronics* 10, Nr. 6: 739–748.

Khan, M J and M T Iqbal. 2005. Modelling and analysis of electrochemical, thermal, and recetant flow dynamics for a PEM fuel cell system. *Fuel Cells* 5, Nr. 4: 463–475.

Kim, Kihyung, Meng Wang, Michael R Von Spakovsky and Douglas J Nelson. 2009. Dynamic synthesis/design and operation/control optimization under uncertainty of a PEMFC system. *ASME International Mechanical Engineering Congress and Exposition, Proceedings* 8: 679–689.

Li, Youcai, Sichuan Xu, Zhigang Yang and Yongxiang Li. 2011. Experiment and simulation study on cold start of automotive PEMFC: 2166–2170.

Mangold, Michael, Silvia Piewek, Olaf Klein and Achim Kienle. 2011. A model for the freeze start behavior of a pem fuel cell stack. *Journal of Fuel Cell Science and Technology* 8, Nr. 3.

Meng, Hua. 2008. A PEM fuel cell model for cold–start simulations. *Journal of Power Sources* 178, Nr. 1: 141–150.

Park, Sang–Kyun and Song–Yul Choe. 2008. Dynamic modeling and analysis of a 20–cell PEM fuel cell stack considering temperature and two–phase effects. *Journal of Power Sources* 179, Nr. 2: 660–672.

Pathapati, P R, X Xue and J Tang. 2005. A new dynamic model for predicting transient phenomena in a PEM fuel cell system. *Renewable Energy* 30, Nr. 1: 1–22.

Pukrushpan, Jay T, Huei Peng and Anna G Stefanopoulou. 2004. Control–Oriented Modeling and Analysis for Automotive Fuel Cel Systems. *Journal of Dynamic Systems Measurement & Control* 126, Nr. 1.

del Real, Alejandro J, Alicia Arce and Carlos Bordons. 2007. Development and experimental validation of a PEM fuel cell dynamic model. *Journal of Power Sources* 173, Nr. 1: 310–324.

Santarelli, M G, M F Torchio and P Cochis. 2006. Parameters estimation of a PEM fuel cell polarization curve and analysis of their behavior with temperature. *Journal of Power Sources* 159, Nr. 2: 824–835.

Shan, Yuyao and Song–Yul Choe. 2006. Modeling and simulation of a PEM fuel cell stack considering temperature effects. *Journal of Power Sources* 158, Nr. 1: 274–286.

Spiegel, Colleen. 2007. *Designing and building fuel cells*. New York: McGraw–Hill.

Springer, T E, T A Zawodzinski and S Gottesfeld. 1991. Polymer Electrolyte Fuel–Cell model. *Journal of the Electrochemical Society* 138, Nr. 8: 2334–2342.

Sundaresan, M and R M Moore. 2005. PEM Fuel Cell Stack Cold Start Thermal Model. *Fuel Cells* 5, Nr. 4: 476–485.

Vasu, G and A K Tangirala. 2008. Control–orientated thermal model for proton–exchange membrane fuel cell systems. *Journal of Power Sources* 183, Nr. 1: 98–108.

Wong, K H, K H Loo, Y M Lai, Siew–Chong Tan and Chi K Tse. 2011. A theoretical study of inlet relative humidity control in PEM fuel cell. *International Journal of Hydrogen Energy* 36, Nr. 18: 11871–11885.

Yan, Qiangu, Hossein Toghiani, Young–Whan Lee, Kaiwen Liang and Heath Causey. 2006. Effect of sub–freezing temperatures on a PEM fuel cell performance, startup and fuel cell components. *Journal of Power Sources* 160, Nr. 2: 1242–1250.

Yerramalla, S, A Davari and A Feliachi. 2002. Dynamic modeling and analysis of polymer electrolyte fuel cell. *2002 IEEE Power Engineering Society Summer Meeting, Vols 1–3, Conference Proceedings*: 82–86.

Nomenclature

E	theoretical voltage (V)
V_{cell}	average cell voltage (V)
$\dot{P}_{el}$	stack power (kW)
$\dot{P}_{in}$	energy into the fuel cell (kW)
$\dot{P}_{out}$	energy out of the fuel cell (kW)
$\dot{Q}_{loss}$	heat dissipated (kW)
C_t	stack thermal capacitance (kW)
R	universal gas constant $(J/molK)$
T	temperature (K)
F	Faraday's constant $(C/molK)$
I	current (A)
N_{cell}	number of cells $(-)$
$\Delta\bar{g}_f^0$	change in Gibbs free energy $(J/molK)$
P_{H_2}	hydrogen partial pressure $(-)$
P_{O_2}	oxygen partial pressure $(-)$
M_m	mol. weight of membrane (Kg/mol)
J_{H_2O}	net water–diffusion flux (mol/scm^2)
D_λ	water diffusion coefficient (cm^2/s)
a_{H_2}	hydrogen activity $(-)$
a_{H_2O}	water activity $(-)$
a_{O_2}	oxygen activity $(-)$
i	current density (A/cm^2)
i_n	internal current density (A/cm^2)
i_0	exchange current density (A/cm^2)
$i_{0,a}$	anode exchange current density (A/cm^2)
$i_{0,c}$	cathode exchange current density (A/cm^2)
k_a	anode reaction rate (mol/scm^2)
k_c	cathode reaction rate (mol/scm^2)
n_e	electrons transferred (mol_e/mol_{fuel})
n_{el}	number of electrons $(-)$
n_{drag}	electro osmotic drag $(-)$
t_m	membrane thickness (cm)
K_p	proportional gain

T_i	integral time
T_d	derivative time
Greek symbols	
τ	variable of integration
α_a	anode transfer coefficient $(-)$
α_c	cathode transfer coefficient $(-)$
β	symmetry factor $(-)$
η_{act}	activation overpotential (V)
$\eta_{act,a}$	anode activation overpotential (V)
$\eta_{act,c}$	cathode activation overpotential (V)
η_{conc}	concentration overpotential (V)
η_{ohmic}	ohmic overpotential (V)
λ	membrane water content $(-)$
ρ_{dry}	membrane density (g/cm^3)

Appendix C

Paper II

Rabbani, A & Rokni, M. “Dynamic characteristics of an automotive fuel cell system for transitory load changes”, Journal of Sustainable Energy Technologies & Assessments, 2013; 1: 34–43.

Dynamic characteristics of an automotive fuel cell system for transitory load changes

Abid Rabbani and Masoud Rokni
Thermal Energy Section, Department of Mechanical Engineering, Technical University of Denmark, 2800 Kgs. Lyngby, Denmark.

Abstract

A dynamic model of Polymer Electrolyte Membrane Fuel Cell (PEMFC) system is developed to investigate the behavior and transient response of a fuel cell system for automotive applications. Fuel cell dynamics are subjected to reactant flows, heat management and water transportation inside the fuel cell. Therefore, a control–oriented model has been devised in Aspen Plus Dynamics, which accommodates electrochemical, thermal, feed flow and water crossover models in addition to two–phase calculations at fuel cell electrodes. The model parameters have been adjusted specifically for a 21.2 kW Ballard stack. Controls for temperatures, pressures, reactant stoichiometry and flows are implemented to simulate the system behavior for different loads and operating conditions. Simulation results for transitory load variations are discussed. Cell voltage and system efficiency are influenced by current density and operating temperature as well. Together, air blower and radiator consume 10% of the stack power at steady–state; nevertheless their power consumption could reach 15% during load surges. Furthermore, water crossover in the fuel cell has shown a significant impact on anode inlet flows, humidity and recirculation pump during these load changes. Also, the amount of water saturation at cathode is found to be abruptly fluctuating and its removal from cathode is dependent on operating temperature and reactant stoichiometry.

Key words: *Dynamic simulation, system modeling, fuel cell, PEMFC, water crossover, system control.*

1. Introduction

Fuel cell systems have received substantial attention in recent years and research on these systems has drastically increased mainly due to their inherent virtues of clean and efficient mode of operation. Existing fuel cell systems are categorized based on the type of electrolyte and preferred operating conditions. Among various types of fuel cells, the Proton Exchange Membrane Fuel Cells (PEMFC) is currently the best choice for portable power generation due to its relatively low operating temperature, quick start–up, high power density and efficiency to name a few.

As a power source for automotive applications, PEMFC systems are usually subject to inflexible operating requirements when compared to stationary applications. These systems have to operate at varying conditions related to temperatures, pressures, power load and humidity. PEMFC dynamics are influenced by reactant flows, heat management and water content in the streams as well as within the fuel cell itself. All the auxiliary components, such as air and fuel supply system which include compressors and control valves, and the thermal control system which consists of heat exchangers, coolant pumps and air radiators need to be controlled for optimum operation of fuel cell when the system experiences varying load changes. Understanding the transient behaviour of a PEMFC therefore becomes very beneficial in dynamic modelling of these power modules at a system–level.

Many PEM fuel cell models have been developed in recent years. However, very few of these models are published on dynamic modelling of complete PEMFC systems along with their BoP. Most of the available literature focuses on individual components of these systems, mainly on the fuel cell stack. While, steady–state models of these systems are present in abundance. A generalized dynamic model for fuel cell stack is reported by Amphlett et al. [1]. Another bulk dynamic model used for developing a control system is presented by Yerramalla et al. [2]. A simplistic dynamic model based on cathode kinetics was developed by Ceraolo et al. [3]. Pukrushpan et al. [4] presented a transient dynamic model and elucidated the dynamic characteristics of water transport in PEM fuel cells. A complete PEMFC system model was developed by Pathapati et al. [5] which included the dynamics of flow and pressure in the channels. Hu et al. [6] represented a three–dimensional computational PEM fuel cell model with comparison of different flow fields. In recent years, several improved models were published by Park and Choe [7] and Jia et al. [8] to investigate fuel cell transient electrical responses under various operating conditions.

Heat management in PEMFCs being a critical factor in its operations and performance is accounted for in open literature as well. Issues related to temperature dynamics are dealt and studied by Vasu and Tangirala [9], which could predict the effects of temperature and feed flows on system transient behaviour. Khan and Iqbal [10] proposed a transient model to predict efficiency in terms of voltage output, and a thermal model including heat transfer coefficients and energy balance for the stack. Shan and Choe [11] analysed the temperature distribution on fuel cells by developing a two–dimensional model. Another control–oriented thermodynamic model is also proposed by del Real et al. [12].Coolant control strategies were suggested by Ahn and Choe [13] after investigation of temperature effects on the system. Jung and Ahmed [14] developed a stack model based on real–time simulator in MATLAB/ Simulink environment and validated it with experimental setup of Ballard Nexa fuel cell. A thermal management system for a PEMFC was designed by Asghari et al. [15]. Influence of temperature on fuel cell's characteristics is also reported by Beicha [16].

The model presented in this study aims at analysis and investigation of a complete PEMFC system and studies its transient response to varying load and operating conditions. According to authors' literature survey, no studies have been conducted on system–level dynamic modelling of PEMFC system with all the necessary BoP components. Previous studies focus on transient response of fuel cell stack under different operating conditions; primarily on individual component analysis. Therefore, a need for a control–oriented dynamic system model is identified, which simulates a fuel cell stack under multiple varying operating conditions and changing auxiliary components outputs. Dynamic characteristics of PEMFC are also attributed to the heat management and water transportation that is scarcely reported in the open literature. Investigations for effects of heat exchangers on fuel cell stack performance and water crossover on anode recirculation operations are therefore selected to be one of the primary objectives here.

Thereby in the entirety of this study, a sizeable focus has been set to devise a dynamic model of the fuel cell stack, which accommodates the electrochemical, thermal, feed flow and water transportation models. A complete system is constructed in Aspen Plus Dynamics by incorporating all the essential auxiliary components and implementing control strategies in order to emulate a real PEMFC system. Effects of these controls and other components are also investigated in this work. A thermal management strategy has been designed and its dynamic impact on fuel cell stack has been reported for the first time. Analysis of water crossover in the fuel cell and its impact on anode recirculation operations has been conducted and suitable findings are reported here. Moreover, two–phase characteristics of concerning material streams are determined which provide suitable insight to saturated water issues in the fuel cell stack. This study also takes into consideration the BoP, such as air blower, valves, coolant pumps and air radiator; making it a thorough tool for predicting PEMFC dynamics and to provide important information for the design of control strategies.

In the current study, the focus is on complete system with all necessary auxiliary components and their effect on system performance rather than effect of individual component on the system. Thus, it differs substantially from previous studies in the sense that not only dynamics of the fuel cell stack are included but responses of all other auxiliary components are also incorporated by applying a detailed control strategy design.

2. System overview

Layout of the proposed PEMFC system is shown in Fig. 1. The system comprises a PEMFC stack, air compressor, humidifier, pumps, heat exchangers and radiator for the cooling circuit, flow valves and controllers. Compressed air, which is fed into cathode of the stack is cooled and humidified prior to its entrance. Pressurized hydrogen from storage tank is regulated by a control valve into the fuel cell anode. Since the stack is not

operated at dead–end mode, a higher fuel stoichiometry is maintained. Unutilized fuel from anode exhaust is recirculated back to the feed stream via a recirculation pump, thus allowing the fuel to be humidified.

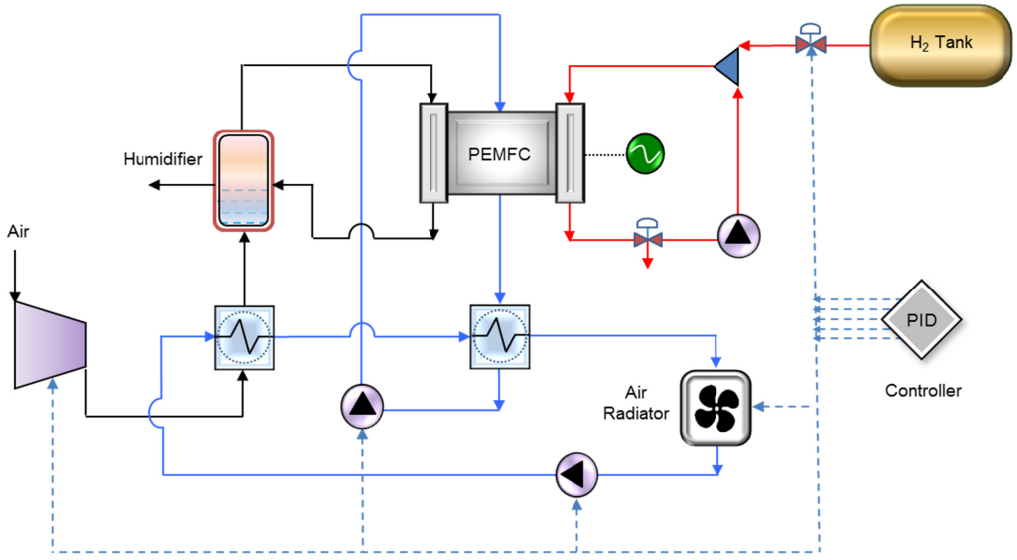

Figure 1. Schematic layout of a complete PEM fuel cell system with auxiliary components.

In order to have a steady–state operation, the fuel cell stack needs to be maintained at a constant operating temperature. Therefore, heat rejected by the stack is absorbed by a liquid coolant which circulates in a circuit associated with the stack and a heat exchanger. An external cooling loop, connected to the aforementioned heat exchanger, in turn cools the water in the internal circuit. This circuit also consists of a heat exchanger to precool air entering the fuel cell and an air radiator for heat rejection. Flow of water is regulated by pumps in the respective circuits. In order to maintain reactant stoichiometry and fuel cell operating temperature at varying loads, PID controllers are deployed to regulate reactant and coolant flows. This emulates the behaviour of fuel cell in real time and helps in analysis of system response under varying operating conditions. Aspen Plus dynamics contains built–in PID controllers. These controllers collect data from various component inlet and outlets which are regarded as pressure, temperature and flow transmitters, and manipulate the corresponding components to reach the desired state. Due to this fact, current system responses and its behaviour are attributed to the formulated control strategy which is based on fuel cell stack limitations and recommendations by the manufacturer. Detailed control mechanisms are illustrated in subsection 2.6. Figure 1 only represents controllable connections initiating from the controller. In calculation as well as reality, the control unit collects information from various temperature, pressure and flow transmitters in

addition to current and voltage data from the fuel cell. Here a simplified view of the system is presented.

1.1 *Fuel Cell stack*

A Ballard fuel cell stack [17] has been specifically adapted in the current study. The fuel cell stack contains 110 cells with a cell area equal to 285 cm^2. Operating temperature of the stack is maintained around 60–70°C with a pressure range of 1.1– 2.2 bar. Maximum power produced from the described stack is 21.2 kW corresponding to a current of 300A; however it is generally operated at lower current ranges to attain higher efficiencies by reducing ohmic and concentration overpotentials within the fuel cell stack. This model, which is based on equations adopted by Hosseinzadeh and Rokni [18], contains some parameters influencing physical characteristics of the system, as well as on operating conditions and membrane properties. Some of these parameters which are obtained for the Ballard stack are shown in Table 1. Here, focus has been set to build up a system which meets the requirements of actual stack running under recommended conditions.

Table 1. Parameter estimation for Ballard Fuel cell stack

Parameter	**Value**
Number of electrons transferred per mole of fuel, n_e $\left(mol_e/mol_{fuel}\right)$	2
Number of electrons for the reaction rate, n_{el} $\left(mol_e/mol_{fuel}\right)$	1 for cathode and 4 for anode
Internal current density, i_n $\left(A/cm^2\right)$	0.002
Symmetry factor, β	0.5
Membrane thickness, t_m (cm)	0.0183
Density of the membrane–dry condition, ρ_{dry} $\left(g/cm^3\right)$	3.28
Molecular weight of membrane, M_m (Kg/mol)	1.1

During PEMFC steady–state operations, coolant pressure should be lower than reactant pressures whereas during start–up, coolant pressure may exceed reactant pressure. It is recommended to operate the anode at a higher pressure than the cathode. Ensuring that cathode pressure is lower than the anode pressure will minimize nitrogen crossover and improve cell stability. In a system with fuel recirculation, the consumption will be slightly above 1.0 stoichiometry as generally 1% to 2% of the flow will be required for purging. In the present study, purge occurrences are neglected. For a maximum service life and efficiency of the stack, Ballard suggests operating conditions within which the stack should operate [17], which are used in the current investigation. Recommended reactant inlet pressures and nominal pressure drops within the fuel cell stack are reported in Fig. 2.

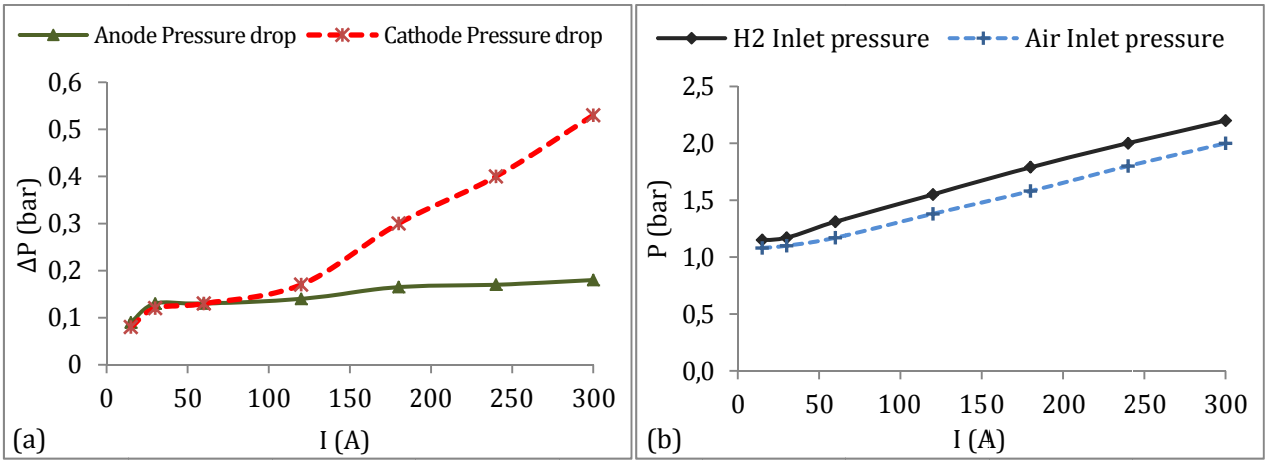

Figure 2. Design validation data from Ballard (a) Nominal pressure drop of reactants within the fuel cell, (b) Reactant inlet pressures corresponding to current drawn.

1.2 *Humidifier*

Dehydration in fuel cell membrane is also a critical issue in PEMFC systems. In order to reduce ionic resistance in the fuel cell, a fully hydrated membrane is desired which enhances ionic crossover between the electrodes, as well as extends its life. Therefore, the reactants in PEMFC need to be humidified before entering the stack. In the proposed configuration, a humidifier is placed in conjunction of cathode inlet and exhaust, where it utilizes the water produced by chemical reaction inside the fuel cells to humidify inlet air. A simplistic energy and mass balance model is developed to cater for fuel cell cathode requirements. Although some empirical models could be considered, these vary over a wide range depending upon the types of humidifiers used. It is therefore assumed that inlet air is optimally humidified after passing through the humidifier. Relative humidity of air entering the cathode is arbitrarily set to 95% in the simulations. This assumption could be justified as it is very close to real operational conditions. On the anode side, fuel is humidified by means of water crossover through cell membrane and recirculation of anode exhaust into the inlet stream, thereby abandoning a need for separate humidifier. Moreover, it can be observed that water cross–over from cathode to anode through the membrane is adequate enough to raise the relative humidity in anode outlet to 100%. This exhaust, when recirculated and mixed with inlet stream maintains the desired humidity levels at anode inlet, which is further discussed in results section.

1.3 *Reactant feed systems*

Auxiliary components such as blowers, pumps and valves regulate flows of material streams in PEMFC systems. For hydrogen feed, a valve is placed between the hydrogen tank and inlet manifold of anode which enables or disables the hydrogen supply. This regulatory valve adjusts high hydrogen pressure of the tank to the desired operating pressure of the fuel cell. Since the system does not operate on dead–end mode, the amount of hydrogen regulated by this valve equals the stoichiometric hydrogen required

by the fuel cell. An air blower regulates the flow and pressure of oxidant into the cathode. The amount of stoichiometric oxygen for fuel cell reaction is manipulated by a controller which regulates the electrical power of the blower, thereby controlling the compression and air flow into the system.

1.4 *Heat Exchangers and thermal management system*

For heat management of the prescribed system, a network of heat exchangers and radiators is deployed. These heat exchangers extract heat produced by the cell stack and maintain the selected operating temperature which is essential for performance and durability of the fuel cell. Although heat exchanger models used here are predefined in Aspen Dynamics, some of the parameters have been assumed on the basis of media entering the hot and cold sides of these heat exchangers. The heat exchanger, which is connected to the internal cooling loop, has liquid water on both its hot and cold side. Therefore, a UA value of 1.0 kW/K is assumed. Whereas, UA values for air pre–cooler and radiator are approximated to be 0.05 kW/K and 0.3 kW/K respectively. In performing the simulations, the pressure drop was assumed to be 0.05 on both sides of heat exchangers. The corrected LMTD is calculated in addition to the corresponding inlet and outlet temperatures of hot and cold streams.

1.5 *Pumps and Blowers*

In the above proposed system, air blower, anode recirculation pump and water pumps are one of the BoP components which are also regulated by the control system. Aspen Dynamics ™ contains models of these units in its library as well. Since the nominal power of the PEMFC is only 21 kW, mass flow rates of fuel and air are very low. For example, at an average load of 10 kW, fuel and air flows are around 0.00014 kg/s and 0.0088 kg/s respectively. Therefore, very low values of isentropic efficiencies are suggested in this paper. The efficiency of a blower ranges from 15% to 48% in the calculations, depending on the air mass flow. Calculated pump efficiencies are also very low for the cooling water circuits and are determined to be around 70%.

1.6 *Control System*

In order to have a stable and efficient operation, the system requires an effective control strategy to regulate system parameters and operating conditions. Typical proportional–integral (PI) controllers, which are widely used in industrial control systems, are employed to regulate different components and flow streams. Key parameters to be controlled in the proposed system are reactant inlet stoichiometries, inlet pressures, coolant inlet and operating temperatures of the stack.

Figure 3a shows fuel and air stoichiometries for the selected fuel cell stack which are proposed by Ballard and in Fig. 3b, recommended temperature difference between stack inlet and outlet is displayed. It can be seen that at low current loads, high amounts of excess reactant flows are desired. This is due to the fact that at low power consumption

and low pressures, water is formed by reactions in cathode side of the cells and it needs to be ejected out of the stack, which is done by supplying high amounts of reactants. While the amount of oxygen consumed depends on the stack current, the amount of oxygen supplied to a fuel cell is directly related to the blower power. Therefore, an algorithm based on the above figure is developed to be the process variable for PI controller, which regulates blower power to maintain the desired oxygen ratio. Similarly, an algorithm for controlling hydrogen flow is devised along with a PI controller, which regulates the control valve opening for optimal fuel supply.

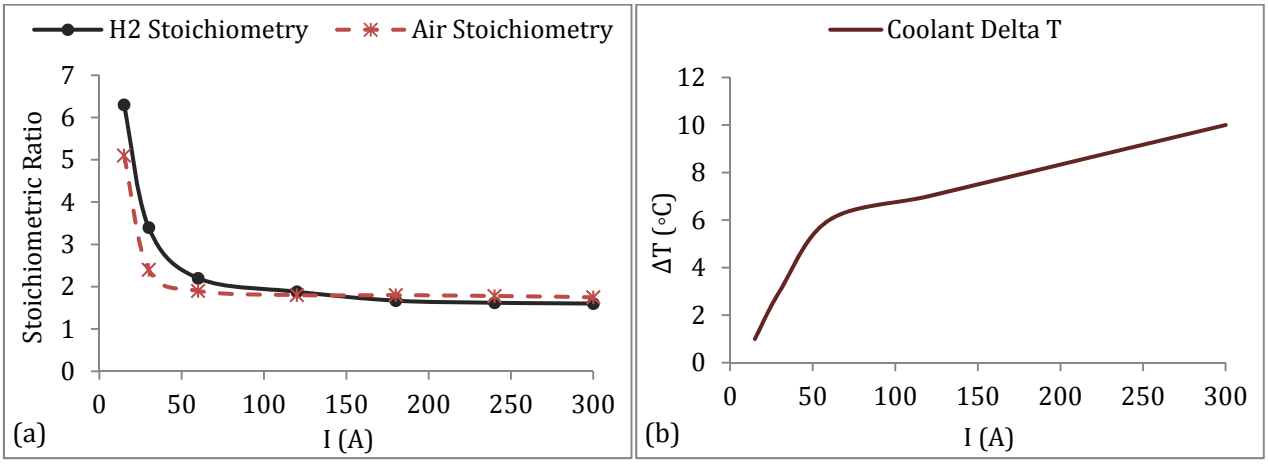

Figure 3. Recommended operating conditions by Ballard, (a) Reactant stoichiometry in the fuel cell, (b) stack inlet and outlet temperature difference maintained by coolant mass flow.

Thermal management in PEMFC systems is of vital importance, basically due to the fact that heat produced in the selected fuel cell cannot be dissipated by convection and radiation through the stack surface. A consistent and stable operation of around 70°C thus requires a liquid cooling system. Since the operating temperature of the fuel cell is not very high, a low temperature difference with the ambient requires having a large heat transfer surface. Thus, an efficient thermal control system becomes of substantial importance to ensure optimum system performance.

As shown in Fig.1, the cooling system for fuel cell consists of internal and external cooling circuits. Also mentioned earlier, the coolant mass flow rate defines the variance in the stack temperature or simply maintains the fuel cell operating temperature. In this case, temperature in the stack can be controlled by coolant flow rate which acts as an input signal and is adjusted by the PI controller. Based on data from Fig. 3b, equations defining stack temperature as a set–point for controller are developed. In addition, the controller simultaneously collects data from temperature transmitter at coolant outlet stream, which then changes the coolant flow accordingly by sending output signals to the driving pump. Employment of such algorithm in the system controller ensures a

stable operation under normal steady–state conditions, however for system start–up scenario, a different approach is required.

Temperature of the coolant entering the stack can similarly be controlled by flow of water in the external circuit. Control signal to the associated pump regulates electrical power of the pump and hence the coolant inlet temperature into the stack. In a similar fashion, temperature of water in the external circuit is dependent on radiator fan speed. PI controllers are used to regulate the fan speed as well.

3. Fuel cell modelling

The characteristics of the PEMFC system described above are implemented in Aspen Plus Dynamics™ which is a simulation tool for process modelling and energy system analysis. The program contains a vast library of components and controls for standard energy processes. The PEMFC stack model presented in this study is based on a model developed by Hosseinzadeh and Rokni [18]. Concentration losses are neglected in the present study, which is justified by the fact that the system does not run at such high current densities where the concentration overpotentials becomes significant. Models for fuel cell and humidifier are also implemented into the code and are based on adopted mathematical models describing the voltages, current densities and their dependence on operating pressures, temperatures and stoichiometric ratios of the reactant gases. This model which incorporates governing equations for cell electrochemical, polarization overpotentials, heat transfers and water diffusion across the membrane is implemented into ASPEN Plus Dynamics and system controls are implemented in order to ensure stable operation of the plant during load changes. Thermodynamic efficiency and net power of the system are determined by the current drawn and voltage produced by the stack. Total energy into the fuel cell is consumed by electrical power output, heat removed by the coolant, heat loss at the stack surface and energy stored by the stack itself. In the current model, a lumped thermal model proposed by Khan and Iqbal [10] is considered. The stack is regarded as a single thermal mass with a heat capacity. With the assumption of stack temperature being equal to coolant temperature at the outlet, heat exchanged with the coolant and hence stack operating temperature could be determined. Subordinate components in the BoP, i.e. anode recirculation and water pumps, air compressor, mixers and heat exchangers are simulated by using default mathematical models contained in Aspen Plus Dynamics library. Table 2 shows a standard set of equations which constitute the model used in the current study.

Table 2. Constitutive equations for PEMFC model.

Average cell voltage	$V_{cell} = E - \eta_{act} - \eta_{ohmic} - \eta_{conc}$	(1)

Nernst equation	$E = \frac{-\Delta \bar{g}_f^0}{n_e F} + \frac{RT}{n_e F} \ln\left(\frac{a_{H_2O}}{a_{H_2} a_{O_2}^{0.5}} \right)$	(2)
Theoretical cell voltage	$E = \frac{-\Delta \bar{g}_f^0}{n_e F} + \frac{RT}{n_e F} \ln\left(P_{H_2}^{-1} P_{O_2}^{-0.5} \right)$	(3)
Change in Gibbs free energy	$\Delta \bar{g}_f^0 = \left(\bar{g}_f^0\right)_{H_2O} - \left(\bar{g}_f^0\right)_{H_2} - \frac{1}{2}\left(\bar{g}_f^0\right)_{O_2}$	(4)
Activation losses in PEMFC	$\eta_{act} = \eta_{act,c} + \eta_{act,a} = \frac{RT}{\alpha_c F} \ln\left(\frac{i + i_n}{i_{0,c}} \right) + \frac{RT}{\alpha_a F} \ln\left(\frac{i + i_n}{i_{0,a}} \right)$	(5)
Ohmic overpotentials	$\eta_{ohmic} = \left(r_{el} + r_{ion}\right) \cdot i$	(6)
Ionic resistance in the cell	$r_{ion} = \frac{C_1 \cdot \left[1 + 0.03i + 0.062 \cdot \left(T/303\right)^2 \cdot i^{2.5}\right]}{\left(\lambda_{ave} - 0.634 - 3i\right) \cdot \exp\left[C_2 \cdot \left(T - 303\right)/T\right]} \cdot t_m$	(7)
Membrane water content	$\lambda_{ave} = 0.043 + 17.18 a_w - 39.85 a_w^2 + 36 a_w^3$	(8)
Water vapour activity	$a_w = P_w / P_{sat}$	(9)
Water profile inside cell membrane	$\lambda_{mem} = \frac{\lambda_c - \lambda_a}{t_m} .z + \lambda_a$	(10)
Transfer coefficient for anode	$\alpha_a = \beta \cdot n_{el}$	(11)
Transfer coefficient for cathode	$\alpha_c = \left(1 - \beta\right) \cdot n_{el}$	(12)
Exchange current density at anode	$i_{0,a} = n_{el} \cdot F \cdot k_a \cdot \exp\left(\frac{\left(1 - \beta\right) \cdot n_{el} \cdot F \cdot E}{RT} \right)$	(13)
Exchange current density at cathode	$i_{0,c} = n_{el} \cdot F \cdot k_c \cdot \exp\left(\frac{-\beta \cdot n_{el} \cdot F \cdot E}{RT} \right)$	(14)
Net water transportation through membrane	$J_{H_2O} = 2 n_{drag} \frac{i}{2F} - \frac{\rho_{dry}}{M_m} D_\lambda \frac{d\lambda}{dz}$	(15)
Water diffusion coefficient	$D_{\lambda>4} = 10^{-6} \exp\left[2416 \cdot \left(\frac{1}{303} - \frac{1}{T} \right) \right] \cdot \left(2.563 - 0.33\lambda + 0.0264\lambda^2 - 0.000671\lambda^3\right)$	(16)

Fuel cell energy balance	$C_t \cdot dT/dt = \dot{P}_{in} - \dot{P}_{out} - \dot{P}_{el} - \dot{Q}_{loss}$	(17)
Faraday's law	$\frac{dN}{dt} = \frac{I}{n_e \cdot F}$	(18)

4. Results and discussion

Simulations for the prescribed system were carried out and reliability of the suggested model is verified and corroborated against design validation data by [17] at different power loads. Model characteristics of the same system at various operating temperatures and power loads have been studied in Hosseinzadeh and Rokni [18]. Figure 4a represents adaptation of the devised model which corresponds to the polarization curve obtained from operational data associated with the given PEMFC stack. The calculated relative error shows a good agreement between the model and data provided. As suggested by the manufacturer, stack temperature range of 60–70°C has been used in simulations of the current system. Selection of other parameters and operating conditions is based upon Fig. 2 and Fig. 3.

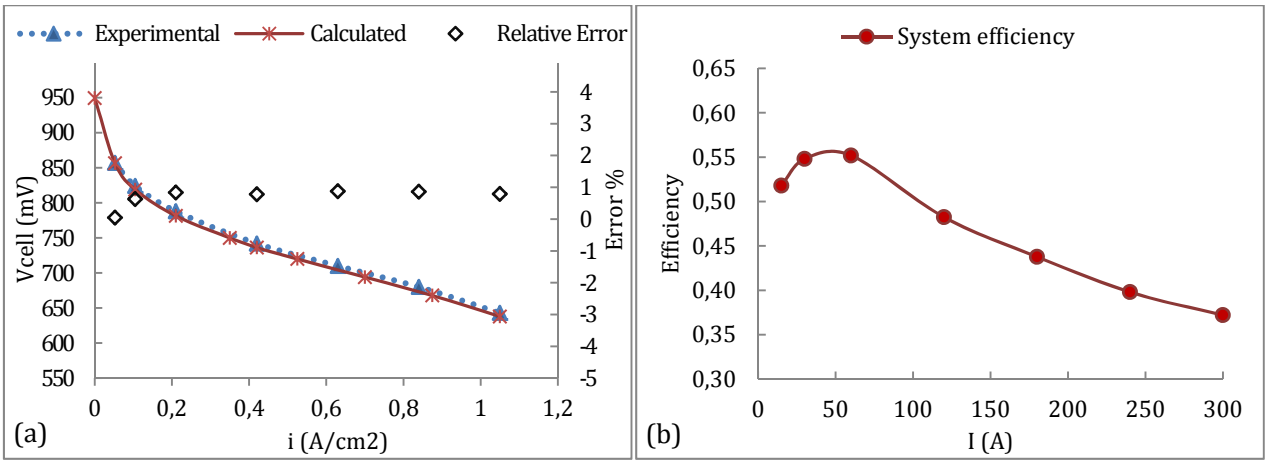

Figure 4. (a) Comparison of Ballard operational data and calculated polarization curves for PEM fuel cell with relative error, (b) Overall system efficiency profile at operating current range.

Fig. 4b exhibits profile of overall system efficiency at corresponding currents. A general trend of decreasing efficiencies with increasing loads can be observed, which is characterised by an increase in ohmic overpotentials in the stack and high power consumption of BoP for cooling of the system. However an exception to the contrary can be noticed at very low currents, where high parasitic losses in BoP render the system efficiency to be lower as well. Nevertheless, higher stack efficiencies at low loads assist the system efficiency to be not as low when compared to that at higher currents. Results for transitory effects under variable load changes (when a current corresponding to a

specific power load is drawn from the stack and varied at any occurrence of time) are discussed below:

1.7 *Cell voltage and temperature variations*

An instance of load change, when current is ramped from 60 A to 100 A at a rate of 20 amperes per second and vice versa, is presented in Fig. 5a and its effects on cell voltage are examined. It can be observed that the cell voltage reduces abruptly with current surge and vice versa. This decline in voltage potential at increase of current density is attributed to the cell overpotentials. However, it is also noticed that cell voltage is also a function of operating temperature and pressure. Since, pressures of the reactants are already regulated; here we will discuss temperature dependency of developed potential differences in the cell. Voltage increases with the elevation of operating temperature. This is due to fast reaction kinetics at the electrodes of individual cell sites when operating at higher temperatures. At the same instance of current ramp as more current is drawn; more heat is produced by the reactions at cell sites, thus elevating the stack temperature. Consequently, the voltage also increases after the initial dip and follows the decreasing profile with the stack temperature as it is controlled towards the desired operating temperature. The opposite could also be observed when the current is reduced back to 60A.

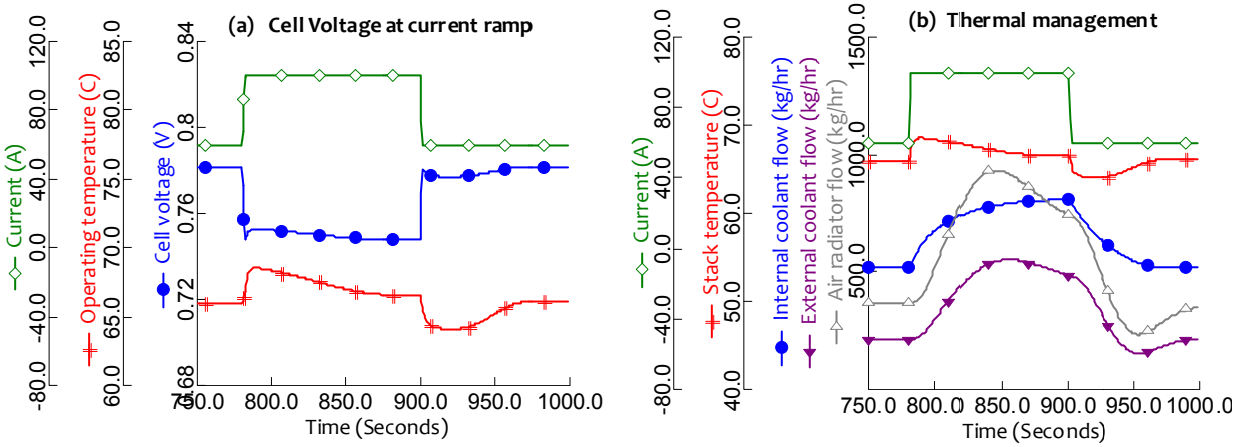

Figure 5. Current ramp–up from 60–100A and vice versa: (a) Changes in cell voltages and operating temperature, (b) Changes in coolant flows to maintain the fuel cell operating temperature.

Since, temperature affects the voltage and overall system efficiency, it becomes important to have a stable operating temperature and therefore an efficient thermal management system. As can be seen in the Fig. 5b, coolant flow rates in both cooling circuits and an air radiator maintain the temperature of the stack, though it is very slow compared to the reaction kinetics affecting the stack voltage. Ramping of current increases the operating temperature of stack thereby actuating controls to contemplate this increase. Flow in the internal cooling circuit, which is coupled with the fuel cell stack is increased to extract heat and maintain the desired temperature difference

between the stack inlet and outlet. Flow in the external cooling circuit is pumped up to retain the inlet temperature to 60°C. Air flow in radiator is also increased to maintain temperature of external cooling loop around 50°C by rejecting the heat to the surroundings. Rate of coolant flows in respective streams is associated with the power consumed by coolant pumps and air radiator which ultimately affects the overall system efficiency. It is also observed that air radiator being a liquid–gas heat exchanger has the slowest reaction time out of the three. Since temperature controls are slow compared to electrochemical reactions, overall thermal control strategy has a fair impact on stack voltage which undergoes frequent load changes.

5.1 System efficiency and power consumption

As can be seen in the Fig. 6a, when the stack current is altered from 60A to 100A, there is a reduction in system efficiency, mainly due to the associated voltage drop. Overall efficiency of the system is as much affected by air blower and radiator fan, as by the fuel cell stack itself. It can be observed that power produced by the stack increases with current drawn. Also, power consumed by auxiliary components increases, thereby reducing system efficiency from 55.5% to 50%. Once decreased, there is an abrupt rise in efficiency due to increase in voltage and it fluctuates at around 50% mark due to slow temperature controls and fluctuating power consumption by air radiator.

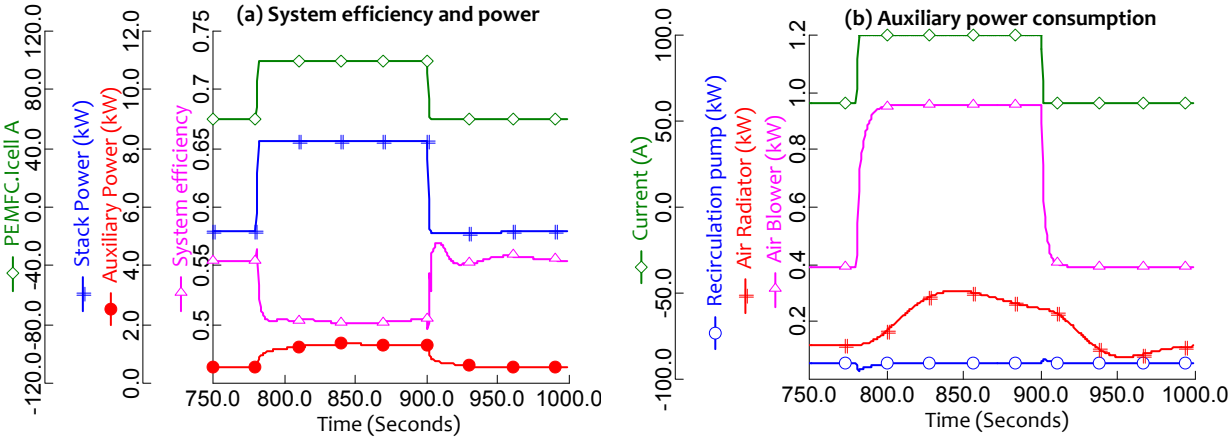

Figure 6. (a) System efficiency, stack power output and power consumed, and (b) Auxiliary power consumption.

Figure 6b elaborates on power consumption in the system. Being a major consumer in the system, power consumption of air blower rises with increase in current and this incremental profile can be associated to the increased mass flow of air required to maintain oxidant stoichiometry in the fuel cell. After the initial rise, power consumption of air blower becomes constant; however the consumption graph of air radiator takes more time to become stable. This is due to the fact that flow in air radiator is manipulated to control the temperature and is a slow process. Together, air

blower and radiator consume 10% to that of stack power, whereas a coolant and recirculation pumps account for 1.0–1.3% when operating at 60A.

On the other hand, at higher currents of 100 A, power consumed by air blower and radiator constitutes 15% of the total stack power. For a swift temperature control and a thermally stable operation, air radiator requires more power or a larger heat exchanger area which would further reduce efficiency during these load variations. Power consumption of coolant pumps is not shown in the above figure because increase in internal and external coolant flows affects the auxiliary power consumption to a very small extent as compared to air compressor and radiator. Anode recirculation pump also consumes very low power; however the peaks at current surge are a noticeable detail, which is addressed later in the results.

5.2 Effects of water transportation in fuel cell

In PEMFCs, water management is a critical issue since the performance of fuel cell is strongly influenced by its internal water distribution. Figure 7a shows net water diffusion in the cell when current is changed from 60A to 100A and back. In the figure, positive values for water crossover designate transportation of water from cathode to anode of the fuel cell and vice versa. With increasing currents, more water is produced in the cathode which supports back–diffusion towards the anode until the system reaches back to steady–state and there is almost no net water crossover. Some negative peaks are also observed at the start of current change, which are due to electro–osmotic drag.

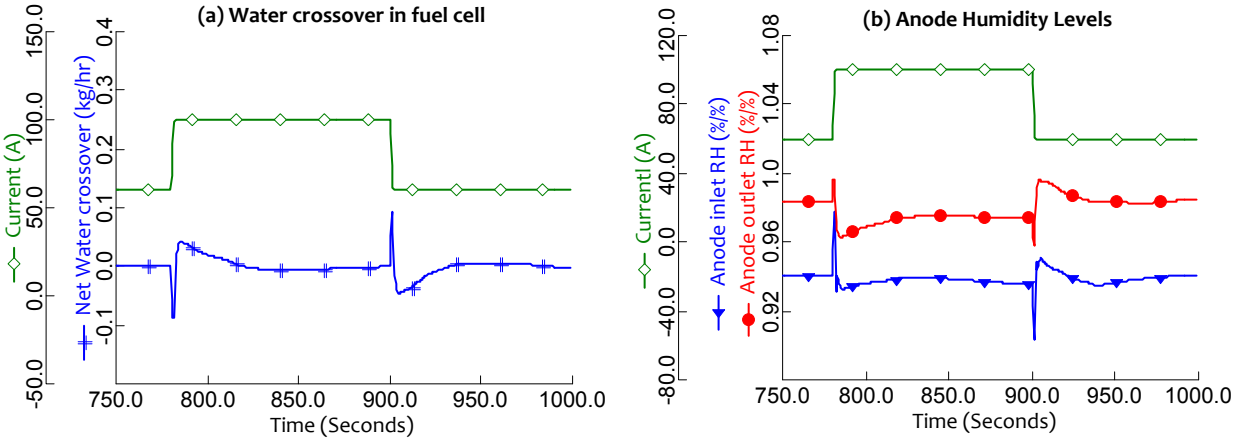

Figure 7. Current ramp–up from 60–100A and vice versa: (a) Water crossover through PEMFC membrane, (b) Effect of water transportation on anode RH.

As more current is drawn, there is a rapid increase in hydrogen ion flux towards the cathode, thereby supporting water crossover through electro–osmotic drag. Back–diffusion rate is increased with the production of water on the cathode side and subsequently water flux is directed towards fuel cell anode. The reverse can said to be

true when current is ramped down from 100 A to 60A. Effect of water distribution can also be observed in anode inlet and outlet relative humidity. Whereas for the cathode, since it is assumed that air enters at a constant relative humidity of 95%, the outlet humidity is always above 100%. Therefore, results for only anode are discussed here.

From Fig. 7b, it could be further observed that relative humidity at anode outlet decreases with a current surge, though an abrupt increase is detected at the start of this change. Sudden ramping of the current consumes more hydrogen, leaving higher molar fraction and partial pressure of water in the anode, thus the peak of high relative humidity. With the rise in stack temperature, water activity on anode side is reduced and water diffusion from cathode increases and consequently stabilizes to almost zero net–water crossover with the control of operating temperature. As there is no external humidification apparatus for fuel and recirculation of anode exhaust aides in humidifying the anode, water crossover has a significant impact on anode operations which are discussed below.

5.3 Fuel and oxidant flows

Figure 8 depicts the variations in reactant inlet flows when the load on fuel cell is varied. It is interesting to notice the fluctuations in the anode inlet and outlet. When the current is ramped up from 60A to 100A, more hydrogen is consumed increasing the utilization factor at that instance. This can be seen in Fig. 8b where mass flow at anode exhaust suddenly decreases. Changes in temperature can also be noted at these current surges as the air stream is cooled by external cooling circuit.

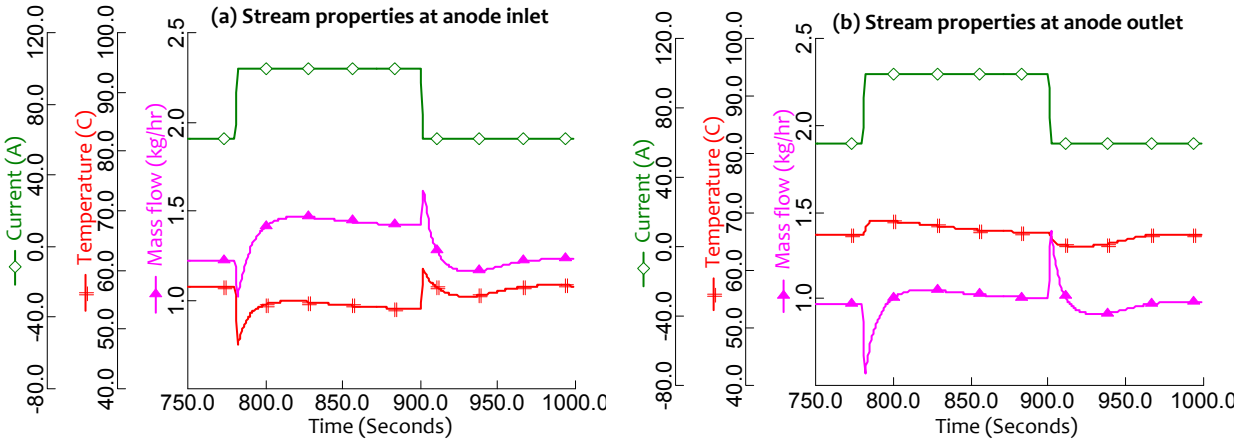

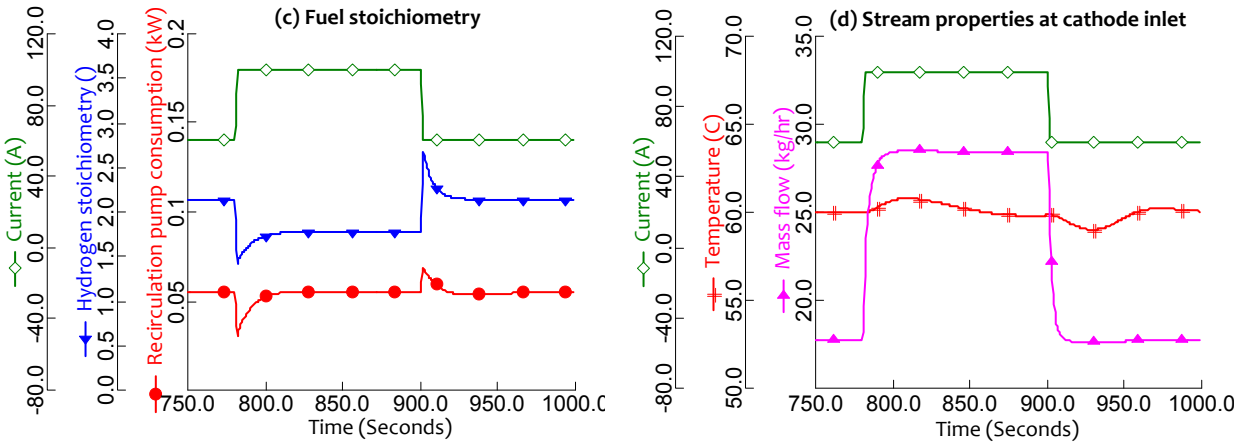

Figure 8. Current ramp–up from 60–100A and vice versa:, (a) Stream properties at anode inlet and (b) outlet respectively, (c) Effect on fuel stoichiometry and recirculation pump, (d) Air flow into the cathode.

Control of fuel stoichiometry takes some time to readjust to the desired level. Although, anode outlet flow is disturbed by fuel stoichiometry, it is also affected by the water content in anode outlet (70% mass fraction), which depends on the net water crossover within the cell. Initial peaks at both load changes are also attributed to the electro–osmotic drag which is a function of current density. Since anode inlet is supported by recirculation from anode exhaust, the changes within the stack influence it considerably. In Fig. 8a, fuel flow at anode inlet follows a similar trend to that of anode exhaust, as well as the inlet temperature. Rapid reduction in temperature is due to lower volume of recirculation which is at around 69°C whereas dry hydrogen from the tank is at 25°C. Fluctuations in water content at anode inlet disturb fuel flow controls and relative humidity constantly; they remain within acceptable ranges however. Figure 8c shows the fuel stoichiometry changes and power consumed by recirculation pump, which are affected by the depletion of hydrogen at anode cell sites and water diffusion during the current surges. On cathode side (Fig. 8d), as expected, the air flow which is regulated by a controller increases when the current is ramped up and steadies along with the system. There is no specific temperature control of inlet air in this model, though external coolant flows manipulate the air temperature which is further preheated by the humidifier before entering the stack. Air temperature varies around 60°C which is equal to the controlled temperature for coolant entering the stack; however temperature difference at anode inlet is significantly higher during these load variations. Such temperature gradients incur adverse effects as they form thermal stresses in the stack with co–flow configuration and reduce its life cycle.

5.4 Effects of water saturation at cathode

Water removal from a fuel cell cathode is dependent on stack temperature and pressure drop. Temperature is more critical factor of the two, since at high temperature the water

will be in vapour state and easier to remove. Stack water production increases with current and is also dependent on the number of cells. The exact amount of liquid water product depends on cathode outlet temperature. Inlet humidity also contributes to liquid water saturation in the fuel cell, as reported in Wong et al. [19]. Figure 9 provides information on the amount of liquid water at outlet of the cathode channel for two different current surge amplitudes.

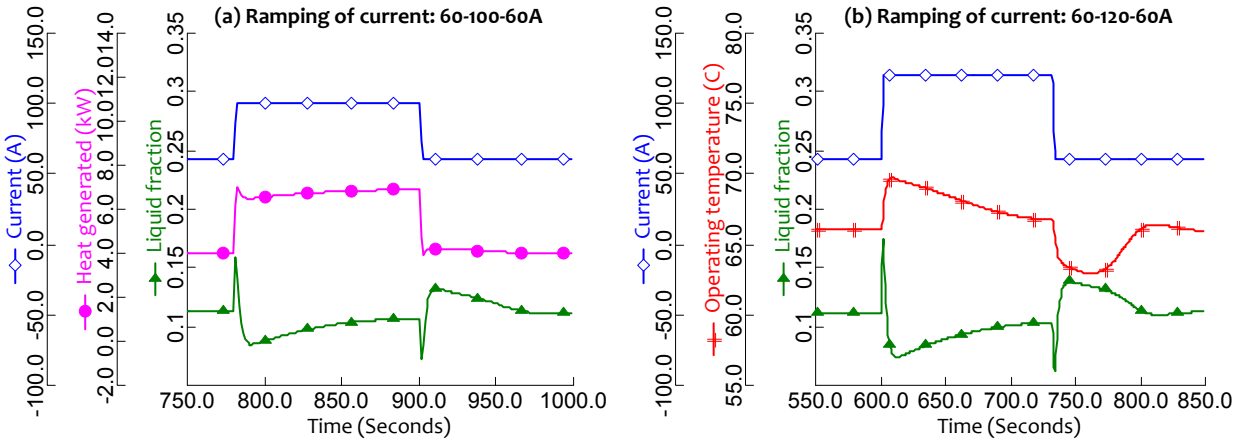

Figure 9. Water crossover through PEMFC membrane; (a) Current ramp–up from 60A to 100A and vice versa, (b) Current ramp–up from 60A to 120A and back.

It can be seen in Fig. 9a, that there is an abrupt increase in amount of liquid water at cathode when the current is ramped from 60A to 100A. When higher currents are drawn, reactions within the fuel cell are accelerated which demand more intake of fuel and oxidant. Consequently these reactions produce more water when compared to production at low currents. Since the stack temperature does not elevate till that instance, higher percentage of produced water is saturated at fuel cell cathode. Heat produced by cell reactions then elevates the stack temperature, thereby reducing saturated water at the outlet. Moreover, condensation of water at cell sites produces additional heat which rapidly increases the stack temperature. It can be further noticed in Fig. 9a that heat produced in the stack lowers as water liquid fractions drop. On the other hand, when current is reduced back to 60A, a similar but opposite profile is observed and the amount of liquid water tends to increase with a sink in stack temperature. Therefore, at low temperatures and currents, water removal is a dominant factor and stoichiometries are determined by the minimum flow rates required for water removal which in the present case are more than adequate to provide the necessary concentrations. Figure 9b shows water saturation results when ramping of current is set from 60A to 120A instead. Although the data profile is analogous to that of Fig. 9a, it is noted that amplitude of these peaks is higher when compared. Apparently, the amount of liquid water at cathode exit is same for both cases when the fuel cell is operating at steady state. Heat produced by condensation requires additional flow of coolant to

maintain stack operating temperature, yet it does not affect the system efficiency to a greater extent as liquid pumps do not consume that much power.

5. Conclusions

In this study, a comprehensive dynamic model of a PEMFC system along with the auxiliary components is presented and a substantial emphasis has been set to devise a control–oriented dynamic model of the fuel cell stack, which accommodates the electrochemical, thermal, feed flow and water transportation models. Main contributions of the proposed model are ascribed to the dynamic system responses, which is characterized mainly by heat management and water transportation within the fuel cell.

It is observed that thermal management strategy greatly influences voltage output and system efficiency which increase with stack operating temperature. Moreover, slow temperature controls affect the stability of fuel cell operations. In order to contemplate fast electrochemical changes in the stack, high coolant mass flow rates are applied. Power consumed by liquid coolant pumps is minimal and have no considerable effect on system efficiency, whereas air radiator consumes most of the power in thermal management system. Further, work is required on air radiator to ensure thermal stability of fuel cell operations and prolonged stack lifetime. A 5% increase in power consumption of air blower and radiator is observed during load variations for the cases presented here.

Furthermore, water crossover in the fuel cell has shown a significant impact on PEMFC anode operations. Anode inlet flows, humidity and recirculation pump are influenced by net water diffusion during load changes. Temperature changes at anode inlet are considerably higher during load variations and have a negative impact as they generate thermal stresses in the stack and reduce its lifetime. Also, amount of saturated water at cathode is dependent on operating temperature which apparently pertains to thermal management strategy of the system. At low currents and temperatures, reactant stoichiometries are determined by the minimum flow rates required for water removal from the stack.

Acknowledgement

The authors would like to thank the Danish Energy Agency for financial support and our industrial partner, H2Logic, for their collaboration and technical support.

References

[1] J. C. Amphlett, R. F. Mann, B. A. Peppley, P. R. Roberge, A. Rodrigues, A model predicting transient responses of proton exchange membrane fuel cells, J. Power Sources 61(1996) 183–188.

[2] S. Yerramalla, A. Davari, A. Feliachi, Dynamic modeling and analysis of polymer electrolyte fuel cell, IEEE Power Engineering Society Summer Meeting 1–3 (2002) 82–86.

[3] M. Ceraolo, C. Miulli, A. Pozio, Modelling static and dynamic behaviour of proton exchange membrane fuel cells on the basis of electro–chemical description, J. Power Sources 113 (2003) 131–144.

[4] J. T. Pukrushpan, H. Peng, A. G. Stefanopoulou, Control–Oriented Modeling and Analysis for Automotive Fuel Cel Systems, J. Dynamic Systems Measurement & Control 126 (2004) 14–25.

[5] P. R. Pathapati, X. Xue, J. Tang, A new dynamic model for predicting transient phenomena in a PEM fuel cell system, Renewable Energy 30 (2005) 1–22.

[6] G. Hu, J. Fan, S. Chen, Y. Liu, K. Cen, Three–dimensional numerical analysis of proton exchange membrane fuel cells (PEMFCs) with conventional and interdigitated flow fields, J. Power Sources 136 (2004) 1–9.

[7] S.K. Park , S.Y. Choe, Dynamic modeling and analysis of a 20–cell PEM fuel cell stack considering temperature and two–phase effects, J. Power Sources 179 (2008) 660–672.

[8] J. Jia, Y. Wang, Q. Li, Y. T. Cham, M. Han, Modeling and Dynamic Characteristic Simulation of a Proton Exchange Membrane Fuel Cell, IEEE Transactions on Energy Conversion 24 (2009) 283–291.

[9] G. Vasu, A. K. Tangirala, Control–orientated thermal model for proton–exchange membrane fuel cell systems, J. Power Sources 183 (2008) 98–108.

[10] M. J. Khan, M. T. Iqbal, Modelling and analysis of electrochemical, thermal, and reactant flow dynamics for a PEM fuel cell system, Fuel Cells 5 (2005) 463–475.

[11] Y. Shan, S.Y. Choe, Modeling and simulation of a PEM fuel cell stack considering temperature effects, J. Power Sources 158 (2006) 274–286.

[12] A. J. del Real, A. Arce, C. Bordons, Development and experimental validation of a PEM fuel cell dynamic model, J. Power Sources 173 (2007) 310–324.

[13] J.W. Ahn, S.Y. Choe, Coolant controls of a PEM fuel cell system, J. Power Sources 179 (2008) 252–264.

[14] J.H. Jung, S. Ahmed, Dynamic model of PEM fuel cell using real–time simulation techniques, J. Power Electronics 10 (2010) 739–748.

[15] S. Asghari, H. Akhgar, B. F. Imani, Design of thermal management subsystem for a 5kW polymer electrolyte membrane fuel cell system, J. Power Sources 196 (2011) 3141–3148.

[16] A. Beicha, Modeling and simulation of proton exchange membrane fuel cell systems, J. Power Sources 205 (2012) 335–339.

[17] Ballard Mark9 SSL, Product manual and integration guide 2008.

[18] E. Hosseinzadeh, M. Rokni, Development and validation of a simple analytical model of the Proton Exchange Membrane Fuel Cell (PEMFC) in a fork–lift truck power system, Intl. J. Green Energy, In Press (2012) DOI: 10.1080/15435075.2012.678525.

[19] K. H. Wong, K. H. Loo, Y. M. Lai, S.–C. Tan, C. K. Tse, A theoretical study of inlet relative humidity control in PEM fuel cell, Intl. J. Hydrogen Energy 36 (2011) 11871–11885.

Nomenclature

E	theoretical voltage (V)
V_{cell}	average cell voltage (V)
$\dot{P}_{el}$	stack power (kW)
$\dot{P}_{in}$	energy into the fuel cell (kW)
$\dot{P}_{out}$	energy out of the fuel cell (kW)
$\dot{Q}_{loss}$	heat dissipated (kW)
C_t	stack thermal capacitance (kW)
R	universal gas constant $(J/molK)$
T	temperature (K)
F	Faraday's constant $(C/molK)$
I	current (A)
N_{cell}	number of cells $(-)$
$\Delta\bar{g}_f^0$	change in Gibbs free energy $(J/molK)$
P_{H_2}	hydrogen partial pressure $(-)$

P_{O_2}	oxygen partial pressure $(-)$
M_m	mol. weight of membrane (Kg/mol)
J_{H_2O}	net water–diffusion flux (mol/scm^2)
D_λ	water diffusion coefficient (cm^2/s)
a_{H_2}	hydrogen activity $(-)$
a_{H_2O}	water activity $(-)$
a_{O_2}	oxygen activity $(-)$
i	current density (A/cm^2)
i_n	internal current density (A/cm^2)
i_0	exchange current density (A/cm^2)
$i_{0,a}$	anode exchange current density (A/cm^2)
$i_{0,c}$	cathode exchange current density (A/cm^2)
k_a	anode reaction rate (mol/scm^2)
k_c	cathode reaction rate (mol/scm^2)
n_e	electrons transferred (mol_e/mol_{fuel})
n_{el}	number of electrons $(-)$
n_{drag}	electro osmotic drag $(-)$
t_m	membrane thickness (cm)

Greek symbols

α_a	anode transfer coefficient $(-)$
α_c	cathode transfer coefficient $(-)$
β	symmetry factor $(-)$
η_{act}	activation overpotential (V)
$\eta_{act,a}$	anode activation overpotential (V)
$\eta_{act,c}$	cathode activation overpotential (V)
η_{conc}	concentration overpotential (V)
η_{ohmic}	ohmic overpotential (V)
λ	membrane water content $(-)$
ρ_{dry}	membrane density (g/cm^3)

Appendix D

Paper III

Rabbani, A & Rokni, M. “Effect of nitrogen crossover on purging strategy in PEM fuel cell systems”, accepted for Journal of Applied Energy, 2013.

Effect of nitrogen crossover on purging strategy in PEM fuel cell systems

Abid Rabbani and Masoud Rokni

Thermal Energy Section, Department of Mechanical Engineering, Technical University of Denmark, 2800 Kgs. Lyngby, Denmark.

Abstract

A comprehensive study on nitrogen crossover in polymer electrolyte membrane fuel cell (PEMFC) system with anode recirculation is conducted and associated purging strategies are discussed. Such systems when employed in automobiles are subjected to continuous changes in load and external operating conditions, making it important to investigate the dynamic performance of the system during transitory conditions. The model developed here is able to predict nitrogen crossover in excellent agreement with the design validation data of the stack. The results show that with pure recirculation, voltage and system efficiency decline due to nitrogen accumulation in fuel cell. Different purging techniques are simulated to address hydrogen dilution issue at reaction sites. Anode bleed out of 3% is found to be limit for prevention of N_2 buildup and retains the concentration levels to less than 1%. An alternate strategy for automatic initiation of anode recirculation purge was simulated by employing nitrogen detectors. It is observed that purge interval is a direct function of current density and H_2 residual flow rates. Moreover, during transient load changes, automatic purge catered well to prevent nitrogen levels from rising when compared to a fixed purge interval strategy. This model can be used as a base for control and development of anode purge strategies for automotive fuel cell systems.

Key words: *Dynamic simulation, fuel cell, PEMFC, nitrogen crossover, anode purge.*

Introduction

Hydrogen is being anticipated as the fuel of the future and fuel cells are gaining significant importance in power generation technologies and in establishing the hydrogen economy. Polymer Electrolyte Membrane Fuel Cells (PEMFCs) run on hydrogen as a fuel, which only produces water when used with air as the oxidant. These

types of fuel cells will prove to be vital in reducing our dependency on fossil fuels and diminish harmful emissions into the atmosphere. Further advantages of PEMFCs include low operating temperatures, high power density and swift start–ups making them an ideal candidate for automotive applications. Conversely, these automobiles operate in an environment subjected to continuous changes in load and external operating conditions, which compromises durability and reliability of the fuel cells.

In a typical PEMFC, hydrogen is fed into the anode of the fuel cell stack and oxygen/air into the cathode, while the water produced from cell reactions is ejected out of the cathode outlet. Since the current generated in the fuel cell is a direct measure of the rate of electrochemical reactions, power produced by the stack is associated with the rate at which the reactants are consumed. Ideally, all of the hydrogen and oxygen needed for any specific power of the fuel cell stack would be consumed and only water and unused nitrogen of the air would leave the system. However, not all hydrogen and oxygen delivered at the reaction stoichiometry reaches the cell sites. At a stoichiometry of 1.0, the reactant partial pressure at the stack exit reaches very close to 0, which can cause fuel starvation leading to irreversible damage to the stack in addition to a lower power output [1]. Therefore, higher stoichiometries of reactants are fed into the system. In most systems, the unused hydrogen is recirculated back into the feed stream, thereby increasing the system efficiency.

As already mentioned, one of the benefits of PEMFCs is their high power density which is essential for portable applications. Recent advancements in manufacturing have made these stacks more compact by significantly reducing the thickness of Membrane Electrode Assembly (MEA), though enhances gas crossover across the membrane resulting in current losses within the fuel cell itself. One of these gases is nitrogen from the air, which permeates from the cathode to anode and gets concentrated in the anode due to recirculation. Similarly, water produced on the cathode side is also transported towards the anode through the membrane. This build–up of nitrogen and water reduces the concentration of hydrogen in anode channels and obstructs hydrogen molecules to reach cell reaction sites effectively, which adversely affects the voltage developed in the cell [2], [3] . Also, H_2 starved areas are developed within the fuel cell which can also result in carbon corrosion [4], [5]. Furthermore, additional flow of these crossed over gases increases the power consumption of recirculation pump, thereby adding to the efficiency loss due to the voltage drop [6]. In most systems with anode recirculation, N_2 build–up is usually avoided by frequently purging a certain percentage of the anode outlet gas before mixing it with the inlet stream. An alternative approach is to continuously bleed a small fraction of the recirculation stream. While both mentioned approaches release some portions of nitrogen as well as water vapor from the recirculated stream, it also purges unused hydrogen. In this context, the amount purge fraction and time intervals of these purging techniques are of particular interest to the authors. An optimum strategy would cease the build–up of N_2 with a compromise of minimum H_2 wastage. In this paper, we present a dynamic model of N_2 build–up in

anode under recirculation and compare different purge strategies for optimal system performance.

Literature available on water and gas crossover through PEMFC membranes is not uncommon. Kocha et al. [2] characterized gas crossovers by applying an in–situ electrochemical technique to determine hydrogen crossover rates and devised a model to predict the extent of nitrogen accumulation along the anode flow fields. Ahluwalia and Wang [7] modeled and analyzed the buildup of N_2 in the recirculating anode gas and the impact of this buildup on the performance of 90 kW PEMFC stack. Catalano et al. [8] reported the effects of relative humidity on gas permeability and swelling in Nafion membranes used in fuel cells. Baik and Kim [9] calculated nitrogen permeability coefficients (NPC) by employing a mass spectrometer and analyzed N_2 crossover under open circuit voltage and power generation conditions. Ismail et al. [10] conducted a parametric study to investigate the effect of transport properties of GDLs on fuel cell performance. Weber [3] reported the effects of membrane pinholes and increase in gas–permeation on PEMFC's performance. It was also shown that water and thermal management is also affected where there are large pinholes in the membrane.

There are a few published papers investigating the purge process modeling in general or specifically pertaining to individual aspects of the process. Zhu et al. [11] experimentally determined the critical flow rate in anode exhaust stream by manual purging of Nexa Power module. Tang et al. [12] also investigated the transient response of the aforementioned module and identified factors influencing its performance. Zhai et al. [13] also presented their study on anode water flooding and simulated the gas purge effect for medium current densities. Gou et al. [14] presented a one–dimensional computational model to study the dynamic behavior of pressure in anode flow field during the purge process. It was shown that different current densities had minimal influence on the pressure drop and the pressure swing during this transient process. A dynamic three–phase transport model was developed by Wang et al. [15], which lead in identification of the optimum water uptake parameters for purge cycles during startup from subfreezing temperatures and subsequent shutdowns. Karimaki et al. [16] setup a test bench to study inert gas buildup effects on fuel cell stack and introduced the use of online hydrogen sensor to measure gas crossover across the cell. Promislow et al. [17] built a simple analytical model to describe the steady state profile of anode N_2 concentration in PEMFCs with straight gas channels and identified an optimum bleed rate for the specified stack.

Some others have published papers addressing the anodic dead–end mode of operations in the fuel cell anode. Hou et al. [18] developed a dynamic voltage model for a 'dead–ended' FC to simulate hydrogen purging in order to prevent water accumulation in the anode. Muller et al. [19] also correlated N_2 accumulation with a 20–cell temporal fuel cell performance operating in a 'dead–end' mode by estimating permeability characteristics of typical Nafion membranes. Siegel et al. [20] modeled a PEM fuel cell

operating with a 'dead–end' mode and experimentally verified the evolution of liquid water and nitrogen fronts along the length of anode channels. They further developed the 1D model with periodically–purged anode channels and incorporate simple resistance model for predicting nitrogen permeance and water transportation through the membrane and presented their findings in Yesilyurt et al. [21]. Another experimental study was conducted by Choi et al. [22] in which purge characteristics of a cathodic dead–end mode PEMFC for a submarine were analyzed.

Although, there are a few publications dealing with nitrogen crossovers and associated purge processes, but to the best of authors' knowledge, there is no available study on intricate details of nitrogen crossovers and the effect of purge cycles on the fuel cell performance during transient operations. The present work attempts to simulate the dynamic characteristics of the PEMFC system operating with purge cycles, and investigate its performance during transitory load changes. For this purpose, a comprehensive fuel cell model with all the necessary auxiliary components is built and system simulations are carried out by employing a detailed control scheme in order to emulate a practical operation environment. N_2 accumulation in fuel cell anode and its effect on system performance is investigated, and in view of this buildup, different purging strategies are assessed. At last, an alternate method for nitrogen detection and automatic purging is proposed and compared with conventional methods during different stages of external load changes. This model could be regarded as a basic foundation in design and optimization of purge cycles for automotive systems running PEMFCs.

System configuration

Layout of the PEMFC system under investigation is shown in Fig. 1. The system comprises a PEMFC stack, air compressor, humidifier, pumps, heat exchangers and radiator for the cooling circuit, flow valves and controllers. Hydrogen from storage tank is regulated by a control valve into the fuel cell anode. On the cathode side, compressed air which is fed into stack is cooled and humidified prior to its entrance into fuel cell flow fields. Since the stack is not operated at dead–end mode, a higher fuel stoichiometry is maintained. Unused fuel from anode exhaust is recirculated back to the anode inlet via a recirculation pump. Recycling of the exhaust stream eliminates the need of fuel humidifier as it holds enough water to humidify the fuel. Liquid water present in the anode exhaust is collected in a water trap, whereas the remaining water present in the stream is purged with the other gases by a solenoid valve before mixing with the inlet stream. In addition to electrical power, heat is produced by the stack. This heat is absorbed by a liquid coolant which circulates in a circuit associated with the stack and a heat exchanger. An external cooling loop, connected to the aforementioned heat exchanger, in turn cools the water in the internal circuit. This circuit also consists of a

heat exchanger to precool air entering the fuel cell and an air radiator for heat rejection. Flow of water is regulated by pumps in the respective circuits.

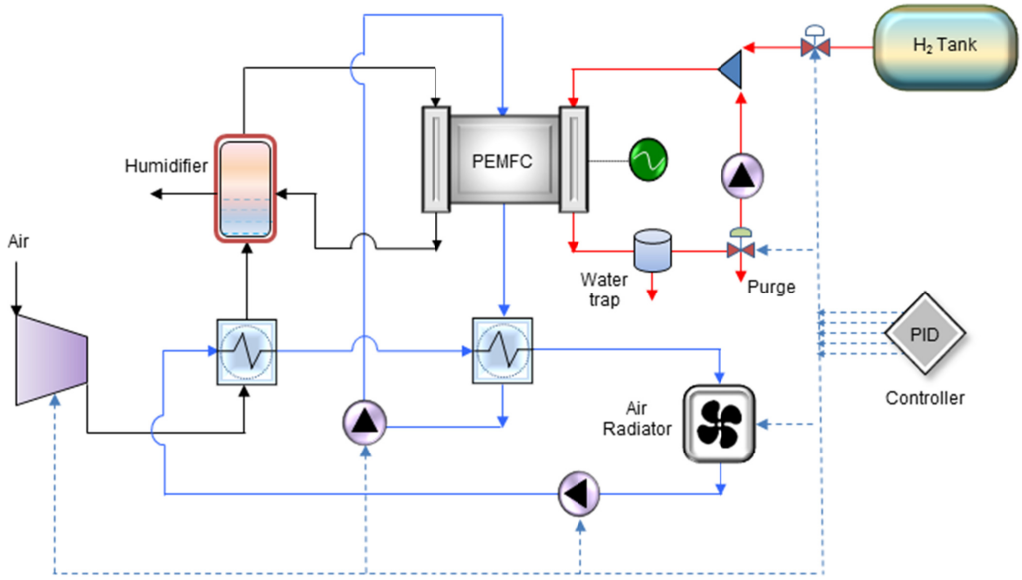

Figure 1. Schematic layout of the PEMFC system

PID controllers are deployed to regulate reactant and coolant flows. These controllers collect data from various component inlet and outlets which are regarded as pressure, temperature and flow transmitters, and manipulate the corresponding components to reach the desired state. Due to this fact, current system responses and its behavior are attributed to the formulated control strategy which is based on fuel cell stack limitations and recommendations by the manufacturer. Detailed control mechanisms are illustrated in subsequent subsection.

Fuel Cell stack

A Ballard fuel cell stack [23] has been selected for the current study. The fuel cell stack contains 110 cells with a cell area equal to 285 cm^2. Maximum power produced from the described stack is 21.2 kW corresponding to a current of 300A; however it is generally operated at lower current ranges to attain higher efficiencies by reducing ohmic and concentration overpotentials within the fuel cell stack. This model, which is based on equations adopted by Hosseinzadeh and Rokni [1], contains some parameters influencing physical characteristics of the system, as well as on operating conditions and membrane properties. Here, focus has been set to build up a system which meets the requirements of actual stack running under recommended conditions, see Table 1. During PEMFC steady-state operations, coolant pressure should be lower than reactant pressures whereas during start-up, coolant pressure may exceed reactant pressure.

Pressure in the anode is usually set higher than to that of the cathode, which will minimize nitrogen crossover and ensure cell stability.

Table 1. Nominal operating conditions for PEMFC stack

Reactant Parameter		Current (A)					
		15	30	60	120	240	300
Fuel (Pure Hydrogen)							
Inlet stoichiometry Min.		6.3	3.4	2.2	1.9	1.6	1.6
Nominal Inlet Pressure	(kPa)	115	116	131	155	200	220
Pressure Drop	(kPa)	9	13	13	14	16	18
Oxidant (Ambient Air)							
Inlet stoichiometry Min.		5.1	2.4	1.8	1.8	1.8	1.8
Nominal Inlet Pressure	(kPa)	108	110	117	138	180	200
Pressure Drop	(kPa)	8	13	12	16	40	53
Relative Humidity	(%)	95	95	95	95	95	95
Coolant							
Inlet Temperature Max.	(°C)	60	60	60	60	60	60
Outlet Temperature Max.	(°C)	61	63	66	67	68	70
Minimum Coolant flow	(lpm/cell)	0.05					

Balance of Plant

A brief overview of balance of plant (BoP) components is presented in this section, though a detailed description is reported in authors' previous work [24]. In the proposed configuration, a humidifier is placed in conjunction of cathode inlet and exhaust, where it utilizes the water produced by chemical reaction inside the fuel cells to humidify inlet air. It is assumed that inlet air is optimally humidified after passing through the humidifier. Relative humidity of air entering the cathode is arbitrarily set to 95% in the simulations. This assumption could be justified as it is very close to real operational conditions. Auxiliary components such as blowers, pumps and valves regulate flows of material streams in PEMFC systems. For hydrogen feed, a valve is placed between the hydrogen tank and inlet manifold of anode which enables or disables the hydrogen supply. Since the system does not operate on dead–end mode, the amount of hydrogen regulated by this valve equals the stoichiometric hydrogen required by the fuel cell. An air blower regulates the flow and pressure of oxidant into the cathode.

A network of heat exchangers and radiators is deployed for heat management of the system. Although heat exchanger models used here are predefined in Aspen Dynamics™, some of the parameters have been assumed on the basis of media entering

the hot and cold sides of these heat exchangers. The heat exchanger, which is connected to the internal cooling loop, has liquid water on both its hot and cold side. Therefore, a UA value of 1.2 kW/K is assumed. Whereas, UA values for air pre–cooler and radiator are approximated to be 0.1 kW/K and 0.3 kW/K respectively. Models for pumps and blowers are also contained in Aspen Dynamics™ library. Since the nominal power of the PEMFC is only 21 kW, mass flow rates of fuel and air are very low. For example, at an average load of 10 kW, fuel and air flows are around 0.00014 kg/s and 0.0088 kg/s respectively. Therefore, very low values of isentropic efficiencies are suggested in this paper. The efficiency of a blower ranges from 15% to 48% in the calculations, depending on the air mass flow. Calculated pump efficiencies are also very low for the cooling water circuits and are determined to be around 70%.

Control System

A system requires an effective control strategy to regulate system parameters and operating conditions to ensure a stable and effective operation [25]. Proportional–integral (PI) controllers, which are widely used in industrial control systems, are employed to regulate different components and flow streams. Key parameters to be controlled in the proposed system are reactant inlet stoichiometries, inlet pressures, coolant inlet and operating temperatures of the stack.

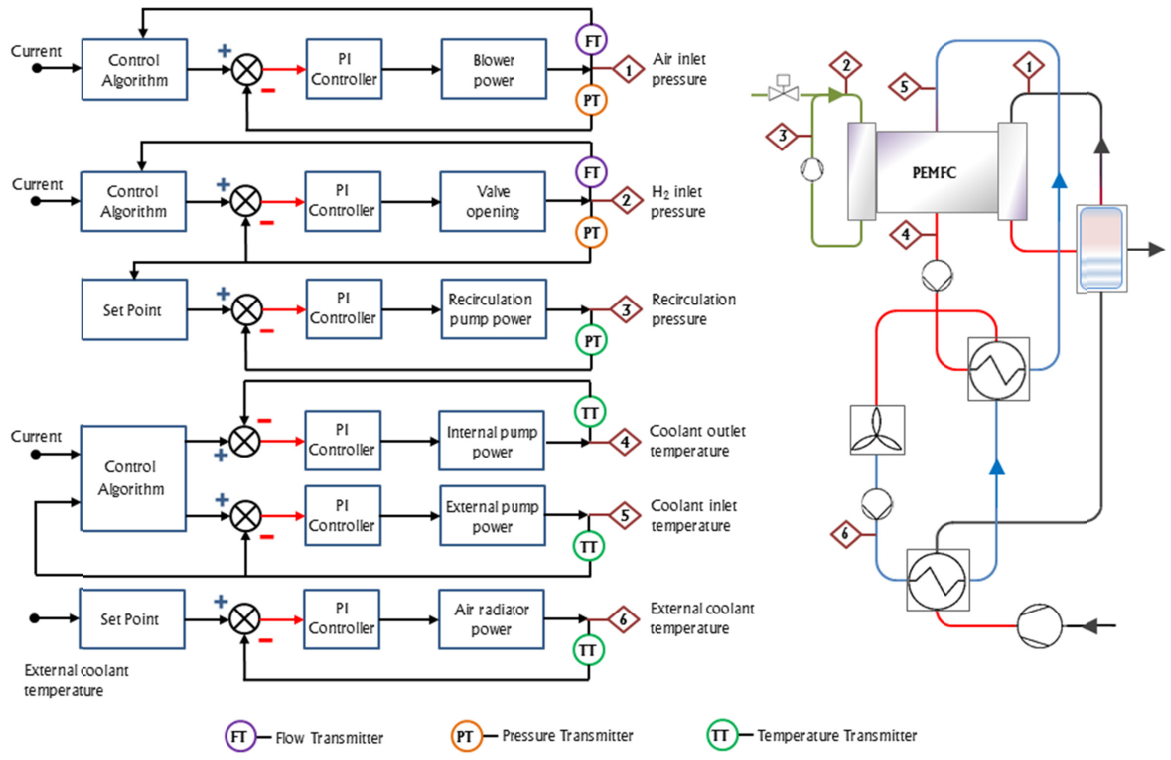

Figure 2. Basic control blocks for the PEMFC system

While the amount of oxygen consumed depends on the stack current, the amount of oxygen supplied to a fuel cell is directly related to the blower power. Therefore, an algorithm based on the above figure is developed to be the process variable for PI controller, which regulates blower power to maintain the desired oxygen ratio. Similarly, an algorithm for controlling hydrogen flow is devised along with a PI controller, which regulates the control valve opening for optimal fuel supply.

Fig. 2 describes the process and manipulated variables implemented in the control scheme. Temperature in the stack can be controlled by coolant flow rate which acts as an input signal and is adjusted by the PI controller. Based on data from table 1, equations defining stack temperature as a set–point for controller are developed. In addition, the controller simultaneously collects data from temperature transmitter at coolant outlet stream, which then changes the coolant flow accordingly by sending output signals to the driving pump. Employment of such algorithm in the system controller ensures a stable operation under normal steady–state conditions, however for system start–up scenario, a different approach is required. Temperature of the coolant entering the stack can similarly be controlled by flow of water in the external circuit. Control signal to the associated pump regulates electrical power of the pump and hence the coolant inlet temperature into the stack. In a similar fashion, temperature of water in the external circuit is dependent on radiator fan speed. PI controllers are used to regulate the fan speed as well.

Model formulation

Nitrogen crossover

For PEMFC membranes, high proton conductivity and low ionic resistance has been achieved by directing significant efforts towards minimizing membrane thickness which subsequently promotes water crossovers across it to humidify the anode side of the fuel cell [26]. Moreover, high power density is also attributed to the membrane thickness in addition to GDL and stack assembly. Limitations for physical stability of the cell and gas crossovers have to be balanced by selection of a membrane with reasonable thickness. It is however reported by [9] and [27] that membrane thickness and equivalent weight does not considerably effect the gas permeability coefficients, but influence of water content in the membrane is significant enough. [28] suggested that in fact N_2 crossover is the sum of two parallel processes; gas diffusion through polymer and water phase of the ionomer respectively. Their simple model was correlated to the functional form by [7]. Here, a similar permeation model of [20] with a scale factor of 8 and equations with the influence of stack temperature and membrane water uptake is used.

$$K_{N_2} = \alpha_{N_2}(0.0295 + 1.21 f_v - 1.93 f_v^{\,2}) \times 10^{-11} \times \exp\left[\frac{E_{N_2}}{R}\left(\frac{1}{T_{ref}} - \frac{1}{T}\right)\right] \quad (1)$$

The activation energy for nitrogen, E_{N_2} is assumed to be 24 kJ/mol, α_{N_2} is scale factor, R is the universal gas constant, T_{ref} is 303K and f_v is the volumetric ratio of water in the membrane and is given by;

$$f_v = \frac{\lambda_{mem} V_w}{V_{mem} + \lambda_{mem} V_w} \quad (2)$$

where λ_{mem} is the membrane water content, V_{mem} and V_w are molar volumes of dry membrane and liquid water.

In a PEMFC, concentration gradient across the membrane is the driving force for N_2 diffusion from cathode to anode. Since concentration of a certain species could be related to its partial pressure in a volume, the nitrogen flux is calculated from the partial pressures of N_2 in cathode and anode of the fuel cell.

$$J_{N_2} = K_{N_2} \frac{P_{N_2,ca} - P_{N_2,an}}{t_{mem}} \quad (3)$$

where t_{mem} is the thickness of the membrane and is assumed to be constant in the current simulations.

For flow model of anode and cathode, the model uses mass balance to calculate the inlet and outlet properties of streams. The partial pressures of different species are determined from the properties of the gas streams entering and leaving the system, gas and water crossovers, products formed and depletion of reactants during chemical reactions within the fuel cell stack model. Equations for water transportation across the membrane and losses associated with hydrogen crossover are shown in the table 2.

Fuel cell stack model

Aspen DynamicsTM, which is a simulation tool for process modeling and energy system analysis, is used to construct the system model of the configuration described above. The program contains a vast library of components and controls for standard energy processes, making it a suitable candidate for system level simulations. One such dynamic model is presented by [29] . The PEMFC system studied here is based on previous studies by [1], [24] and [30]. The model code is developed and implemented in Aspen Custom ModelerTM. A simple model of humidifier is also executed into the code. This model which incorporates governing equations for cell electrochemical, polarization overpotentials, heat transfers and water diffusion across the membrane is employed into

Aspen Dynamics and system controls are implemented in order to ensure stable operation of the plant during load changes. Thermodynamic efficiency and net power of the system are determined by the current drawn and voltage produced by the stack. Total energy into the fuel cell is consumed by electrical power output, heat removed by the coolant, heat loss at the stack surface and energy stored by the stack itself. In the current model, a lumped thermal model proposed by [31] is considered. The stack is regarded as a single thermal mass with a heat capacity. With the assumption of stack temperature being equal to coolant temperature at the outlet, heat exchanged with the coolant and hence stack operating temperature could be determined. Subordinate components in the BoP, i.e. anode recirculation and water pumps, air compressor, mixers and heat exchangers are simulated by using default mathematical models contained in Aspen Dynamics library. Table 2 shows a standard set of equations which constitute the model used in the current study.

Table 2. Constitutive equations for PEMFC model.

Average cell voltage	$V_{cell} = E - \eta_{act} - \eta_{ohmic} - \eta_{conc}$	(4)
Nernst equation	$E = \frac{-\Delta\bar{g}_f^0}{n_e F} + \frac{RT}{n_e F}\ln\left(\frac{a_{H_2O}}{a_{H_2} a_{O_2}^{0.5}}\right)$	(5)
Theoretical cell voltage	$E = \frac{-\Delta\bar{g}_f^0}{n_e F} + \frac{RT}{n_e F}\ln\left(P_{H_2}^{-1} P_{O_2}^{-0.5}\right)$	(6)
Change in Gibbs free energy	$\Delta\bar{g}_f^0 = \left(\bar{g}_f^0\right)_{H_2O} - \left(\bar{g}_f^0\right)_{H_2} - \frac{1}{2}\left(\bar{g}_f^0\right)_{O_2}$	(7)
Activation losses in PEMFC	$\eta_{act} = \eta_{act,c} + \eta_{act,a} = \frac{RT}{\alpha_c F}\ln\left(\frac{i+i_n}{i_{0,c}}\right) + \frac{RT}{\alpha_a F}\ln\left(\frac{i+i_n}{i_{0,a}}\right)$	(8)
Concentration overpotentials	$\eta_{conc} = \eta_{conc,c} + \eta_{conc,a} = \frac{RT}{n_e F}\ln\left(1-\frac{i}{i_{\lim,c}}\right) + \frac{RT}{n_e F}\ln\left(1-\frac{i}{i_{\lim,a}}\right)$	(9)
Ohmic overpotentials	$\eta_{ohmic} = \left(r_{el} + r_{ion}\right)\cdot i$	(10)
Ionic resistance in the cell	$r_{ion} = \frac{C_1 \cdot \left[1 + 0.03i + 0.062\cdot\left(T/303\right)^2 \cdot i^{2.5}\right]}{\left(\lambda_{ave} - 0.634 - 3i\right)\cdot\exp\left[C_2\cdot\left(T-303\right)/T\right]}\cdot t_m$	(11)
Membrane water content	$\lambda_{ave} = 0.043 + 17.18a_w - 39.85a_w^2 + 36a_w^3$	(12)
Water vapor activity	$a_w = P_w / P_{sat}$	(13)
Water profile inside cell membrane	$\lambda_{mem} = \frac{\lambda_c - \lambda_a}{t_m}.z + \lambda_a$	(14)

Transfer coefficient for anode	$\alpha_a = \beta \cdot n_{el}$	(15)
Transfer coefficient for cathode	$\alpha_c = (1-\beta) \cdot n_{el}$	(16)
Exchange current density at anode	$i_{0,a} = n_{el} \cdot F \cdot k_a \cdot \exp\left(\frac{(1-\beta) \cdot n_{el} \cdot F \cdot E}{RT}\right)$	(17)
Exchange current density at cathode	$i_{0,c} = n_{el} \cdot F \cdot k_c \cdot \exp\left(\frac{-\beta \cdot n_{el} \cdot F \cdot E}{RT}\right)$	(18)
Net water transportation through membrane	$J_{H_2O} = 2n_{drag}\frac{i}{2F} - \frac{\rho_{dry}}{M_m} D_\lambda \frac{d\lambda}{dz}$	(19)
Water diffusion coefficient	$D_{\lambda>4} = 10^{-6} \exp\left[2416 \cdot \left(\frac{1}{303} - \frac{1}{T}\right)\right] \cdot \left(2.563 - 0.33\lambda + 0.0264\lambda^2 - 0.000671\lambda^3\right)$	(20)
Fuel cell energy balance	$C_t \cdot {dT}/{dt} = \dot{P}_{in} - \dot{P}_{out} - \dot{P}_{el} - \dot{Q}_{loss}$	(21)
Faraday's law	$\frac{dN}{dt} = \frac{I}{n_e \cdot F}$	(22)

Results and discussion

Using the PEMFC stack data and control parameters summarized in table 1, simulations for the system are carried out using Aspen Plus Dynamics program. Reliability of the fuel cell model and dynamic behavior of the system under consideration have already been reported in authors' previous studies [24], [32]. These studies have reported transient response of different components of the system as well as their mutual dependencies on control strategies, thermal management and water transportation of the fuel cell stack under different operating scenarios; such as system start–up and during transitory load changes. Here, simulation results for the effect of nitrogen crossover and associated purging of anode recirculation are presented. Stack temperature range of 60–70°C has been used in simulations of the current system.

Gas Buildup at anode

Based on the permeability of N_2 and partial pressure gradient across the membrane, simulations for the prescribed system were conducted and corroborated against validation data by stack manufacturer [23]. Fig. 3 presents the simulated net nitrogen crossover in the fuel cell stack against the experimental data. The corresponding relative error advocates a reasonable agreement between the simulations and stack trial data.

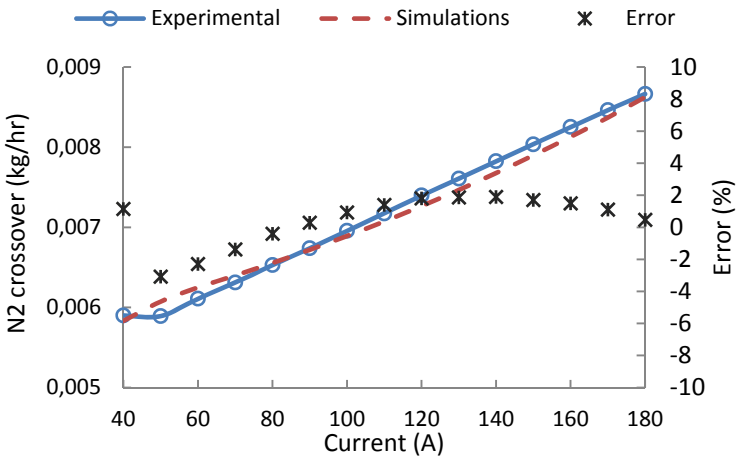

Figure 3. Calculated nitrogen crossover rates against experimental data

Current drawn from the fuel cell is set to a constant 120 A with no purging of the anode recirculation loop. Since pure H_2 is used as the fuel, there is no presence of nitrogen in anode inlet of the fuel cell at the start–up. Fig. 4a shows the N_2 crossover form cathode to anode side of the fuel cell during the start–up operations of the stack. It is observed that as the temperature and water uptake of the membrane increases, N_2 permeance increases, thereby increasing nitrogen crossover from the cathode to the anode side of the cell. An abrupt decline in temperature is noticed at around 120 s, which is due to the control initializations of coolant flows to maintain the stack operating temperature. Details of the control setup and thermal management of the system are reported in [24]. N_2 permeance decreases with the sudden reduction in temperature and subsequently reducing the crossover at that instant of time. However, as the system stabilizes to steady state, the permeance becomes constant but N_2 crossover tends to decrease as can be seen in Fig. 4b. This is due to the fact that N_2 accumulation in the anode reduces the concentration gradient across the cells.

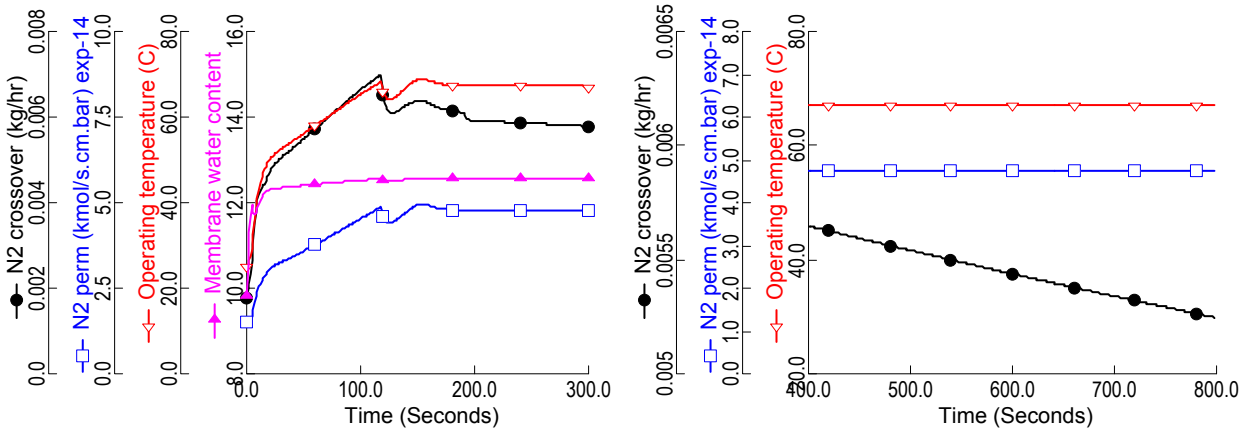

Figure 4. N_2 permeance and crossover rate at (a) fuel cell start–up and (b) Steady–state operations

Depletion of hydrogen in the anode due to nitrogen accumulation leads to a slow decay of the cell voltage. Fig. 5a represents the voltage decay due to increase in N_2 fractions and corresponding decrease in H_2 concentrations in the fuel inlet. Although voltage decay shows a linear relation with nitrogen accumulation, its impact over extended operations results in hydrogen starved regions in the cell resulting in increased cathode overpotential and resistive losses [21]. Another issue related to anode recirculation is the accumulation of water, which clogs flow fields and results in lower concentrations of H_2 as well. Fig. 5b points to the gradual increase in liquid water at anode outlet.

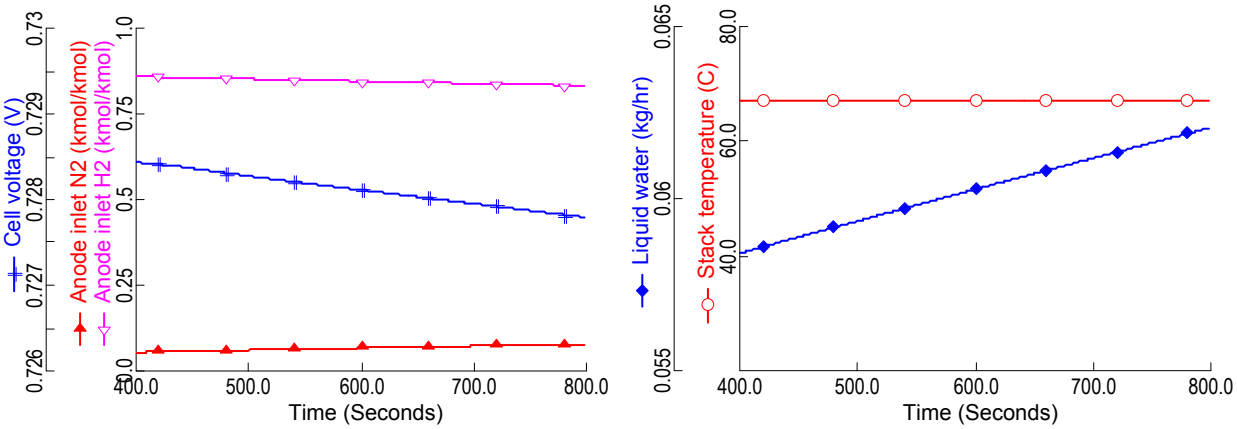

Figure 5. (a) Cell voltage decay due to N_2 buildup and (b) Increment in liquid water at anode exhaust

Anode outlet bleed

As shown above, N_2 accumulation could lead to dilution of hydrogen in the fuel. Moreover, power consumption of recirculation pump increases due to additional flow of nitrogen and water vapor. One way of preventing accumulation of these gases is venting of anode exhaust often called as bleeding. Although N_2 and water are vented out of the system, bleeding also wastes unused hydrogen resulting in lower system efficiency realizing a need for an optimized bleed percentage. Here, different bleed fractions of the anode recirculation stream are simulated and their impact on the system is analyzed. Fig. 6a displays the amount of N_2 present in the anode inlet against different bleed fractions at a drawn current of 120 A.

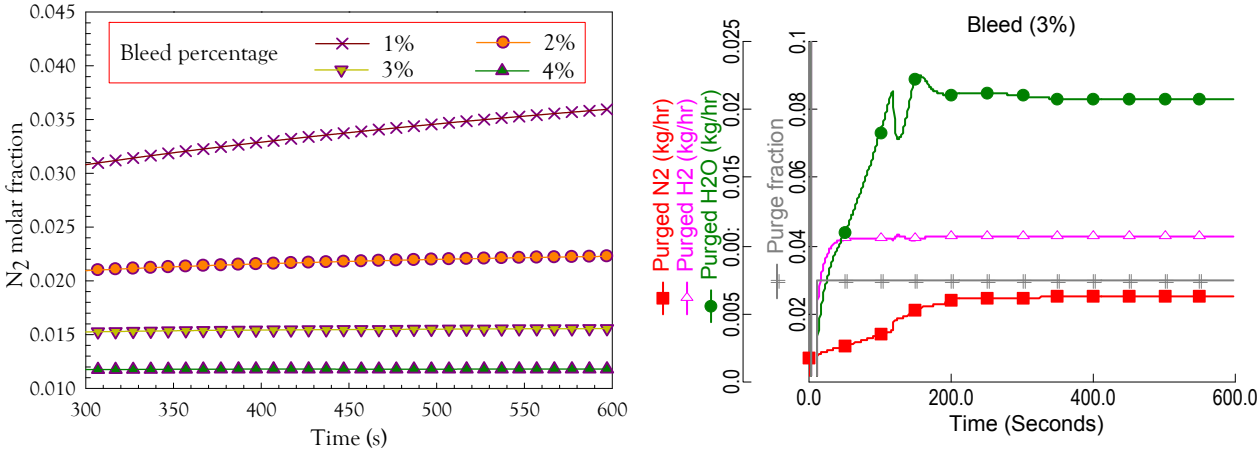

Figure 6. N_2 levels for different bleed fractions at anode inlet and (b) Composition of bleed stream from system start–up

It can be seen that N_2 keeps on increasing when the vent out fraction is 1% and remains constant around 3% of the anode exhaust. At this bleed rate, molar N_2 remains close to 1.5% of the fuel entering the stack. Fig. 6b shows the constituent flow rates of 3 % vented stream. A large amount of water is also vented along with nitrogen. A constant loss of hydrogen at a rate of 0.011 kg/hr (2% of the supplied fuel) would suffice to prevent gas accumulation in anode of the PEMFC.

Anode outlet purge

A purge of the anode recirculation is another method to reduce nitrogen and water levels in the fuel inlet. A purge is initiated by opening of a solenoid valve placed at the anode outlet. This valve opens for a short duration (purge time), removing a portion of gases in the stream. The time between these purges is referred to as purge interval. Though any combination of these could be assumed, here arbitrary values of 0.6s, 0.3s, 0.9s and 60s of purge valve opening time, opening duration, valve closing time and purge interval are selected respectively. Here, a steady state analysis is conducted by drawing a current of 120 A and the valve opening is set to purge 20% of the exhaust stream. Modeling of the valve and its pressure effects have been neglected here as it falls out of the scope of study. However, [14] have studied the behavior of pressure during purge process and reported a uniform distribution of pressures for short purge times as used in current simulations. In addition, it is reported that fluctuations in anode pressure due to frequent purging, also supports liquid water removal from the channels. Fig. 7a shows a semi–stable cell voltage during these purge events. As soon as the purge is initiated, it removes both liquid water and nitrogen gas and recovers the voltage drop caused by reduced active cell sites.

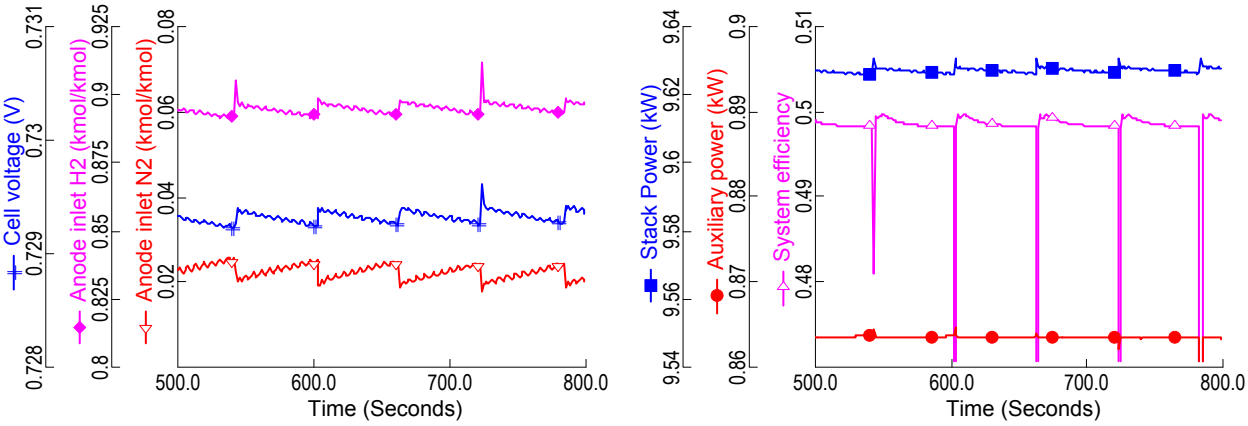

Figure 7. Performance of Fuel cell for fixed purge interval of 60 s, (a) Voltage rejuvenation with semi–stable profile and (b) system efficiency and power during purge sequences

N_2 and H_2 fractions could also be noticed to change with each purge. During the purge intervals, there is a steady buildup of nitrogen which gradually decays the cell voltage which lowers the efficiency. This can be seen in Fig. 7b where efficiency of the system increases with each purge and slowly lowers before the next purge event. It is also noticed that there is an abrupt decline in the system efficiency at purge instances. This is due to the fact that unused hydrogen leaving the purge valve reduces the recyclable amount, thus these drop lines. Change in power consumption of auxiliary components is minimal as only low–power recirculation pump is affected by the purge. Since the total purge time is only 1.8 s and purge interval is 60 s, it is cumbersome to determine the average efficiency lost for long durations of fuel cell operations. Nonetheless, amount of H_2 vented to the atmosphere could be determined to assess the economics of the operations. Fig. 8 explicates that around 0.08 kg/hr (1.2% of supplied fuel) of H_2 is wasted per purge event with interval of 60 s.

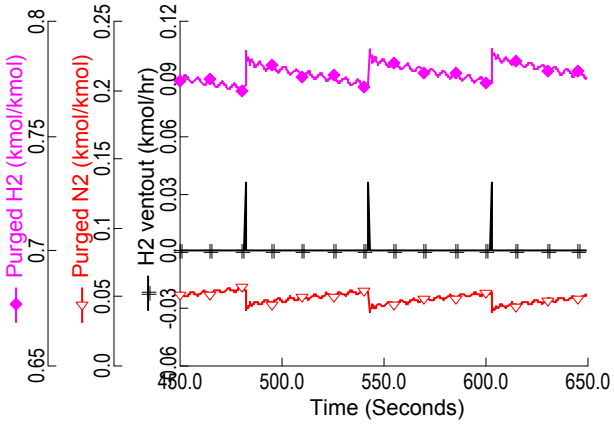

Figure 8. Molar fractions at purge routines and H_2 vent out rate

Automatic Anode purge

As mentioned earlier that in addition to reducing the fuel cell voltage, enrichment of nitrogen could lead to corrosion of the electrodes. With the ageing of the cell membrane it tends to get thinner and due to the degradation, micro cracks and pinhole regions are generated which further increase N_2 crossover. Another approach simulated in the present investigation is the use of an automatic control for optimization of purge intervals. For practical diagnosis of fuel cell systems, nitrogen at anode inlet could be detected by arc emission spectroscopy methods. Signal from these detectors is transmitted to the controller, where it adjusts the parameters for effective purges. An optimum purge sequence would prevent N_2 buildup at a minimum expense of released hydrogen. Optimization of the purge routine could be carried out by manipulation of many variables such as valve opening and closing times, purge time, purge interval and purge stream fractions. Simulations for different combinations of these variables for different power loads would require tremendous amount of time and effort. For the sake of comparison purposes, only purge intervals are chosen to be the manipulated variable in the present simulations.

According to [23], molar N_2 fraction of 5% or less has no or minimal effect on stack life. A purge initiation limit of 3% has been set i.e. the purge event will occur only when N_2 molar concentration of 3% or more is detected at anode inlet. Simulations for two different currents are carried out here. Voltage recovery and efficiency profiles for automatic purging are found to be similar to that of fixed time interval as the purge process is same. However, N_2 crossover in the cell changes with current density as reported by [2]. Typically N_2 crossover increases with current density, as more heat is produced to raise the temperatures and increase nitrogen permeance. Yet in a system such as the one under investigation, system controls maintain the temperature of the stack and prevent excessive gas crossovers. Also, stoichiometric ratios of anode determine the flow rate of supplied H_2 and are inversely proportional to the N_2 concentration in the anode exit stream [9].

Figure 9a shows N_2 and H_2 levels in anode recirculation after purging and corresponding flow rate of hydrogen purged to the atmosphere. When the current drawn during steady state operation is 120 A, H_2 is purged at a rate of 0.08 kg/hr, similar to the rate at fixed interval purge in Fig 8. However, automatic purging interval is found to be around 85 s, saving 15 s per purge. In Fig. 9b, when the current is drawn at 60 A, H_2 purge rate is reduced to 0.06 kg/hr and purge interval is found to be 55 s. This is due to the fact that H_2 flow rate at a low current density is relatively smaller compared to that at a high current density, so is the anode exit flow rate. Therefore, low currents will result in a high N_2 levels in the anode exhaust which will require frequent purging. Fuel losses associated with current case are found to be 0.8% of the supplied fuel. Based on the data from table 1, higher stoichiometric ratios are used at low currents.

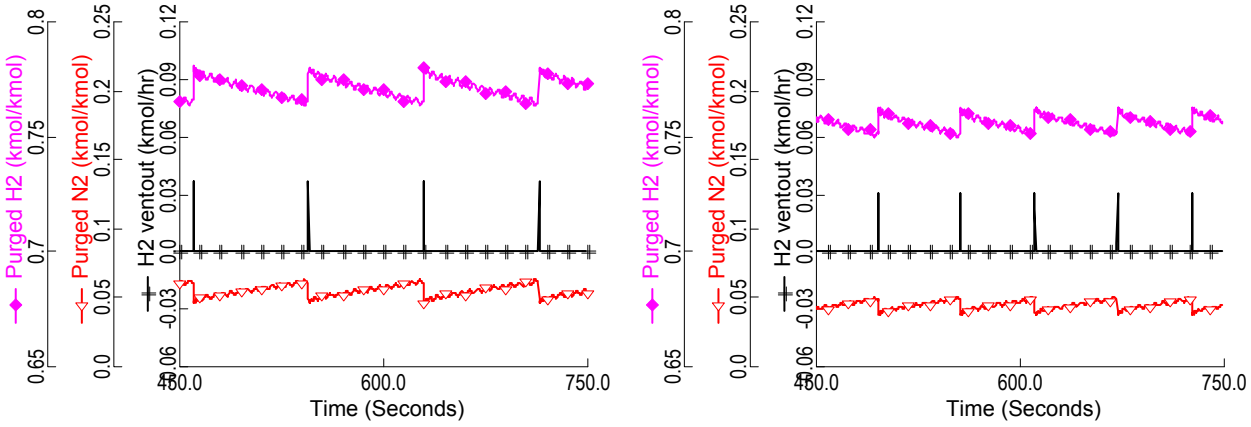

Figure 9. Automatic purge intervals and corresponding molar fractions of purges stream (a) at drawn current of 120 A, and (b) 60 A

Anode purge at load changes

PEMFC systems have to operate at varying load and operating conditions when used in automotive applications. Nitrogen concentration would vary with changing loads which requires an efficient purging strategy to cater these dynamics. For this particular simulation, current load is changed from 120 A to 60 A and vice versa at 380 s and 410 s respectively. Results for different purging methods are presented in Fig. 10 and Fig. 11.

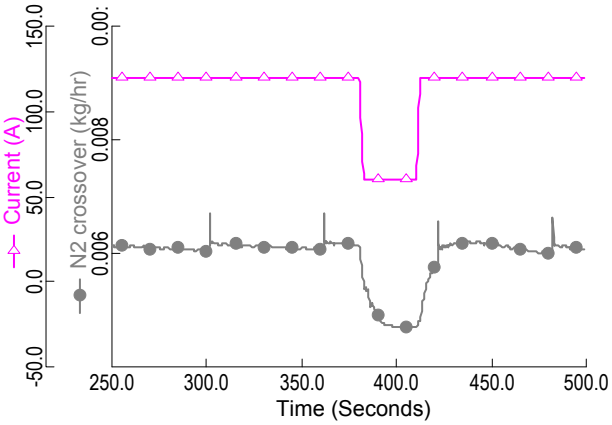

Figure 10. N_2 crossover through membrane for fixed purge interval routine during load changes from 120 A to 60 A and vice versa

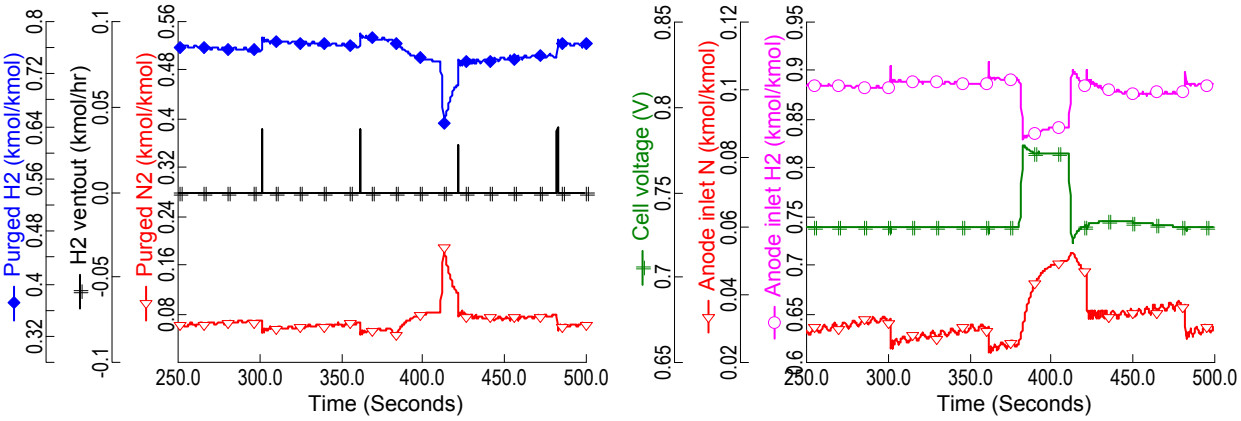

Figure 11. Effect of load changes of 120–60–120 A on fixed purge interval, (a) H_2 purge rate (b) N_2 concentration at anode inlet and cell voltage

Fig. 10 portrays nitrogen crossover during the load changes for a fixed purge interval of 60 s. As the current is decreased, nitrogen flux towards the anode is reduced. N_2 concentration at anode exit also decreases as shown in Fig. 11a. However, N_2 levels at anode inlet tend to increase (Fig. 11b). As explained above, this is attributed to the low residual flows of H_2 at low current densities. On the other hand, when the current is elevated to 120A at 410 s, sudden shortage of H_2 is observed until the time taken by flow valves to adjust. Reduced stoichiometry of hydrogen results in N_2 concentration spike as well. Voltage change as a function of current density is evident in the figure, though voltage revival during purges is not that pronounced.

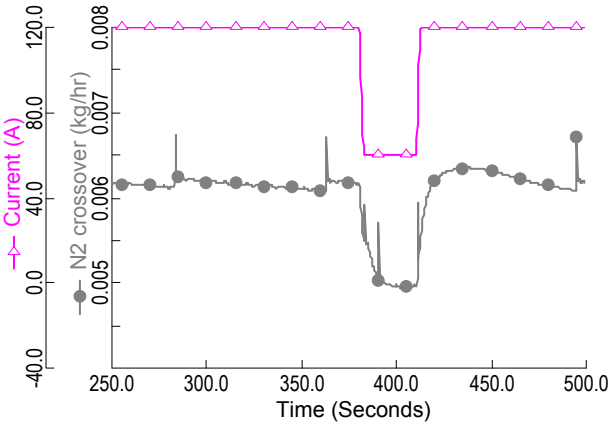

Figure 12. N_2 crossover through membrane for automatic purge interval sequence during load changes from 120 A to 60 A and vice versa

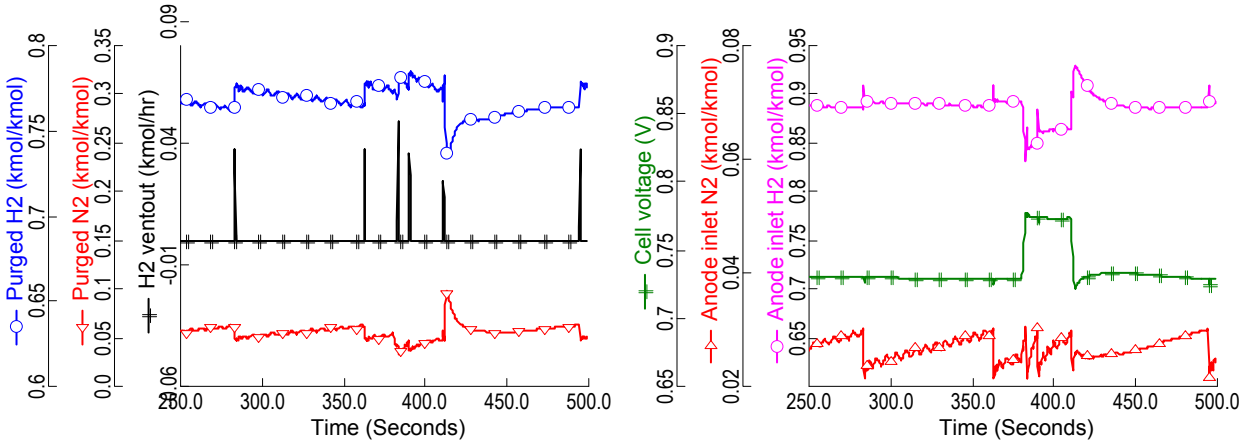

Figure 13. Effect of load changes of 120–60–120 A on automatic purge interval, (a) H_2 purge rate (b) N_2 concentration at anode inlet and cell voltage

Effects of load changes to the nitrogen crossover and system performance during automatic purge are reported in Fig. 12. Nitrogen crossover shows similar trend when compared to fixed time interval. When the current is lowered to 60 A, low residual H_2 increases nitrogen levels at anode exit. As the molar N_2 concentration reaches 3%, automatic purge control activates the purge process. Here again, only purge intervals are varied for automatic purging. It can be seen in Fig. 13a that several instances of purge occur between 380–410 s. Purge rate of H_2 varies with the unused fuel at the anode exit. Unlike fixed time interval, N_2 concentrations at anode inlet are retained to lower levels for automatic purge controls (Fig. 13b). Due to these frequent purges however the amount of wasted fuel will increase to that of fixed purges. Fuel wastage and therefore efficiency of the system operating with automatic purges will depend on the transient load changes.

For steady state case, the system with the anode outlet bleed has the highest amount of fuel wastage at 2% of the supplied fuel. Whereas, the fixed purge and automatic purge routines account for 1.2% and 0.8% of fuel loss respectively. However, during transient load changes, the automatic technique loses more fuel due to frequent purging compared to steady state operations. For the transient case discussed here, the fuel wastage becomes equal for automatic and fixed purging. However, the nitrogen concentration levels remain within the acceptable limits for the automatic purge only. This helps in prevention of carbon corrosion by H2 starved areas formed due to N2 accumulation within the cells, which in turn results in prolonged stack lifetime. Based on the results discussed above, the applicability of nitrogen detectors and automatic purge shows promise as a diagnostic tool for prediction of gas crossovers and act as a building block for devising purge strategies depending upon the load and mode of application.

Conclusions

A comprehensive study on dynamics of nitrogen crossovers in PEMFC system with recirculation was conducted and its effects on purging strategy were discussed. The model developed to predict nitrogen crossover was in good agreement with the design validation data of the stack. The results exhibit that with pure recirculation, voltage and system efficiency declines due to nitrogen accumulation in fuel cell. Different purging methodologies were simulated to address hydrogen dilution issue at reaction sites. Anode bleed out of 3% is found to be the limit for prevention of N_2 buildup and retains the concentration levels to less than 1%. Also, cell voltage degrades linearly with N_2 buildup and rejuvenates at purge sequences. An alternate strategy for automatic initiation of anode recirculation purge by employing nitrogen detectors was simulated. Using the same purge time for various cases, it is shown that purge interval is lowered for low currents mainly due to low H_2 residual flows rates. Moreover, during transient load changes, automatic purge catered well to prevent nitrogen levels from rising when compared to a fixed purge interval strategy. This method has proven to be feasible for predicting gas crossovers during purge sequences at different loads and can be used as a base for optimizing and development of anode purge strategies for PEMFC systems.

Acknowledgements

The authors would like to thank the Danish Energy Agency for financial support and our industrial partner, H2Logic, for their collaboration and technical support.

References

1. Hosseinzadeh E, Rokni M: Development and validation of a simple analytical model of the Proton Exchange Membrane Fuel Cell (PEMFC) in a fork–lift truck power system. *International journal of green energy* 2013; 10(5):523–43.

2. Kocha SS, Deliang Yang J, Yi JS: Characterization of gas crossover and its implications in PEM fuel cells. *AIChE Journal* 2006, 52:1916–1925.

3. Weber: Gas–crossover and membrane–pinhole effects in polymer–electrolyte fuel cells. *Journal of the Electrochemical Society* 2008, 155:B521–31.

4. Reiser CA, Bregoli L, Patterson TW, Yi JS, Yang JD, Perry ML, Jarvi TD: A reverse–current decay mechanism for fuel cells. *Electrochemical and Solid–State Letters* 2005, 8:A273–A276.

5. Meyers JP, Darling RM: Model of carbon corrosion in PEM fuel cells. *Journal of the Electrochemical Society* 2006, 153:A1432–A1442.

6. Bessarabov D: Gas Permeability of Proton–Exchange–Membranes. In *PEM Fuel Cell Diagnostic Tools*. Edited by Haijiang Wang, Xian–Zi Yuan and HL. Boca Raton, Fla.: Taylor & Francis; 2011:558.

7. Ahluwalia RK, Wang X: Buildup of nitrogen in direct hydrogen polymer–electrolyte fuel cell stacks. *Journal of Power Sources* 2007, 171:63–71.

8. Catalano J, Myezwa T, De Angelis MG, Baschetti MG, Sarti GC: The effect of relative humidity on the gas permeability and swelling in PFSI membranes. *International Journal of Hydrogen Energy* 2012, 37:6308–6316.

9. Baik KD, Kim MS: Characterization of nitrogen gas crossover through the membrane in proton–exchange membrane fuel cells. *International Journal of Hydrogen Energy* 2011, 36:732–739.

10. Ismail MS, Hughes KJ, Ingham DB, Ma L, Pourkashanian M: Effects of anisotropic permeability and electrical conductivity of gas diffusion layers on the performance of proton exchange membrane fuel cells. *Applied Energy* 2012, 95:50–63.

11. Zhu WH, Payne RU, Tatarchuk BJ: Critical flow rate of anode fuel exhaust in a PEM fuel cell system. *Journal of Power Sources* 2006, 156:512–519.

12. Tang Y, Yuan W, Pan M, Li Z, Chen G, Li Y: Experimental investigation of dynamic performance and transient responses of a kW–class PEM fuel cell stack under various load changes. *Applied Energy* 2010, 87:1410–1417.

13. Zhai S, Zhou S, Sun P, Chen F, Niu J: Modeling study of anode water flooding and gas purge for PEMFCs. *Journal of Fuel Cell Science and Technology* 2012, 9.

14. Gou J, Pei P, Wang Y: The dynamic behavior of pressure during purge process in the anode of a PEM fuel cell. *Journal of Power Sources* 2007, 162.

15. Wang X, Tajiri K, Ahluwalia RK: Water transport during startup and shutdown of polymer electrolyte fuel cell stacks. *Journal of Power Sources* 2010, 195:6680–6687.

16. Karimäki H, Pérez LC, Nikiforow K, Keränen TM, Viitakangas J, Ihonen J: The use of on–line hydrogen sensor for studying inert gas effects and nitrogen crossover in PEMFC system. *International Journal of Hydrogen Energy* 2011, 36:10179–10187.

17. Promislow K, St–Pierre J, Wetton B: A simple, analytic model of polymer electrolyte membrane fuel cell anode recirculation at operating power including nitrogen crossover. *Journal of Power Sources* 2011, 196:10050–10056.

18. Hou Y, Shen C, Yang Z, He Y: A dynamic voltage model of a fuel cell stack considering the effects of hydrogen purge operation. *Renewable Energy* 2012, 44:246–251.

19. Müller EA, Kolb F, Guzzella L, Stefanopoulou AG, McKay DA: Correlating nitrogen accumulation with temporal fuel cell performance. *Journal of Fuel Cell Science and Technology* 2010, 7:210131–2101311.

20. Siegel JB, Bohac S V, Stefanopoulou AG, Yesilyurt S: Nitrogen Front Evolution in Purged Polymer Electrolyte Membrane Fuel Cell with Dead–Ended Anode. *Journal of the Electrochemical Society* 2010, 157:B1081–93.

21. Yesilyurt S, Siegel JB, Stefanopoulou AG: Modeling and Experiments of Voltage Transients of Polymer Electrolyte Membrane Fuel Cells With the Dead–Ended Anode. *Journal of Fuel Cell Science and Technology* 2012, 9.

22. Choi JW, Hwang Y–S, Seo J–H, Lee DH, Cha SW, Kim MS: An experimental study on the purge characteristics of the cathodic dead–end mode PEMFC for the submarine or aerospace applications and performance improvement with the pulsation effects. *International Journal of Hydrogen Energy* 2010, 35:3698–3711.

23. Ballard Mark9 SSL: Product manual and integration guide. 2008.

24. Rabbani A, Rokni M: Dynamic characteristics of an automotive fuel cell system for transitory load changes. *Sustainable Energy Technologies and Assessments* 2013, 1.

25. Hwang J–J: Thermal control and performance assessment of a proton exchanger membrane fuel cell generator. *Applied Energy* 2013, 108:184–193.

26. Wang Y, Chen KS, Mishler J, Cho SC, Adroher XC: A review of polymer electrolyte membrane fuel cells: Technology, applications, and needs on fundamental research. *Applied Energy* 2011, 88:981–1007.

27. Cheng X, Zhang J, Tang Y, Song C, Shen J, Song D, Zhang J: Hydrogen crossover in high–temperature PEM fuel cells. *Journal of Power Sources* 2007, 167:25–31.

28. Mittelsteadt C, Umbrell M: Gas Permeability in Perfluorinated Sulfonic Acid Polymer Electrolyte Membranes. *MEETING ABSTRACTS– ELECTROCHEMICAL SOCIETY –ALL DIVISIONS CD ROM EDITION–* 2005.

29. Barelli L, Bidini G, Gallorini F, Ottaviano A: Dynamic analysis of PEMFC–based CHP systems for domestic application. *Applied Energy* 2012, 91:13–28.

30. Hosseinzadeh E, Rokni M, Rabbani A, Mortensen HH: Thermal and water management of low temperature Proton Exchange Membrane Fuel Cell in fork–lift truck power system. *Applied Energy* 2013, 104:434–444.

31. Khan MJ, Iqbal MT: Modelling and analysis of electrochemical, thermal, and recetant flow dynamics for a PEM fuel cell system. *Fuel Cells* 2005, 5:463–475.

32. Rabbani A, Rokni M: Start–up Analysis of a PEM Fuel Cell System in Vehicles. *International Journal of Green Energy* 2013, 11:01–21.

Nomenclature

E	theoretical voltage (V)
V_{cell}	average cell voltage (V)
$\dot{P}_{el}$	stack power (kW)
$\dot{P}_{in}$	energy into the fuel cell (kW)
$\dot{P}_{out}$	energy out of the fuel cell (kW)
$\dot{Q}_{loss}$	heat dissipated (kW)
C_t	stack thermal capacitance (kW)
R	universal gas constant $(J/molK)$
T	temperature (K)
F	faraday's constant $(C/molK)$
I	current (A)
N_{cell}	number of cells $(-)$
$\Delta\overline{g}_f^0$	change in Gibbs free energy $(J/molK)$
P_{H_2}	hydrogen partial pressure $(-)$
P_{O_2}	oxygen partial pressure $(-)$
M_m	mol. weight of membrane (Kg/mol)
J_{H_2O}	net water–diffusion flux (mol/scm^2)
D_λ	water diffusion coefficient (cm^2/s)
E_{N_2}	activation energy (kJ/mol)
K_{N_2}	nitrogen permeance $(k\,mol/(s \cdot cm \cdot bar))$
a_{H_2}	hydrogen activity $(-)$
a_{H_2O}	water activity $(-)$
a_{O_2}	oxygen activity $(-)$
i	current density (A/cm^2)
i_n	internal current density (A/cm^2)

i_0	exchange current density $\left(A/cm^2\right)$
$i_{0,a}$	anode exchange current density $\left(A/cm^2\right)$
$i_{0,c}$	cathode exchange current density $\left(A/cm^2\right)$
k_a	anode reaction rate $\left(mol/scm^2\right)$
k_c	cathode reaction rate $\left(mol/scm^2\right)$
n_e	electrons transferred $\left(mol_e/mol_{fuel}\right)$
n_{el}	number of electrons $(-)$
n_{drag}	electro osmotic drag $(-)$
t_m	membrane thickness (cm)

Greek symbols

α_a	anode transfer coefficient $(-)$
α_c	cathode transfer coefficient $(-)$
α_{N_2}	perm scale factor $(-)$
β	symmetry factor $(-)$
η_{act}	activation overpotential (V)
$\eta_{act,a}$	anode activation overpotential (V)
$\eta_{act,c}$	cathode activation overpotential (V)
η_{conc}	concentration overpotential (V)
η_{ohmic}	ohmic overpotential (V)
λ	membrane water content $(-)$
ρ_{dry}	membrane density $\left(g/cm^3\right)$

Appendix E

Paper IV

Rabbani, A & Rokni, M. “Dynamic Simulation of a Proton Exchange Membrane Fuel Cell System for Automotive Applications”, Proceedings of Sustainable Energy & Environmental Protection (SEEP) Conference, Dublin, 2012; 311–316.

Dynamic simulation of a proton exchange membrane fuel cell system for automotive applications

R. A. Rabbani[1] and M. Rokni[2]

1. Technical University of Denmark, Kgs. Lyngby, Denmark; email: raar@mek.dtu.dk
2. Technical University of Denmark, Kgs. Lyngby, Denmark; email: mr@mek.dtu.dk

ABSTRACT

A dynamic model of the PEMFC system is developed to investigate the behaviour and transient response of the fuel cell system for automotive applications. The system accounts for the fuel cell stack with coolant, humidifier, heat exchangers and pumps. Governing equations for fuel cell and humidifier are implemented into the code and are based on adopted mathematical models describing the voltages and current densities and their dependence on operating pressures, temperatures and stoichiometric ratios of the reactant gases. As a result, this model can predict both steady and transient states. The model parameters have been adjusted specifically for a 21.2 kW Ballard stack [1]. This model also incorporates the effects of water cross–over in the fuel cell membrane. Controls for temperatures, pressures, reactant stoichiometry and flows are implemented to simulate the system behaviour for different loads and operating conditions. Simulation results for system start–up and variable loads are discussed. Results for system efficiency, auxiliary power consumption, feed flow effects and water crossover are presented. Transitory effects of liquid water saturation at cathode are also determined. This study can provide sufficient insight for further in–depth analysis of PEMFC and prove to be a basis for efficient control and design methodologies.

Keywords: Dynamic simulation, PEM fuel cell, water crossover, Control system

1 INTRODUCTION

Fuel cells are recognized to be one of the future power supply systems. The proton exchange membrane fuel cells (PEMFC) currently appear to be the preferred fuel cell for a variety of mobile applications, mainly due to its relatively low operating temperature,

quick start–up, high power density and efficiency, system robustness and low degradation due to corrosion.
Fuel cell operating requirements in vehicles are more inflexible than stationary applications. These systems have to operate at varying conditions related to temperatures, pressures, power load and humidity. All the auxiliary components constitute the balance of plant (BoP). These auxiliary components, such as the air and fuel supply system which include compressors and control valves, and the thermal control system which comprise heat exchangers, coolant pumps and air radiators are essential for the successful operation of the fuel cell system. Therefore, system level dynamic modelling will be a useful tool in analysis of PEMFC systems.

There are quite a few PEM fuel cell models available in the literature. Fuel cell and stack level transient modelling is performed in the dynamic model developed by [2]. A simplistic dynamic model based on cathode kinetics was developed in [3]. A dynamic model in MATLAB/Simulink was developed in [4] to investigate fuel cell transient electrical responses under various operating conditions. Issues related to temperature dynamics are dealt and studied by [5], which could predict the effects of temperature and feed flows on system transient behaviour. [6] proposed a transient model to predict efficiency in terms of voltage output, and a thermal model including heat transfer coefficients and energy balance for the stack. A thermal management system for a PEMFC was designed in [7] which was oriented towards the flow fields within the stack. Start–up behaviour of PEMFC stacks at sub–zero temperatures have been studied and reported by few researchers. [8] conducted experiments and validated their model based on the results while [9] investigated effects of sub–freezing temperatures on fuel cell performance and start–up.

Compared to all these studies, the model presented in this work aims at analysis and investigation of a complete PEMFC system and study its transient response to operating parameters such as temperature, humidity, pressure and reactant mass flows. One of the objectives of this work is to devise a control–oriented dynamic model of the fuel cell stack, accommodating the electrochemical, thermal and feed flow models. Therefore, Aspen Plus Dynamics™ is used to develop a dynamic stack model with liquid coolant circuit incorporated in it, which allows for a detailed analysis of the thermal interaction with the surroundings. Moreover, the present model can provide suitable insight to saturated water issues in the fuel cell stack. Two–phase characteristics of concerning material streams are also determined.

2 SYSTEM CONFIGURATION

Figure 1 shows the schematics of fuel cell system analyzed in this study. It includes all the components contained in the system, such as PEMFC stack, air compressor, humidifier, pumps, heat exchangers and radiator for the cooling circuit, flow valves and

controllers. Compressed air is cooled and humidified before entering to the cathode of the stack. On the other side, pressurized hydrogen from storage tank is fed to the anode of fuel cell. Since a higher fuel stoichiometry is maintained, anode exhaust is recirculated back to the feed stream via a recirculation pump.

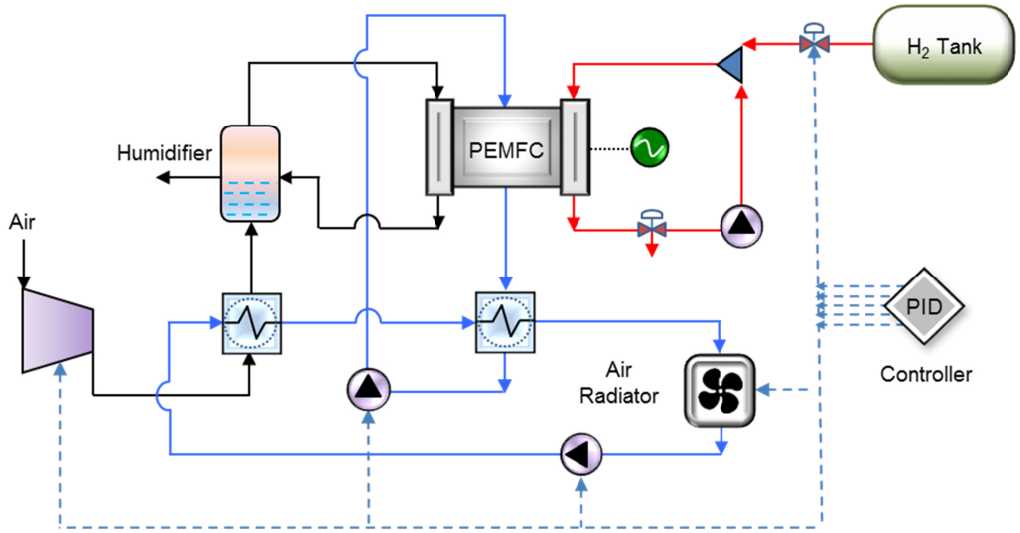

Figure 1. Schematic of a complete PEM fuel cell system with auxiliary components

Heat produced in the stack is absorbed by the coolant which circulates in a circuit associated with the stack and a heat exchanger. An external cooling loop, connected to the aforementioned heat exchanger, in turn cools the water in the internal circuit. This circuit also comprises of a heat exchanger to precool air into the fuel cell and an air radiator for heat rejection. Flow of water is regulated by pumps in the respective circuits.

In this study, a Ballard fuel cell stack [1] has been specifically adapted. The model, which is based on equations adopted by [10], however, contains some parameters which are attributed to the physical characteristics of the system, as well as on operating conditions and membrane properties. Some of these operating conditions for the Ballard stack are shown in Table 1. Current research aims to build up a system which meets the requirements of actual stack running under recommended conditions. The fuel cell stack contains 110 cells with the cell area equal of 285 cm^2. Operating temperature of the stack is maintained around 60–70°C. Maximum power produced from the described stack is 21.2 kW corresponding to a current of 300A; however it is generally operated at lower current ranges to reduce ohmic and concentration overpotentials and thus higher efficiencies.

Table 1. Operating conditions for fuel cell stack recommended by manufacturer (Ballard).

Stack power (kW)	Fuel inlet pressure (bar)	Air inlet pressure (bar)	Inlet temperature (°C)	Operating temperature (°C)	Fuel stoichiometry	Air stoichiometry
1.4	1.15	1.08	60	61	6.3	5.1
2.7	1.16	1.10	60	63	3.4	2.4
5.1	1.31	1.17	60	66	2.2	1.8
9.7	1.55	1.38	60	67	1.7	1.8
18.0	2.00	1.80	60	68	1.6	1.8
21.2	2.20	2.00	60	70	1.6	1.8

Due to the lack of sufficient experimental data, it is assumed that the inlet air flow is optimally humidified after passing through the humidifier. The relative humidity of the air entering the cathode is set to 95% in the calculations; although other values can be chosen. This assumption could be justified as it is very close to the real operational conditions. On the anode side, there is no humidifier and the fuel can reach the desired humidity by means of recirculation and water production at anode exit.

Figure 1 only represents controllable connections initiating from the controller. In calculation as well as reality, the control unit collects information from various temperature, pressure and flow transmitters in addition to current and voltage data from the fuel cell. Here a simplified view of the system is presented.

3 METHODOLOGY

The characteristics of the PEMFC system described above are implemented in Aspen Plus Dynamics ™ which is a simulation tool for process modelling and energy system analysis. The program contains a vast library of components and controls for standard energy processes. The PEMFC stack model presented in this study is based on a model developed by [10]. Concentration losses are neglected in the present study, which is justified by the fact that the system does not run at such high current densities where the concentration overpotentials becomes significant. Models for fuel cell and humidifier are also implemented into the code and are based on adopted mathematical models describing the voltages, current densities and their dependence on operating pressures, temperatures and stoichiometric ratios of the reactant gases. This model which incorporates governing equations for cell electrochemical, polarization overpotentials, heat transfers and water diffusion across the membrane is implemented into ASPEN Plus Dynamics and system controls are implemented in order to ensure stable operation of the plant during load changes. The thermodynamic efficiency and

net power of the system are determined by current drawn and voltage produced by the stack. The total energy into the fuel cell is consumed by the electrical power output, heat removed by the coolant, heat loss at the stack surface and energy stored by the stack itself. In the current model, a lumped thermal model proposed by [6] is considered. The subordinate components in the BoP, i.e. anode recirculation and water pumps, air compressor, mixers and heat exchangers are modelled using the default mathematical models provided in Aspen Plus Dynamics.

4 CONTROL SYSTEM

This section presents methodology of controlling system parameters and operating conditions for the system to have a stable operation. Classic proportional–integral (PI) controllers, which are widely used in industrial control systems, are employed to regulate different components and flow streams. Key parameters to be controlled in the proposed system are reactant inlet stoichiometries, inlet pressures, coolant inlet and operating temperatures of the stack.

As shown in Table 1, the recommended fuel and air stoichiometries for the selected fuel cell stack and their inlet pressures, temperature difference between stack inlet and outlet need to be controlled. It can be seen that at low current loads, high amounts of excess reactant flows are desired. This is due to the fact that at low power consumption and low pressures, water formed due to the reaction in the cathode side of the cells needs to be ejected out of the stack, which is done by supplying high amounts of air. Therefore, an algorithm based on the above figure is developed to be the process variable for the PI controller, which regulates the compressor power in order to maintain the desired oxygen ratio. Similarly, an algorithm for controlling hydrogen flow is devised along with a PI controller, which regulates the control valve opening for optimal fuel supply.

Thermal management in PEMFC systems is of vital importance, basically due to the fact that heat produced in the selected fuel cell cannot be dissipated by convection and radiation through the stack surface. A consistent and stable operation of around 70°C thus requires a cooling system, preferably with a liquid coolant. Since the operating temperature of the fuel cell is not very high, a low temperature difference with the ambient requires having a large heat transfer surface. Therefore, an efficient thermal control system becomes of substantial importance to ensure optimum system performance. In this case, the temperature in the stack can be controlled by the coolant flow rate which acts as an input signal and is controlled by the PI controller. Based on Ballard recommendations, an algorithm for start–up, shut–down and normal operations is thus developed which sets the process variable for the controller. Coolant flow is manipulated by sending output signals to the driving pump. Temperature of the coolant entering the stack can similarly be controlled by the flow of water in the external circuit. Control signal to the associated pump regulates the electrical power of the pump and

hence the coolant inlet temperature into the stack. In a similar fashion, the temperature of water in the external circuit is dependent on radiator fan speed. PI controllers are used to regulate the fan speed as well.

5 RESULTS AND DISCUSSION

Reliability of the suggested model has been verified and validated against experimental data by [10], where the characteristics of the model were studied at various operating temperatures and power loads. As suggested by the manufacturer, stack temperature range of 60–70°C has been used in the simulations of the current system. In case of PEMFC, dynamic behaviour of a start–up is of particular importance to ensure a short start–up time and an efficient operation. In current simulations, the initial temperature of the stack is assumed to be 25°C. Other parameters and operating conditions are selected from section 2.

Here, results for a start–up case are summarised, when a current corresponding to a specific power load is drawn from the stack. As can be seen in the Fig. 2a, when the stack is started at current of 60 A, it takes approximately 300 seconds to reach stable operating temperature. At start, the flow in cooling circuits is set to the lowest value since it is desired to raise the stack temperature to its optimal operation. Coolant flow in the internal circuit is fixed to 290 kg/hr as recommended by the manufacturer. Flow in the internal cooling circuit increases, once the stack temperature difference increases by 15°C. Flow in external circuit is regulated to maintain stack inlet temperature of internal cooling circuit. Air flow in radiator starts to maintain temperature of external cooling loop to around 50°C. It can be observed that the voltage reduces abruptly when simulation time is around 155 seconds. At this stage, the decrease in cell temperature and voltage is caused by the sudden increase in coolant flow into the stack, which aims to maintain the stack operating temperature.

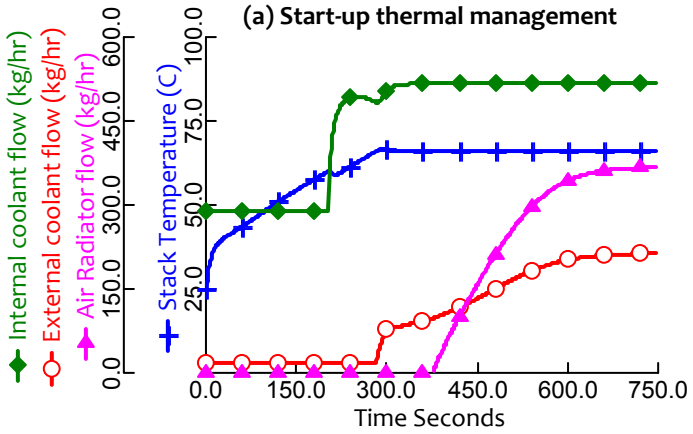

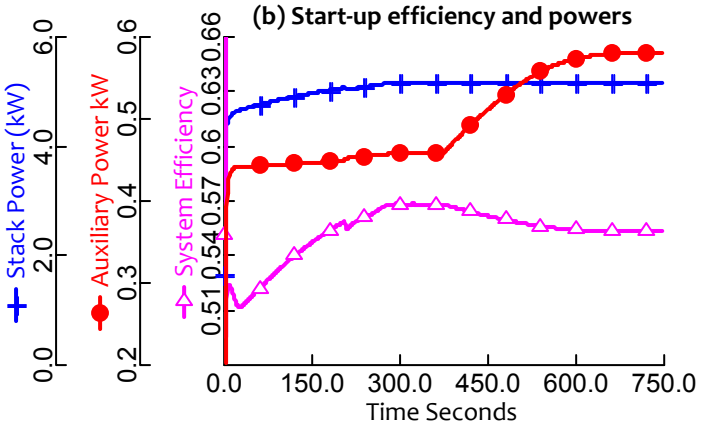

Figure 2. System start–up (a) Stack temperature and corresponding coolant flows at current of 60A, (b) System efficiency, stack power output and power consumed by auxiliary components

Overall efficiency of the system is as much affected by compressor and fan, as by the fuel cell stack itself. Is can be observed from Fig. 2b, that power produced by the stack increases with operating temperature untill it reaches steady–state conditions. Also, power consumed by the air compressor becomes constant after a few seconds into the start. Although, efficiency of the system follows a similar trend, it decreases once the radiator fan is turned on at around 370 seconds. Together, air compressor and radiator consume 10% to that of stack power, whereas a coolant and recirculation pumps account for 1.0–1.3% of it. This is also noticed in figures above; increase in internal and external coolant flows at time 200 and 370 seconds respectively, elevates the auxiliary power consumption to a very small extent as compared to air compressor and radiator.

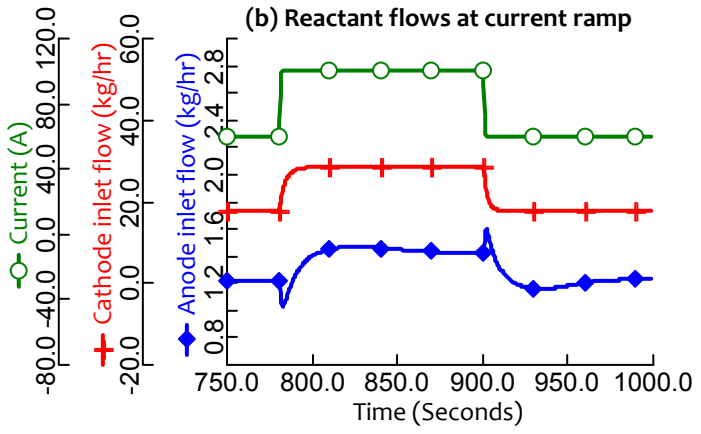

In addition to the start sequence of the aforementioned model, transitory effects under variable load are investigated as well. An instance of load change, when current is ramped from 60 A to 100 A at a rate of 20 Amperes per second and vice versa, is presented in Fig. 3a and its effect on cell voltage is examined.

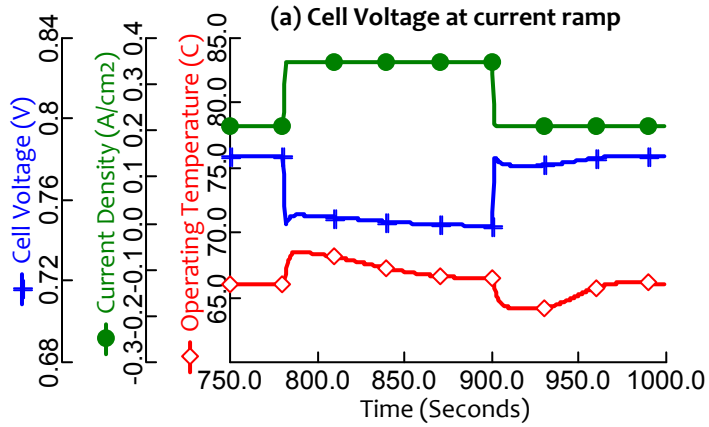

Figure 3. Current ramp–up from 60–100A and vice versa: (a) Changes in cell voltages and operating temperature, (b) Variations in fuel and air inlet flows

Decline in voltage potential at increase of current density is a well–established fact. However, it is also noticed that cell voltage is also a function of operating temperature and pressure. Since, pressures of the reactants are already regulated to be at the optimum; here we will discuss temperature dependency of developed potential differences in the cell. Voltage decreases steadily with the decrease in operating temperature. This fact is due to the reason being fast reaction kinetics at the electrodes of individual cell sites. The opposite could also be observed when the current is reduced back to 60A.

Fig. 3b depicts the variations in reactant inlet flows when the load on fuel cell is varied. As expected, the air flow into the cathode, regulated by a controller, increases when the current is ramped up and steadies along with the system. It is however interesting to notice the fluctuations in the anode inlet. Since anode inlet is supported by recirculation from anode exhaust, the changes within the stack influence it considerably. Although, anode flows also tend to increase as the current is increased, they are affected by the water content in the anode outlet (70% mass fraction), which depends on the net water crossover within the cell. Initial peaks at both load changes are attributed to the electro–osmotic drag which is a function of current density.

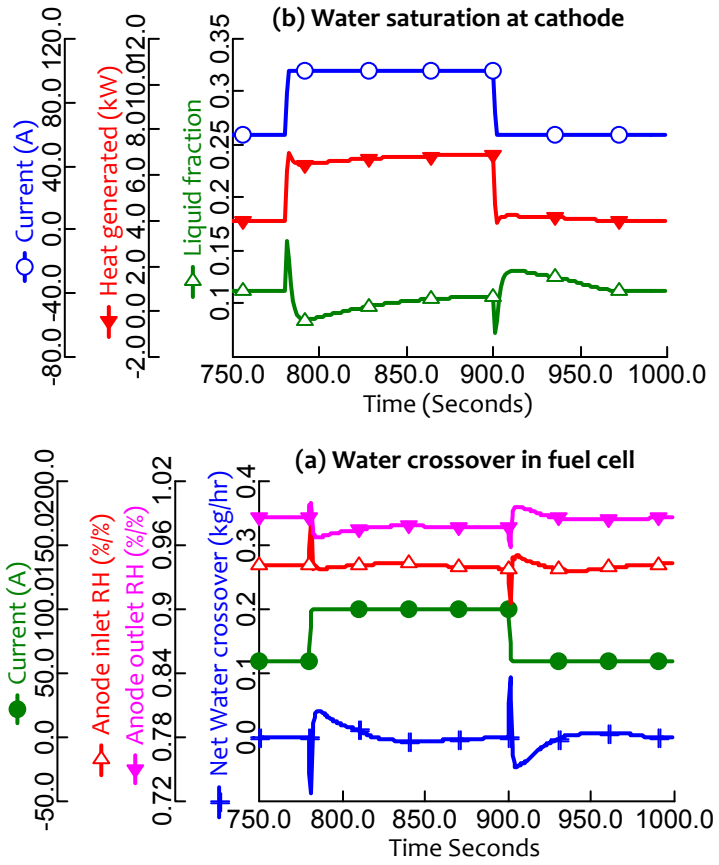

Figure 4. Current ramp–up from 60–100A and vice versa: (a) Amount of liquid water at cathode outlet, (b) Variation in net water crossover and anode RH.

Water management is a critical issue since the performance of PEM fuel cell is strongly influenced by its internal water distribution. As discussed above, water crossover within the cell influences anode inlet stream. Fig. 4a shows net water diffusion in the cell when the current is changed from 60A to 100A and back. At high currents, more water is produced in the cathode which supports back–diffusion towards the anode until the system reaches back to steady–state and there is almost no net water crossover. The peaks observed at the start of current change are due to electro–osmotic drag as mentioned above. Effect of water distribution can also be observed in anode inlet and outlet relative humidities. Whereas for the cathode, since it is assumed that air enters at a constant relative humidity of 95%, the outlet humidity is always above 100%. Therefore, results for only anode are discussed here.

Removal of water from the cathode is dependent on stack temperature and pressure drop. Temperature is the more critical factor, since at high temperature the water will be in the vapour state and easier to remove. Inlet humidities also contribute to liquid water saturation in the fuel cell, which is reported in [11]. It can be seen in Fig. 4b, that the amount of liquid water at cathode decreases at high currents. Heat produced by cell

reactions elevates the stack temperature, thereby reducing saturated water at the outlet. On the other hand, reduction in stack current and temperature increases the liquid water. Therefore, at low temperatures and currents, water removal is the dominant factor and stoichiometries are determined by the minimum flow rates required for water removal which in the present case are more than adequate to provide the necessary concentrations. Moreover, condensation of water at cell sites produces additional heat which requires higher coolant flows to maintain the stack operating temperature, though it does not affect the system efficiency to a greater extent, since liquid pumps do not consume that much power.

6 CONCLUSIONS

This work has presented a comprehensive dynamic model of a fuel cell system along with the BoP. The model is oriented towards the control of associated operating conditions for the fuel cell module. Main contributions of the proposed model are attributed to the system response methodology, which incorporates stack thermal behaviour in addition to fuel cell electrochemistry and flow mass and energy balance. Emulation of the presented system shows that the results are in good agreement with the manufacturer's data. It is observed that voltage system efficiency increase with operating temperature. Air radiator does not affect system start–up, though consumes 10% of stack power together with the air compressor. Furthermore, water crossover in the stack affects the flows and humidity in anode recirculation. Also, removal of liquid water from cathode is dependent on operating temperature. Further analysis is required to study water diffusion in the cell, however based on these results; this model can be used for optimizing and designing operational strategies for PEMFC systems for automotive applications.

ACKNOWLEDGEMENT

The authors would like to thank the Danish National Advanced Technology Foundation for financial support and our industrial partners, H2Logic, for their collaboration and technical support.

REFERENCES

[1] Ballard Mark9 SSL, "Product manual and integration guide." 2008.

[2] S.–K. Park and S.–Y. Choe, "Dynamic modeling and analysis of a 20–cell PEM fuel cell stack considering temperature and two–phase effects," *Journal of Power Sources*, vol. 179, no. 2, pp. 660–672, 2008.

[3] M. Ceraolo, C. Miulli, and A. Pozio, "Modelling static and dynamic behaviour of proton exchange membrane fuel cells on the basis of electro–chemical description," *Journal of Power Sources*, vol. 113, no. 1, pp. 131–144, 2003.

[4] J. Jia, Y. Wang, Q. Li, Y. T. Cham, and M. Han, "Modeling and Dynamic Characteristic Simulation of a Proton Exchange Membrane Fuel Cell," *IEEE Transactions on Energy Conversion*, vol. 24, no. 1, pp. 283–291, 2009.

[5] G. Vasu and A. K. Tangirala, "Control–orientated thermal model for proton–exchange membrane fuel cell systems," *Journal of Power Sources*, vol. 183, no. 1, pp. 98–108, 2008.

[6] M. J. Khan and M. T. Iqbal, "Modelling and analysis of electrochemical, thermal, and recetant flow dynamics for a PEM fuel cell system," *Fuel Cells*, vol. 5, no. 4, pp. 463–475, 2005.

[7] S. Asghari, H. Akhgar, and B. F. Imani, "Design of thermal management subsystem for a 5kW polymer electrolyte membrane fuel cell system," *Journal of Power Sources*, vol. 196, no. 6, pp. 3141–3148, 2011.

[8] Y. Li, S. Xu, Z. Yang, and Y. Li, "Experiment and simulation study on cold start of automotive PEMFC," pp. 2166–2170, 2011.

[9] Q. Yan, H. Toghiani, Y.–W. Lee, K. Liang, and H. Causey, "Effect of sub–freezing temperatures on a PEM fuel cell performance, startup and fuel cell components," *Journal of Power Sources*, vol. 160, no. 2, pp. 1242–1250, 2006.

[10] E. Hosseinzadeh and M. Rokni, "Development and validation of a simple analytical model of the Proton Exchange Membrane Fuel Cell (PEMFC) in a fork–lift truck power system," *International journal of green energy*, vol. To be publ, 2012.

[11] K. H. Wong, K. H. Loo, Y. M. Lai, S.–C. Tan, and C. K. Tse, "A theoretical study of inlet relative humidity control in PEM fuel cell," *International Journal of Hydrogen Energy*, vol. 36, no. 18, pp. 11871–11885, 2011.